Università degli Studi di Firenze
Dottorato di Ricerca in Scienze Chimiche XIV ciclo

Magnetism and magnetic anisotropy of spin clusters

Tesi di Dottorato di

Lorenzo Sorace

Coordinatore:
Prof. Giacomo Martini
Università di Firenze

Tutore:
Prof. Dante Gatteschi
Università di Firenze

Novembre 2001

CONTENTS

1. Introduction

Molecular magnetism is a rapidly developing field of research aiming to use molecular building blocks to obtain new types of magnets, whose properties are different from those of the classical magnets based on metallic or ionic lattices. The initial development tried to accept the challenge of synthesizing molecular magnets characterized by spontaneous magnetization at temperatures higher than room temperature. This resulted in two classes of materials[1,2] ordering as bulk ferrimagnets above 300 K. Later the interest shifted back to magnetic molecules themselves understood as zero dimensional magnetic materials. In this case the challenge was that of making magnetic molecules as large as possible in order to investigate the fascinating area of mesoscopic matter. A beautiful example of where chemical ingenuity can lead is a quasi spherical cluster comprising thirty iron(III) ions which was reported by Muller et al..[3,4] But finite size molecules, as opposed to one-, two- and three-dimensional structures are also of interest as test tubes in which to experiment the best conditions for designing molecular materials with expected magnetic properties. I will refer to this class of molecules as spin clusters, defined as molecular systems made up of more than one center bearing unpaired electrons and whose magnetic properties are largely determined by the interactions between the spin carriers. As a consequence the resulting magnetic properties of these systems are different from the simple sum of those of the single centers, either open-shell organic molecules or paramagnetic metal ions. The use of the techniques of molecular and supramolecular chemistry to fine tune these properties has been one of the key idea at the basis of the rapid development of molecular magnetism.[5] Indeed the implementation of appropriate strategies to assemble spin carriers in molecular systems may lead to obtain magnetic molecular materials with predetermined properties. Using this approach, molecules which shows magnetic behavior usually associated with solid state extended systems have been synthesized,[6-8] and it has been possible to observe for the first time phenomena which have long been theoretically debated.[9-10] The main

advantage in using the molecular approach for the synthesis of magnetic materials is the possibility of obtaining crystalline materials in which the magnetic systems have identical and well defined properties and orientation, and are much easier to vary. Furthermore, it appears promising in order to obtain materials showing properties usually not associated with magnetism, like solubility in organic solvents or optical transparency to the light and to develop materials showing novel association of physical properties.[11]

To achieve these goals it is necessary to have available different building blocks through which arranging supramolecular architecture with desired magnetic properties: among these, molecules which are characterized by high spin states are obviously particularly appealing. These includes polyradical molecules with intramolecular ferromagnetic coupling between the spins: the use of such ligands coordinated to transition metal ions may result in the assembling of extended structures, and if coupling of suitable intensity is obtained between the radicals two or three dimensional structures with enhanced magnetic features may be obtained. In fact, the exploitation of the coordination properties of open shell ligands to induce large direct exchange interactions between these and the transition metal ions and to obtain the desired supramolecular architecture proved particularly successful. Among the radicals employed, nitronyl-nitroxides were intensively investigated but to obtain larger exchange coupling to the metal ion the use of more powerful donor ligands it is necessary and on this respect the use of semiquinone and poly-semiquinone ligands seems very promising.

It is clear that for a clever design of magnetic molecular materials it is necessary to have simple models available which can be used by the synthetic chemists to decide to use one metal ion or another, or a bridging ligand rather than another, in order to induce ferro- or antiferro-magnetic coupling between the spin carriers. On this respect the role of the Kahn's model,[12] which translated in the molecular orbital oriented language of the 80's the Goodenough-Kanamori rules[13-15] cannot be underestimated. More recently it has become possible also to quantitatively calculate the coupling constants using DFT approaches,[16-18] with an accuracy that only few years ago was unthinkable of. We may be now then safely state that the control of the sign of the magnetic interaction between the building blocks of molecular materials is a solved problem, at least at the isotropic level.

The control of the sign and the intensity of the magnetic interaction is however not sufficient if the magnetic properties of the materials must be efficiently designed. In fact the other important aspect which must be taken into consideration is magnetic anisotropy. This

is well known to affect important properties like the hysteresis cycle,[19] thus determining whether a material must be considered as a soft or a hard magnet. In recent years some attempts have been made to introduce large anisotropy in molecular materials, and hard magnets have been obtained.[20,21] Recently, anisotropy has been shown to play a major role in determining the peculiar magnetic properties of some transition metal ion clusters, which behave like superparamagnets and show hysteresis of the magnetization cycle at low temperature. For these systems, which have been collectively termed Single Molecule Magnets,[6] the origin of the slow relaxation of the magnetization is purely molecular and it is related to the presence of an anisotropy barrier due to the zero field splitting of the ground S multiplet. For a pure easy-axis molecular nanomagnet with integer spin state the barrier to the reorientation of the magnetization is given, at the simplest level of approximation, by DS^2, which is the energy difference between the highest $|M_S|$ value and M_S=0.[§] This situation is usually represented by a double well potential (Figure 1.1), with M_S>0 (spin down) states on the left side and M_S<0 (spin up) on the right one. When the thermal energy is larger than the barrier the magnetization freely fluctuates while below a given temperature the magnetization is frozen in one of the two minima. The magnetization relaxation process is then thermally driven and the relaxation time follows an Arrhenius law $\tau=\tau_0 exp(-\Delta E/kT)$, where ΔE is the height of the anisotropy barrier. It is then clear that to obtain a longer relaxation time it is necessary to get higher spin molecules with large easy-axis anisotropy. Up to now the highest blocking temperature is retained by the first ever discovered single molecule magnet, $Mn_{12}O_{12}(CH_3COO)_{16}(H_2O)_4$, hereafter ***Mn12***, characterized by a ground spin state S=10 and by $D\simeq$0.5 cm^{-1}. Provided that some mixing between the initial and the final states is achieved, i.e. that some degree of transverse anisotropy is present, the magnetization can also relax via underbarrier quantum tunnelling. Macroscopic Quantum Tunnelling of the magnetization was first reported in 1996 for ***Mn12***[22,23] in the thermally activated regime (i.e. tunneling was occurring between higher lying $|M_S|$ states) and soon after for an octanuclear iron cluster $Fe_8O_2(OH)_{12}(tacn)_6$ (where tacn= triazacyclononane) hereafter ***Fe8***,[24] for which the pure quantum tunneling regime was first attained. The different magnetic behaviour for the two clusters was readily traced back to the lower height of the barrier in ***Fe8*** with respect to Mn12 and to its pronounced biaxial character, demonstrated both by HF-EPR and INS measurements.[25,26] Indeed, off-diagonal terms in the spin hamiltonian both at second and fourth order mix the multiplets on the two sides of

[§] For semi-integer ground spin state the barrier height is given by $\Delta E=D(S^2-1/4)$

the barrier and eventually lead *Ms* not being anymore a good quantum number; this is especially true for small |*Ms*| values. A recent study on a derivative of ***Fe8*** with larger transverse anisotropy than the parent original system confirmed this interpretation showing that the tunneling rate for this system is larger than in standard ***Fe8***.[27]

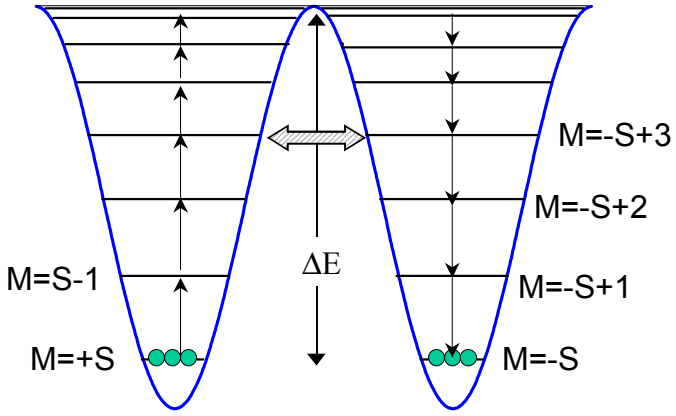

Figure 1.1 *A schematic picture of the magnetization relaxation process in Single Molecule Magnets. The vertical arrows represent the relaxation in the Arrhenius regime, while the horizontal one represents the thermally activated quantum tunneling process.*

It is clear from these brief remarks that in order to successfully design and synthesize new single molecule magnets and/or molecular systems showing peculiar quantum phenomena it is absolutely necessary to accurately define the factors that determine the axial and transverse magnetic anisotropy in a spin cluster. The first step to fulfill this requirement is obviously an accurate measurement of the anisotropy parameters. This means not only the determination of their quantitative values - which is by no means a trivial task - but also - when possible - the determination of their orientation with respect to the molecular frame, which requires measuring single crystals. The necessity of developing measurement techniques capable of resolving the large anisotropies of these systems without loosing in sensitivity is then evident.[28] In this sense, the recently developed techniques of Cantilever Torque Magnetometry[29] and micro-SQUID magnetometry[30] and the advances in HF-EPR spectroscopy played a major role in increasing our knowledge of these systems. The latter technique proved particularly powerful for gathering detailed information on the

magnetic parameters, and then about the factors governing the low temperature spin dynamics of different single molecule magnets.

Once that the experimental characterization of the anisotropy in spin clusters has been achieved it is absolutely necessary to develop suitable models for the interpretation of the results, which may help to design new systems with expected characteristics. Unfortunately inclusion of anisotropy in DFT based calculations is still far from the required level of accuracy and the rationalization of anisotropy in magnetic molecular materials is then still mainly based on the use of simple considerations about the corresponding anisotropy of the building blocks. Ligand field theories, which have long been used for the rationalization of anisotropic properties of transition metal ions,[31] may then in principle provide a useful way to get also a quantitative estimate of the resulting anisotropy in molecular clusters. While earlier applications of ligand field theory were using perturbative approaches and idealized symmetries due to the inherent limitation of computing facilities of that time, the current availability of computer programs which accomplish the complete diagonalization of the ligand field matrix considering the real structure of the molecule can help one in rationalizing the anisotropy of single ions in term of their electronic structures. To further investigate the limits and the potentialities of this approach new experimental data on simple mononuclear systems are absolutely necessary: on this respect, the possibility opened by HF-EPR spectroscopy of addressing non-Kramers ion systems with large anisotropy - usually silent at conventional EPR frequencies - may provide us with a new testing ground. [32-34]

Up to now, the situation is much less advanced for what concerns our knowledge of the key factors affecting the magnetic properties of systems containing orbitally degenerate magnetic centers, like rare-earth ions. For these ions it has not been possible to work out simple relations which may help in the design of molecules with predetermined exchange interactions. This is an unfortunate situation because rare earth ions, with their large and anisotropic magnetic moments, are appealing building blocks in the molecular approach to magnetic materials.[19] Indeed, they have long been exploited in solid state physics to vary the compensation temperature of permanent magnets and to affect the magnetic properties of extended lattices. On this respect the analysis of the magnetic behavior of simple molecular systems containing rare-earth ions exchange coupled to isotropic spin carriers is of fundamental importance to develop suitable models for the rationalization of the exchange interactions in these systems.

This thesis is organized as follows: Chapter 2 is dedicated to a brief survey of the main features of HF-EPR, while in Chapter 3 calculation models of spin hamiltonian mainly based on ligand field theories will be covered. Particular attention will be paid to the Angular Overlap Model, which we have employed with some success in the rationalization of anisotropic properties of both isolated transition metal ions and of spin clusters. In Chapter 4 the results of a thorough multitechnique approach to characterize anisotropic properties and spin dynamics of description of the properties a new SMM of apparent structural simplicity will be presented. Finally the metal-radical approach is faced in Chapter 5 and 6 by magnetically characterizing several systems containing semiquinones radical ligands. In the former chapter the use of polyradical ligands as suitable building blocks to create new extended lattices is investigated whereas in the latter the structural and magnetic properties of a simple series of rare-earths containing complexes will be investigated with the aim of obtaining some useful hints for the rationalization of the magnetic coupling in these systems.

References

1. J. M. Manriquez, Yee G. T. , R. S. McLean, A. J. Epstein, and J. S. Miller, *Science* **252**, 1415 (1991).
2. S. Ferlay, T. Mallah, R. Ouahè, P. Vellet, and M. Verdaguer, *Nature* **378**, 701 (1995).
3. A. Muller, P. Kogerler, and A. W. M. Dress, *Coord. Chem. Rev.* **222**, 193 (2001).
4. A. Muller, M. Luban, C. Schroder, R. Modler, P. Kogerler, M. Axenovich, J. Schnack, P. Canfield, S. Bud'ko, and N. Harrison, *ChemPhysChem* **2**, 517 (2001).
5. O. Kahn, *Magnetism: A Supramolecular Function* (Kluwer, Dordrecht, 1996).
6. G. Christou, D. Gatteschi, D. N. Hendrickson, and R. Sessoli, *MRS Bulletin* **25**, 66 (2000).
7. R. Sessoli, D. Gatteschi, A. Caneschi, and M. A. Novak, *Nature* **365**, 141 (1993).
8. A. Caneschi, D. Gatteschi, N. Lalioti, C. Sangregorio, R. Sessoli, G. Venturi, A. Vindigni, A. Rettori, M. G. Pini, and M. A. Novak, *Angew. Chem. Int. Ed. Engl.* **40**, 1760 (2001).
9. L. Gunther and B. Barbara, *Quantum Tunneling of Magnetization-QTM '94* (Kluwer, Dordrecht, 1995).

10. R. J. Glauber, *J. Math. Phys.* **4**, 294 (1963).
11. E. Coronado, J. R. Galan-Mascaros, C. J. Gomez-Garcia, and V. Laukhin, *Nature* **408**, 447 (2000).
12. O. Kahn, *Angew. Chem. Int. Ed. Engl.* **24**, 834 (1985).
13. J. B. Goodenough, *J. Phys. Chem. Solids* ***6***, 287 (1958).
14. J. B. Goodenough, *Magnetism and the Chemical Bond;* (Interscience, New York, 1963).
15. J. Kanamori, *J. Phys. Chem. Solids* **10**, 87 (1959).
16. I. Ciofini, C. A. Daul, and A. Bencini, *Recent Advances in Density Functional Methods* V. Barone, A. Bencini, and P. Fantucci (World Scientific, Singapore, Part III, 2001).
17. E. Ruiz, J. Cano, S. Alvarez, and P. Alemany, *J. Am. Chem. Soc.* **120**, 11122 (1998).
18. T. Soda, Y. Kitagawa, T. Onishi, Y. Takano, Shigeta Y., H. Nagao, Y. Yohioka, and K. Yamaguchi, *Chem. Phys. Lett.* **319**, 223 (2000).
19. A. H. Morrish, *The Physical Principles of Magnetism* (John Wiley & Sons, Inc., New York, 1966).
20. S. Turner, O. Kahn, and P. Rabardel, *J. Am. Chem. Soc* **118**, 6428 (1996).
21. J. Zhang, J. Ensling, V. Ksenofontov, P. Gütlich, A. J. Epstein, and J. S. Miller, *Angew. Chem. Int. Ed. Engl.* ***37*** , 657 (1998).
22. J. R. Friedman, M. P. Sarachik, J. Tejada, and R. Ziolo, *Phys. Rev. Lett.* **76**, 3830 (1996).
23. L. Thomas, F. Lionti, R. Ballou, D. Gatteschi, R. Sessoli, and B. Barbara, *Nature* **383**, 145 (1996).
24. C. Sangregorio, T. Ohm, C. Paulsen, R. Sessoli, and D. Gatteschi, *Phys. Rev. Lett.* **78**, 4645 (1997).
25. A. L. Barra, D. Gatteschi, and R. Sessoli, *Chem.-Eur. J.* **6**, 1608 (2000).
26. R. Caciuffo, G. Amoretti, A. Murani, R. Sessoli, A. Caneschi, and D. Gatteschi, *Phys. Rev. Lett.* **81**, 4744 (1998).
27. A. L. Barra, F. Bencini, A. Caneschi, D. Gatteschi, C. Paulsen, C. Sangregorio, R. Sessoli, and L. Sorace, *ChemPhysChem* **2**, 523 (2001).
28. A. Cornia, D. Gatteschi, and R. Sessoli, *Coord. Chem. Rev.* **219-221**, 573 (2001).
29. M. J. Naughton, J. P. Ulmet, A. Narjis, S. Askenazy, M. V. Chaparala, and A. P. Hope, *Rev. Sci. Instrum.* **68**, 4061 (1997).

30. W. Wernsdorfer, *Ph.D. Thesis*, Joseph Fourier University, Grenoble (France) 1996.
31. A. Bencini and D. Gatteschi, *Transition Metal Chemistry,* B.N. Figgis and G. Melson (Marcel Dekker, New York 1982) Vol. 8, p.1.
32. A. L. Barra, D. Gatteschi, R. Sessoli, G. L. Abbati, A. Cornia, A. C. Fabretti, and M. G. Uytterhoeven, *Angew. Chem. Int. Ed. Engl.* **36**, 2329 (1997).
33. A. Bencini, I. Ciofini, and M. G. Uytterhoeven, *Inorg. Chim. Acta* **274**, 90 (1998).
34. J. Telser, L. A. Pardi, J. Krzystek, and L. C. Brunel, *Inorg. Chem.* **37**, 5769 (1998).

2. High field/High frequency EPR: an overview

Throughout this thesis, high frequency/high field EPR spectroscopy (hereafter HF-EPR) has been extensively employed to gain fundamental information concerning the anisotropy of the investigated systems. HF-EPR is defined as EPR performed with a spectrometer working at a frequency significantly higher than Q-Band (35 GHz) corresponding to resonant fields for the free electrons significantly higher than those generated by conventional electromagnets.[1] It is now well accepted that the lower frequency limit to properly speak of HF-EPR is 95 GHz (W-Band), for which the g=2 resonant field is around 3.3 T.[2] The increasing interest toward this technique is mainly due to recent technological developments that made possible to overcome the technical difficulties that are connected with working at high frequencies and high field. In this chapter we will briefly review the peculiar features of HF-EPR, the advantages and disadvantages that it presents when compared to conventional EPR spectroscopy, and some of the experimental setups which have been proposed in the literature. Finally, we will present the main feature of the HF-EPR spectrometer operating in Pisa where much of the HF-EPR spectra presented in this thesis have been recorded.

2.1 Comparison with conventional EPR

The most obvious advantage concerning the use of HF-EPR is the increase in resolution of the g-factor, which - following resonance condition $h\nu=g\mu_B B$ - directly scales with frequency. This allows simplification of spectra of quite complex systems that have many overlapping transitions at low frequency and often allows direct measurements of g factors from powder spectra. This may provide very important information for studying biomolecules: indeed, in the course of electron transfer processes several radical species are

often generated.[3] To distinguish them by the small differences in their g-factor and hyperfine interactions, high fields are required. This argument also holds for separating different sites of different cofactor orientations in biomolecules. As an example, the g-tensor anisotropy of tyrosyl radical in PSII is completely resolved at High Frequency and this provides very important information on their orientation in the cell membranes.[4] Even in simpler coordination complex systems, the use of high field and high frequency may be helpful in resolving g-factor which due to exchange or dipolar broadening [5] and/or overlapping of the lines resulting from anisotropic hyperfine coupling,[6] give very complex patterns at conventional frequency.

The other peculiar feature of HF-EPR, which is much more important for the scope of this thesis, is the possibility of completely resolving the fine structure of a spin multiplet, thus giving access to the determination of zero field splitting parameters even when these are quite large. This is obviously important not only for studying anisotropic characteristics of molecular complexes, but also for the study of the active sites of metallo-proteins.[7-11] It is worth mentioning here, as an example, the determination of the large ZFS of Iron(III)-hemoglobin (D about 10 cm^{-1}), one of the first multifrequency HF-EPR studies dating back to the early 70s.[12] The use of multifrequency spectrometers allows to separate field-dependent contribution from field independent ones in the spin hamiltonian, with the former being increasingly relevant on increasing field and frequency. The interplay between field dependent and field independent terms may have two effects, which we will examine in details in the following. Given our special interest toward high-spin transition metal ion containing systems we will consider the Zero Field Splitting terms as the only field independent contribution to the spin hamiltonian, neglecting nuclear spin involving interactions:

$$\mathbf{H} = \mu_B \mathbf{B} \cdot \mathbf{g} \cdot \mathbf{S} + \mathbf{S} \cdot \mathbf{D} \cdot \mathbf{S} \qquad (2.1.1)$$

where we have neglected, for the sake of simplicity, higher order Zero Field Splitting contributions (see Chapter 3). At low field the **S·D·S** term is often larger than the Zeeman one and this results in complex spectral patterns which are often impossible to correctly assign. Increasing the frequency, and then the field of investigation, results in such cases in a strong simplification of the spectra, as the field independent part will act only as a minor perturbation effect over the dominating Zeeman term. This is the effect which is exploited in

the analysis of high spin clusters with relatively high anisotropy, where the use of high field leads to a dramatic simplification of the spectra. This often allows straightforward qualitative interpretation of the spectra. If one considers as an example an axial system in the high field limit - $\mu_B gB >> D$ - *2S* allowed transitions ($\Delta Ms = \pm 1$) are expected whose resonance field are given by :

$$B_r(M_s) = \frac{g_e}{g}\left[B_0 + (2M_s + 1)\frac{D'}{2} \right] \qquad (2.1.2)$$

Here $D' = (3\cos^2\theta - 1)D/g_e\mu_B$ and θ is the angle of the magnetic field with respect to the unique axis. This yield transitions separated by $2D'$ for magnetic field parallel to the unique axis and by D' for field perpendicular to the unique axis, thus providing the value of the Zero Field Splitting by simple inspection of the spectra (see Figure 2.1). Effects of higher order axial terms of the Spin Hamiltonian may also be easily identified as they lead to irregularity in the spacing of the lines.

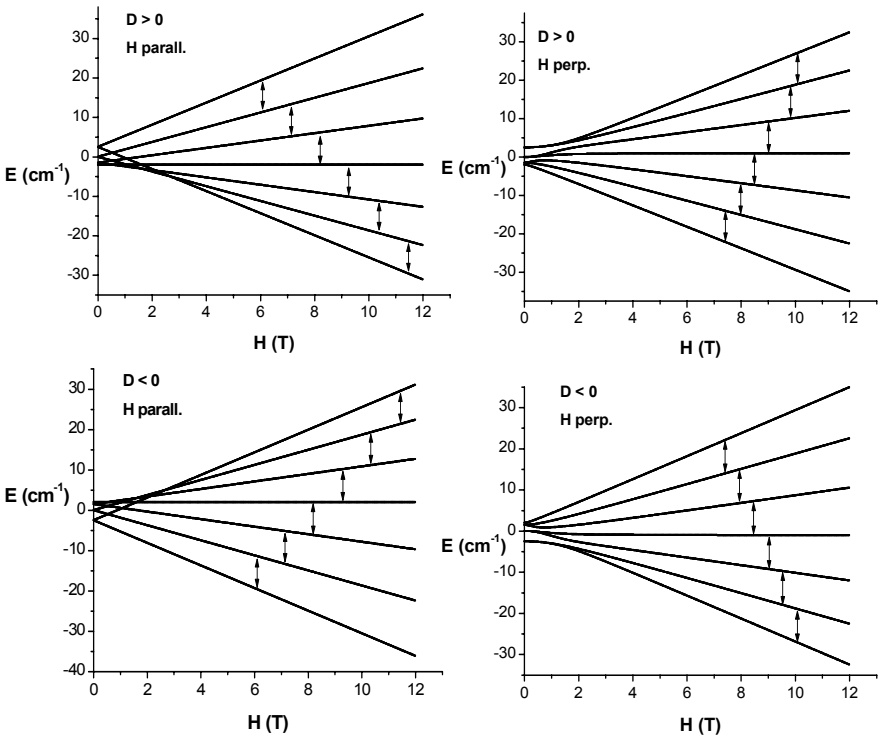

Figure 2.1 *The four graphs show the different situations which may be encountered in the high field limit for an axial system (S=3, $|D|=0.5$ cm^{-1}), allowing to readily assign sign and magnitude of the ZFS. Adapted from ref. [13]*

Furthermore, using HF-EPR results in a Zeeman energy which is comparable to kT at low temperature (at 245 GHz, $g_e\mu_B B_0$ corresponds to ca. 12 K) and thus in stronger depopulation effects with respect to conventional EPR. As an example at infinite temperature - where transition probabilities are computed on the assumption of equal population of the various spin levels - the six allowed transitions for an S=3 ground state are expected to show a relative intensity pattern 6:10:12:12:10:6, while at room temperature, assuming an exciting frequency of 245 GHz, the relative intensity pattern will be 6:9.6:11.1:10.7:8.6:5.[13] Finally, at 5 K the relative intensities will follow the completely different pattern 6:0.95:0.1:0.01:0.00082:0.000047, thus displaying a spectacular population effect. The temperature dependence of the relative intensities of the signals may then directly provide the sign of zero field splitting: indeed it is clear that at low enough temperature only the lowest *Ms* state is populated and only one transition will then be observable. The parallel one will then occur at low field and the perpendicular one at high field for $D<0$, while the reverse will hold for $D>0$. On increasing temperature the spectral intensity will move toward the center of the spectrum, and if all the transitions are observed the spin state may be unequivocally determined simply by counting the number of transitions.

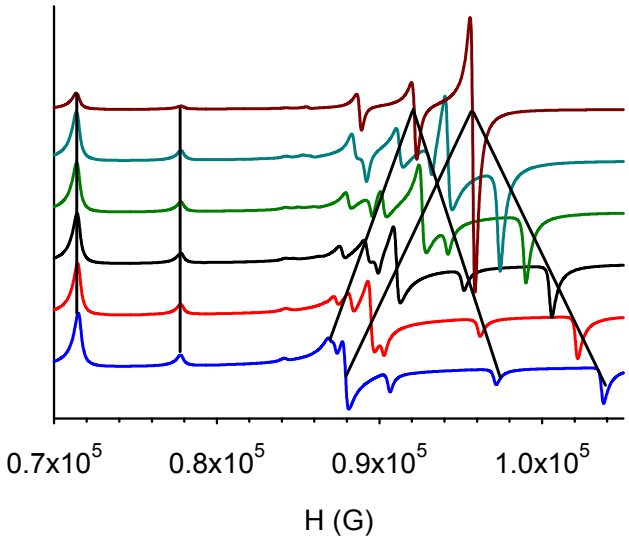

Figure 2.2 *The evolution of calculated HF-EPR spectra (ν=245 GHz, T=5 K) for an S=3 system with D=-0.3 cm^{-1} when passing from axial (brown spectrum) to completely rhombic symmetry (blue spectrum), is shown in the figure. The parallel region at low field remains unchanged on increasing E (step of 0.02 cm^{-1}) whereas the perpendicular transitions split in two inequivalent directions, x and y. The different behavior of parallel and perpendicular transitions is evidenced by black lines only for -3 → -2 and -2 → -1 transitions for the sake of simplicity.*

Switching on a transverse anisotropy term, E, leads to identify two principal directions, says x and y, in the formerly isotropic perpendicular plane. While this obviously does not

affect the parallel type transitions, it has a large effect over the perpendicular ones. Thus, an increasing splitting of the perpendicular transitions into two distinct sets of lines is observed on increasing *E* (see Figure 2.2).

Finally, in the limit of a completely rhombic system (i.e. *E/D*=1/3), a peculiar EPR spectrum is expected in the high field region. Indeed, as **D** tensor is a traceless one, *E/D*=1/3 means that D_{xx}=0, D_{yy}=-D_{zz} and the sign of *D* in this limit becomes meaningless. This results in a spectrum which simultaneously shows the features expected for axial *D*<0 and *D*>0 systems and is then symmetric with respect to g=2. Thus two sets of lines at high- and low field, corresponding to transitions in *y* and *z* direction respectively, with line-line separation of 2*D* are observed, together with a feature at g=2 which may be labeled as *x*. Lowering temperature will result in this case in an enhancement of the intensity of both the highest and lowest field feature, and of the g=2 one, corresponding to the transitions from the ground *Ms* state in the three directions *x*, *y*, *z*

When at low field the field independent part of the spin hamiltonian is dominating, e.g when systems with large Zero Field Splitting are investigated, a completely different situation is encountered. In general at low frequency the EPR spectrum is either defined in terms of effective g values, as it is the case for Kramers ions such as Co(II), Fe(III) etc. or - for some limiting case - e.g. non-Kramers ions with a ZFS much larger than the microwave quantum, no EPR spectrum is observed at conventional frequencies. Indeed, either the microwave energy is not enough to achieve resonance, or the resonance would appear at magnetic fields far exceeding those available in standard EPR spectrometers. Notwithstanding this, integer spin systems with large ZFS are not always “EPR-silent” at conventional fields and frequencies: if one consider, e.g. an S=2 system, when the symmetry is lower than axial transitions within the $|M_S|$= 2 doublet are partially allowed due to state-mixing introduced by transverse anisotropy and become EPR-visible,[14] particularly when parallel mode detection is used.[15,16] Both for Kramers and non-Kramers ions however, while at low frequency the spectra are simple and quite uniformative from a chemical point of view, drastically increasing the frequency result in much more complicated spectra, which contain a lot of information on the spin hamiltonian parameters. In such cases, the use of a so-called broadband approach,[17] i.e. an investigation at several different frequencies, allowing to analyze very different spectral regions, is strongly advised, yielding the possibility of observing complete EPR spectra even from systems formerly known to be EPR silent (see Chapter 3 for detailed references to this subject).

For systems with a large negative axial anisotropy, it is sometimes convenient to record spectra on loose powders; the high magnetic field employed in HF-EPR will then orient the crystallites with the easy axis along the field, thus yielding pseudo single crystal spectra which may be easily interpreted.[18,19]

Among others advantages the use of HF-EPR may provide, it is worth mentioning the extension of the time range over which spectral line shapes are sensitive to the molecular motions of spin labels. For 250 GHz EPR, a sensitivity to reorientational correlation times as short as 1 ps is possible. On this respect HF-EPR of spin labeled biopolymers is expected to be an important technique for linking the structure of biopolymers to their dynamics and function. Additional benefits also include extra sensitivity to rotational diffusion processes and the ability to study line-broadening mechanisms as part of multifrequency measurements.

Recently it has become possible to perform also pulsed HF-EPR experiments. However, as this has not been a subject of this thesis, we will only give here a brief account - based on ref. [2]- of the peculiar advantages of this technique over conventional pulsed EPR, which are especially exploited in the study of biological processes. Pulsed HF-EPR in the form of two-dimensional field-swept electron spin echo spectroscopy gives real-time access to specific cofactor–protein slow motions on the ns time-scale, and even to their spatial anisotropy that is generated by anisotropic weak interactions within the binding site. Furthermore ENDOR at high Zeeman fields takes additional advantage of the magnetoselection of molecular subensembles in powder or frozen-solution samples. Thereby, even in the case of small g-anisotropies, ENDOR can provide single-crystal-like information about hyperfine interactions, including anisotropic hydrogen bonding to the protein. Finally, by properly adjusting the Zeeman field in multifrequency pulsed EPR experiments, weakly and strongly interacting nuclei in the cofactor–protein system can be differentiated by their ESEEM and ENDOR spectra.

2.2 Experimental Setup

2.2.1 Microwave sources

A HF-EPR spectrometer may differ from a conventional EPR one in various or all of its components. The first difference lies in the microwave source. Two different kinds of

sources are usually employed in HF-EPR, namely solid state diode with frequency multiplicator and FIR-laser. The former are now being increasingly employed even in the X-Band spectrometers, in place of the formerly used Klystron. The advantage of solid state diode lies mainly in the large stability of the source and in the easy use; on the contrary the main problem is that they present a large power loss when using high-order multiplicator; practically, over 450 GHz the power output is so small that the use of these devices is not feasible. In such cases the only practical microwave source of reasonable output power at very high frequency (ν>450 GHz) are FIR lasers, which may provide a large number of discrete frequencies by just using different lasing gas or different laser transitions for the same lasing gas. The main drawbacks in using FIR lasers is that they are more unstable and more complex to operate and maintain with respect to solid state sources.

Other sources available for intermediate range of some hundred GHz, which are however much less diffuse than the former ones, are carcinotrons and gyrotrons. In detail the former have been employed in one of the first studies in HF-EPR,[12] while the latter have been recently proposed as a valid microwave source for FTEPR.[20] The main advantages of gyrotrons lie mainly in the fact that the frequency of the emitted radiation is determined by the strength of a static magnetic field. This allows production of high power at high frequency without the generation of damagingly large energy densities from slow wave structures. Presently these microwave generators and amplifiers developed by various research laboratories and industrial firms deliver 10^3 –10^5 W in the CW mode of operation, 10^6 W in 1 s pulses and 10^7 W in pulses of 10 s duration.[21,22] The magnetic fields necessary to generate frequencies in the range of 10–30 GHz are produced with the use of permanent magnets and water cooled solenoids. However to provide radiation of millimeter and submillimeter wavelength from strongly oversized interaction spaces superconducting magnets which produce homogeneous static magnetic fields up to 10–15 T in volumes of 10 cm diameter are needed.[22] This makes the use of gyrotrons as microwave source very expensive, thus strongly limiting their diffusion.

2.2.2 Magnets

The other main difference between HF-EPR and EPR spectrometers obviously concerns the magnetic field source: with the high frequency employed the free electron resonates at fields which are most conveniently produced by superconducting magnets (see Table 2.1):

the relatively easy availability of this kind magnets has surely been one of the key technical achievement responsible for the recent development of HF-EPR. Notwithstanding this, the building of superconducting magnets suitable for HF-EPR is not an easy task, given the high stability and high homogeneity required in sweeping mode for this kind of measurements. This is particularly true when the whole spectrum, from zero to maximum field, of a high spin or highly anisotropic system is needed, as it is the case for the system discussed in this thesis. On the contrary, it can be simply overcome in the case of narrow-range spectra, like those of radicals and defect centers, which may be recorded by operating a superconducting magnet in persistent mode combined with a sweeping coil.

ν /GHz	λ /mm	E /cm^{-1}	H_r(g=2) /T
9.5 (X-band)	30	0.32	0.34
24 (K-band)	12.5	0.8	0.86
35 (Q-band)	8.5	1.2	1.25
95 (W-band)	3	3.2	3.4
130 (D-band)	2.3	4.3	4.6
190	1.6	6.3	6.8
245	1.2	8.2	8.75
330	0.91	1.1	11.8
570	0.52	19	20.4
1000	0.3	33.4	35.7

Table 2.1 *Representative EPR microwave frequencies with associated wavelengths, energies and magnetic fields for resonance at g=2*

For very high frequency even superconducting magnets, producing fields not larger than 18 T, are not enough powerful. Indeed, as it is clear from Table 2.1, a free electron resonates at fields larger than 18 T for frequency above 500 GHz. The solution in this case is given by the use of resistive magnets, that can reach fields up to 30 T. Even if their field homogeneity and reproducibility are not as good as for superconducting magnets this is usually not a problem, as very high field are employed for analysis of high-spin, highly anisotropic species containing transition metal ions, with fairly broad EPR transitions. The main problem connected with the use of resistive magnets is the need for huge electric power supplies (typically 10^7 W) which make them available for specialized laboratories

only. Hybrid magnets, concentrical combinations of resistive magnet inside a superconducting one, may also be employed in this field region, and can reach Higher fields, up to 40 T: however, they are even less diffuse than resistive ones and are available only in a few laboratories all over the world. Ultra high fields, larger than 40 T, are also available by use of pulsed magnetic fields but their use in EPR would require major adaptation to the spectrometer and has not yet been reported.

2.2.3 Probeheads

Most of the efforts for the development of HF-EPR are aimed at the extension at millimeter and sub-millimeter waves of the general design of the conventional microwave bridge used up to Q-Band. The main problem along this path is the availability and/or the design and realization of devices able to carry on the function of the low-frequency analogue. In conventional EPR the propagation of the radiation is made by using mono-modal metallic rectangular waveguides, metallic cavities and the other devices present in a typical microwave bridge. The technical development allowed to actually transfer the standard microwave techniques to spectrometers employing frequency up to 150 GHz: a commercial W-Band spectrometer employing resonant cavity, designed to allow single crystal study,[9,10,23-25] has been recently commercialized by Bruker (see Chapter 7 for a description of this instrumental setup). A remarkable feature of this kind of spectrometer is the increase of the absolute sensitivity - which theoretically scales up as much as $f^{7/2}$ in some systems[26] - with respect to conventional EPR. This is due both to the increased filling factor η, which is a result of the smaller dimension of resonators at high frequency (for W-Band the cavity volume is about 1/1000 of those of X-Band) and to the increased population difference between the different spin levels.

Above 150 GHz diffraction losses increase dramatically, as spurious standing waves build up more easily on mechanical imperfections of the waveguides. Furthermore as the dimension of the cavity in the fundamental mode of resonating is equal to the microwave wavelength, it become increasingly difficult to build up a rectangular or cylindrical cavity on which operating at high frequency (see Table 2.1).

The simplest way to overcome these problems is the use of oversized single pass probe, without any resonating structure. Setups of this kind, which have been widely used for measurements discussed in this thesis, allow ultra wide band investigation and are very easy

both to use and to build. On the other hand, they are obviously low sensitive (typically 10^{11}spin G^{-1} Hz^{-1}) and thus a quite large amount of sample is needed to detect a signal. Furthermore the control on the phase and shape of the signal is poor and propagation effects may complicate the interpretation of the spectra.

Quasi- optical methods were first suggested by the Cornell group[27] to try to solve some of these problems and have been implemented by others groups.[6,28] Indeed when the wavelength is comparable to the devices used, as is the case in HF-EPR, geometrical optics, which ignores the wave like nature of the radiation is inappropriate. On the contrary, in quasi-optic, which identifies both a formalism and a technique, the radiation waves are described by a Gaussian beam which is a modified plane wave whose amplitude decreases not- monotonically as one moves radially from the optical axis.[1] In this experimental setup the microwaves are propagated as a single-mode free-space Gaussian beam outside the cryostat and in a corrugated pipe structure inside the cryostat. The first part of this path is achieved using a number of high-performance, broadband quasi-optical components which should provide a low-loss transmission line system. In these systems, the aim is to transmit a single mode and reduce coupling to higher order modes to a minimum. The resonating structure used is usually an open Fabry-Perot one: this consists of a quartz concave mirror coated with a micronic layer of silver or gold and a planar metallic mesh supported on a thin quartz sheet that acts as a partially transmitting planar mirror. Even if the use of an open resonator typically reduces the absolute sensitivity by a factor between 10 and 100 with respect to the best performance of single-mode resonator, the concentration sensitivity, which is often the important factor, may be comparable in the two cases. It is obviously possible to use different setups, like non-resonating structure, a solution which is usually preferred for systems with large linewidth.

Another possible solution has been recently proposed by Mola et al.[29], who developed a non-modulated high-frequency resonant perturbation detection technique. This may be employed when the radiation wavelength is large compared to the sample dimensions: due to the high Q-factor (which may range form 5000 to 20000) of the resonance small changes in the sample lead to large changes in the electromagnetic field response and thus to extremely enhanced sensitivity, which is a critical factor for very small samples with corresponding weak signals.[30] To monitor the phase and amplitude of millimeter-wave radiation transmitted through the cavity containing the sample under investigation a Millimeter Vector Network Analyzer was used. This device, which employs

purely solid-state electronics, allows measurements over an extended frequency range from 8–350 GHz. The MVNA operates at high frequency by using a Schottky diode to multiply and then modulate the frequency of a sweepable centimeter source, *S1* - an YIG whose output is in the range 8 – 18 GHz - by integer multiples. Detection is then achieved by mixing the mm-wave signal with the signal from a second cm source *S2* , at a second Schottky diode harmonic mixer 2HM. It is thus possible to generate frequencies in the range N(8-18 GHz) - where N is an integer from 1 to 20 - i.e to 8 to 350 GHz, by excitation of the desired harmonic N.

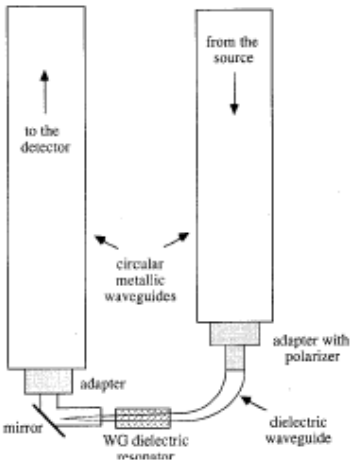

Figure 2.3 *Schematic drawing of the probe using the WGMDR. After ref. [33]*

A different approach has been carried out by the Pisa group, by developing a Whispering Gallery Mode Dielectric Resonator.[31-34] This peculiar type of resonating structure proved to be very effective in supporting a very large frequency range with attractive *Q* values and an extremely simple and cheap fabrication. In this experimental setup (Figure 2.3), at the end of the metallic waveguide an adapter connects the radiation to a fused quartz dielectric circular waveguide. The dielectric waveguide is curved at a right angle with a bending radius sufficient to avoid irradiation losses outside the guide. The horizontal part of the guide is tapered up to very small diameters useful for good coupling of the radiation at frequencies of interest to the resonator flanking the guide. This is just made of two similar polyethylene disks placed parallel to each other, and the space separating the disks is filled with the sample of interest. The termination of the dielectric waveguide, a very sharp and regular tip, is employed as a very efficient dielectric antenna irradiating with good directivity. The emitted radiation is recovered by inserting the antenna in a metallic

conducting waveguide with a small diameter. After a right angle path obtained by means of a 45° aluminum mirror the radiation is then sent to the return metallic waveguide which finally convoys it to the detector.

2.2.4 Detection systems

Finally, the detection system in HF-EPR is usually constituted by helium cooled InSb bolometer which has a response in the range of microseconds and is sensitive enough in a fairly broad frequency range, from GHz to THz. If faster detection is needed, Schottky diodes can be used at the expense of the sensitivity, which may fall by two orders of magnitude.

2.3 The italian HF-EPR spectrometer in Pisa

In Figure 2.4 a general block scheme of the HF-EPR spectrometer developed at IFAM-CNR in Pisa, which can be adapted to different configurations, is reported.

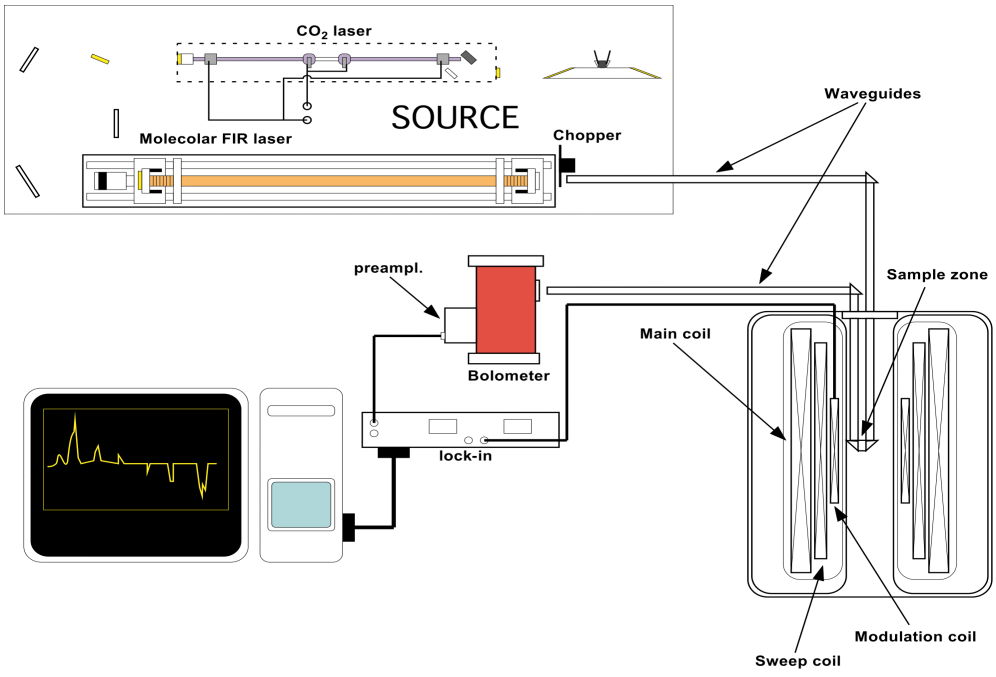

Figure 2.4 *General setup of the HF-EPR spectrometer in Pisa.*

The superconducting magnet is made up by the combination of a main coil that can reach a maximum field of 12 Tesla with a maximum sweep rate of 0.21 Tesla/min and a sweep coil that can be swept 0.2 T keeping the Main coil persistent at a fixed field. The use of the sweep coil reduces the liquid helium boil off and is useful for the study of signals not broader than 0.1 T ca., i.e. for analysis of radicals, defect centers, etc. The Field stability when the magnet is made persistent is of 1 mT/hour.

The sources employed in Pisa include a home built CO_2 pumped Millimetre Laser emitting a number of lines between 148 and 316 GHz (148 - 240- 240- 245 - 316) using different lasing gases and a Gunn diode emitting at 95 GHz equipped with a doubler and a tripler offering the 190 GHz and 285 GHz frequencies. The detector is a fast InSb hot electron bolometer cooled to liquid helium temperature. The probe employed for the spectra recorded for this thesis is working in traveling wave configuration without resonating structures: this gives an absolute sensitivity of 10^{12}spin/Gauss Hz at room temperature. As we have seen in the previous paragraphs, resonators based on the use of Dielectric Resonators working in the Whispering Gallery Modes are also developed in the laboratory but have not been used for the spectra presented in this thesis.

Finally, the temperature control is achieved through a PID system which regulates the liquid helium flux and the heating in a continuous flow cryostat which achieve a temperature stability of 0.01 K at 4.2 K

2.4 Quantitative analysis of the results

As we have seen in the previous paragraphs, one of the main advantages when using HF-EPR with S>1/2 spin systems is the possibility of often considering the situation of high-field limit achieved: this makes the use of perturbation theory to simulate the spectra possible. However, when the Zeeman energy cannot be considered to be large compared to the zero field splitting, it is necessary to diagonalize the complete matrix. This situation is encountered both for the above mentioned EPR silent ions, which have large Zero-Field splitting, and for system with large ground spin state.

Simulation procedures have been developed during past years which generally make use either of a full diagonalization combined with an interpolation technique to search for the transition fields or of the eigenfields and related methods which directly give the

transition fields.[35,36] In any case the main problem, beyond the order of the matrices that need to be diagonalized, is the reconstruction of the polycrystalline powder spectrum by accumulation of single-crystal spectra.[37] The number of single-crystal spectra that need to be calculated depends on the interplay of the two main factors which determine the whole spread of the spectrum: the experimental microwave frequency and the anisotropy of the system (**g** anisotropy and ZFS). Different strategies have been designed for that purpose which are adapted to the simulation of a high-spin system with large ZFS.[38,39]

We have however found that, for the systems which were object of study during this thesis the best suited and more flexible approach to simulation of both HF-EPR and X-Band EPR is the program developed by Weihe,[39] which has been successfully tested by various groups working in the field during past years.[24,40-46] The simulation procedure carried on by using this program may be intuitively divided into three separate steps:

(1) Definition of the model. The hamiltonian modeling the system under study is defined by the researcher. In principle any conventional spin-Hamiltonians can be used, as well as ligand field matrices and one is completely free to define the model: throughout this thesis, we employed the Spin Hamiltonian defined in (2.1.1), where the principal values of **D** tensor were parameterized according to $D=3/2D_{zz}$, $E=1/2(D_{xx}-D_{yy})$. In some cases higher order Zero Field Splitting terms proved to be necessary to obtain a satisfactory simulation. As we will see in the following chapters, determination of higher order term in spin hamiltonian may be of paramount importance when dealing with problem concerning quantum effect in molecular nanomagnet. The matrix representations of the Hamiltonian (2.1.1) is then used as input for the following step of the simulation. Obviously, this is not a specific step for the employed program package, since any analysis of EPR spectra would involve a definition of the model.

(2) Calculation of the resonance magnetic fields and calculations of the corresponding transition probabilities for all the different orientations of the paramagnetic species with respect to the magnetic field. Energies are calculated by means of matrix diagonalizations, without use of any perturbation theory; forbidden transitions are also considered ($|\Delta M_s|>1$). This step is obviously the time consuming part of the whole simulation procedure; however, with a normal PC (PIII, 450 MHz) it takes just 530 seconds to calculate this for a powder (1200 orientations, 150 fields interval) of an S=6 system.

(3) Finally, the last step, which is computationally much cheaper, is the folding in of a band-shape function for each transition: different bandshape functions are available and

distribution of value of the Spin Hamiltonian parameters (*g*-strain, *D*-strain) may be taken into account. This step is separated from (2) in order to make it possible to use several bandwidths for each set of line positions calculated in step (2).

References

1. W. R. Hagen, *Coord. Chem. Rev.* **192**, 209 (1999).
2. K. Möbius, *Chem. Soc. Rev.* **29**, 129 (2000).
3. P. Dorlet, A. Boussac, A. W. Rutherford, and S. Un, *J. Phys. Chem. B* **103**, 10945 (1999).
4. P. Dorlet, A. W. Rutherford, and S. Un, *Biochem.* **39**, 7826 (2000).
5. B. Cage, A. K. Hassan, L. Pardi, J. Krzystek, L. C. Brunel, and N. S. Dalal, *J. Magn. Reson.* **124**, 495 (1997).
6. E. J. Reijerse, P. J. Van Dam, A. A. K. Klaassen, W. R. Hagen, P. J. M. Van Bentum, and G. M. Smith, *Appl. Magn. Res.* **14**, 153 (1998).
7. P. J. Bratt, M. Rohrer, J. Krzystek, M. C. W. Evans, L. C. Brunel, and A. Angerhofer, *J. Phys. Chem. B* **101**, 9686 (1997).
8. M. Rohrer, T. F. Prisner, O. Brugmann, H. Kass, M. Spoerner, A. Wittinghofer, and H. R. Kalbitzer, *Biochem.* **40**, 1884 (2001).
9. M. V. Gastel, M. Huber, M. Verbeer, G. W. Canters, M. J. Boulanger, M. E. P. Murphy, and E. J. J. Groenen, *Biophys. J.* **78**, 143 (2000).
10. M. Van Gastel, M. J. Boulanger, G. W. Canters, M. Huber, M. E. P. Murphy, M. P. Verbeet, and E. J. J. Groenen, *J. Phys. Chem B* **105**, 2236 (2001).
11. A. Fournel, S. Gambarelli, B. Guigliarelli, C. More, M. Asso, G. Chouteau, R. Hille, and P. Bertrand, *J. Chem. Phys.* **109**, 10905 (1998).
12. Y. Alpert, Y. Couder, J. Tuchendler, and H. Thome, *Biochim. Biophys. Acta* **322**, 37 (1973).
13. A. L. Barra, L. C. Brunel, D. Gatteschi, L. Pardi, and R. Sessoli, *Acc. Chem. Res.* **31**, 460 (1998).
14. H. J. Gerritsen and E. S. Sabisky, *Phys. Rev.* **132**, 1507 (1963).
15. A. Abragam and B. Bleaney, *Electron Paramagnetic Resonance of Transition Ions* (Dover Publications, New York, 1986).

16. K. A. Campbell, E. Yikilmaz, C. V. Grant, W. Gregor, A. F. Miller, and R. D. Britt, *J. Am. Chem. Soc.* **121**, 4714 (1999).
17. A. K. Hassan, L. A. Pardi, J. Krzystek, A. Sienkiewicz, P. Goy, M. Rohrer, and L. C. Brunel, *J. Magn. Reson.* **142**, 300 (2000).
18. A. L. Barra, A. Caneschi, D. Gatteschi, and R. Sessoli, *J. Am. Chem. Soc.* **117**, 8855 (1995).
19. D. P. Goldberg, J. Telser, J. Krzystek, A. G. Montalban, L. C. Brunel, A. G. M. Barrett, and B. M. Hoffman, *J. Am. Chem. Soc.* **119**, 8722 (1997).
20. L. R. Becerra, G. J. Gerfen, B. F. Bellew, J. A. Bryant, D. A. Hall, S. J. Inati, R. T. Weber, S. Un, T. F. Prisner, A. E. Mcdermott, K. W. Fishbein, K. E. Kreischer, R. J. Temkin, D. J. Singel, and R. G. Griffin, *J. Magn. Reson. Series a* **117**, 28 (1995).
21. G. S. Nusinovich and M. E. Read, *Ieee Trans. on Plasma Science* **27**, 355 (1999).
22. M. Thumm, *Int. J. Infrared Millimeter Waves* **22**, 377 (2001).
23. J. W. A. Coremans, O. G. Poluektov, E. J. J. Groenen, G. C. M. Warmerdam, G. W. Canters, H. Nar, and A. Messerschmidt, *J. Phys. Chem.* **100**, 19706 (1996).
24. J. Mrozinski, A. Skorupa, A. Pochaba, Y. Dromzee, M. Verdaguer, E. Goovaerts, H. Varcammen, and B. Korybut-Daszkiewicz, *J. Mol. Struct.* **559**, 107 (2001).
25. A. Bouwen, A. Caneschi, D. Gatteschi, E. Goovaerts, D. Schoemaker, L. Sorace, and M. Stefan, *J. Phys. Chem. B* **105**, 2658 (2001).
26. J. R. Pilbrow, *Transition Ion Electron Paramagnetic Resonance* (Oxford University Press, Oxford, 1990).
27. K. A. Earle, D. S. Tipikin, and J. H. Freed, *Rev. Sci. Instrum.* **67**, 2502 (1996).
28. G. M. Smith, J. C. G. Lesurf, R. H. Mitchell, and P. C. Riedi, *Rev. Sci. Instrum.* **70**, 1787 (1998).
29. M. Mola, S. Hill, P. Goy, and M. Gross, *Rev. Sci. Instrum.* **71**, 186 (2000).
30. B. H. Ward, I. B. Rutel, J. S. Brooks, J. A. Schlueter, R. W. Winter, and G. L. Gard, *J. Phys. Chem. B* **105**, 1750 (2001).
31. G. Annino, M. Cassettari, M. Fittipaldi, L. Lenci, I. Longo, M. Martinelli, C. A. Massa, and L. A. Pardi, *Appl. Magn. Reson.* **19**, 495 (2000).
32. G. Annino, M. Cassettari, M. Fittipaldi, I. Longo, M. Martinelli, C. A. Massa, and L. A. Pardi, *J. Magn. Reson.* **143**, 88 (2000).
33. G. Annino, M. Cassettari, I. Longo, M. Martinelli, P. J. M. Van Bentum, and E. Van Der Horst, *Rev. Sci. Instrum.* **70**, 1787 (1999).

34. G. Annino, M. Cassettari, and M. Martinelli, *Appl. Magn. Reson.* **20**, 97 (2001).
35. Belford G. G., Belford R. L., and Burkhalter J. F., *J. Magn. Reson.* **11**, 251 (1973).
36. L. Cugunov, A. Mednis, and J. Kliava, *J. Magn. Reson. Series A* **106**, 153 (1994).
37. D. M. Wang and G. R. Hanson, *J. Magn. Reson. Series A* **117**, 1 (1995).
38. M. J. Mombourquette and J. A. Weil, *J. Magn. Reson.* **99**, 37 (1992).
39. C. J. H. Jacobsen, E. Pedersen, J. Villadsen, and H. Weihe, *Inorg. Chem.* **32**, 1216 (1993).
40. A. L. Barra, A. Caneschi, D. Gatteschi, and R. Sessoli, *J. Magn. Magn. Mater.* **177**, 709 (1998).
41. A. L. Barra, D. Gatteschi, and R. Sessoli, *Chem.-Eur. J.* **6**, 1608 (2000).
42. G. L. Abbati, L. C. Brunel, H. Casalta, A. Cornia, A. C. Fabretti, D. Gatteschi, A. K. Hassan, A. G. M. Jansen, A. L. Maniero, L. Pardi, and C. Paulsen, *Chem.-Eur. J.* **7**, 1796 (2001).
43. M. J. Knapp, J. Krzystek, L. C. Brunel, and D. N. Hendrickson, *Inorg. Chem.* **39**, 281 (2000).
44. C. Duboc-Toia, H. Hummel, E. Bill, A. L. Barra, G. Chouteau, and K. Wieghardt, *Angew. Chem. Int. Ed. Engl.* **39**, 2888 (2000).
45. D. Burdinski, E. Bill, F. Birkelbach, K. Wieghardt, and P. Chaudhuri, *Inorg. Chem.* **40**, 1160 (2001).
46. B. Pilawa, M. T. Kelemen, S. Wanka, A. Geisselmann, and A. L. Barra, *Europhys. Lett.* **43**, 7 (1998).

3. Calculation of Spin Hamiltonian parameters

3.1 Introduction

Even if the theoretical background for rationalizing the magnetic anisotropy in molecular materials is well developed, in this field quanto-mechanical calculation models based on Density Functional Theory have not yet been pushed to the required level of sophistication. However ligand field models have long been used to describe the low symmetry properties of paramagnetic species,[1] and they can provide an excellent basis for the description of the magnetic anisotropy of molecular magnets. In this chapter we wish to resume some fundamental aspect concerning magnetic anisotropy and show with some example how it is possible to rationalize it. We will first recall some basic aspects of crystal field and ligand field theory, with a specific section being devoted to the description of the Angular Overlap Model. We will then outline the main features of the spin hamiltonian approach, focusing our attention on Zero Field Splitting terms. A recently developed computer program which allows for the calculation of spin hamiltonian parameters starting from electronic parameters within the framework of the Angular Overlap Model will then be presented and the results obtained with this program discussed. The starting point will be an overview of the results recently obtained through HF-EPR spectra of some so called EPR silent ions.[2-13] These are ground state integer spin complexes with high zero field splitting, which -apart for some exceptions - usually do not show any EPR signal at conventional frequencies (see Chapter 2). For the interpretation of HF-EPR spectra of these systems, ligand field techniques have been mainly used. This is an approach which has been widely used for the interpretation of the EPR spectra of well behaved paramagnetic ions [14,15] but the availability of spectra for EPR silent ions now requires a critical evaluation of the validity of ligand field theory especially concerning the possibility to calculate the zero field splitting. Finally, we will focus on the origin of the anisotropy in single molecule

magnets, starting from the analysis of simple model system to end with the real building blocks of the SMM.

3.2 Crystal Field Theory[1,16,17]

3.2.1 Fundamentals of Crystal Field Theory

The main terms of the non-relativistic hamiltonian for free many-electron atoms are:

$$\mathbf{H} = \sum_{k=1}^{n}\left\{\frac{1}{2m}\mathbf{p}_k^2 - \frac{Ze^2}{r_k} + \right\} + \sum_{k=1}^{n}\zeta(r_k)\mathbf{l}_k \cdot \mathbf{s}_k + \sum_{k<\lambda}^{n}\frac{e^2}{r_{k\lambda}} \qquad (3.2.1)$$

the first term is the sum of hydrogen-like terms for single electrons, the second one is the sum of the single electron spin orbit interaction, while the third sum contains the interelectronic repulsion. The hydrogen-like part is common to all electron configurations and therefore only shifts the energies without affecting the relative differences; conversely both the second and the third term will contribute to the energy differences in many electron configuration, as we will see in the following.

We may neglect, as a first step, the two-electron part of (3.2.1) and the spin-orbit interaction and consider each single electron moving in an average field due to the nucleus and to the remaining electrons and that this average field is spherically symmetric. Within this assumption, the solution of the hydrogen-like part of the Schrödinger equation of (3.2.1) for a free metal ion yields the five degenerate d orbitals, which are the product of a radial function R_{nl} defined by the quantum numbers n and l and of a spherical harmonic Y_l^m, depending on the quantum number m:

$$\begin{aligned} d(m_l = 0) &= R_{nl}\sqrt{\left(\frac{1}{2\pi}\right)}\cdot\sqrt{\left(\frac{5}{8}\right)\left(3\cos^2\theta - 1\right)} \\ d(m_l = \pm 1) &= R_{nl}\sqrt{\left(\frac{1}{2\pi}\right)}\cdot\sqrt{\left(\frac{15}{4}\right)sin\theta\cdot\cos\theta\cdot e^{\pm i\varphi}} \\ d(m_l = \pm 2) &= R_{nl}\sqrt{\left(\frac{1}{2\pi}\right)}\cdot\sqrt{\left(\frac{15}{16}\right)sin^2\theta\cdot e^{\pm i\varphi}} \end{aligned} \qquad (3.2.2)$$

When an ion is placed in a ligand environment with symmetry lower than spherical, the energies of its partly filled *d*- orbitals (and to a lesser extent *f*-orbitals for lanthanides) are

split by the electrostatic field of the ligand. This is an immediate consequence of the lowering of the symmetry as, even in the regular octahedral geometry, group theory tells us that the highest dimension of irreducible representation is three.

This is the basis of Crystal Field Theory, whose deeply symmetry based formalism was developed by Bethe in 1929.[18] Crystal Field Theory is a purely electrostatic, non-bonding approach, where the metal ion is placed in a field due to its ligands, which are approximated by negative point charges and thus assumed to be fixed and unpolarizable. An interesting point is that while the theory treats the electron of the metal center quantum mechanically those of the surrounding medium are treated classically.

The effect of the ligands over the energy diagram of a metal ion is described by an operator **V,** sum of one-electron operators which are the sum over all the ligands of the electrostatic potentials associated with the j-th electron of the partly filled shells of the metal ion at a given distance (r_{ij}) from the *Z*-negatively charged i-th ligand:

$$\mathbf{V} = \sum_{j=1}^{nel.} \mathbf{V}_j = \sum_{j=1}^{nel.} \sum_{i=1}^{nlig} \frac{Z_i e^2}{r_{ij}} \tag{3.2.3}$$

The problem thus reduces to the solution of the secular determinant with matrix elements of the type $< \varphi_l \mid \mathbf{V} \mid \varphi_k >$. It is worth highlighting here that Crystal Field Theory is not treating each ligand separately but considers them as a whole, exploiting the total symmetry of the surrounding of the metal ion, whose symmetry properties are retained by **V**. This is best understood expanding each one-electron $\mathbf{V}_j$ in terms of spherical harmonics centered at the metal nucleus:

$$\sum_i \frac{Z_i e}{r_{ij}} = \sum_{k=0}^{\infty} \sum_{q=-k}^{k} \frac{4\pi}{(2k+1)} \sum_i Z_i e^2 Y_k^{q^*}(\theta_i, \varphi_i) \cdot \left(\frac{r_<^k}{r_>^{k+1}} \right) \cdot Y_k^q(\theta_j, \varphi_j) \tag{3.2.4}$$

here $r_>$ usually refers to electron nucleus distance and $r_<$ to the nucleus-ligand distance.[§] The first spherical harmonic, $Y_k^q(\theta_i, \varphi_i)$ refers to the ligands and the second to the electron, both defined by their polar coordinates.

It is evident that the use of a certain set of spherical harmonics critically depends on the geometry of the system. Indeed, **V** must obviously transform as the totally symmetric

[§] $r_<$ and $r_>$ are in fact the shorter and longer radial vectors connecting the origin to the electron and to the charge; the assignment follows by reasonably assuming that the electron does not move far apart from the nucleus.

representation in the symmetry group concerned and this introduces severe limitations on the use of given Y_k^q, thus strongly simplifying (3.2.4). It should be reminded here that the group theoretical transformations of the spherical harmonics are determined by their *k* value, i.e. by their angular momentum quantum number, whose rotation properties were first defined by Bethe [18] deriving the characters of their reducible representation in a given symmetry group:

$$X(\alpha)=\sin((L+1/2)\alpha)/\sin(\alpha/2)$$
$$X(E)=2L+1 \qquad (3.2.5)$$

where α is the rotation angle for any given symmetry operation and X(E) is the character for the identity operator.

The symmetry of the surroundings further contributes to simplify Eq. (3.2.4) by zeroing some terms; thus, if the symmetry group possess a fourfold, a threefold or a twofold axis of symmetry (or a symmetry plane), only terms characterized by q values multiple of 4, 3 and 2 (including q=0) respectively, can be retained.

Further simplification in (3.2.4) is introduced by considering that the matrix element of the Crystal Field operator should also behave as total symmetric representation of the group: this means that the orbital function coupled by **V**, i.e. by the different spherical harmonics, depends on the symmetry.

To rule out which terms of (3.2.4) are retained it is worth considering here, as a preliminary step, the nature of the function $<\varphi_l|$ and $|\varphi_k>$ over which each $\mathbf{V}_j$ is operating. This depends on how the effect of the interelectronic repulsion term of hamiltonian (3.2.1) is accounted for, i.e. either according to the strong field formalism or to the weak field one. In the weak field scheme, the interelectronic repulsion term of the spin hamiltonian is considered to be dominating over the effect induced by the surrounding of the metal ion, which is treated as a perturbation. The functions over which the crystal field operator is operating are then the free ion terms, characterized by $^{(2S+1)}$L. As these are many-electron functions while Crystal field operator is a sum of one-electron operators, free ion terms are decomposed in linear combinations of $|l,m_l>$ functions to evaluate the matrix element of **V**. On the other hand, if the effect of the crystal field is assumed to be dominating over the interelectronic repulsion term, the latter is considered as a perturbation, and thus the crystal field is just operating over the monoelectronic *d* orbitals defined in (3.2.2). In both cases low symmetry effects and spin-orbit coupling are introduced as a final perturbation. What is

more important, the one-electron functions are then of the type $|l,m_l>$, where l=2 for *d* orbitals ad l=3 for *f* orbitals, and may then be expressed in terms of spherical harmonics, Y_k^q. As both the operator and wavefunction can be expressed in terms of spherical harmonics the matrix element is of the form $<Y_a|\mathbf{Y_b}|Y_c>$. A very useful way to calculate this matrix element (and thus matrix element of **V**) makes use of the irreducible tensor operator C_k^q - where k is the tensor rank and q identifies its component - related to spherical harmonics by:

$$C_k^q = \left(\frac{4\pi}{2k+1}\right)^{\frac{1}{2}} Y_k^q \tag{3.2.6}$$

This allows us to derive the matrix element of **V** by using the Wigner-Eckart theorem, that states that two one-electron functions which may be expressed in terms of their general angular momentum $|j,m_j>$ can be coupled by a general tensor operator, C_k^q to yield:

$$< jm_j \mid C_k^q \mid j'm_j'>= (-1)^{j-m_j} \begin{pmatrix} j & k & j' \\ -m_j & q & m_j' \end{pmatrix} < j \parallel C_k \parallel j'> \tag{3.2.7}$$

here $< j \parallel C_k \parallel j' >$ is a reduced matrix element of the tensor operator independent of m_j, and the term in parenthesis is a Wigner 3-j symbols. Eq. (3.2.7) is an extremely valuable relation as it allows one to derive integrals of any wavefunctions coupled by an operator which may be written in angular momentum terms. Moreover, 3-j symbol have fundamental properties which reduces the number of integrals to be evaluated and simplify their calculation:

1- They are equal to zero unless $j + j' \geq k \geq |j - j'|$

2- The sum of the elements of the second row must be zero for a 3-j symbol to be non-zero

3-When the second row is multiplied by -1 the value of the 3-j symbol is multiplied by $(-1)^{j+k+j'}$

4- Even permutations of the column leave the value of 3-j symbols unchanged, while odd permutations of the column multiply the value by $(-1)^{j+k+j'}$

From the first condition it immediately follows that only harmonics with k ≤ 4 can couple two *d* orbitals (for which j=j'=2) thus drastically reducing number of the terms of (3.2.4) to be evaluated.

Once this procedure is completed, the magnitude of the obtained matrix element are expressed in terms of radial integrals, α_n, which for 3*d* electrons are:

$$\begin{aligned}\alpha_2 &= Ze^2 \int R_{3d} \frac{r^2}{a^3} R_{3d} r^2 dr = Ze^2 \frac{\bar{r}^2}{\bar{a}^3} \\ \alpha_4 &= Ze^2 \int R_{3d} \frac{r^4}{a^5} R_{3d} r^2 dr = Ze^2 \frac{\bar{r}^4}{\bar{a}^5}\end{aligned} \tag{3.2.8}$$

For octahedral and tetragonal groups, the crystal field energy splitting are usually reported as the Ballhausen ligand field parameters, *Dq*, *Ds*, *Dt*:[19]

$$\begin{aligned}Dq &= \frac{1}{6} Ze^2 \frac{\bar{r}^4}{\bar{a}^5} = \frac{1}{6}\alpha_4 \\ Ds &= \frac{2}{7} Ze^2 \left(\frac{\bar{r}^2}{\bar{a}^3} - \frac{\bar{r}^2}{\bar{b}^3} \right) = \frac{2}{7}\left(\alpha_2(a) - \alpha_2(b)\right) \\ Dt &= \frac{2}{21} Ze^2 \left(\frac{\bar{r}^4}{\bar{a}^5} - \frac{\bar{r}^4}{\bar{b}^5} \right) = \frac{2}{21}\left(\alpha_4(a) - \alpha_4(b)\right) = \frac{4}{7}(Dq(a) - Dq(b))\end{aligned} \tag{3.2.9}$$

where *a* and *b* identify the axial and equatorial ligand, respectively.

3.2.2 Crystal Field Theory: a critical evaluation

Crystal Field Theory had a great initial success that arose from the small number of parameters and the fact that crystal potentials of the correct symmetry can be written down. Moreover, while the approximation of ligand with point charges is quite a raw one, it qualitatively predicts both the spectroscopic behavior of the ions depending on their site geometry - like number and relative energies of transitions in an electronic spectrum - and what kind of magnetic properties a complex of a d^n ion in a given symmetry should possess.

However, as most of the obtained results rely on the symmetry basis of the model, as soon as symmetry is lowered from very regular ones things are getting worse. On this respect, as the effect of the surrounding is considered as a whole it does not provide a basis to understand what happens when only some ligands are changed. Moreover, on lowering the symmetry, the number of radial parameters necessary to describe the electronic energy levels drastically increases: this is already clear from the example of tetragonal symmetry of Equation (3.2.9). Furthermore, the chemical significance of these integrals becomes increasingly difficult to work out; referring again to Eq. (3.2.9), while *Dt* may be related to the relative strength of axial and equatorial crystal fields, little or no chemical information

has been derived from *Ds* as a function of the ligand or of the metal ion in tetragonal complex. Moreover, radial parameters cannot be calculated from first principles, as the point charge approximation which is at the basis of the theory is clearly inadequate to describe molecular complexes. Indeed, it was early recognized that one of the main reasons of the poor quantitative results obtained by purely electrostatic model of Crystal Field Theory is the neglecting of any kind of overlap between the ligand and the metal ion, which becomes increasingly important on increasing covalency. This results in a failure when trying to get any reliable chemical information about metal-ligand bond within the framework of Crystal Field Theory.

3.3 Ligand Field models

The general term Ligand Field Theory is applied to any development of crystal field theory recognizing some covalent character of metal-ligand bond.[17] Within this framework, this theory provides a basis for understanding many of the wide range of spectroscopic observables in terms of the electronic structures of transition metal complexes. However, what is probably more important is that the parameters of the theory have some chemical significance and can be related - with some caution - to a specific metal-ligand interaction. Predictions can then in principle be made over electronic energies of species containing a specific metal-ligand interaction by transferring the obtained parameters from a given complex to another.

The symmetry of the surroundings is introduced in Ligand Field Theory as a consequence of ligand positions and it is not at the basis of the model as it is for Crystal Field Theory.

The main starting point of Ligand Field Theory is to recognize that when overlap between ligand and metal orbitals is admitted, the orbitals can possess σ- or π- bonding or antibonding character. A degree of covalency is then introduced in the model by the recognition of the fact that the parameters value are strictly symmetry defined for each specific metal-ligand interaction, and that interelectronic repulsion parameters are reduced with respect to the free ion (where they are well defined as they are derived from atomic theory). Indeed, the ability to incorporate these parameters into the bonding description of metal complexes is the real power of ligand field theories. We have already mentioned how

the effect of interelectronic repulsion term may be taken into account in the strong and in the weak field approaches. It is worth noting here that the difference between the two approaches retains mainly an historical and didactic importance nowadays. Indeed modern ligand field based programs exploit the performances of modern computers, which make diagonalization of the complete hamiltonian matrix, including spin orbit coupling and low symmetry effects, feasible (see paragraph 3.9).

The usual approach is to obtain numerical values of radial parameters from the fits of spectra and then to interpret the resultant values in terms of bonding interactions with the ligands. It is well known, for example, that *Dq* varies with the bonding interaction of the ligand with the metal center, while the relative *Dq* values do not depend significantly on the metal ion. This yield the well known *spectrochemical series*, where the ligand are ordered according to increasing *Dq*:

$I^- < Br^- < CrO_4^{2-} < S^{2-} < N_3^- < F^- < OH^- < CO(NH_2)_2 \approx C_2O_4^{2-} \approx O^{2-} < H_2O < SCN^- < C_5H_5N \approx NH_3 < H_2NCH_2CH_2NH_2 \approx$ tren $< NO_2^- \approx$ 2,2'-bpy $\approx$ phen $< CN^- <$ CO

This behavior would be difficult to rationalize on the basis of simple Crystal Field Theory since ligands with small charge have high *Dq* values. However, it is easily understood if one takes into account the π-bonding ability of the ligands: indeed, good π-acceptors have high *Dq* while good π-donors have low *Dq* values.

In the following two sections we will see how spin-orbit coupling and interelectronic energy terms are also affected by taking into account covalency, and the chemical significance which could be assigned to them.

3.4 Determination of interelectronic repulsion energy

The evaluation of interelectronic repulsion energy mainly consists in calculating a series of matrix element of the type $< ab \,|1/r_{12}|\, cd >$, where $<ab|$ and $|cd>$ are product of monoelectronic functions. In analogy to the expansion of the crystal field, we may expand this potential in terms of spherical harmonics as:

$$\frac{1}{r_{12}} = \sum_{l=0}^{\infty} \sum_{m=-l}^{l} \frac{4\pi}{2l+1} \frac{r_<^l}{r_>^{l+1}} Y_l^m(\theta_1, \varphi_1) Y_l^m(\theta_2, \varphi_2) \qquad (3.4.1)$$

The calculation is then carried on by expressing spherical harmonics in terms of normalized Legendre functions:

$$Y_l^m(\theta,\varphi) = P_l^m(\cos\theta)\frac{1}{\sqrt{2\pi}}e^{im\varphi} \tag{3.4.2}$$

and defining two new functions:

$$c^k\left(lm_l, l'm_l'\right) = \sqrt{\frac{2}{(2k+1)}}\int_0^\pi P_k^{m_l-m_l'}\cos\theta P_l^{m_l}\cos\theta P_{l'}^{m_l'}\cos\theta\sin\theta d\theta \tag{3.4.3A}$$

$$R^k(abcd) = e^2\int_0^\infty\int_0^\infty \frac{r_<^k}{r_>^{k+1}}R_a^1R_b^2R_c^1R_d^2r_1^2dr_1r_2^2dr_2 \tag{3.4.3B}$$

It can be demonstrated that the repulsion integral may be expressed in terms of these functions as:

$$\begin{aligned} &< ab\left|\frac{e^2}{r_{12}}\right|cd >= \delta\left(m_s^a, m_s^c\right)\delta\left(m_s^b, m_s^d\right)\delta\left(m_l^a + m_l^b, m_l^c + m_l^d\right)\times \\ &\times\sum_{k=0}^{\infty}c^k\left(l^a m_l^a l^c m_l^c\right)c^k\left(l^d m_l^d l^b m_l^b\right)R^k(abcd) \end{aligned} \tag{3.4.4}$$

Here the sum over k is reduced to k=0,2,4 for d orbitals, due to the limitation of the above stated triangle rule (see paragraph 3.2)

When ab= cd two special integrals are obtained, namely Coulomb integral (J) and exchange integral (K), which are always positive and defined as:

$$J(ab) =< a(1)b(2)\left|\frac{e^2}{r_{12}}\right|a(1)b(2) > \tag{3.4.5A}$$

$$K(ab) =< a(1)b(2)\left|\frac{e^2}{r_{12}}\right|b(1)a(2) > \tag{3.4.5B}$$

It can be demonstrated that the energy of each Slater determinants may be written in terms of these two integrals as:

$$E(\Psi) = \sum_n h_a + \sum_{m<n} J_{m,n} - \sum_{m<n} K_{m,n} \cdot \delta(s_m, s_n) \qquad (3.4.6)$$

where the first term is the sum of one electron energies, which for the free ion are usually the shielded d orbitals, and the second and third term are the interelectronic repulsion contribution. The problem in evaluating the repulsion integral can then be divided in two steps: first, expressing a multielectronic wavefunctions in terms of a sum of two electron products - i.e. expanding the Slater determinants - and then to the evaluation of *J* and *K* in terms of the radial integrals. These are parameterized as $F^k=R_k(abcd)$, and further simplification in the expression of the interelectronic repulsion energy is obtained by setting: $F_0=F^0$, $F_2= F^2/49$ and $F_4=F^4/449$. An alternative set of radial parameters, usually employed, has been developed by Racah, and they are defined as: $A= F_0- 49F_4$, $B= F_2- 5F_4$, $C= 35F_4$.

It is probably worth highlighting two aspects of the adoption of this formalism: first, the energy difference between states of the same configuration is not affected by $A(F_0)$, which has effect only on the average energy of the configuration; second, all the components of a given degenerate free ion terms present the same interelectronic repulsion energy. Moreover, it is important to bear in mind that the radial integrals are properties of the outer orbital and can then be strongly affected by the overlap between the orbital of the ligand and the d orbitals of the metal. This means that covalence between metal and ligand plays a major role in determining the interelectronic repulsion. Indeed, the interelectronic repulsion parameters are generally found to decrease on increasing covalence: this is quite obvious assuming a progressive expansion of the electron cloud on increasing covalence, which clearly leads to minor repulsive energy. This reduction is usually described in terms of a variation of $\beta=B_{complex}/B_{free\ ion}$ on varying the ligand, keeping fixed the *C/B* ratio to the free-ion value (about 4.00). In such a way it has been possible to define a series, on increasing donating power of the ligand and decreasing B, historically named *nephelauxetic series:*[20]

Free ion > F^- > H_2O > $CO(NH_2)_2$ > NH_3 > $H_2NCH_2CH_2NH_2$ ≈ $C_2O_4^{2-}$ ≈ CO_3^{2-} > NCS^- > Cl^- ≈ CN^- > Br^- > N_3^- > I^- > S^{2-} > diarsine

Two contributions accounts for this effect, namely central field covalency and symmetry restricted covalency. The former is strictly connected with the donor power of the ligands: indeed its lone pairs will tend to screen the d orbitals from the nucleus, thus leading to a lowering of the effective nuclear charge and then to an expansion of the d shell. In terms of the radial parameters this may be seen in a reduction of both F_2 and F_4 which are proportional to Z_{eff}. The second contribution, which is smaller, is connected with the differential radial expansion of d-orbitals which is brought by σ- and π- delocalization from the ligand, the σ- being generally larger.[16]

3.5 Spin-orbit coupling energy

The third term of hamiltonian (3.2.1) is spin-orbit coupling, which plays a crucial role in determining magnetic properties and EPR behavior of transition ion complexes. The origin of this term, whose actual value for a free ion can be derived from Dirac relativistic equation, lie in the magnetic interaction between the orbital magnetic moment of the electron and the electric field of the nucleus.[1] It is important to note that as spin-orbit interaction is localized on metal-nucleus the covalency, which tends to delocalise the electrons on the ligands, reduces the magnitude of spin orbit coupling with respect to the free-ion value.

The monoeletronic spin-orbit coupling operator is composed of three terms. $\zeta(r)$ is operating on the radial part of the wavefunctions, while $\mathbf{l}_k$ and $\mathbf{s}_k$ operate on the orbital and the spin part respectively. It is then possible to factor out the effect on the radial part as $\langle R(r)|\zeta(r)|R'(r)\rangle$ as $\zeta/\hbar^2$. The $\mathbf{l}_k\cdot\mathbf{s}_k$ part $\langle d|\mathbf{l}\cdot\mathbf{s}|d'\rangle$ can be calculated by expressing the ket and the bra in terms of the relevant spin and orbital components, $\langle m_l,m_s|$ and $|m_l',m_s'\rangle$ and considering that:[17]

$$\mathbf{l}\cdot\mathbf{s} = \mathbf{l}_x\mathbf{s}_x+\mathbf{l}_y\mathbf{s}_y+\mathbf{l}_z\mathbf{s}_z = \tfrac{1}{2}(\mathbf{l}_+\mathbf{s}_-+\mathbf{l}_-\mathbf{s}_+) + \mathbf{l}_z\mathbf{s}_z. \qquad (3.5.1)$$

The matrix elements to be evaluated have then the form:

$$\langle m_l,m_s|\ [\tfrac{1}{2}(\mathbf{l}_+\mathbf{s}_-+\mathbf{l}_-\mathbf{s}_+) + \mathbf{l}_z\mathbf{s}_z\ ]\ |m_l',m_s'\rangle \qquad (3.5.2)$$

It easily follows that, for this term to be non-zero, $m_l + m_s = m_l' + m_s'$, i.e. either:

i) $m_l = m_l'$ *and* $m_s = m_s'$ (diagonal elements)

ii) $m_l = m_l \pm 1$ *and* $m_s = m_s'$-/+1 (off-diagonal elements)

It is important to note that this analysis applies to the *d* orbitals expressed as complex functions, (3.2.2) while we are concerned with the effect over the real *d* orbitals, which are linear combinations of these.

To evaluate the effect of spin-orbit coupling over a many electron atomic term, i.e. in the weak-field limit, the spin-orbit operator is written in terms of the total angular and spin momentum, **L** and **S**:

$$H = \sum_{i=1}^{nelec} \zeta(r_i)\mathbf{l}_i \cdot \mathbf{s}_i = \lambda \mathbf{L} \cdot \mathbf{S} \qquad (3.5.3)$$

where λ is the spin orbit coupling within a given Russell-Saunders multiplet,[1] which is related to the spin orbit coupling constant of the ion ζ by the relation $\lambda = \pm\zeta/2S$. The plus sign applies to configuration d^n with $1 \leq n \leq 4$ and the minus sign to $6 \leq n \leq 9$. For high spin d^5 ions no spin-orbit coupling is operative at first-order as they are orbital singlet states.

If one assumes a strong-field coupling scheme the evaluation of the spin-orbit coupling matrix element reduces to the proper sum of (3.5.2)-like element, obtained after the expansion of the corresponding Slater determinants in terms of product of monoelectronic wavefunctions.

As spin-orbit coupling can couple states of different spin it is necessary to solve the hamiltonian matrix for all the possible states and this can lead to quite large matrix (the largest being 252 x 252 for a d^5 ion): however, as its effect depends on the magnitude of the coupling constant ζ and on the energy difference between the ground state and the admixed one it is sometimes possible in the calculation to neglect some of the higher energy states, thus reducing the matrix size. At any rate, as we already noticed above, this is no more an important issue, given the current performances of computers.

3.6 The Angular Overlap Model

The Angular Overlap Model[21-24] is one of the first, simplest and most widely used approaches to include covalency. This is a particularly appealing approach to the description of electronic properties of transition metal ion complexes, as it allows the use of parameters directly related to the σ- and π- bonding ability of the ligands, which may be easily controlled by the synthetic chemist. Moreover, it is possible to use the real coordination geometry around the metal ion site, thus including effects due to the low symmetry of the ligand field.[25] Even if it was originally based on a particular molecular orbital framework, the model developed and was later popularized by Gerloch[25] and by the Florence group[26] as a ligand field theory for which the parameters should be assumed to be consistent with chemical information. The key idea underlying the model is best explained by looking at the three main assumptions characterizing the AOM:[24]

(1) The energy of any *l* orbital E_l [#] is obtained as a perturbation.

(2) If the *l*-basis is defined relative to a coordinate system XYZ then the perturbation matrix due to a ligand placed on Z is diagonal

(3) Contributions from different ligands are additive.

Following assumption (1) and (2) the matrix element in the angular overlap model for a ligand on the *z* axis may be expressed as:

$$\langle \lambda_i | H_{aom} | \lambda'_j \rangle = \delta_{\lambda\lambda'}\delta_{ij}\, e_{\lambda i} \qquad (3.6.1)$$

Here, $\lambda_i = \sigma, \pi_S, \pi_C, \delta_S, \delta_C$ identifies the irreducible representation of d orbitals and their components in the space group $C_{\infty v}$, and the factor δ_{ij} reflects the assumption of diagonal overlap for a ligand on the *z* axis. The chemical significance of e_σ and e_π is evident in a molecular orbital approach, and in this framework $e_{\delta S}$ and $e_{\delta C}$ are usually assumed to be zero. However, the actual meaning of e_λ is slightly different in the AOM approach and we will analyze it in more detail. The antibonding effect on a given *d* orbital is assumed to be proportional to the square of the overlap integral S_{ML} between that metal orbital and the ligand orbital of corresponding symmetry. This follows from two assumptions that allows the use of the Wolfsberg-Helmolz approximation when solving the secular determinant:

[#] While in the following we will only refer to d orbitals, AOM application for rare earth ions are also quite common,(see for example [78]) and were at the basis of the model development[79]

first, the energy of the ligand orbital interacting with the metal ion is supposed to be much more negative than those of the central ion and that the overlap between metal and ligand orbital is small. In this framework the solution of the secular equations leads to the following expressions for the destabilization energies over the metal l-orbitals:

$$E_{\lambda}^{*} = \frac{\left(H_{M}^{\lambda} + H_{L}^{\lambda}\right)^{2}}{H_{M}^{\lambda} - H_{L}^{\lambda}} \left(S_{ML}^{\lambda}\right)^{2} \tag{3.6.2}$$

where H_M and H_L are the energy - prior to perturbation - of the ligand and of the metal orbital. As each monoelectronic *d* orbital is written as the product of a radial and an angular part, the overlap integral S_{ML} can be as well factorized as:

$$S_{ML} = \Xi_{\lambda} S_{ML}^{*} \tag{3.6.3}$$

where Ξ_λ accounts for the influence of the angular function of the central ion on the overlap between metal and ligand orbital of λ symmetry and S^*_{ML} is the radial overlap integral, which obviously depends on metal-ligand distance only. This leads to the expression:

$$E_{\lambda}^{*} = e_{\lambda} \left(\Xi_{\lambda}\right)^{2} \tag{3.6.4}$$

Here e_λ, which identifies the semiempirical parameters of the AOM, has been set:

$$e_{\lambda} = \frac{\left(H_{M}^{\lambda} + H_{L}^{\lambda}\right)}{H_{M}^{\lambda} - H_{L}^{\lambda}} \left(S_{ML}^{\lambda *}\right)^{2} \tag{3.6.5}$$

In the general case where more than one ligand is interacting with the metal ion, the metal axis system is considered to be fixed and the problem reduces, following assumption (3), to sum the effects of each ligand upon the d orbitals. This is done by considering for each ligand a new reference system *x′y′z′* with the *z′* in the ligand-nucleus direction, associated with a primed set of d orbitals. The evaluation of any matrix element of the type $< u \mid H^{k}_{AOM} \mid v>$ then reduces to calculate matrix element between orbitals of the primed system. This rotation does not affect the radial parameters e_λ defined in (3.6.5) but has effect over Ξ_λ. Any d orbital of λ symmetry , which we shall call $|w>$, may then be written as a linear combination of d' by using the rotation operator **F**, which leads XYZ to *x′y′z′:*

$$| w >= \sum_{w'=1}^{w'=5} | t' > \mathbf{F}_{wt'} \tag{3.6.6}$$

from which follows:

$$< t' | H^k_{AOM} | w' >= \delta_{t'w'} e_{t'L(K)} \tag{3.6.7}$$

as we required the perturbation to be diagonal. Here $e_{t'L(K)}$ is obviously the same as e_λ for the given k-ligand. Within this formalism, any matrix element relative to perturbation given by a ligand at a general position (θ_k, φ_k) can then be written as:

$$< u | H^k_{AOM} | v >= \sum_{t'=1}^{5} \mathbf{F}^k_{ut'} \mathbf{F}^k_{vt'} < t' | H^k_{AOM} | t' >= \sum_{t'=1}^{5} \mathbf{F}^k_{ut'} \mathbf{F}^k_{vt'} e_{t'L(k)} \tag{3.6.8}$$

Here, u and v identifies any two d orbitals in the XYZ reference system, and 1',..,5' identifies the orbitals in the *x'y'z'* framework. It has to be stressed that for symmetry lower than C_{2v} the *d* orbitals *xz*, z^2, x^2-y^2 span the same irreducible representation and then assumption (2) is not completely justified. This is especially true when trying to obtain magnetic anisotropy properties, which may be strongly affected by the mixing of orbitals with different spatial orientations, while neglecting of this kind of low-symmetry effect has usually only small effect over electronic properties. Even if some models accounting for the presence of off-diagonal terms have been proposed,[27] low symmetry effect are usually taken into account by using the real atomic coordinates of the complex as obtained by X-Ray structure solution.

Finally, to obtain the complete perturbation effect over a given *d* orbital, the sum over all the ligands has obviously to be performed:

$$< u | H^k_{AOM} | v >= \sum_{k=1}^{nlig} \sum_{t=1}^{5} \mathbf{F}^k_{ut} \mathbf{F}^k_{vt} e_{tL(K)} \tag{3.6.9}$$

The most appealing feature of the AOM, beside the fact that it includes overlap and then covalence is considered lies in the fact that the energy levels of complex molecule are

obtained by adding the perturbation of each ligand L upon the orbitals of the central ion taking into account their geometric relationship to each other. This makes the use of this model feasible to describe the spectromagnetic properties of molecules for which e_λ, and thus ligands or metal-ligand distances, are different. Finally, the intuitive character of the model and - at least in principle- the possibility to translate its semiempirical parameters with some chemical significance, from one system to another may be very appealing in designing systems with predetermined properties.

3.7 The spin Hamiltonian and the single ion anisotropy

The concept of spin hamiltonian was first introduced by Pryce[28] and Abragam and Pryce[29] -in the context of Crystal Field Theory- and has been subsequently developed for the description of the electron paramagnetic resonance results of the ions of the iron and lanthanides groups and diluted in diamagnetic hosts.[30] Throughout the years this approach proved to be very useful as a large amount of experimental information obtained by means of different spectroscopies could be summarized in a simple form, without loosing in accuracy from the theoretical point of view.

The approach consists in replacing the true hamiltonian of the system with an effective one which operates on the spin variables of the system only. It is then an operator equivalent that is designed to act on spin coordinates only and give the same results as the "true" hamiltonian discussed in the previous sections, which may be difficult to handle. The spin coordinates that are used are not necessarily the true ones but may rather be fictitious: this is especially true in the case of systems with $S>1/2$. Indeed, as we have seen above, the ground state of a paramagnetic ion interacting with neighboring ligands often consists of a group of electronic levels whose separation is of the order of a few wavenumbers. The behavior of this group may be described through the definition of an effective spin S', such that the total number of levels in the group is $2S'+1$: although the spin hamiltonian does not describe the actual eigenfunctions of the system it correctly describes the way in which they change on varying magnetic field.

The spin hamiltonian is then just a parametric approach which is nevertheless very helpful for the interpretation of sets of experimental data, as it allows a first rationalization of the properties of the complexes. It is important to bear in mind that any spin hamiltonian

does two things: it provides a means of describing a large amount of different experimental results in a compact and easily comparable way, but it provides as well a starting point for a theoretical interpretation of the results, which may then be related with more fundamental properties of the system.[31] The main advantages in the use of a spin hamiltonian are the relatively low number of terms which are implied in the description of the experimental data and the possibility of easily taking into account many different interactions just by adding the appropriate terms to the hamiltonian. A simple form of spin hamiltonian which will be useful for our following interpretation of experimental results of anisotropic magnetic system is:

$$\mathbf{H} = \mu_B \mathbf{B} \cdot \mathbf{g} \cdot \mathbf{S} + \sum_{k,q} B_k^q \mathbf{O}_k^q \qquad (3.7.1)$$

where we neglected interactions involving the nuclei (hyperfine and superhyperfine interactions and nuclear Zeeman effect). The first term is the Zeeman electronic effect and accounts for the anisotropy shown by a system in the way it responds to an external field, while the second one is the Zero Field Splitting term, which identifies the splitting of states belonging to the same S multiplet and different M_S values, leading to a preferential axis (or plane) for the orientation of the magnetization of the molecule. The $\mathbf{O}_k^q$ are the so-called Stevens operator equivalents,[30,32] defined in Table 3.1. They were introduced by Stevens to determine the crystal field potentials of rare earth ions: with this formalism single ion anisotropy is expressed through a series expansion in terms of magnetic multipoles.

n=2	$\mathbf{O}_2^0 = 3\mathbf{S}_z^2 - S(S+1)$ $\mathbf{O}_2^2 = 1/2(\mathbf{S}_+^2 + \mathbf{S}_-^2)$
n=4	$\mathbf{O}_4^0 = 35\mathbf{S}_z^4 - 30S(S+1)\mathbf{S}_z^2 + 25\mathbf{S}_z^2 - 6S(S+1) + 3S^2(S+1)^2$ $\mathbf{O}_4^2 = 1/2[7\mathbf{S}_z^2 - S(S+1) - 5), (\mathbf{S}_+^2 + \mathbf{S}_-^2)]^{\otimes}$ $\mathbf{O}_4^3 = 1/2[\mathbf{S}_z, (\mathbf{S}_+^4 + \mathbf{S}_-^4)]^{\otimes}$ $\mathbf{O}_4^4 = 1/2\,(\mathbf{S}_+^4 + \mathbf{S}_-^4)$

Table 3.1 *Explicit form of even Stevens operators up to fourth order.* $[A,B]^{\otimes}$ *is used as a shorthand for 1/2(AB+BA).* $\mathbf{S}_{\pm} = \mathbf{S}_x \pm i\mathbf{S}_y$ *(After ref.[30])*

The term corresponding to k=2, which describes the effect of the quadrupolar interaction, can be written also as:

$$\mathbf{H_2} = \mathbf{S}\cdot\mathbf{D}\cdot\mathbf{S} \tag{3.7.2}$$

with **D** is a symmetric traceless tensor which can also be explicitly rewritten as:

$$\mathbf{H_2} = D\left[\mathbf{S}_z^2 - S(S+1)/3\right] + E\left(\mathbf{S}_x^2 - \mathbf{S}_y^2\right) \tag{3.7.3}$$

where $D = \frac{1}{3}B_2^0$ and $E = B_2^2$

For cubic symmetry $D = E = 0$. For axial symmetry E=0 and if $D > 0$ the anisotropy is of the easy-plane type while if $D < 0$ it is of the easy-axis type. The number of terms to be retained in (3.7.1) depends both on the spin value and on the symmetry of the the center. Only term with k ≤ 2S will be present; this leads to the conclusion that terms with k=4, describing hexadecupolar interactions, are present only for S ≥ 2 while for k=6 to be present S ≥ 3 is necessary: this is only the case of rare-earths and actinides ions. Concerning the symmetry, for a system with S ≥ 2 in tetragonal symmetry only k= 0 and 4 are needed, for trigonal symmetry only k=0 and 3, while for orthorhombic symmetry only 0, 2 and 4. It should be noted here that the $\mathbf{O}_k^0$ operators describe a purely axial anisotropy and do not mix states with different M_S values, while the $\mathbf{O}_k^q$ operators of equation (3.7.1), with $q \neq 0$ introduce some degree of transverse anisotropy, coupling states differing in M_S by $\pm q$.

The above mentioned anisotropies, namely g-anisotropy and Zero Field Splitting can only occur if an orbital contribution is present in the ground state. It should however be considered that - with the exceptions of the ions which have an orbitally degenerate ground state of T type - orbital degeneracy will be removed by Jahn-Teller distortions.[33] One may then assume in first approximation that the ground state does not possess orbital contribution. At this level of approximation the system is isotropic, because it is only orbital component which can feel differences between different orientations. The anisotropy is introduced in the system by spin-orbit coupling, that admixes excited states with orbital contribution into the ground one. As we have previously mentioned, this phenomenon can be described by the hamiltonian $\mathbf{H} = \sum_i \zeta_i \, \mathbf{l_i}\cdot\mathbf{s_i}$: as ζ_i is small for constituent atoms of organic radicals, the magnetic anisotropy is small in these systems, while it is much larger for

transition metal ions (especially for second and third row) and lanthanides, which are indeed well known to possess a large anisotropy.

3.8 Magnetic Anisotropy in Polynuclear compounds

The effect of the interaction between two spins, $\mathbf{S}_1$ and $\mathbf{S}_2$, is described by the hamiltonian $\mathbf{H}=\mathbf{S}_1\mathbf{J}_{12}\mathbf{S}_2$, where $\mathbf{J}_{12}$ is a general tensor which may be decomposed in the sum of three terms, namely an isotropic, an antisymmetric and an anisotropic one:

$$\mathbf{H}=J_{12}\mathbf{S}_1\cdot\mathbf{S}_2+\mathbf{d}_{12}\cdot\mathbf{S}_1\times\mathbf{S}_2+\mathbf{S}_1\cdot\mathbf{D}_{12}\cdot\mathbf{S}_2 \qquad (3.8.1)$$

where J_{12} is a scalar, $\mathbf{d}_{12}$ is a polar vector and $\mathbf{D}_{12}$ is a symmetric traceless tensor.

The $\mathbf{J}_{12}$ tensor may have two different origins, namely through-space and through-bond interactions.[34] The former contribution can be seen, at the simplest level, as arising from magnetic dipolar interaction between $\mathbf{S}_1$ and $\mathbf{S}_2$, while the latter originates from exchange coupling between the two spins. Through space contribution may be easily calculated assuming that the spins are localized on isolated centers, and that the separation between different centers is large compared to the spatial extension of the magnetic dipoles. This dipolar point approximation is in general good for polynuclear metal ion complexes characterized by low covalency, while it breaks down for polyradicals. The appropriate form of the tensor calculated in this approximation is:

$$\mathbf{J}_{12}=\mu_B^2\frac{\mathbf{g}_1\cdot\mathbf{g}_2-3(\mathbf{g}_1\cdot\mathbf{R})(\mathbf{R}\cdot\mathbf{g}_2)}{R^3} \qquad (3.8.2)$$

where $\mathbf{g_1}$ and $\mathbf{g_2}$ are the $\mathbf{g}$ tensors of the center 1 and 2 respectively, and $\mathbf{R}$ is the unitary vector parallel to the line connecting the two centers. For a pair of spins the dipolar interactions tends to align them parallel to each other, giving rise to an easy axis type anisotropic term, with the axis parallel to $\mathbf{R}$.

The through-bond anisotropic component arises from spin-orbit coupling mixing of excited states into the ground state. To evaluate this term it is customary to use the so-called Moriya approximation,[35] which estimates the exchange determined anisotropic contribution through $\mathbf{D}_{12} \propto (\Delta g/g_e)^2 J_{12}$, where Δg is the difference $(g-g_e)$, g_e is the free electron value and J_{12} is the exchange coupling constant. The main drawback is that J_{12}

refers to the coupling between the ground states on the two centers, while in the Moriya approximation the coupling between one center in the ground state and the other in the excited state should be used. Experimental results showed that in many cases the Moriya approximation may provide even the wrong sign.[34] In general it must be expected that for centers with $g \approx g_e$ (like organic radicals and S-ion as Mn(II), Fe(III), Gd(III)) $\mathbf{D}_{12} \approx 0$ for the spin-orbit determined contribution.

It is then clear that the appropriate spin hamiltonian to describe a system of N interacting spins will be a sum containing terms arising both from single ion properties, and from the interactions between the spin pairs:

$$\mathbf{H} = \sum_{i<j} J_{ij}\mathbf{S}_i \cdot \mathbf{S}_j + \mu_B \mathbf{B} \sum_i \mathbf{g}_i \cdot \mathbf{S}_i + \sum_i \mathbf{S}_i \cdot \mathbf{D}_i \cdot \mathbf{S}_i + \sum_{i<j} \mathbf{S}_i \cdot \mathbf{D}_{ij} \cdot \mathbf{S}_j \qquad (3.8.3)$$

here we have neglected the antisymmetric exchange term of (3.8.1) and only the second order single ion anisotropy terms of (3.7.1) have been considered for the sake of simplicity.

Provided that the total spin strong exchange limit is achieved - i.e. J_{ij} is larger than any other interaction in (3.8.3) and then S is a good quantum number, the global anisotropy of the system may finally be expressed by using the hamiltonian:

$$\mathbf{H} = \mathbf{S} \cdot \mathbf{D} \cdot \mathbf{S} \qquad (3.8.4)$$

where $\mathbf{S}=\sum_i \mathbf{S}_i$. At the same time the Zeeman term of (3.8.3) may be expressed in the strong-exchange limit as a function of the total spin number using $\mathbf{H} = \mu_B \mathbf{B} \cdot \mathbf{g} \cdot \mathbf{S}$.
In this assumption:

$$\mathbf{D} = \sum_i d_i^S \mathbf{D}_i + \sum_{i<j} d_{ij}^S \mathbf{D}_{ij} \qquad (3.8.5)$$

A relation relying on the same approach describes the dependence of the global **g** tensor on the individual ones:

$$\mathbf{g}_S = \sum_i c_i^S \mathbf{g}_i \qquad (3.8.6)$$

Explicit expression for coefficients c_i, d_i and d_{ij} may be found in ref. [34]

According to (3.8.5) the single ion contribution to the magnetic anisotropy of a polynuclear compound can be calculated as a weighted sum of individual contribution if the

nature of the total spin state is known. It is important to stress that both Eq. (3.8.5) and (3.8.6) are tensorial ones, which means that the principal directions of the various tensors must be taken into account. Once the individual, intermediate and total spin states are definite, the c_i^S , d_i^S and d_{ij}^S coefficients are readily calculated by projecting the individual spins on the total spin.[34] The value of the coefficients can be calculated with recurrent formulae, easily implemented by a computer program.

3.9 Calculation models for Spin Hamiltonian parameters

Given the discussion carried on up to now the need for an appropriate model of calculation of spin hamiltonian parameters is evident, starting from information on electronic parameters and from some kind of approximation (ligand field, MO, etc.). It is worth mentioning here that the problem of calculating spin hamiltonian parameters in the general case for which no specific approximation to the non relativistic many electron wavefunction is assumed has been analyzed by several authors. In particular, Solomon and Neese recently presented a method aimed to derive equations for the calculations of Spin Hamiltonian parameters for the case of $FeCl_4^-$, for which all states are well described by single determinantal function.[36]

On the other hand, a very simple model to account for anisotropy is introduced as a simple perturbational approach to ligand field theory. If the ground state can be adequately described by using only the functions within a given Russell-Saunders multiplet *D* and *E* may be easily calculated as:

$$\begin{aligned} D &= \frac{1}{2}\lambda\left[g_z - \frac{1}{2}\left(g_x + g_y\right)\right] \\ E &= \frac{1}{4}\lambda\left(g_x - g_y\right) \end{aligned} \tag{3.9.1}$$

where g_i (i=x,y,z) are calculated according to the perturbative relation:

$$g_i = g_e + 2\lambda\sum_n \frac{< 0 \mid \mathbf{L}_i \mid n >< n \mid \mathbf{L}_i \mid 0 >}{E(0) - E(n)} \tag{3.9.2}$$

here $|0\rangle$ and $|n\rangle$ identify the ground and any excited states, respectively. However, for more accurate calculations in the ligand field limit it is necessary to completely diagonalize the Hamiltonian matrix.

Among the different general and practical computational methods relating electronic properties to Spin Hamiltonian parameters we will focus in the following on the Angular Overlap approach. As we have seen, indeed, this seems to be a very well suited model to explain the experimental results given the chemical significance of its parameters. Moreover, recently different programs based on the Angular Overlap approach became available which starting from the energy levels calculated by electronic parameters are working out Spin Hamiltonian parameters [37,38] We will describe in some detail the working principle of the program presented in ref. [37] using which the results presented in the following sections have been obtained.

The energy levels are computed as the eigenvalues of the Hamiltonian:

$$\mathbf{H} = \mathbf{H_{AOM}} + \mathbf{H_{ER}} + \mathbf{H_{SOC}} \tag{3.9.3}$$

here, $\mathbf{H_{AOM}}$ is the ligand field Hamiltonian expressed in terms of AOM parameters, $\mathbf{H_{ER}}$ is the interelectronic repulsion term, and $\mathbf{H_{SOC}}$ is the spin-orbit coupling part of the hamiltonian. The matrix element of Eq. (3.9.3) are calculated using all of the states arising from the d^n configuration, and without any perturbational approximation. The employed basis set is $|\alpha LSJM_J\rangle$, where L and S are the usual quantum orbital and spin angular momentum, J is the total angular momentum operator, and α is any additional quantum number needed to define the state. In such a way the calculation procedure is greatly simplified as $\mathbf{H_{SOC}}$ is diagonal on $|JM_J\rangle$, while the calculation of $\mathbf{H_{AOM}}$ and $\mathbf{H_{ER}}$ is greatly simplified by the use of irreducible tensor operators. From the diagonalization of the matrix of (3.9.3), the eigenvectors are obtained:

$$\psi_k = \sum_k c_k \, | \alpha LSJM_J \rangle \tag{3.9.4}$$

The obtained energy levels are further split by Zeeman interaction when a magnetic field is applied:

$$\mathbf{H_{Zeem}} = \mu_B \mathbf{B} \cdot (k\mathbf{L} + g_e \mathbf{S}) \tag{3.9.5}$$

The program calculates the Zeeman splitting by diagonalizing the matrix built up with elements:

$$< \psi_i \mid \mu_B \mathbf{B} \cdot (k\mathbf{L} + g_e \mathbf{S}) \mid \psi_K > \tag{3.9.6}$$

As the energy involved in Zeeman interactions are usually much smaller than those of ligand-field only the states of ground manifold are included in (3.9.6). The energy level pattern calculated by this procedure, and its behavior in various magnetic fields, is then reproduced by the program using the spin Hamiltonian formalism and deriving the corresponding parameters. As we have seen in the previous paragraphs this is a very useful formalism to describe the behavior of a d^n ion in a magnetic field. However, while in the case of Kramers ions the Zeeman splitting can always be interpreted in terms of ground doublet effective spin, and a procedure has been developed in the past which calculated the spectromagnetic properties of such systems (e.g Co(II) pseudooctahedral complexes) by treating (3.9.5) as a first-order perturbation the situation is more complicated for non Kramers ions and a more general approach is needed.

The Spin Hamiltonian employed in the program for the general case of a non-Kramers ion is of the form:

$$\mathbf{H} = \beta \mathbf{B} \cdot \mathbf{g} \cdot \mathbf{S} + \sum_{l=2}^{l \le 2S} \sum_{m=-l}^{l} B_{lm} \boldsymbol{T}_{lm}(S) \tag{3.9.7}$$

Here $\boldsymbol{T}_{lm}(S)$ are combination of the spherical tensor $\mathbf{T}_{lm}(S)$:

$$\boldsymbol{T}_{l0} = \mathbf{T}_{l0} \ (l \text{ even}) \tag{3.9.8A}$$

$$\boldsymbol{T}_{l0} = \mathrm{i}\mathbf{T}_{l0} \ (l \text{ odd}) \tag{3.9.8B}$$

$$\boldsymbol{T}_{lm} = [(-1)^m \mathbf{T}_{lm} + \mathbf{T}_{l-m}]/\sqrt{2} \tag{3.9.8C}$$

$$\boldsymbol{T}_{l-m} = \mathrm{i}[(-1)^m \mathbf{T}_{lm} + \mathbf{T}_{l-m}]/\sqrt{2} \tag{3.9.8D}$$

$\mathbf{T}_{lm}$ are irreducible tensor operators which may be calculated by means of Wigner-Eckart theorem using 3j Wigner symbols (see (3.2.7)) and then they transform in the same way as the spherical harmonics. They are somewhat different from the $\mathbf{O}_k^q$ Stevens operators defined in Eq. (3.7.1), but can be related to those by using simple formulas which have been tabulated by Rudowicz.[39] Accordingly the parameters B_{lm} of Equation (3.9.7) and B_k^q of Equation (3.7.1) have different meaning, and care must be exerted when comparing data

obtained by using the two different formalism as literature is quite confusing on this point (see ref.[39]), especially for negative values of m.

The parameters of the Hamiltonian (3.9.7) are evaluated by the program through a numerical fitting procedure that compares the energy levels obtained, for different magnetic field values and orientations through the use of Eqs.(3.9.3)-(3.9.6) ($E_i^{AOM}(\theta,\phi,H)$) to the ones obtained from the spin hamiltonian approach ($E_i^{SH}(\theta,\phi,H)$). The function which is minimized by varying the spin hamiltonian parameters is then:

$$\sum_{i=1}^{2S+1}\sum_{\vartheta,\varphi}\sum_{B_1,B_2}\frac{\left\{\left[E_{i+1}^{SH}(\vartheta,\varphi,B)-E_i^{SH}(\vartheta,\varphi,B)\right]-\left[E_{i+1}^{AOM}(\vartheta,\varphi,B)-E_i^{AOM}(\vartheta,\varphi,B)\right]\right\}^2}{\left[E_{i+1}^{AOM}(\vartheta,\varphi,B)-E_i^{AOM}(\vartheta,\varphi,B)\right]} \quad (3.9.9)$$

3.10 Ligand Field based interpretation of HF-EPR spectra of "silent ions"

In the following we will shortly overview some of the most significant recent report in HF-EPR of EPR silent ions together with the discussion of the Ligand Field models used for interpreting their properties.

3.10.1 S= 1 Ions

a-Vanadium(III)

V(III) is a d^2 ion, which in octahedral symmetry has a ground $^3T_{1g}$ state. Low symmetry components of the ligand field and spin orbit coupling remove the orbital degeneracy, but at any rate a large zero field splitting is observed. A particularly simple example is provided by the spectra of the aquo ion present in the vanadium doped alum $CsGa(SO_4)_2\cdot 12H_2O$. The site symmetry of the tripositive ion is S_6, splitting the ground orbital triplet in a ground singlet and an excited doublet. The distortion corresponds to a trigonally compressed octahedron. Single crystal and polycrystalline powder spectra in the range 95- 285 GHz were reported by Tregenna-Piggot et al.[7] which showed that the ZFS is large, D= 4.7735 cm^{-1}, and the g values fairly anisotropic, $g_{\|}$= 1.9549, $g_{\perp}$= 1.8690. The experimental data were reproduced by using the Angular Overlap Model,[38] and the employed parameters were the same used for the interpretation of the UV/Vis and Raman spectra: e_σ= 6950 cm^{-1}, $e_{\pi\perp}$= 930 cm^{-1}, $e_{\pi//}$= 0, with the Racah parameters B= 644 cm^{-1}, C= 2960 cm^{-1}. In order to

reproduce the zero field splitting and the g values the spin orbit coupling constant, ζ, was reduced to ca. 80% of the free ion value, and the orbital reduction factors were taken as: $k_{//}$= 0.910, $k_{\perp}$= 0.866. Rather surprisingly the ZFS was found to be very sensitive to deuteration. In fact D= 4.8581 cm^{-1} was found for the deuterated sample: this was attributed to a slight distortion in the coordination sphere of Vanadium on deuteration. The use of a different AOM-based program, developed in our laboratory,[37] was in substantial agreement with these results, even if we had to employ lower reduction of the spin-orbit coupling (90% of the free ion value) and of the orbital reduction factor (k=0.95). These sample calculations showed that even very subtle distortions of the coordination sphere of Vanadium can easily result in quite large effect on ZFS, thus supporting the explanation of the large variation of Zero Field Spliting on deuteration. The extreme sensitivity of the SH parameters to small distortions is associated with the T_{1g} ground state. Similar effects were previously observed for high spin Co(II).[40]

b-Nickel(II)

Octahedral Ni(II), d^8, has an orbitally non-degenerate ground state ($^3A_{2g}$) and its complexes show quite large Zero Field Splitting, that can range from a few to tens of wavenumbers. Nickel is a very fortunate case for the application of ligand field theory, as a large amount of electronic data is available in literature, and determination of Spin Hamiltonian parameters has been achieved using conventional EPR for some complexes in the past.[15,41,42] On the other hand, HF-EPR has up to now been employed only in three cases to study Ni(II) complexes. These involved a macrocyclic complex Ni(sarcophagine)$(ClO_4)_2$,[11] a Ni doped sample of $Zn(en)_3(NO_3)_2$[4] and a Zn-doped Haldane chain, $[Ni(C_2O_4)(dmiz)_2]_n$.[9] Further studies are actually in progress on different complexes from various laboratories and preliminary results are quite encouraging, both in term of spectral simulation and of correlation between ligand field and ZFS parameters.[43]

In the case of Ni(sarc) Mrozinski et al.[11] reported an axial Zero Field Splitting with D=1.400 cm^{-1}, with $g_{||}$=2.125, $g_{\perp}$= 2.143: a trigonal compression along a line connecting two C atoms of the encapsulating macrocycle was invoked to be responsible for the positive value of the Zero Field Splitting. The observed ZFS is quite large if compared to the one expected on the basis of ligand field parameters derived for similar macrocycles. Indeed, sample calculations employing Angular Overlap Model showed that the calculated anisotropy is much lower than the observed one; more importantly, calculation showed that

idealized trigonal compression would actually result in a negative ZFS. On the other hand, the observed results (D=1.87 cm^{-1}, E=0.38 cm^{-1}) for the $[Ni_xZn_{1-x}(C_2O_4)(dmiz)_2]_n$ chain, where the high level of Zinc doping lead to completely isolated Nickel centers, were easily justified on the basis of the coordination sphere of the nickel, NiN_2O_4.[9] Indeed, the observed value for D is intermediate between the value observed through X-Band studies for NiO_6, usually quite high, and those for NiN_6, much lower, in agreement with the weaker ligand field of the oxygen compared to the nitrogen donor. Ligand field parameters for this system for both imidazole-type ligand and oxalate were readily available in literature.[16] Starting from those parameters and using the real structure of the complex the above mentioned AOM-based program yielded a quite good agreement in term of reproduction of experimental data: D= 1.86 cm^{-1}, E= 0.24 cm^{-1}.[44]

3.10.2 S= 2 Ions

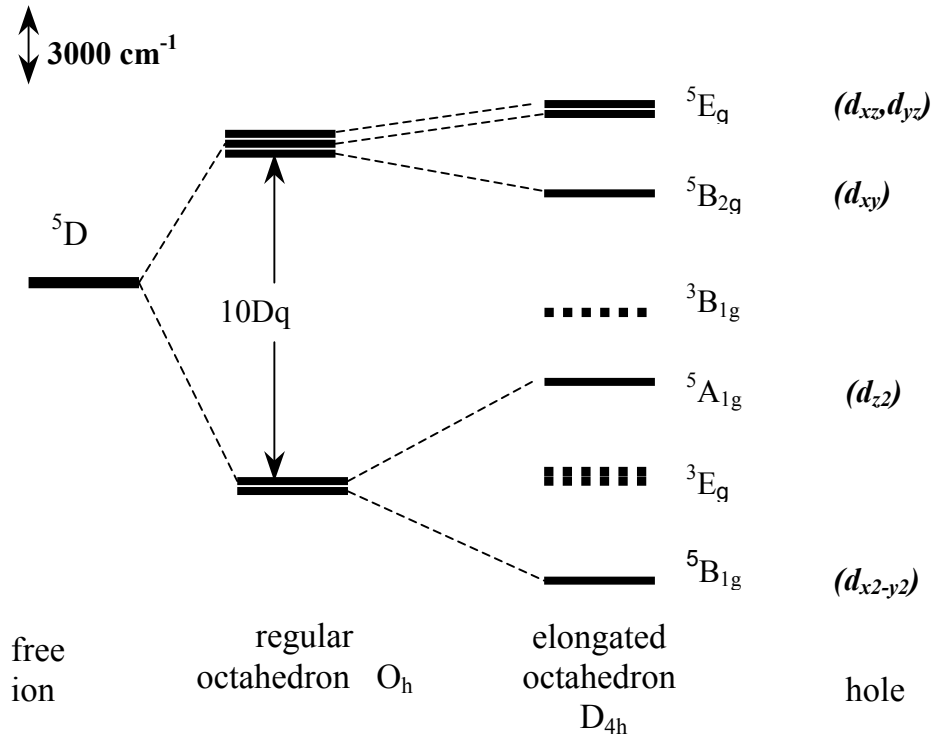

Figure 3.1 *Schematic view of the energy levels for a d^4 ion. The free ion state, the splitting in a regular octahedral ligand field and in a tetragonally elongated octahedral environment are represented. In the last case the low lying triplet states are also drawn as dotted lines. The energies are calculated with the program of ref.[37] using standard ligand field parameters for a MnO_6 chromofore as discussed in paragraph 3.10.2.*

S= 2 states are observed in d^4 and d^6 ions. The former in octahedral symmetry have a ground ^5E_g level, which is unstable due to Jahn-Teller effects: similar considerations hold

for d^6 in a tetrahedral environment. In general for d^4 ions the Jahn-Teller distortion is a tetragonal elongation which leaves the e_g unpaired electron in the z^2 orbital; this splits the ground state in a $^5A_{1g}$ and a $^5B_{1g}$, the latter lying lowest, and yields a negative ZFS. A schematic picture of these levels is given in Figure 3.1.

Another peculiar feature of S=2 systems is the possibility of having fourth order terms in the crystal field Hamiltonian.[30] The magnitude of these terms, which have been shown to be of capital importance in promoting the Quantum Tunnelling of the magnetization on ***Mn12***,[45] can now be derived by HF-EPR.

The theory that relates the Zero Field Splitting parameters to the ligand field ones is well established[6] and can be employed at different levels of approximation. Using perturbation theory an acceptable level of approximation requires:

$$D=D_0+D_1 \qquad (3.10.1)$$

here D_0 is the zero field splitting parameter estimated by considering only the contribution of states belonging to ^5D according to Eqs. (3.9.1) and (3.9.2): obviously the + sign applies to d^4 and the – to d^6 ions. For example, the g values for a d^4 ion in a rhombic distorted environment can be calculated as:

$$\begin{aligned} g_z &= g_e - \frac{8\lambda}{\Delta E(xy \rightarrow x^2-y^2)} \\ g_x &= g_e - \frac{2\lambda}{\Delta E(yz \rightarrow x^2-y^2)} \\ g_y &= g_e - \frac{2\lambda}{\Delta E(xz \rightarrow x^2-y^2)} \end{aligned} \qquad (3.10.2)$$

However it is now well known that (3.10.2) is not able to adequately reproduce the experimental ZFS parameters. Improvements can be introduced through D_1 that takes into account the contribution of the lower spin multiplicity states which can mix into the ground state via spin-orbit coupling. On the basis of first-order perturbation theory D_1 can then be calculated to be:

$$D_1 = -\frac{\zeta^2}{4\Delta} \qquad \Delta = 6B + 5C - \Delta E(xz, yz \rightarrow z^2) \qquad \text{for elongated } d^4 \text{ ions} \qquad (3.10.3a)$$

$$D_1 = -\frac{\zeta^2}{12\Delta} \qquad \Delta = 6B + 5C - \Delta E(xz, yz \rightarrow x^2-y^2) \qquad \text{for compressed } d^4 \text{ ions} \qquad (3.10.3b)$$

Here Δ is the energy difference between the ground state ($^5A_1$ for compressed systems and $^5B_1$ for elongated ones) and the first triplet excited state (^3E) that mixes in it through spin-orbit coupling (see Figure 3.1).

As literature data dealing with Eqs. (3.10.3) are quite confusing[46] we will review some of the results obtained up to now by using this approach. It will be shown that even if it works quite correctly on a qualitative point of view, it seems to underestimate the value of the anisotropy, both for Cr(II) and some of the Mn(III) to date reported. To overcome these problems, the best approach at the Ligand Field level is given by complete diagonalization of the d^n matrix.

a-Manganese(III)

Mn(III) complexes have been increasingly studied since the availability of high frequency and high fields in recent years,[2,3,6,10,12,13] and further work is currently in progress to gain better insights in key factors determining magnetic anisotropy. In many cases reported so far the parameters obtained by simulations of HF-EPR spectra have been explained on the basis of simple considerations based on the foundations of ligand field theory outlined in the previous paragraph.

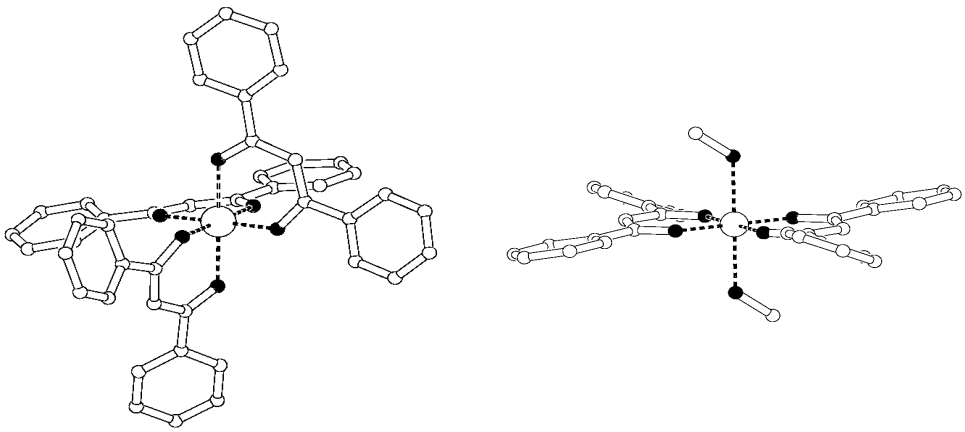

$[Mn(dbm)_3]$ $[Mn(dbm)_2(CH_3OH)_2]^+$

Figure 3.2. *Schematic view of the structure of $[Mn(dbm)_3]$ and $[Mn(dbm)_2(CH_3OH)_2]^{+\cdot}$ The hydrogen atoms are not reported for the sake of clarity.*

The first example of resolved HF-EPR spectra on a Mn(III) complex, namely $[Mn(dbm)_3]$ (see Figure 3.2) was reported in 1997 by Gatteschi et al..[2] This system, which presents an elongated octahedral coordination environment of Mn(III) with slightly rhombic distorsion, was an excellent testing ground for the ligand field approach at the different

levels of approximations presented in the previous paragraph, relying on the electronic parameters obtained by the UV-vis spectra. Use of (3.9.1) and (3.10.2) lead to D_0=-1.4 cm^{-1}, and even inclusion of excited triplet states by using equation (3.10.3), lead to D_1=-2.3 cm^{-1}, i.e. to a global D value of -3.7 cm^{-1}, about 20% lower than the observed value. For the sake of comparison, the use of the above mentioned AO program[37] neglecting all the S<2 states yielded a largely underestimated value of D=-1.35 cm^{-1}, in agreement with the results obtained by using Eqs. (3.9.1) and (3.10.2). Finally, the inclusion of all of the Russell Saunders states by taking into account the orthorhombic distortion leads to D=-4.55 cm^{-1} and E=0.28 cm^{-1} in very good agreement with the experimental values obtained by the simulation of the spectra, D=-4.35 cm^{-1} and E=0.26 cm^{-1} with $g_x=g_y$=1.99 and g_z=1.97.

$[Mn(dbm)_3]$		$[Mn(dbm)_2(CH_3OH)_2]Br$	
Mn-O(1)	2.109(2)	Mn-O(1)’	1.896(4)
Mn-O(2)	1.917(2)	Mn-O(2)	1.908(4)
Mn-O(3)	2.142(2)	Mn-O(3)’	2.240(5)
Mn-O(4)	1.931(2)	Mn-O(1)	1.896(4)
Mn-O(5)	1.935(2)	Mn-O(2)’	1.908(4)
Mn-O(6)	1.908(2)	Mn-O(3)	2.240(5)
O(1)-Mn-O(2)	88.3(1)	O(1)-Mn-O(2)'	88.3(2)
O(1)-Mn-O(3)	175.4(1)	O(1)-Mn-O(2)	91.7(2)
O(1)-Mn-O(4)	89.5(1)	O(1)-Mn-O(3)	91.4(2)
O(1)-Mn-O(5)	90.6(1)	O(1)-Mn-O(3)’	88.6(2)
O(1)-Mn-O(6)	93.2(1)	O(2)-Mn-O(3)	89.6(2)
O(2)-Mn-O(3)	90.2(1)	O(2)-Mn-O(3)'	90.4(2)
O(2)-Mn-O(4)	92.5(1)	O(1)-Mn-O(1)’	180.0
O(2)-Mn-O(5)	89.1(1)	O(2)-Mn-O(2)’	180.0
O(2)-Mn-O(6)	178.5(1)	O(3)-Mn-O(3)'	180.0
O(3)-Mn-O(4)	86.2(1)		
O(3)-Mn-O(5)	93.7(1)		
O(3)-Mn-O(6)	88.4(1)		
O(4)-Mn-O(5)	178.4(1)		
O(4)-Mn-O(6)	87.9(1)		
O(5)-Mn-O(6)	90.5(1)		

Table 3.2 *Distances (Å) ed angles (°) in the coordination sphere of* $[Mn(dbm)_3]$ *and* $[Mn(dbm)_2(CH_3OH)_2]Br$.

Following that approach a substituted derivative, $[Mn(dbm)_2(CH_3OH)_2]Br$, has been synthesized and its HF-EPR spectra recorded at two different frequencies, 190 and 285 GHz (see Figure 3.3). The crystal structure of this complex has been recently solved:[47] for our purpose it is sufficient to take into account the coordination sphere of Mn(III) (see Figure 3.2), whose relevant parameters are reported in Table 3.2 together with those of $[Mn(dbm)_3]$. It is evident from the parameter of this table that the Jahn-Teller elongation of the Mn-$O_{methanol}$ bond is very pronounced: on the basis of simple considerations a negative and nearly axial ZFS can then be predicted.

The spectra recorded at 285 GHz show two low field transitions that can be used to predict an initial value of D. Indeed, for an S=2 system with negative and axial anisotropy the lowest M_s levels are separated by $3D$, thus suggesting a value of D=-3.1 cm^{-1}. Moreover the splitting between the first two lines can be attributed to the presence of a small term of transverse anisotropy (E/D<0.1), which has been found also in $[Mn(dbm)_3]$. With these starting values we performed a satisfactory simulation of the spectra recorded at 190 GHz and 285 GHz (see Figure 3.3, left and right respectively) with the parameters D=-3.46 cm^{-1}, E=0.13 cm^{-1} and an isotropic g=1.99. The obtained D value is much smaller than in the parent original complex and the transverse anisotropy is as well reduced.

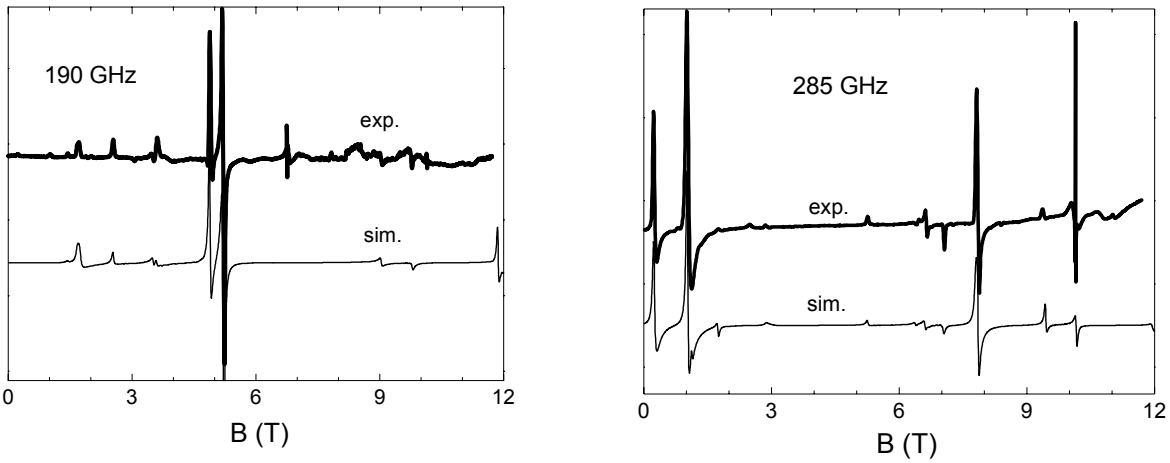

Figure 3.3. *Polycrystalline powder EPR spectrum of $[Mn(dbm)_2(CH_3OH)_2]Br$ recorded at 190 (left) and 285 GHz (right) and 10 K (bold line). The simulations have been obtained using the parameters reported in Table 3.3.*

A clue to explain this behavior lies in the much larger distance of the axial ligand in this derivative with respect to $[Mn(dbm)_3]$, which is likely to induce a much lower ligand field. This results in a lower value of $\Delta E(xz,yz \rightarrow z^2)$ in Equation (3.10.3a) and then in a lower D_1. At the same time, the lower transverse anisotropy can be related to a smaller variation in the

equatorial distances. It should be stressed that dbm and methanol can be assumed to lie in close position within the spectrochemical series and it is only the elongation of the Mn-$O_{methanol}$ ligands that leads to this effect.[16] The solution UV-vis spectra showed the typical features of a tetragonally elongated Mn(III), with fairly broad transition around 9400 cm^{-1} ($^5A_1 \leftarrow {}^5B_1$), 16400 cm^{-1} ($^5B_2 \leftarrow {}^5B_1$) and 20250 cm^{-1} ($^5E \leftarrow {}^5B_1$). The substitution of the observed UV-vis transition and of a spin-orbit coupling constant (ζ=345 cm^{-1}) slightly reduced with respect to the free-ion value in Eqs.(3.9.1) and (3.9.2) gives D_0=-1.34 cm^{-1}. Correcting this value by D_1 calculated through Eqs. (3.10.3) gives a global value of D=-3.18 cm^{-1}, with an underestimation of about 10%.

Following the same approach outlined in ref [2] for an orthorhombic system, and assuming $e_{\pi(MeOH)}$=1000 cm^{-1} (z refers to the axial ligand, while x and y identify the equatorial ones) we got the following parameters to be employed in the AO calculation: $e_{\pi(MeOH)}$=1000 cm^{-1}, $e_{\sigma(MeOH)}$=4000 cm^{-1}, $e_{\sigma(dbm)}$ =9370 cm^{-1} and $e_{\pi(dbm)}$=2925 cm^{-1}. Neglecting the contribution from excited states with S<2 resulted again in an underestimated D value(D=-1.17 cm^{-1}, about one third of the real value). Finally, including all the excited Russell-Saunders triplet states in the AO calculation and assuming an r^{-6} dependence of the Dq [48] on the metal oxygen distance for the equatorial ligand (Dq_{O1}=1670 cm^{-1}, Dq_{O2}= 1610 cm^{-1}, e_π/e_σ=0.3) lead to an almost perfect agreement with the experimental parameters: D=-3.45 cm^{-1}, E=0.14 cm^{-1}. The D and E values experimentally observed and those calculated with the perturbative approach and with the AOM approach are summarized in Table 3.3 for $[Mn(dbm)_3]$ and $[Mn(dbm)_2(CH_3OH)_2]Br$.

		exp	**Eqs. (3.9.1) (3.10.2)**	**Eq. (3.10.3)**	**AOM(a)**	**AOM(b)**
$[Mn(dbm)_3]$	D/cm^{-1}	-4.35	-1.4	-3.7	-1.35	-4.55
	E/cm^{-1}	0.26	-	-	-	0.28
$[Mn(dbm)_2(CH_3OH)_2]Br$	D/cm^{-1}	-3.46	-1.34	-3.18	-1.17	-3.45
	E/cm^{-1}	0.13	-	-	-	0.14

Table 3.3. *Experimental and calculated values for the spin hamiltonian parameters of two Mn(III) elongated octahedral Manganese(III) complexes. The calculated values are obtained by the perturbative treatments (Eqs. (3.9.1) and (3.10.2) and Eq. (3.10.3) in the text) and by the computational program based on the Angular Overlap Model[37] taking into account: a) only the ground quintet state for the d^4 configuration; b) also the excited electronic states with lower multiplicity.*

In agreement with sample calculation on model systems of Mn(III), inclusion of higher lying singlet states do not modify the obtained results.[2] These findings then clearly show that the AOM approach is very well suited for a rational and quantitative justification of the spin hamiltonian parameters in system for which enough spectroscopic information is known.

b-Chromium(II)

The aquo-ion of Cr(II) has recently been studied in frozen solution by HF-EPR.[5] The advantages of using frozen solutions rely on the possibility of obtaining a true powder pattern spectra, while the use of powder pressed in pellet often results in decrease of intensity due to the reflection of the microwave at the surface of the pellet and to a broadening of some transition which is still not well understood, but seems to be strictly related with the thickness of the pellet compared to the microwave.[9] Moreover the use of a water solution is of great interest in the perspective of performing HF-EPR on biological systems in this solvent.

This system offered a good testing ground for ligand field theory, as it has been thoroughly studied in the past years through electronic absorption spectroscopy.[49] On the basis of the above stated consideration, the negative (D=-2.20) $cm^{-1}$and purely axial ZFS was easily related to a tetragonally elongated structure. A quantitative explanation of the obtained results was achieved with the use of second order perturbation theory, relating ZFS to fundamental parameters:

$$D=-3(\rho+\lambda^2/\Delta)\cos 2\delta \qquad (3.10.4a)$$

$$E=-3^{1/2}(\rho+\lambda^2/\Delta)\sin 2\delta \qquad (3.10.4b)$$

where Δ is the ligand field splitting between $^5B_{1g}$ and the excited $^5T_{2g}$, whose tetragonal field splitting is neglected, ρ the spin-spin coupling and λ is the spin orbit coupling constant, while δ accounts for orthorhombic distortion, and in this case should then be set to zero. It should be noted that in the framework of a spin Hamiltonian approach, spin-spin coupling is formally equivalent to the effects of mixing brought about by higher-order spin-orbit coupling terms[5,30].

The use of values found in literature for Δ, λ and ρ, gave a value of D=-1.98 cm^{-1} in reasonable agreement with the experimental value D=-2.20 cm^{-1}. On the other hand, the use of Eqs. (3.9.1) and (3.10.3) lead to a large underestimation of D (D_0= -0.77 cm^{-1}, D_1= - 0.95

cm^{-1}, D_{tot}= -1.72 cm^{-1}). A more accurate calculation was based on the exact diagonalisation at different fields of the matrix:

$$\mathbf{H} = \frac{Dq}{12}\left(\mathbf{O}_4^0 + 5\mathbf{O}_4^4\right) + \frac{Ds}{3}O_2^0 - \frac{Dt}{12}\mathbf{O}_4^0 + \lambda\mathbf{L}\cdot\mathbf{S} + \beta\mathbf{B}\cdot\left(\mathbf{L} + g_e\mathbf{S}\right) - \\ - \rho\left\{(\mathbf{L}\cdot\mathbf{S})^2 + \frac{1}{2}(\mathbf{L}\cdot\mathbf{S}) - \frac{1}{3}L(L+1)S(S+1)\right\} \qquad (3.10.5)$$

where both $\mathbf{O}_k^q$ and *Dq*, *Ds*, *Dt* have been defined in the previous paragraphs, while ρ and λ have the same meaning as in (3.10.4). This procedure yielded a slightly more accurate reproduction of the observed *D* value, *D*=-2.04 cm^{-1}.

c- High-spin tetrahedral Iron(II)

As ferrous ion in tetrahedral environment is present in various Iron-Sulfur proteins,[50] it is evident the interest toward systems of this kind for future investigation of active sites of metalloenzymes. Recently, a study appeared on a model system of the simplest Iron-sulfur protein, namely rubredoxin, where a single Fe(II) atom is bound by four cysteinyl ligand in a nearly tetrahedral arrangement. The HF-EPR study of this model system, $[Fe(SPh_4)][PPh_4]_2$[8] can be thought of as a first step of applying this technique to high spin metallo-protein sites. The obtained ZFS parameters of *D*=5.84 cm^{-1}, *E*=1.42 cm^{-1} were interpreted on the basis of Eqs. (3.10.4), using for ρ and λ values found in literature and a tetrahedral ligand field splitting between ^5E and $^5T_2$ Δ=6000 cm^{-1}, as derived from optical data. To get a good reproduction of the experimental values the parameter δ, which accounts for distortion from tetrahedral symmetry, was set to 100°, thus leading to a mainly $^5A_1$ ground state with a small admixture of $^5B_1$, in agreement with the presence of a non-negligible transverse anisotropy. Interestingly, the comparison of HF-EPR and Mössbauer spectra pointed out that the latter technique tends to overestimate the *D* value, while it seems to correctly evaluate the degree of rhombicity (i.e. the *E/D* ratio).

3.11 Sample calculations of Single Ion anisotropy using AOM

In these final paragraphs we will try to define some principles for the rationalization of the origin of the anisotropy in magnetic molecular materials, with a special focus to single molecule magnets, by using the above described program based on AOM. This may help in

developing suitable strategies for introducing the appropriate anisotropy in the molecules and thus to get Single Molecule Magnet behavior at higher temperatures. The starting point is obviously that of getting some clues for the control of the magnetic anisotropy in simple molecules. We will present in the following some sample calculation - whose results are summarized in Table 3.4 - on both real and model systems which are of interest as constituent of Single Molecule Magnets, Fe(III) and Mn(III). In particular, as both of these ions have $S \geq 2$, their description involves the use of fourth order terms of the spin hamiltonian, whose calculation will be presented here. This is a very important point, as it has been clearly shown that $\mathbf{O}_4^q$ operators with q=2,4 are of fundamental importance in promoting the Quantum Tunneling of the Magnetization in some Single Molecule Magnets.[45,45,51]

3.11.1 Iron(III) mononuclear complexes

Fe(III) is a ^6S ion: nevertheless the combined effect of spin-orbit coupling and structural distortion is well known to give rise to appreciable Zero Field Splitting in coordination complexes of this ion.[15] We performed some test calculation assuming two kinds of distortions from octahedral geometry in an intermediate ligand field strength (Dq=1460 cm^{-1}). Assuming the quite commonly encountered trigonal distortion, we found that a variation of θ (Figure 3.5) by 5° with respect to octahedral geometry (for which θ = 54.73°) leads to D=0.420 cm^{-1} for compression and D=-0.340 cm^{-1} for elongation.

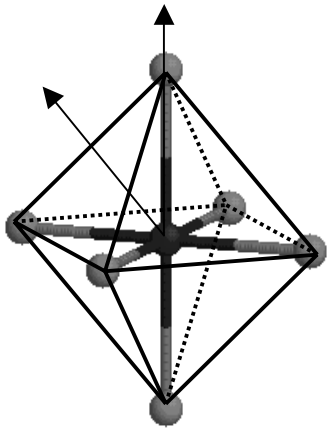

Figure 3.5 *Scheme of trigonal distortion. The parameter which describes the distortion is the angle between the two arrows (*θ *in the text).*

Conversely, assuming a tetragonal distortion, with a 10% variation of *Dq* between axial and equatorial ligands, leads to D=-0.282 cm^{-1} for compression and D=0.308 cm^{-1} for elongation he behavior of fourth-order terms with respect to these two distortions deserves some comment. In D_{3h} symmetry of the trigonal distorted octahedron both B_4^3 and B_4^0 parameters are negative, and their absolute value seems not to depend much on the direction of the distortion. For tetragonal distortion the symmetry zeroes the B_4^3 term and leads to a non-zero value of the B_4^4. It has to be noted that, in contrast to what happens for trigonal distortion, in this case both B_4^0 and B_4^4 terms are positive for elongation and compression.

The point which is probably of much interest in the perspective of designing new SMM is that several calculations showed that the combination of different distortion, and then of the presence of a resulting low symmetry (i.e. non regular) distortion lead to much smaller value of the anisotropy.

In recent years a relatively large number of clusters containing Fe(III)-diketonate units bridged by alkoxo-groups has been synthesized which possess interesting magnetic properties that have been carefully determined by several techniques (HF-EPR, High field Magnetization studies, torque magnetometry).[52-58]Interestingly a series of diketonate complexes of Fe^{III} was fully characterized in term of spectroscopic parameters by Fatta and Lintvedt in 1971,[59] thus making an analysis in term of AOM feasible. As a first step the validity of this approach in determining the anisotropic characteristic of this kind of systems was tested trying to reproduce the D and E value of the $Fe(acac)_3$ (acac = acetylacetonate) and of $Fe(dpm)_3$ (dpm = 2,2,6,6-tetramethyl-3,5-heptanedionate) complex as derived by simulation of EPR [60] and HF-EPR spectra [52] respectively. The results were very promising as, using the real geometry of the chromophore as determined from crystallographic structure and the parameter reported in literature, a very good agreement was obtained in term of D and E for both systems.[52]

3.11.2 Manganese(III) model systems

As we have already seen above in discussing the HF-EPR results on Mn(III) systems, this ion in a tetragonally distorted coordination geometry present a large ZFS. Indeed, test calculation performed in such a an environment, with Dq=1600 cm^{-1} ± 5% clearly evidences the much larger Zero Field Splitting of this system with respect to Fe(III), giving a D value of + 4.72 cm^{-1} and –4.83 cm^{-1} for compressed and elongated system respectively. The results of the calculation of fourth order terms for this ion shows that B_4^4 term is quite

insensitive to the direction of the distortion, varying only by a factor three and maintaining the sign, while B_4^0 term presents a much larger variation - by a factor 10^2 - from elongation to compression. Moreover, the comparison of these results with those obtained for Fe(III) clearly shows that no straightforward assumption can be made on the relative values of these terms for different ions, in contrast to what established for second-order terms.

Ions[a]	**Distortion**	**Ligand field parameters**	**Calculated spin hamiltonian parameters**
Mn (III)	Tetragonal Elongation	Dq(ax)= 1520 cm^{-1} Dq(eq)= 1680 cm^{-1} $2e_\pi/e_\sigma$= 0.4	g_z= 1.96 $g_{x,y}$= 1.99 D=-4.83 cm^{-1} B_4^0=-4.006*10^{-6} cm^{-1} B_4^4=6.5734*10^{-3} cm^{-1}
Mn (III)	Tetragonal compression	Dq(ax)= 1680 cm^{-1} Dq(eq)= 1520 cm^{-1} $2e_\pi/e_\sigma$= 0.4	g_z= 2.000 $g_{x,y}$= 1.97 D = 4.72 cm^{-1} B_4^0 = -5.9*10^{-4} cm^{-1} B_4^4 = 1.8*10^{-3} cm^{-1}
Fe(III)	Tetragonal Elongation	Dq(ax)= 1400 cm^{-1} Dq(eq)= 1540 cm^{-1} $2e_\pi/e_\sigma$ = 0.4	g_{iso}= 2.000 D = 0.308 cm^{-1} B_4^0 = 3.7*10^{-4} cm^{-1} B_4^4 = 1.6*10^{-3} cm^{-1}
Fe(III)	Tetragonal Compression	Dq(ax)= 1540 cm^{-1} Dq(eq)= 1400 cm^{-1} $2e_\pi/e_\sigma$= 0.4	g_{iso}= 2.000 D = -0.282 cm^{-1} B_4^0 = 4.3*10^{-4} cm^{-1} B_4^4 = 6.6*10^{-3} cm^{-1}
Fe(III)	Trigonal elongation	Dq = 1470 cm^{-1} $2e_\pi/e_\sigma$= 0.4 θ=49.73°	g_{iso} = 2.000 D = -0.264 cm^{-1} B_4^0 = -3.7*10^{-4} cm^{-1} B_4^3 = -6.6*10^{-3} cm^{-1}
Fe(III)	Trigonal compression	Dq = 1470 cm^{-1} $2e_\pi/e_\sigma$= 0.4 θ=59.73°	g_{iso} = 2.000 D = 0.311 cm^{-1} B_4^0 = -4.0*10^{-4} cm^{-1} B_4^3 = -6.4*10^{-3} cm^{-1}

Table 3.4 *Summary of the Spin Hamiltonian parameters calculated for different ions and distortions on model systems using AOM. Further sample calculations may be found in ref.[37]*
[a] The following electronic parameters were used. Mn(III): ζ = 315 cm^{-1}, B = 1140 cm^{-1}, C = 3675 cm^{-1}. Fe(III): ζ= 450 cm^{-1} B= 536 cm^{-1}, C= 3260 cm^{-1}

3.12 Analysis of the global anisotropy of Polynuclear complexes through AOM

Much less work has been performed, up to now, on polynuclear compounds using the AOM approach. This is mainly due to three problems: i) an exact description of the ground state of the cluster is often difficult to obtain, and then the d_i^S and d_{ij}^S coefficients defined in Eq. (3.8.5) are not exactly known ii) the determination of the ligand field parameters in polynuclear systems is often complicated by the presence of bridging atoms, whose role has long been debated[27,61] iii) the number of parameters may be too large to get a meaningful result.

Nevertheless, we have recently obtained some qualitatively interesting results on analysis of the anisotropy the relatively simple Single Molecule Magnet $Fe_4(OCH_3)_6(DPM)_6$, hereafter ***Fe4*** (Figure 3.6),[52] and in that of ***Mn12***[62], by mean of the AOM based program described in ref. [37].

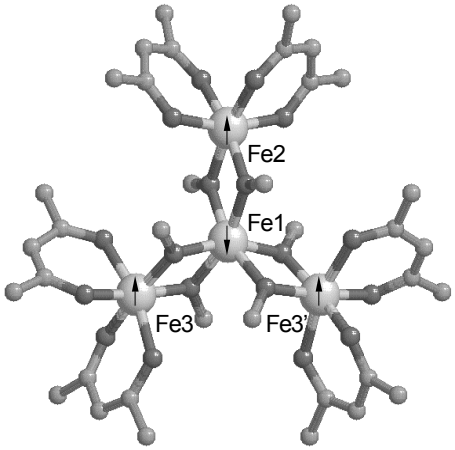

Figure 3.6 *The structure of the* ***Fe4*** *cluster. The arrows indicate the spin structure arising from the antiferromagnetic coupling of the central iron with the external ones. A C_2 axis passes through Fe1 and Fe2*

3.12.1 Fe4

The magnetic properties of ***Fe4*** will be described in detail in Chapter 4 but we will rapidly summarize them here to clarify the discussion of obtained results. This relatively simple cluster has an S=5 ground state arising from the antiferromagnetic coupling of the central Fe(III) with the three external ones. The projection coefficient c_i^S, d_i^S and d_{ij}^S were calculated assuming a coupling scheme in which the three external iron ions are

ferromagnetically coupled together and the resulting intermediate spin ($\mathbf{S}_{233'}$) is antiferromagnetically coupled to the central one ($\mathbf{S}_1$) to give the resultant S=5. Using the crystal structure position of the different ligands for each of the iron centers we were able to get the right sign of the global calculated anisotropy. However the quantitative comparison with the experimental results showed that the calculated value accounted only for a 30% of its magnitude. As we will see in Chapter 4 a single-crystal HF-EPR analysis has recently shown the calculated direction of the easy axis to be very near to the real one.[63] These experiments have shown that fourth order terms are absolutely necessary to account for a meaningful description of the anisotropy of the system. To work out the relations between local and cluster fourth order terms is by no means an easy task and at this stage we could not compare the calculated single-ion fourth order terms with the experimental data. To get deeper insights into the anisotropy of Fe(III) clusters further calculations on Ga(III)-doped sample[64] are currently in progress.

3.12.2 Mn12

An estimation of the contribution of single ion anisotropy up to fourth order terms in the ground state of ***Mn12*** – whose structure is sketched in Figure 3.7 - was first reported by Villain et al. [65] on the basis of two different coupling schemes. No quantitative calculation of the spin levels is possible in ***Mn12*** due to the exceedingly high number of states. It is however possible to make a guess of the prevailing nature of the ground state by choosing appropriate ways of coupling the individual spins to give the total spin S. In the first suggested scheme (Figure 3.8a) the eight Mn(III) of the external ring were ferromagnetically coupled to give an intermediate spin S'=16 and this was subsequently coupled to the intermediate spin S''= 6 resulting from the ferromagnetic coupling of the four Mn(III), to yield the total S=10 state (Figure 3.8b). In the second coupling scheme, the four Mn(III) which are bridged by two oxide ions to one Mn(IV) are antiferromagnetically coupled to the latter (Figure 3.9a) to yield four intermediate spins S'= ½. The idea here is that the corresponding coupling constant must be very large. The S'= ½ intermediate spins are then coupled ferromagnetically to the remaining four Mn(III) to give a resultant spin of S=10 (Figure 3.9b). The two coupling schemes correspond to different wavefunctions, therefore the relative contributions of the individual spins to the ground state are different from each other: this means that the corresponding c_i^S, d_i^S and d_{ij}^S values are different in the two case. In particular for the scheme depicted in Figure 3.9 the intermediate spins are

S'= ½, and then they do not give any contribution to the zero field splitting of the ground state.

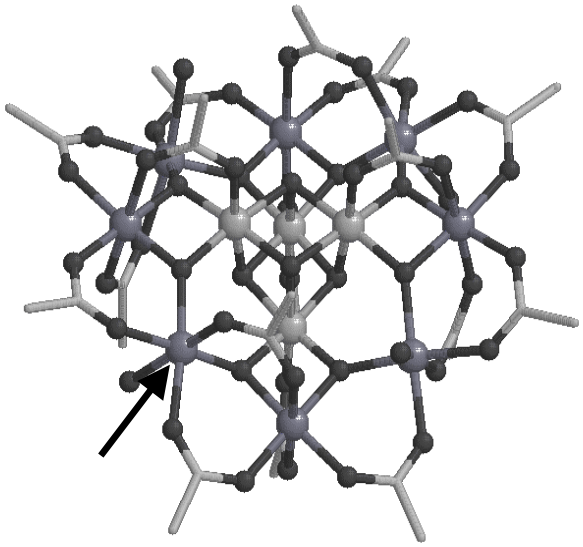

Figure 3.7 *A picture of* ***Mn12****. The arrow evidences the Mn(III) site of Mn3 whose single ion ZFS is relevant to the determination of the cluster anisotropy assuming the so-called Florentine coupling.*

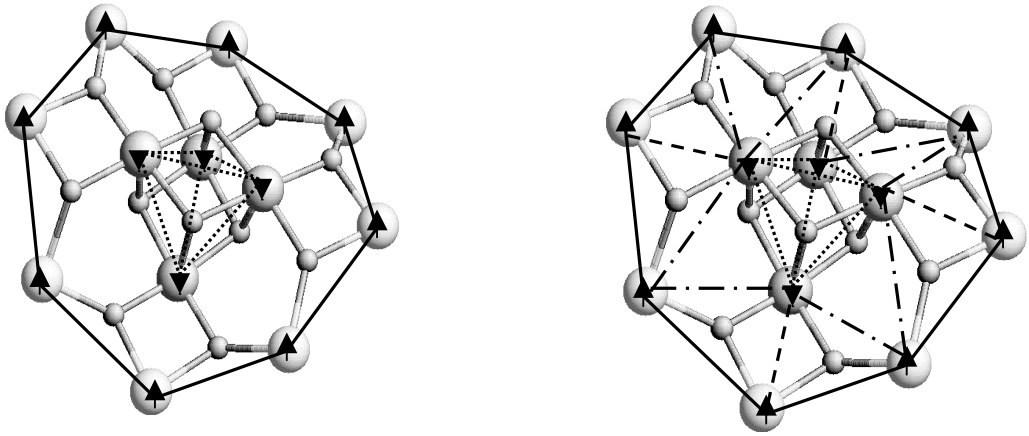

(a) (b)

Figure 3.8 *(a) The eight external Mn(III) ions are ferromagnetically coupled (continuous line) to yield an intermediate spin S'=16; the four Mn(IV) are ferromagnetically coupled (dotted line) to give the intermediate spin S''= 6.*
(b) The two intermediate spins are antiferromagnetically coupled to give the total spin S=10

In such a way only the four Mn(III) which are not coupled to give the intermediate spin *S'* contribute to the Zero Field Splitting of the cluster. These are the ones bound by two

μ-oxo bridged oxygen, an apical water molecule and three acetate, of which two in the equatorial plane and one apical: one of these sites is evidenced by an arrow in Figure 3.7. On the other hand in the scheme depicted in Figure 3.9 all the Mn(III) spins contribute to the zero field splitting of the ground state.

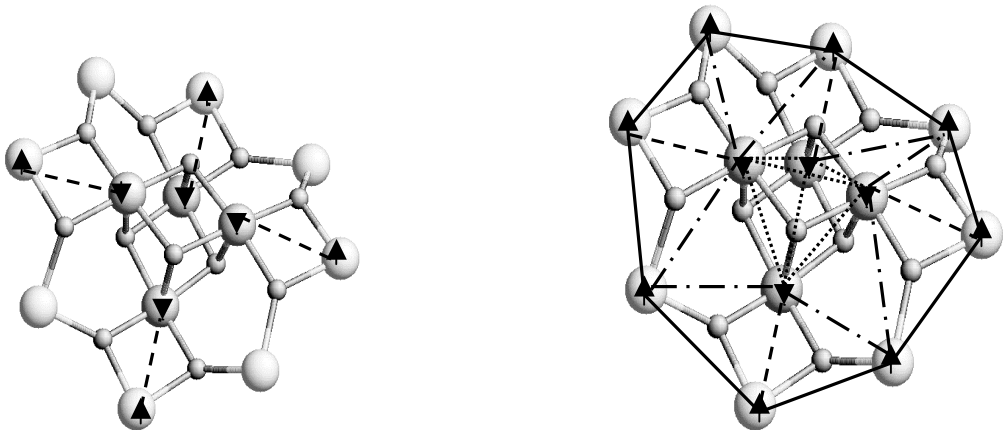

(a) (b)

Figure 3.9 *The spins of the four Mn(IV) and of four of the external Mn(III) ions are antiferromagnetically coupled to yield the four intermediate spins S'=1/2. The four intermediate spins are ferromagnetically coupled to the four remaining Mn(III) to give the total spin S=10. In this coupling scheme only the latter Mn(III) are contributing to the Zero Field Splitting of the ground spin state of the cluster*

After calculation of the d_i^S corresponding to the coupling defined by Scheme 2 (Florentine coupling) using spin-projection techniques the axial second order term of the single ion anisotropy was predicted to be about –3.3 cm^{-1}: this is a reasonable value on the basis of the literature data concerning the Zero Field Splitting of Mn(III). With the same procedure the absolute values of the single ion fourth order terms were estimated to be about 1/1000 of the cluster fourth order terms, crucial in determining the tunneling process.[65]

Given the widespread interest toward this molecule [66-72] we attempted a sample calculation using the above mentioned AOM-based program. As a first step we assumed an orthorhombic geometry for the Mn(III) site, thus neglecting the angular distortion, and we considered only the coupling scheme where only one Mn(III) contributes to the cluster ZFS. While the ligand field parameter concerning acetate and water were easily found in literature,[16] we remained with the problem of finding a good set of parameters for the two μ-oxo groups. We tackled this problem looking for a set of ligand field parameters which

could reproduce the D value of Manganese (III) doped rutile. The value of D = -3.4 cm^{-1} reported in the literature[73] for this system was satisfactorily reproduced assuming a small tetragonal elongation, with Dq= 1560 ± 10 cm^{-1} and a ratio $2e_\pi / e_\sigma$ = 0.34. The Racah parameters B and C and the spin-orbit coupling coefficient ζ were assumed to be that of the free ion, while a small degree of covalence was accounted for by the orbital reduction factor, *k*, set to 0.75.

Donor atom	Ligand field parameters
O1(μ-oxo)	Dq= 1570 cm^{-1} $2e_\pi/e_\sigma$= 0.34
O2 (μ-oxo)	Dq= 1570 cm^{-1} $2e_\pi/e_\sigma$= 0.34
O4 (basal acetate)	Dq= 2030 cm^{-1} $2e_\pi/e_\sigma$= 0.34
O5 (basal acetate)	Dq= 2030 cm^{-1} $2e_\pi/e_\sigma$= 0.34
O3(apical water)	Dq= 1200 cm^{-1} $2e_\pi/e_\sigma$= 0.34
O6(apical acetate)	Dq= 1700 cm^{-1} $2e_\pi/e_\sigma$= 0.34

Table 3.5 *Parameters for the calculation of Zero Field Splitting parameters of Mn^{III} in* ***Mn12****. k (orbital reduction factor) = 0.75, ζ = 315 cm^{-1} , B = 1140 cm^{-1}, C = 3675 cm^{-1}. Calculated Spin Hamiltonian parameters and further details on calculations are reported in the text.*

The parameter set reported in Table 3.5 was then employed to obtain Spin hamiltonian parameters of the Mn(III) in ***Mn12***; this yielded D= -3.2(7) cm^{-1}, B_4^0 = -3.3* 10^{-6} cm^{-1}, B_4^4= 2.2*10^{-3} cm^{-1}. This approach then results in a good reproduction of the second-order parameters, while some more uncertainties are shown for fourth-order parameters. Indeed, on the basis of HF-EPR results, the value of the cluster parameters were determined to be D= -0.46 cm^{-1} B_4^0= -2.2*10^{-5} cm^{-1}, B_4^4= ± 4*10^{-5} cm^{-1}. Thus one would expect values of the order of 10^{-2} cm^{-1} for the single ion values of B_4^0 and B_4^4. The observed underestimation of the calculated absolute values of fourth order terms with respect to the expected ones may be explained on the basis of the approximation done in the derivation of ligand field parameters and in the strong simplification of the distortion of the coordination sphere of Mn(III). While this level of approximation seems to be quite good for derivation of second

order parameter, it only works at a qualitative level for higher order terms; for these last ones the calculated sign is correct but their absolute value is not.

Following these encouraging results we calculated the resulting global anisotropy for ***Mn12*** when assuming the ferrimagnetic coupling scheme depicted in Figure 3.8 (Scheme 1). As we mentioned above, in this case both the Mn(III) sites (we will refer in the following to Mn2 for the site evidenced by an arrow in Figure 3.7 and to Mn3 for the other Mn(III) site) and the Mn(IV) one contribute to the global anisotropy. However, as the Mn(IV) single ion anisotropy is well known to be much smaller than Mn(III) one we just derived the ZFS parameters for the latter sites. The projection coefficient for this kind of coupling were calculated by Villain et al.[65] and for both the Mn(III) sites were shown to be equal to d_i=0.02845.

Manganese site	Ligand field parameters		Calculated Spin Hamiltonian parameters
Mn2	O1(μ-oxo)	Dq= 1570 cm^{-1}	g_x=1.996
	O2 (μ-oxo)	Dq= 1570 cm^{-1}	g_y=1.996
	O4 (basal acetate)	Dq= 2030 cm^{-1}	g_z=1.978
	O5 (basal acetate)	Dq= 2030 cm^{-1}	D =-3.19 cm^{-1}
	O3(apical water)	Dq= 1200 cm^{-1}	E= 0.065 cm^{-1}
	O6(apical acetate)	Dq= 1700 cm^{-1}	
Mn3	O1(μ-oxo)	Dq= 1570 cm^{-1}	g_x=1.996
	O2 (μ-oxo)	Dq= 1570 cm^{-1}	g_y=1.995
	O4 (basal acetate)	Dq= 2030 cm^{-1}	g_z=1.977
	O5 (basal acetate)	Dq= 2030 cm^{-1}	D=-3.65 cm^{-1}
	O3(apical acetate)	Dq= 1600 cm^{-1}	E=0.15 cm^{-1}
	O6(apical acetate)	Dq= 1650 cm^{-1}	

Table 3.6 *Parameter set employed for the two Mn(III) sites and best fit spin hamiltonian parameters. $2e_\pi/e_\sigma$ was kept fixed at the value of 0.34.*

To check how low symmetry effects affect the calculation we did not impose any fictitious symmetry for the coordination sphere of the Mn(III) ions. Angular distortion were taken into account by using the real coordination sphere of the two Mn(III) sites, identified as Mn2 and Mn3 respectively, as derived by x-ray diffractometry, while differences in bond

length were taken into account by assuming an exponential dependence of *Dq* parameters on metal-ligand distance. The global cluster anisotropy is then calculated by summing the single ion anisotropic tensor, $\mathbf{D}_2$ and $\mathbf{D}_3$ over all the Mn(III) sites and considering the projection coefficient:

$$\mathbf{D}_{tot} = 8d_i \cdot \left(\sum_{i=1}^{4} \mathbf{R}_i^T \mathbf{D}_2 \mathbf{R}_i + \sum_{i=1}^{4} \mathbf{R}_i^T \mathbf{D}_3 \mathbf{R}_i \right) \qquad (3.12.1)$$

here $\mathbf{R}_i$ are the matrix representation of the symmetry operations of the S_4 axis: $\mathbf{R}_1$ correspond s to the unitary matrix, $\mathbf{R}_3$ to a π rotation around the *z* crystallographic axis, $\mathbf{R}_2$ and $\mathbf{R}_4$ to $\pi/2$ and $3\pi/2$ rotations respectively, combined with a reflection on the plane perpendicular to the *z* axis. Thus, even if in this case the single ion anisotropies show an appreciable degree of transverse anisotropy (see Table 3.6) due to the distortion of Mn(III) coordination sphere, it vanishes when it is projected over the cluster, which maintain the overall tetragonal symmetry. Interestingly the introduction of low symmetry effects does not affect much the results obtained for the single ion anisotropy of site *z*, apart for the obvious introduction of a transverse anisotropy term. The calculated global *D* value (*D*= - 0.55 cm-1) is in very good agreement with those obtained by spectroscopic measurements.[70,74,75]

Finally we would like to point out here that the successful inclusion of low symmetry effects by simply considering the real coordination sphere of the single-ion as determined by X-Ray crystallography may be a very powerful tool in the study of the dynamics of the magnetization in single molecule magnets. In facts several authors have recently evidenced that a distribution of second order transverse anisotropy must be present in ***Mn12*** crystals in order to justify the experimental findings [76]. Chudnovsky et al. [77] have developed a model where crystal dislocations are responsible of the lower symmetry of the spin hamiltonian. We have instead studied in more details the low temperature (83 K) X-ray crystal structure and we have evidenced that the molecules of acetic acid of crystallization are involved in a hydrogen-bond with the oxygen atom of the acetate ligand coordinated to Mn2, as shown in Figure 3.10. As the acetic acid is disordered over two symmetry related position only half of the Mn2 sites are affected by the hydrogen bond.

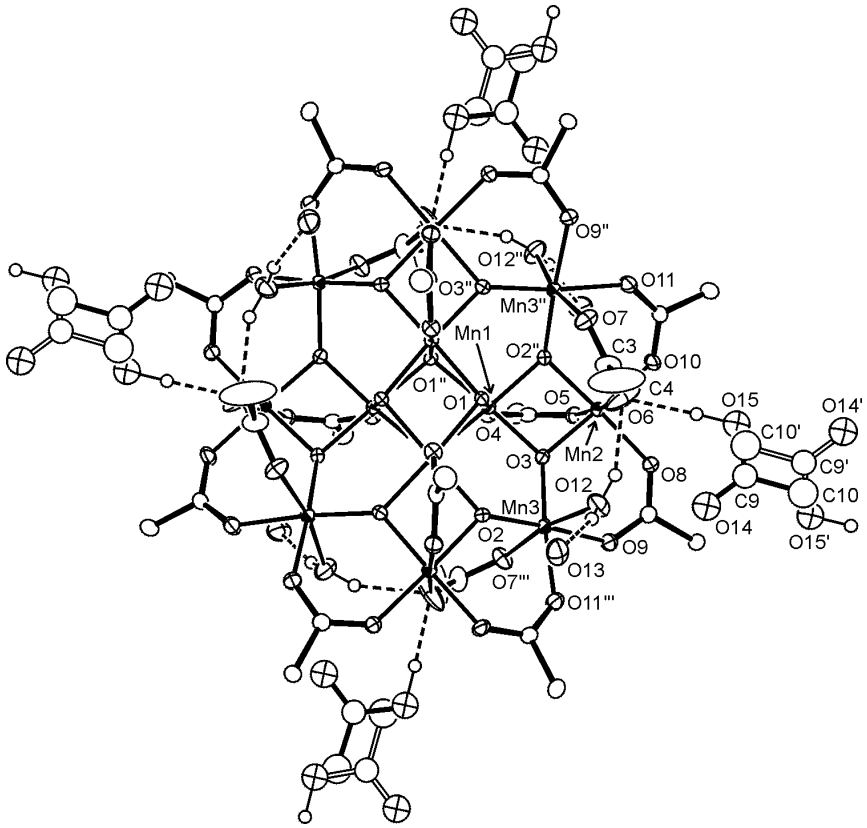

Figure 3.10 *Structure of the [$Mn_{12}O_{12}(CH3COO)_{16}(H_2O)_4$] cluster at 83 K viewed slightly off the S_4 axis, together with the lattice water (O13) and disordered acetic acid (O14, O15, C9, C10) molecules (the two equivalent positions are differentiated by empty and filled backbone of the molecule). Thermal ellipsoids are at 50%-probability level. Hydrogen atoms on O12 and O15 are depicted as small spheres, while the remaining hydrogen atoms are omitted for clarity. The network of hydrogen bonds is shown by dashed lines.*

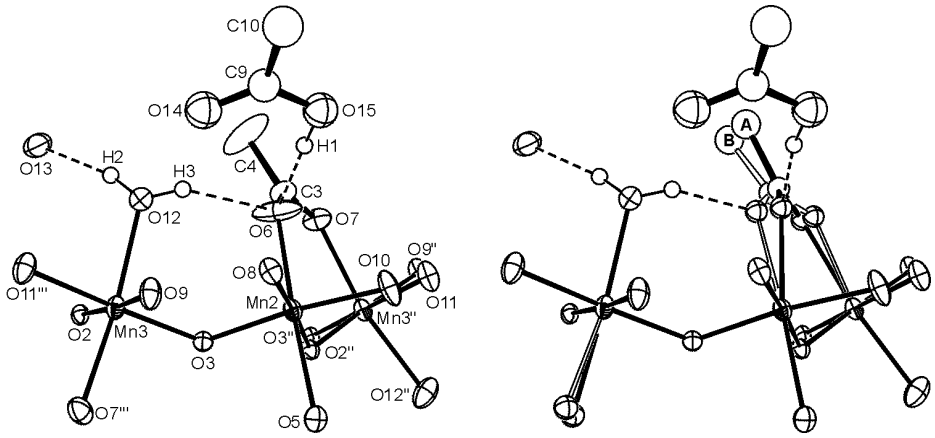

Figure 3.11*. Coordination sphere of Mn2 and Mn3, as determined from anisotropic refinement of the displacement factors of C3, C4, O6 and O7 (left) and from an isotropic model with disorder fitting (right). Thermal ellipsoids are at 50%-probability level. Methyl hydrogen atoms are omitted for clarity.*

We have modeled the observed disorder of the acetate ligand bridging Mn2 to Mn3 with two slightly different coordination modes of the acetate as shown on the right of Figure 3.11. Six different isomeric forms of Mn12 can thus be envisaged which differ in the number (n = 0,1,…,4) and arrangement of hydrogen-bound acetate ligands (Figure 3.12). Two of them (n = 0, 4) have axial S_4 point-group symmetry, whereas isomers with n = 1 and 3 have no symmetry element. For n = 2, two distinct arrangements of hydrogen-bond interactions exist, namely a "cis" isomer in which hydrogen-bound acetates lie on opposite sides of the molecular plane (C_1-symmetry) and a "trans" isomer with hydrogen-bound acetates on the same side (C_2-symmetry). Clearly, a strict S_4 molecular symmetry of each cluster can be retained only in the case of a regular pattern of n = 0 and n = 4 isomers. This would lead to a supercell with doubled lattice constants (a'=b' = 2a) for which no experimental evidence has been found. We conclude that the average molecular symmetry of ***Mn12*** is lower than axial. Assuming that the coordination type A (with H-bonded acetic acid) and type B (without acetic acid) are equally probable and taking into account their statistical distribution on the four sites of the cluster the occurrence of the six isomers is that reported in Table 3.7.

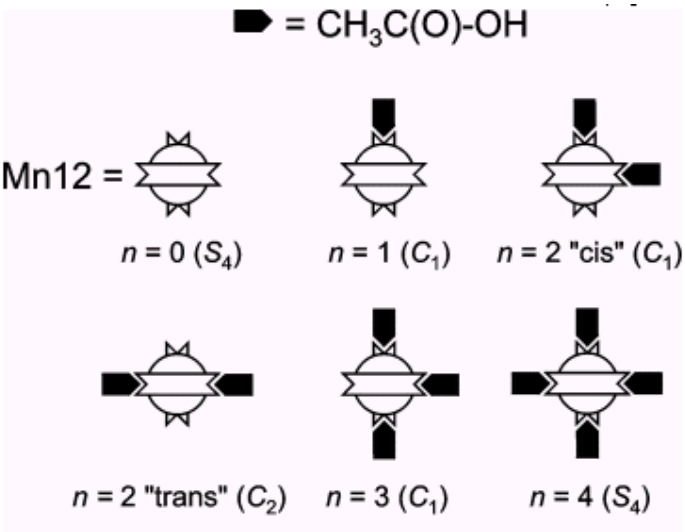

Figure 3.12*. The six hydrogen-bond isomers of* ***Mn12***

In order to evaluate how the disorder in the acetic acid of crystallization affects the magnetic anisotropy of the clusters we have used the AOM approach with the parameters mentioned above using the structural geometries of site A and B and the results are reported in Table 3.8. By using Eq. (3.12.1) we evaluated the anisotropy tensor of the cluster for the

six isomer by replacing D_2 and D_3 with D_2^{α} and D_3^{α} , where α can be either A or B depending on the type of isomer in consideration. The resulting $\mathbf{D}_{tot}$ tensor results to be axial and diagonal in the crystal axes reference frame only in case with n=0 and n= 4 while for the other four cases non-zero off diagonal terms are present. Diagonalization of the matrices provided the *D* and *E* parameters, and the angle θ between the easy axis and the *c* crystallographic axis, which are reported in Table 3.7. The calculated *E* parameters are in good agreement with the values used in [76] to justify the experimental dynamics of the magnetization.

Isomer	**Concentration**	**D (cm^{-1})**	**E(cm^{-1})**	**θ (°)**
n=0	6.25%	-0.528	0	0
n=4	6.25%	-0.554	0	0
n=1	25%	-0.534	$1.63x10^{-3}$	0.3
n=2 cis	25%	-0.541	$1.30\ x10^{-4}$	0.4
n=2 trans	12.5%	-0.541	$3.27x10^{-3}$	0
n=3	25%	-0.548	$1.65x10^{-3}$	0.3

Table 3.7 *Calculated concentration, axial and transverse second order magnetic anisotropy, and the angle formed by the easy axis of magnetization of each isomer with the c crystallographic axis.*

Site	**D (cm^{-1})**	**E (cm^{-1})**	**δ (°)**
Mn2A	-3.42	0.28	11.6
Mn2B	-3.66	0.19	10.7
Mn3A	-3.18	0.07	37.2
Mn3B	-3.06	0.05	37.1

Table 3.8. *Spin hamiltonian parameters obtained for the four different coordination sites of Mn(III) ions found from the X-ray analysis and reported in Figure 3.11. The δ angle is defined by the easy axis direction of each manganese site with the c crystallographic axis. The last site correspond to the Mn3 with an exchange of the axis of Jahn-Teller elongation.*

Our results show that the magneto-crystalline anisotropy is only slightly affected by strong perturbations of the crystal structure as the presence of an hydrogen bond involving the oxygen atom coordinated to the metal ion. It seems therefore quite unreasonable that dislocations, even if present, can induce substantial modification of the magnetic anisotropy

at long distance as proposed in [77]. Dislocations can indeed be the source of a further broadening of the distribution of magnetic anisotropy, but the presence of disordered acetic acid remains the main source of the quadratic transverse anisotropy.

These conclusions has been achieved thanks to an estimation through AO approach of the magnetic anisotropy as the experimental determination of spin hamiltonian parameters of all the isomeric species is unfeasible either by spectroscopic technique or magnetic measurements.

3.13 Conclusions

Controlling the magnetic anisotropy is of fundamental importance in molecular magnetism, because the bulk properties of the materials dramatically depend on it. The understanding of the conditions determining the magnetic anisotropy however is very complex, depending on the nature of the individual magnetic building blocks, and on their relative arrangements. We feel that simple ligand field models, which parameterize the energy levels of individual building blocks, can contribute in first order approximation to help finding the appropriate metal ions and coordination geometries which can produce the expected magnetic anisotropy. The analysis of the data reported up to now for HF-EPR spectra of silent ions clearly points out that while a qualitative interpretation and prediction of the spectral properties can be performed on the basis of simple ligand field consideration for a quantitative analysis the use of the complete ligand field-spin-orbit d^n matrix is necessary. Within this framework the use of an AOM-based approach seems to be very promising, both in term of quantitative reproduction of experimental data and to provide clues to design system with predetermined properties. On this respect the results here presented for the archetypal Single Molecule Magnets ***Mn12*** suggest that even subtle dynamic magnetic properties may be accounted for by this simple but very powerful approach.

References

1. J. S. Griffith, *The Theory of Transition Metal Ions* (Cambridge University Press, Cambridge, 1961).
2. A. L. Barra, D. Gatteschi, R. Sessoli, G. L. Abbati, A. Cornia, A. C. Fabretti, and M. G. Uytterhoeven, *Angew. Chem. Int. Ed. Engl.* **36**, 2329 (1997).
3. D. P. Goldberg, J. Telser, J. Krzystek, A. G. Montalban, L. C. Brunel, A. G. M. Barrett, and B. M. Hoffman, *J. Am. Chem. Soc.* **119**, 8722 (1997).
4. P. J. Van Dam, A. A. K. Klaassen, E. J. Reijerse, and W. R. Hagen, *J. Magn. Reson.* **130**, 140 (1998).
5. J. Telser, L. A. Pardi, J. Krzystek, and L. C. Brunel, *Inorg. Chem.* **37**, 5769 (1998).
6. J. Krzystek, J. Telser, L. A. Pardi, D. P. Goldberg, B. M. Hoffman, and L. C. Brunel, *Inorg. Chem.* **38**, 6121 (1999).
7. P. L. W. Tregenna-Piggott, H. Weihe, J. Bendix, A. L. Barra, and H. U. Gudel, *Inorg. Chem.* **38**, 5928-+ (1999).
8. M. J. Knapp, J. Krzystek, L. C. Brunel, and D. N. Hendrickson, *Inorg. Chem.* **39**, 281 (2000).
9. L. A. Pardi, A. K. Hassan, F. B. Hulsbergen, J. Reedijk, A. L. Spek, and L. C. Brunel, *Inorg. Chem.* **39** , 159 (2000).
10. J. Bendix, H. B. Gray, G. Golubkov, and Z. Gross, *Chem. Commun.* 1957 (2000).
11. J. Mrozinski, A. Skorupa, A. Pochaba, Y. Dromzee, M. Verdaguer, E. Goovaerts, H. Varcammen, and B. Korybut-Daszkiewicz, *J. Mol. Struct.* **559**, 107 (2001).
12. J. Limburg, J. S. Vrettos, R. H. Crabtree, G. W. Brudvig, J. C. De Paula, A. Hassan, A. L. Barra, C. Duboc-Toia, and M. N. Collomb, *Inorg. Chem.* **40**, 1698 (2001).
13. J. Krzystek, J. Telser, B. M. Hoffman, L. C. Brunel, and S. Licoccia, *J. Am. Chem. Soc.* **123**, 7890 (2001).
14. B. R. McGarvey, *Transition Metal Chemistry,* R. L. Carlin (Marcel Dekker, New York 1966) Vol. 3, p.89.
15. A. Bencini and D. Gatteschi, *Transition Metal Chemistry,* B.N. Figgis and G. Melson (Marcel Dekker, New York 1982) Vol. 8, p.1.
16. A. B. P. Lever, *Inorganic Electronic Spectroscopy* (Elsevier, Amsterdam, 1984).
17. A. B. P. Lever and E. I. Solomon, *Inorganic Electronic Structure and Spectroscopy* E. I. Solomon and A. B. P. Lever (Wiley-Interscience, New York, 1999), Vol. 1, p. 1.

18. H. Bethe, *Ann. Phys.* **3**, 133 (1929).
19. C. J. Ballhausen, *Introduction to Ligand Field Theory* (McGraw-Hill, New York, 1962).
20. C. K. Jørgensen, *Modern Aspects of Ligand Field Theory* (North-Holland, Amsterdam, 1971).
21. C. E. Schäffer, *Proc. R. Soc. London A* **297**, 96 (1967).
22. C. E. Schäffer and C. K. Jørgensen, *Mol. Phys.* **9**, 401 (1965).
23. C. E. Schäffer, *Struct. Bonding (Berlin)* **14**, 69 (1973).
24. C. E. Schäffer, *Pure and App. Chem.* **24,** 361 (1970).
25. M. Gerloch and R. F. Mc Meeking, *J. Chem. Soc., Dalton Trans.* 1714 (1981).
26. A. Bencini, C. Benelli, and D. Gatteschi, *Coord. Chem. Rev.* **60**, 131 (1984).
27. R. J. Deeth, M. J. Duer, and M. Gerloch, *Inorg. Chem.* **26**, 2573 (1987).
28. M. H. L. Pryce, *Proc. Phys. Soc. A* **63,** 25 (1950).
29. A. Abragam and M. H. L. Pryce, *Proc. R. Soc. London A* **205,** 135 (1951).
30. A. Abragam and B. Bleaney, *Electron Paramagnetic Resonance of Transition Ions* (Dover Publications, New York, 1986).
31. K. W. H. Stevens, *Magnetism* G. T. Rado and H. Suhl (Academic Press, New York, 1963), Vol. 1, p. 1.
32. K. W. H. Stevens, *Proc. Phys. Soc.* **65**, 209 (1952).
33. R. Englman, *The Jahn-Teller Effect in Molecules and Crystals* (Wiley-Interscience , London, New York, 1972).
34. A. Bencini and D. Gatteschi, *EPR of Exchange Coupled Systems* (Springer-Verlag, Berlin, 1990).
35. T. Moryia, *Magnetism* G. T. Rado and H. Suhl (Academic Press, New York, 1963), Vol. 1, p. 85.
36. F. Neese and E. I. Solomon, *Inorg. Chem.* **37**, 6568 (1998).
37. A. Bencini, I. Ciofini, and M. G. Uytterhoeven, *Inorg. Chim. Acta* **274**, 90 (1998).
38. J. Bendix, *Proceedings of 29th ICCC* , Lausanne, Switzerland, 1992.
39. C. Rudowicz, *J. Phys. C: Solid State Phys.* **18,** 1415 (1985).
40. L. Banci, A. Bencini, C. Benelli, D. Gatteschi, and C. Zanchini, *Struct. Bonding (Berlin)* **52**, 37 (1982).
41. J. Reedijk and B. Nieuwenhuijse, *Rec. Trav. Chim.* **91**, 533 (1972).
42. P. B. Sczaniecki and J. Lesiak, *J. Magn. Reson.* **46**, 185 (1982).

43. G. Rogez, L. Sorace, T. Mallah, and D. Gatteschi, *work in progress* .
44. L. Sorace and L. Pardi, *unpublished results* .
45. A. L. Barra, D. Gatteschi, and R. Sessoli, *Phys. Rev. B* **56**, 8192 (1997).
46. J. Telser, L. A. Pardi, J. Krzystek, and L. C. Brunel, *Inorg. Chem.* **39**, 18341834 (2000).
47. A. Cornia, G. L. Abbati, A. C. Fabretti, and A. Giusti, *manuscript in preparation* .
48. H. Weihe and H. U. Guedel, *J. Am. Chem. Soc.* 6539 (1997).
49. D. G. Holah and J. P. J. Fackler, *Inorg. Chem.* **5**, 479 (1966).
50. R. H. Holm, P. Kennepohl, and E. I. Solomon, *Chem. Rev.* **96,** 2239 (1996).
51. A. L. Barra, D. Gatteschi, and R. Sessoli, *Chem.-Eur. J.* **6**, 1608 (2000).
52. A. L. Barra, A. Caneschi, A. Cornia, F. F. De Biani, D. Gatteschi, C. Sangregorio, R. Sessoli, and L. Sorace, *J. Am. Chem. Soc.* **121**, 5302 (1999).
53. D. Gatteschi, A. Caneschi, R. Sessoli, and A. Cornia, *Chem. Soc. Rev.* **25**, 101 (1996).
54. D. Gatteschi, R. Sessoli, and A. Cornia, *Chem. Commun.* 725 (2000).
55. G. L. Abbati, A. Cornia, A. C. Fabretti, W. Malavasi, L. Schenetti, A. Caneschi, and D. Gatteschi, *Inorg. Chem.* **36**, 6443 (1997).
56. M. Affronte, J. C. Lasjaunias, A. Cornia, and A. Caneschi, *Phys. Rev. B* **60**, 1161 (1999).
57. A. Cornia, M. Affronte, A. G. M. Jansen, G. L. Abbati, and D. Gatteschi, *Angew. Chem. Int. Ed. Engl.* **38**, 2264 (1999).
58. A. Caneschi, A. Cornia, A. C. Fabretti, S. Foner, D. Gatteschi, R. Grandi, and L. Schenetti, *Chem.-Eur. J.* **2**, 2329 (1996).
59. A. M. Fatta and R. L. Lintvedt, *Inorg. Chem.* **11**, 88 (1972).
60. D. Collison and A. K. Powell, *Inorg. Chem.* **29**, 4735 (1990).
61. C. E. Schäffer, *Inorg. Chim. Acta* **300-302**, 1035 (2000).
62. D. Gatteschi and L. Sorace, *J. Solid State Chem.* **159**, 253 (2001).
63. A. Bouwen, A. Caneschi, D. Gatteschi, E. Goovaerts, D. Schoemaker, L. Sorace, and M. Stefan, *J. Phys. Chem. B* **105**, 2658 (2001).
64. G. L. Abbati, L. C. Brunel, H. Casalta, A. Cornia, A. C. Fabretti, D. Gatteschi, A. K. Hassan, A. G. M. Jansen, A. L. Maniero, L. Pardi, and C. Paulsen, *Chem.-Eur. J.* **7**, 1796 (2001).
65. F. Hartmann-Boutron, P. Politi, and J. Villain, *Int. J. Mod. Phys. B* **10**, 2577 (1996).

66. L. Thomas, F. Lionti, R. Ballou, D. Gatteschi, R. Sessoli, and B. Barbara, *Nature* **383**, 145 (1996).
67. M. Clemente-Leon, H. Soyer, E. Coronado, C. Mingotaud, C. J. Gomez-Garcia, and P. Delhaes, *Angew. Chem. Int. Ed. Engl.* **37**, 2842 (1998).
68. J. R. Friedman, *Phys. Rev. B* **57**, 10291 (1998).
69. M. N. Leuenberger and D. Loss, *Europhys. Lett.* **46**, 692 (1999).
70. M. Hennion, L. Pardi, I. Mirebeau, E. Suard, R. Sessoli, and A. Caneschi, *Phys. Rev. B* **56**, 8819 (1997).
71. Z. H. Jang, A. Lascialfari, F. Borsa, and D. Gatteschi, *Phys. Rev. Lett.* **84**, 2977 (2000).
72. M. R. Cheesman, V. S. Oganesyan, R. Sessoli, D. Gatteschi, and A. J. Thomson, *Chem. Commun.*, 1677 (1997).
73. H. J. Gerritsen and E. S. Sabisky, *Phys. Rev.* **132**, 1507 (1963).
74. A. L. Barra, A. Caneschi, D. Gatteschi, and R. Sessoli, *J. Magn. Magn. Mater.* **177**, 709 (1998).
75. I. Mirebeau, M. Hennion, H. Casalta, H. Andres, H. U. Gudel, A. V. Irodova, and A. Caneschi, *Phys. Rev. Lett.* **83**, 628 (1999).
76. K. M. Mertes, Y. Suzuki, M. P. Sarachik, Y. Paltiel, H. Shtrikman, E. Zeldov, E. Rumberger, D. N. Hendrickson, and G. Christou, *Phys. Rev. Lett.* **87**, 227205 (2001).
77. E. M. Chudnovsky and D. A. Garanin, *Phys. Rev. Lett.* **87**, 187203 (2001).
78. B. M. Flanagan, P. V. Bernhardt, S. R. Luthi, M. J. Riley, and E. R. Krausz, *Inorg. Chem.* **40,** 5401 (2001).
79. C. K. Jørgensen, R. Pappalardo, and H.-H. Schmidtke, *J. Chem. Phys.* **39,** 1422 (1963).

4. Magnetic anisotropy and low temperature spin dynamics in a tetranuclear Iron cluster

4.1 Introduction

Notwithstanding the basic comprehension of the mechanism leading to single molecule magnet behavior and to quantum tunneling of the magnetization,[1,2] outlined in the introduction to this thesis, much work has still to be done in this field. Higher blocking temperature for single molecule magnet behavior (i.e. system with higher spin and higher Ising-like anisotropy) are indeed actively looked for, while the actual parameters governing the fine details of quantum tunneling of the magnetization are still debated.[3-12] In an effort to further elucidate these problems, this part of thesis has been devoted to the careful analysis of the magnetic properties of $Fe_4(OMe)_6(dpm)_6$ (where Hdpm=dipivaloyilmethane) hereafter ***Fe4***. This is a recently synthesized molecular nanomagnet,[13] that thanks to its simple structure is of particular interest in the perspective of reaching a detailed description of the magnetic parameters starting from the molecular structure and the single-ion properties. Particular emphasis will be put in the following on the results obtained through single crystal HF-EPR[14] which will be discussed in connection with results recently obtained through the use of different spectroscopic techniques [15-17] and of MicroSQUID magnetometry at very low temperature.[18]

4.2 Description of the structure

The structure of ***Fe4*** is sketched in Figure 4.1. The molecule has a propeller shape and is chiral: however as the system crystallizes in the centrosymmetric space group *C2*/*c* the two enantiomeric species are both present in the crystal. The individual molecules have twofold symmetry around the b axis, passing through Fe_1 and Fe_2, with the four Fe(III) ions lying on the same plane. The normal to this plane makes an angle of 2.1^0 with the *c* direction. The inner Fe atom is in the center of an isosceles triangle - the Fe_2-Fe_3 and Fe_3-Fe_3' distances being 5.372 and 5.550 Å respectively - and three bis(μ-OCH_3) ligands connect it to the three peripheral ones, which complete their coordination by binding two dipivaloylmethanide anions. All the Fe(III) atoms have a highly distorted octahedral environment but different types of distortion. Indeed, examination of interbond angles shows that the coordination environment of Fe_1 approaches 3-fold symmetry quite closely, while the coordination geometry of Fe_2 and Fe_3 is somewhat more irregular due to the presence of both methoxide and dpm anions. In particular, the peripheral metal ions form shorter bonds with OMe^- than with dpm ligands.

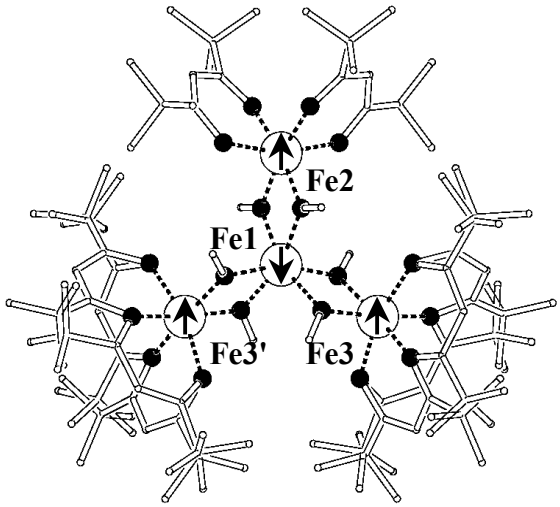

Figure 4.1*. The structure of the* ***Fe4*** *cluster. The arrows indicate the spin structure arising from the antiferromagnetic coupling of the central iron with the external ones. Disordered dpm ligands on Fe3 and Fe3' and their corresponding tert-butyl groups are shown*

Interestingly, a random disorder was found in the co-ordination environment of Fe_3, consisting of a 0.30 -occupancy of the dpm ligands in a different spatial arrangement with respect to the dominant one. To illustrate this, we refer to the overall structure of the Fe/O core, which comprises two parallel layers of c.p. oxygen atoms (maximum deviation: 0.26 Å), one on each side of the ***Fe4*** moiety. Each of the two dpm anions can provide two oxygen donors either on the same (mode A) or on different oxygen layers (mode B).

Finally, as the intermolecular distances are larger than 9Å, the intermolecular interactions are expected to be very weak, thus supporting the assumption that the magnetic behavior is deriving from the properties of the single molecule.

4.3 Static Magnetic properties

The χT vs T plot for ***Fe4*** is shown in Figure 4.2. χT is 11.9 emu K mol^{-1} at 270 K and decreases on lowering the temperature, going through a minimum at T=155 K (χT = 10.96 emu K mol^{-1}), and then increases reaching the value of 14.62 emu K mol^{-1} at 7 K. Below this temperature a small decrease is observed.

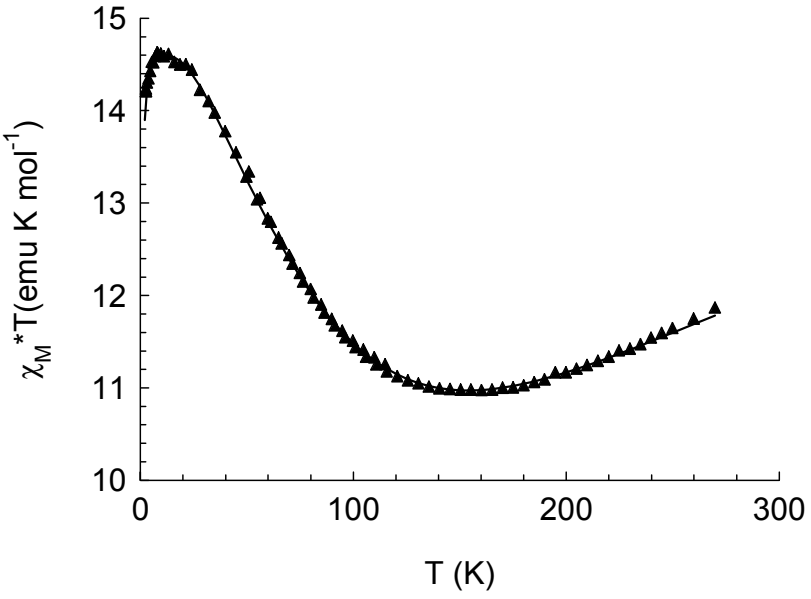

Figure 4.2 *Temperature dependence of the χT product for **Fe4**. The solid line is calculated with J=21.1 cm^{-1}, J'=-1.1cm^{-1}, D(S=5)=-0.2 cm^{-1} (see text for further details)*

The temperature behavior of χT is typical for antiferromagnetic coupling in a system whose spin topology does not allow full compensation of the magnetic moments. In the present case the antiferromagnetic interaction between the central iron ion and the peripheral ones, mediated by the methoxo bridges, leads to a ground state with $S=5$ and the spin structure schematized in Figure 4.1, where all the peripheral spins are aligned parallel to each other but antiparallel to the central one. The observed χT value at the maximum (14.62 emu K mol^{-1}) is in good agreement with the value expected from Curie law for a completely populated $S=5$ with $g=2$, 15 emu K mol^{-1}.

A satisfactory fit of the magnetic data was obtained by assuming a C_3 symmetry for the exchange coupling pattern and taking into account the next-nearest neighbor interactions between peripheral iron ions, according to Scheme 4.1:

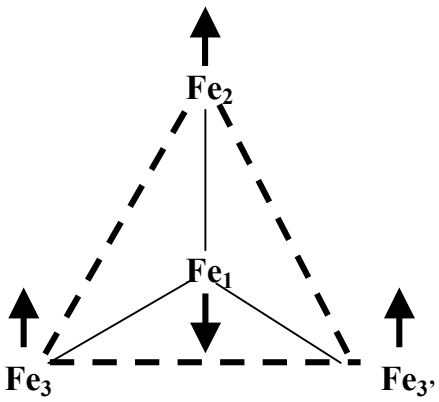

Scheme 4.1

The exchange Hamiltonian employed was then:

$$\mathbf{H}_{ex} = J(\mathbf{S}_1\mathbf{S}_2 + \mathbf{S}_1\mathbf{S}_3 + \mathbf{S}_1\mathbf{S}_4) + J'(\mathbf{S}_2\mathbf{S}_3 + \mathbf{S}_3\mathbf{S}_4 + \mathbf{S}_2\mathbf{S}_4) \qquad (4.3.1)$$

and the best fit parameters are $g=1.97$, $J=21.1$ cm^{-1} , and $J'=-1.1$ cm^{-1} . The presence of next-nearest neighbor interactions in clusters of this spin topology has already been taken into account to reproduce the magnetic properties of various Cr(III) clusters [19,20] for which *J'/J*

=0.1. The first excited state is a double-degenerate $S = 4$ state lying ca. 60 cm^{-1} above the $S = 5$ ground state. The degeneration arises from the 3-fold symmetry that we have assumed for the exchange coupling pattern. The best fit J value is in the range expected for dialkoxo-bridged Fe(III) complexes[21] and well agrees with the value J=22.1 cm^{-1} calculated by using an empirical relation between J and the length of the bridge established for Fe(III) oxo-bridged dimers.[22] The small decrease of χT observed below 7 K is not due to saturation as is observed also in a weak magnetic field (10 mT) and in principle might be originated either by intercluster antiferromagnetic interactions or by the presence of zero field splitting of the ground S= 5 spin multiplet. The absence of significant intermolecular contacts as well as the HF-EPR spectra, discussed below, are strongly in favor of the latter hypothesis.

4.4 HF-EPR spectra: powder investigation

The HF-EPR spectra of ***Fe4*** recorded at 245 GHz, shown in Figure 4.3, present several lines at fields below the resonance of the free electron (8.75 T) and a broad band at higher field. The spacing of the lines at low field is roughly regular and can be attributed to a fine structure arising from the zero field splitting of the ground S = 5 multiplet. While at low temperature the most intense line of the regular pattern is the one at lowest field, on increasing the temperature the intensity moves toward the center of the spectrum. A similar trend is observed on the high-field feature even if the fine structure is not resolved. On increasing temperature a set of narrow signals at g = 2 also gains intensity, suggesting that it can be attributed to excited spin multiplets. They are marked with an asterisk in Figure 4.3. As we have seen in Chapter 3 in the limit of strong field an S = 5 spin multiplet with uniaxial magnetic anisotropy should give a spectrum with 10 lines, for each principal direction of **g**. In a powder averaged spectrum 10 lines arise from the crystallites with the unique axis parallel to the field, which are separated by $2D/g\mu_B$. The g factor of Fe(III), a ^{6}S ion, is close to the free electron value and can be considered as quasi isotropic.[23] The crystallites with the unique axis perpendicular to the magnetic field give also 10 lines with a separation which is half of the previous one, while the contribution of intermediate orientations is averaged to zero in the first-derivative spectrum by

the integration over the powder distribution. In the high magnetic field used in HF-EPR experiments, the most negative M_S states of the $S = 5$ multiplet are selectively populated at low temperature, and therefore the lines relative to the transition -5 → -4 are the most intense and occur at $H = (g_e/g)H_0 + 9D/g\mu_B$ when the field is parallel and at $H = (g_e/g)H_0 - (9/2)D/g\mu_B$ when the field is perpendicular to the unique axis. The fact that the low-field parallel transition is enhanced on decreasing temperature is an unambiguous indication that D is negative. This implies an Ising-type magnetic anisotropy with the unique axis corresponding to the preferential direction of magnetization. Simulated spectra are also shown in Figure 4.3. The simulations have been obtained by using a perturbative approach, with $D = -0.20$ cm^{-1} , $g_{||} = 2.003$, and $g_{\perp} = 2.023$.

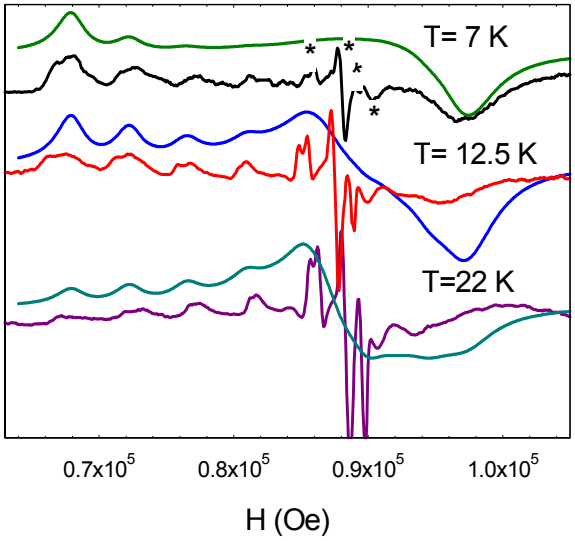

Figure 4.3 *HF-EPR spectra at 245 GHz and three different temperatures of a polycrystalline sample of* ***Fe4*** *pressed in a pellet (lower spectra) and simulated curve with S=5, D=-0.2 cm^{-1}. The bands marked with an asterisk were first assigned to an excited multiplet S=4*

The number and the positions of the features and their temperature dependencies are correctly reproduced. The features marked with an asterisk were initially assigned to transitions within excited $S = 4$ multiplets with much smaller ZFS, and they were independently fit; we will however see in the following that this assignment is wrong and we will then not discuss further about this here. The introduction of a rhombic term in the spin Hamiltonian gave no significant

improvement to the simulation. The successful simulation of the spectra using a single spin Hamiltonian suggests that intercluster interactions are very weak as expected for the presence of the bulky *tert*-butyl groups on the ligands. The experimentally determined zero field splitting of the ground $S = 5$ spin multiplet can reproduce the small decrease in the χT product at low temperature, as shown in Figure 4.2, where the solid line is the χT value calculated for a powder average using $S = 5$ and $D = -0.20$ cm^{-1}. Given that the height of the barrier for the reorientation of the magnetization is calculated as $\Delta = DS_z^2 = 7.2$ K slow magnetic relaxation is expected at low temperatures.

4.5 Single crystal W-Band EPR spectra of Fe4: results and discussion

In order to push further the characterization of the magnetic ground state of ***Fe4*** we decided to perform a single crystal HF-EPR study on this system. The values of the ZFS parameters determined from the HF-EPR powder spectra suggested the possibility to carry on this investigation in W- band (95 GHz), where all the features of the spectrum are shown. A well defined advantage of W- band spectrometers is their sensitivity which, due to the presence of a resonant cavity, is much higher than that currently available at higher frequencies . This allows the use of tiny single crystals, 0.4×0.4×0.4 mm^3 (see Figure 4.4)

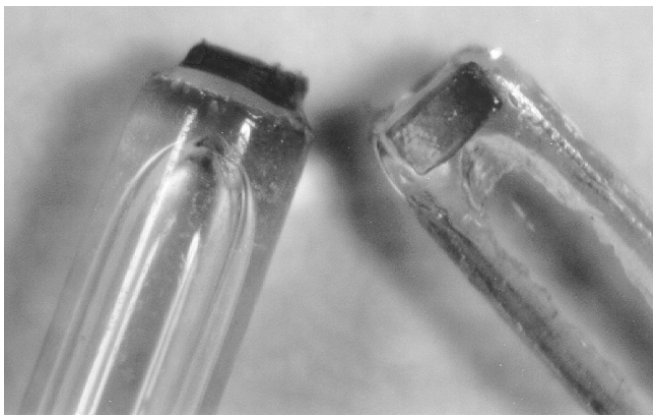

Figure 4.4. ***Fe4*** *single crystals mounted for W-band measurements in the (bc) plane (on the bottom of the tube) and (a*c) plane (on the side), respectively. The tube's outer diameter is 0.9mm.*

The single crystal analysis provided evidence for the principal directions of the ZFS tensor and it confirmed the presence of three disordered sites in the unit cell. As we have seen above, these had been previously observed in the X-Ray structure analysis [13], but the EPR data provide direct access to the spin Hamiltonian parameters of the three disordered sites. We will see in the following that these data may be important for the interpretation of some anomalies in the relaxation of the magnetization of ***Fe4*** at low temperatures.

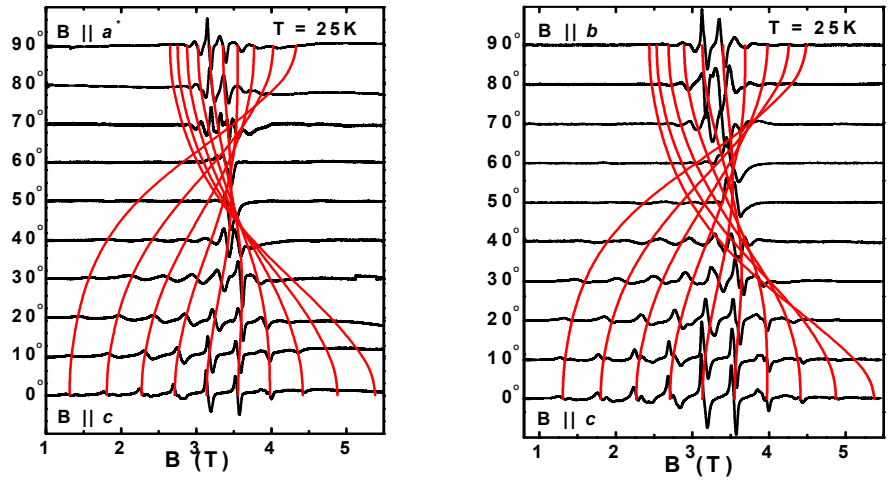

(a) ***(b)***

Figure 4.5*. Angular variation of the* ***Fe4*** *W-band EPR single crystal spectra at 25K in the (a*c) plane (a) and the (bc) plane (b). The solid lines are the calculated angular dependence using the parameters for center AA from Table 4.1.*

As a consequence of the molecular symmetry, *b* is necessarily one of the magnetic axes and the analysis of the spectra recorded in the *(a*c)* plane directly leads to the identification of the two remaining magnetic axes. The maximum width of the W-band EPR spectrum in both planes (see Figures 4.5) has been clearly observed close to the *c* direction while it is minimum along *a** and *b*.

Due to the experimental errors it was not possible to distinguish the crystallographic *c* axis from the normal to the plane defined by the four Fe(III) ions. We may conclude that, within experimental errors, the crystallographic *c* axis is the easy axis of the magnetization, while *a** is the third magnetic axis. It should be noted that these results are essentially in agreement with the predictions obtained through the Angular Overlap approach described in Chapter 3. The angular variation of the spectra measured at T=25K in the (*a*c*) and (*bc*) planes (see Figure 4.5a

and b) clearly shows the characteristic features of a quasi-axial S = 5 center: ten approximately equidistant transitions along the *c* direction (θ=0°) are nearly collapsing to one line upon rotation to the magic angle (54.74°) and yield a pattern of near-equidistant lines with half the splitting in the *a** and *b* directions (θ=90°).

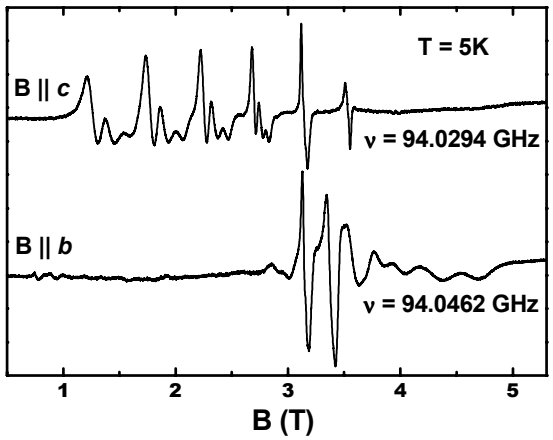

Figure 4.6 *W- band EPR single crystal spectra at 5K along the parallel (~ c axis) and a perpendicular directions (b axis), respectively.*

The negative sign of *D* obtained from the powder HF-EPR study[13] is confirmed by the observation of the effects due to population distribution, with higher intensities for the low-field lines in the parallel spectra relative to the high field ones, and the opposite effect in the perpendicular spectrum. This becomes even more obvious in the T=5 K spectra (see Figure 4.6), in which the high-field lines are vanishing for the parallel direction, as well as the low-field lines in the perpendicular orientation. The observed line-line separations are consistent with the above reported value of D=-0.2 cm^{-1}. Another feature is most clearly observed in the low-temperature spectrum with the field parallel to *c* (Figure 4.6), but also at higher temperatures: each of the EPR lines is composite and consists of three transitions – two of nearly equal intensity and a weaker one– which we attribute to the three different paramagnetic centers with similar properties, but slightly different D-values.

The observation of three centers can be directly related to the three isomers known to occur for the studied compound. Since the co-ordination sphere of Fe2 is not disordered, we can conclude on the basis of the occupancy factor (see paragraph 4.2) that the crystal is essentially a

mixture of three isomers corresponding to AA, AB and BB combinations on the Fe3 and Fe3' sites (see Figure 4.7). On the basis of the occupancy factor of the disordered dpm ligands the relative abundance of the three isomers may be calculated to be, by a simple statistic consideration, 0.49, 0.42 and 0.09, respectively.

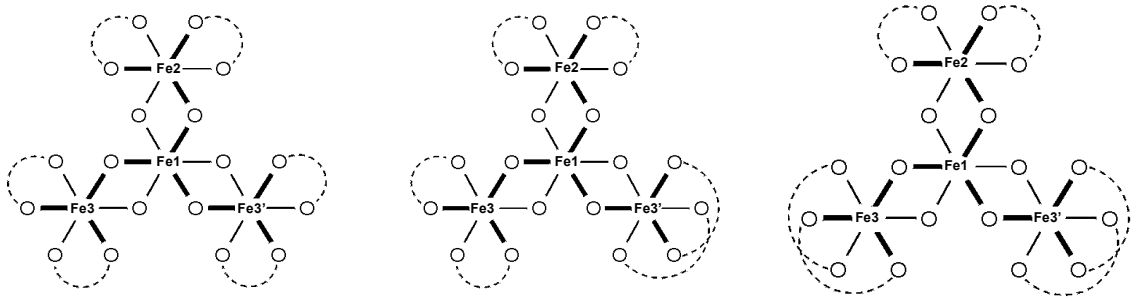

Figure 4.7*.A schematic drawing of the three isomers (from left to right: AA, AB, BB), showing the different binding modes of the dpm anions on Fe3 and Fe3'.*

In Figure 4.8a, it is shown that the spectrum recorded at 25 K with the magnetic field parallel to *c* is quite well simulated using these ratios for the intensities of the three spectra. By passing from the AA to the AB centre contribution a reduction (nearly 8%) in D is observed (see Table 4.1). This is about doubled (to 15%) when both sites are in the B-mode.

A clear identification of the transition fields belonging to different centers was possible only along the parallel direction (Figures 4.6 and 4.8a). The distances between neighboring lines are not equal to each other, increasing from the center of the spectrum to the extremes. This suggests that contributions from higher order terms in the crystal field interactions are of non-negligible importance. We then employed for simulations a complete fourth order Hamiltonian:

$$\mathbf{H}= \mu_B \mathbf{S}\cdot\mathbf{g}\cdot\mathbf{B} + D\mathbf{S}_z^2+E(\mathbf{S}_x^2-\mathbf{S}_y^2)+B_4^0\mathbf{O}_4^0 + B_4^2\mathbf{O}_4^2 + B_4^4\mathbf{O}_4^4 \qquad (4.5.1)$$

where $\mathbf{O}_4^0$ $\mathbf{O}_4^2$ an $\mathbf{O}_4^4$ are the operators listed in Table 2.1.[24] The parameters g_z, D and B_4^0, which essentially determine the line positions in the parallel spectrum, could be accurately determined for all three centers (see Table 4.1).

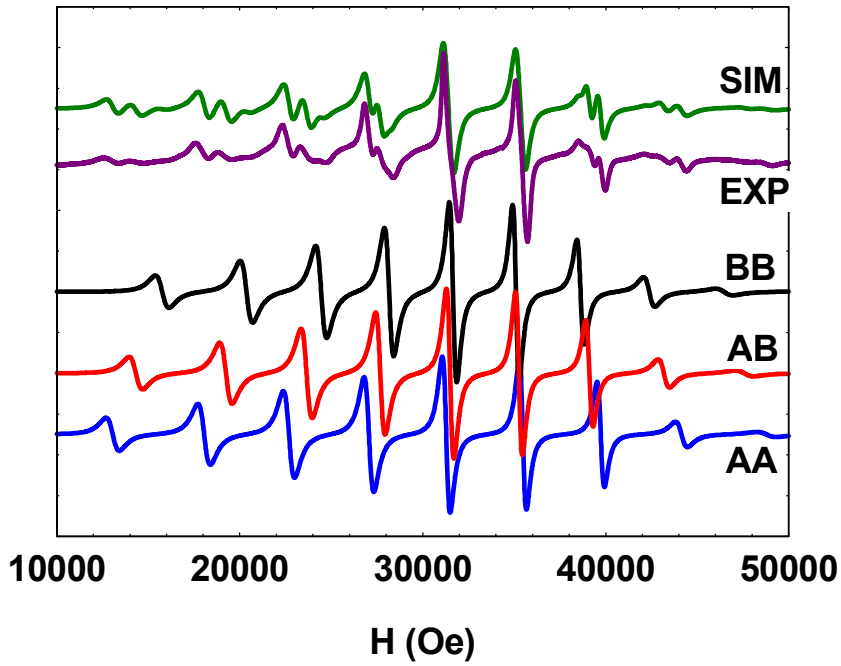

Figure 4.8 *(upper) W- band EPR spectrum along the c axis at 25K; simulated spectra for the three isomers using the parameters from Table 4.1 and the intensity ratios 0.49:0.42:0.09. The upper line is the sum of the three calculated spectra. (lower) W- band EPR spectra along the* a^* *and b axes, respectively, at 25K, together with the simulated spectra for centre AA (red and blue lines, respectively) using the parameters from Table 4.1.*

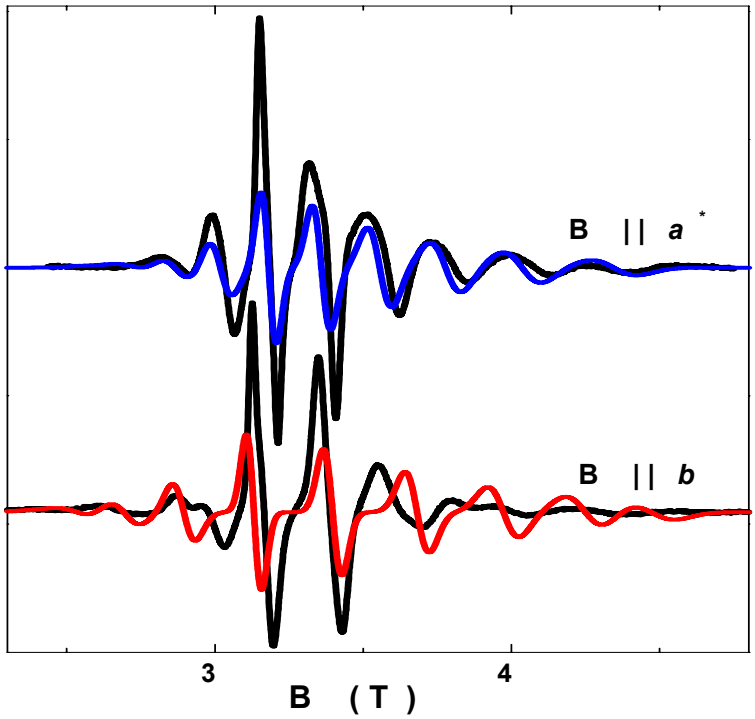

Parameter	Centre AA	Centre AB	Centre BB
g_x	1.995 ± 0.005	-	-
g_y	1.997 ± 0.005	-	-
g_z	2.009 ± 0.005	2.009 ± 0.005	2.009 ± 0.005
D (cm^{-1})	-0.206 ± 0.001	-0.190 ± 0.002	-0.175 ± 0.002
E (cm^{-1})	-0.010 ± 0.003	-	-
B_4^0 (cm^{-1})	(-1.1 ± 0.2) x 10^{-5}	(-1.6 ± 0.2) x 10^{-5}	(-1.6 ± 0.2) x 10^{-5}
B_4^2 (cm^{-1})	(-0.8 ± 0.3) x 10^{-4}	-	-
B_4^4 (cm^{-1})	(-0.4 ± 0.3) x 10^{-4}	-	-

Table 4.1*. Spin-Hamiltonian parameters for the three different isomers occurring in* ***Fe4***

The lines are quite broad and the linewidths (peak-to-peak of the derivative) increase from about 50 mT to 120 mT from the center towards the outermost peaks of the spectra, i.e. from small to large $|M_s|$ values of the S = 5 states involved (Figures 4.6 and 4.8).

This suggests a distribution in the D-values resulting from a local strain induced effect. A similar M dependence of the linewidth was previously observed in the single crystal HF-EPR spectra of another SMM, namely ***Fe8***.[2] The linewidth broadening could be reasonably well simulated by considering a distribution in the values of the zero field splitting parameters *D* and *E* around their average value, while the intensities ratio in the spectrum could be well reproduced by considering a Boltzmann factor with T = 25K (see Figure 4.8a). The line broadening was simulated considering broadening factors $f_1 = f_2 = 1.1 \times 10^{-5}$ cm^{-1}/T :

$$\Gamma = \Gamma_0 (1 + f_1|dB_i/dD| + f_2|dB_i/dE|) \qquad (4.5.2)$$

where Γ_0 is the linewidth in the absence of the broadening effect, Γ is the broadened linewidth and B_i is the resonance magnetic field for a specific resonance.[25]

Within experimental accuracy, the maximum extent for all three spectra appeared along the same direction (the *c* direction). The calculated angular variation in Figure 4.5 is obtained from

the refined spin-Hamiltonian parameters of the dominant center AA. However, an angular variation in the perpendicular plane (*a*b*) reveals a slight in-plane anisotropy (Figure 4.8b). Because of the overlap between lines and the large linewidths, the transitions could not be univocally assigned to the three different centers. Approximate values could be determined for the orthorhombic parameters of the dominant isomer (see Table 4.1), assuming the three centers to be co-axial. This assumption cannot be expected to be entirely correct, as the only local symmetry element for the clusters is the *b*-axis. In fact, only the centers characterized by AA and BB combinations hold this symmetry axis, while for the AB type centers even this symmetry is not valid anymore. Consequently, the different isomers, and in particular the AB-type centers, would have different principal axes of the interaction tensors, which would certainly add to the difficulty of the spin-Hamiltonian analysis.

Attempts were made also to record the X-band spectra of single crystals. In fact, the spectra and their angular variation could be measured, and were visible up to 90K above which they became too broad and disappeared. Even at low temperature the lines are quite broad, from 185 G along the *c* direction up to 500 G along the *b* axis. Moreover, three overlapping spectra from the three isomers are expected. Probably for these reasons, the analysis was not feasible even starting from the parameters derived from the W-band spectra, and no valuable information about the spin-Hamiltonian parameters could be extracted. This is again a confirmation of the important role of high frequency EPR in the characterization of SMM.

With increasing temperature excited multiplets begin to be populated, since two S=4 states are lying only 60 cm^{-1} above the ground S=5 states, as we mentioned previously. In principle additional spectra corresponding to these states might be observed. However, this is not the case in the single crystal W-Band spectra shown in Figure 4.9a. In fact with increasing temperature the lines become broader and the separation between the transition fields decreases, until above 200 K only a single broad line is observed at $g \approx 2$ (see figure 4.9a). Figure 4.9b displays the temperature dependence of the distance between the two central lines, which results from the superposition of the lines belonging to the three centers. A similar temperature dependence of the resonance field positions has been reported for a family of Cu(II) trimers.[26]

This behavior was attributed to the presence in the observed signal of contribution from different states in fast thermal equilibrium. In this framework the decreasing of the line-line

separation with increasing temperature for ***Fe4*** could be attributed to the increasing contribution of higher spin states whose fast relaxation times, due to the large number of multiplets arising from the coupling of the four Iron (III) ions, does not permit the observation of a spectrum. In agreement with the fast relaxation time of the excited multiplets no signal was found in the single-crystal spectra, both in W- and X-band, which could originate from a thermally populated excited spin manifold, in spite of careful temperature dependent measurements. A different explanation had then to be searched for the central features in the high-frequency powder spectra, and for a specific X-band spectrum showing an excited-state-like temperature dependence,[13] (see Figure S4.1) which were earlier justified on the basis of a signal coming from the S=4 state.

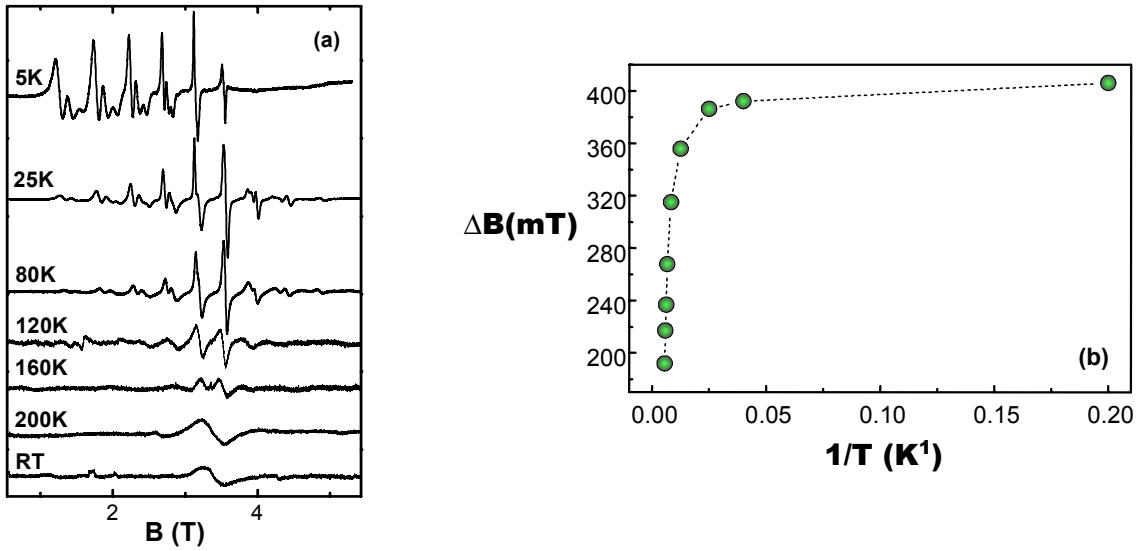

Figure 4.9 *(a) The variation of the single crystal spectrum along the c axis with temperature. (b) The variation of the separation between the central transitions ΔB_c with temperature. The dotted line is a guide for the eye.*

The new powder X-Band spectra (see Figure 4.10), whose features are in agreement with what expected from the determined spin-Hamiltonian parameters, could not reproduce the earlier result (Figure S4.1), which seems then to have originated from the presence of impurities like the dimer $Fe_2(OMe)_2(dpm)_2$, a secondary product of the synthesis.

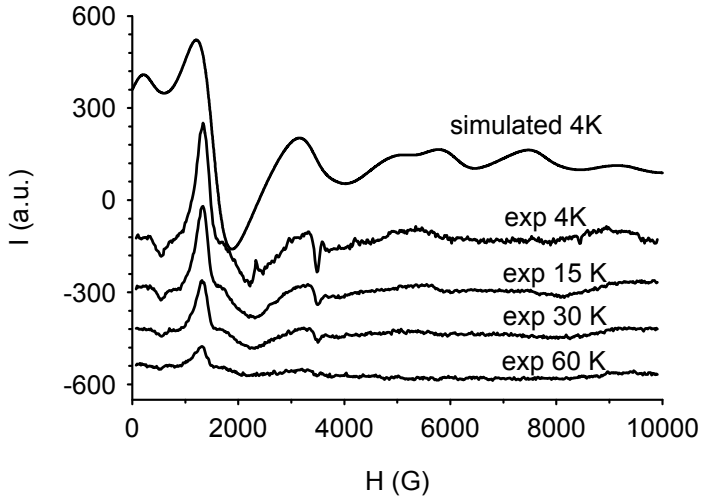

Figure 4.10 *Temperature dependence of powder X-Band EPR spectra, and spectrum simulated at 4K using parameters reported in table 4.1.*

On the other hand, new high-frequency (230 GHz) powder spectra again showed an enhanced intensity of the central feature on increasing temperature (See Figure 4.11).

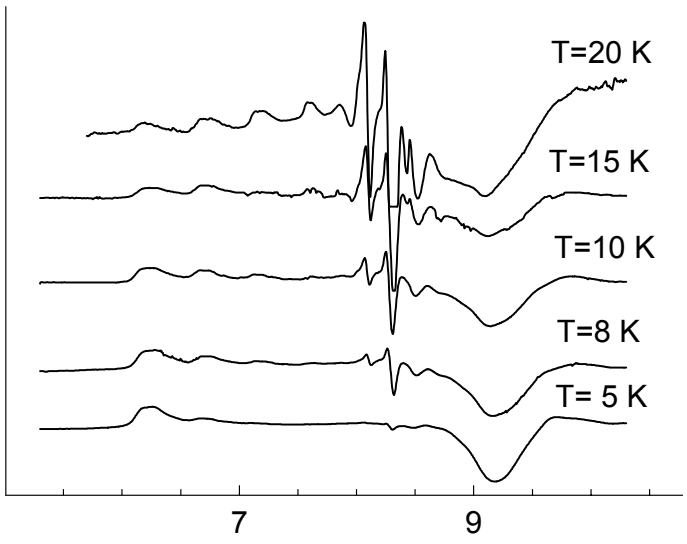

Figure 4.11 *New HF-EPR powder spectra (230 GHz)*

The central feature is outstanding in the powder spectra at higher temperatures because of different reasons: the narrower width of the central transitions, the increasing population of the low |M| states and the extremes in the angular variation occurring in this region close to the magic angle (see Figure 4.5). Even in the single-crystal W-band spectra the central lines have an unexpectedly high amplitude due to the first two of these effects.

4.6 Inelastic Neutron Scattering

The value of spin hamiltonian parameters up to fourth order have been recently determined, using Inelastic Neutron Scattering, both for ***Mn12*** and ***Fe8***.[27-29] This is indeed another very powerful technique in giving information concerning the Zero Field Splitting of the ground multiplet of high-spin molecule which may be seen as complementary to HF-EPR. To further clarify the energy level pattern of ***Fe4***, INS experiments have then recently been performed[15] using the high-energy resolution spectrometer IN5 at the ILL in Grenoble. The INS spectra were consistent with what expected for a S=5 ground state presenting an easy- axis type anisotropy oriented along the pseudo C_3 symmetry axis perpendicular to the Iron plane and a small rhombic contribution in the plane due to the lack of exact C_3 symmetry. It should be noted that the spectrum itself does not reveal clearly, in this case, the presence of three different species. However, following the results of single crystal HF-EPR, three different sets of parameters for the three different isomers showing different population were taken into account during the simulation process of INS spectra. The obtained results were essentially in agreement with the above discussed ones of single crystal HF-EPR analysis. However, while the obtained values for D were in quite good agreement between HF-EPR and INS for all the isomers, the comparison of the best fit parameters for the transverse anisotropy revealed a large discrepancy between the two experiments. Indeed, as may be easily seen in Table 4.2, the E value obtained by simulation of INS spectra was the double of that obtained by HF-EPR analysis of AA.

The possibility of this difference being due to alteration of the ZFS parameters following deuteration of the sample, necessary for INS experiment, was ruled out by recording a HF-EPR

spectra which was superimposable with that of the non-deuterated sample in the same condition. (Figure 4.12).

		Isomer AA	***Isomer AB***	***Isomer BB***
D	*(INS)*	-0.204 ± 0.002	-0.191 ± 0.002	-0.175
D	*(EPR)*	-0.206 ± 0.001	-0.190 ± 0.002	-0.175 ± 0.002
E	*(INS)*	-0.021 ± 0.001	-0.009 ± 0.001	-
E	*(EPR)*	-0.010 ± 0.003	-	-
B_4^0 x10^5	*(INS)*	-1.2 ± 0.2	-2.7 ± 0.2	-1.6
B_4^0 x10^5	*(EPR)*	-1.1 ± 0.2	-1.6 ± 0.2	-1.6 ± 0.2
B_4^2 x10^4	*(INS)*	-	-	-
B_4^2 x10^4	*(EPR)*	-0.8 ± 0.3	-	-
B_4^4 x10^4	*(INS)*	-	-	-
B_4^2 x10^4	(*EPR)*	-0.4 ± 0.3	-	-

Table 4.2 *Comparison of best fit parameters obtained by single crystal HF-EPR and INS for the three different* ***Fe4*** *isomers, AA, AB and BB. The ratio between the three isomers has been assumed to be the same for INS and HF-EPR. Values are expressed in* cm^{-1}*. Adapted from ref. [15]*

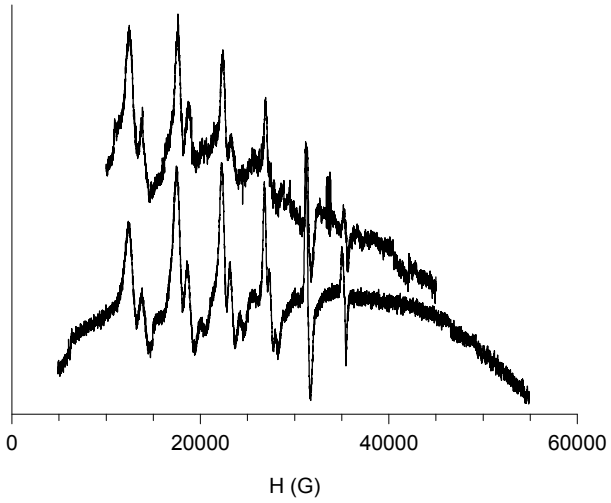

Figure 4.12 *Comparison between single crystal HF-EPR spectra recorded at 5 K with field parallel to the easy axis for deuterated (upper) and non-deuterated(lower) sample*

Quite large differences between transverse anisotropy parameter obtained by single crystal HF-EPR spectra and INS experiment have been already reported for ***Fe8***.[2,29] The origin of this discrepancy may be attributed to the differences between the two spectroscopies: in particular, while INS is a Zero-field technique, HF-EPR employs high magnetic fields. As a consequence in EPR measurements the ZFS terms in the Spin Hamiltonian are deduced from their effect on the level scheme in the presence of a strong magnetic field, and the data interpretation requires complementary assumptions on the parameters defining the Zeeman term while Inelastic neutron scattering (INS) can in principle give a detailed picture of the low lying energy levels from a straightforward analysis of spectra taken with zero magnetic field. Therefore the fitting of the obtained results may be more sensitive to some terms at zero field and to different ones at higher fields, thus yielding different values of the parameters in the two cases. Finally, it should be noted that some variation of the relative population of the three isomers has been revealed by HF-EPR spectra depending on the crystal, and this is probably a factor which may affect the simulation of INS spectra, for which the three signals are not resolved and it is then not possible to estimate their relative intensity.

Concerning the off-diagonal fourth order parameter the sensitivity of the INS experiment was not sufficient to determine them: however, simulations performed using the HF-EPR determined parameters gave no improvements of the quality of the simulation of INS spectra. Higher-resolution and lower energy transfer INS experiments are planned in the next future to have an independent estimate of these parameters.

4.7 Dynamic Magnetic Properties.

4.7.1 Ac susceptibility

The dynamic magnetic susceptibility of ***Fe4*** at very low temperature is shown in Figure 4.13. The real component, χ', increases on lowering temperature, as expected for a paramagnet, down to ca. 1 K. Below this temperature it goes through a maximum, whose position strongly depends on the frequency of the oscillating field. In the same temperature range the imaginary component, χ'', becomes different from zero and shows a frequency-dependent maximum,

which is observed at lower temperatures compared to χ'. Below 0.2 K a further increase in χ'' is observed, with a sharp maximum at frequencies lower than 100 Hz.

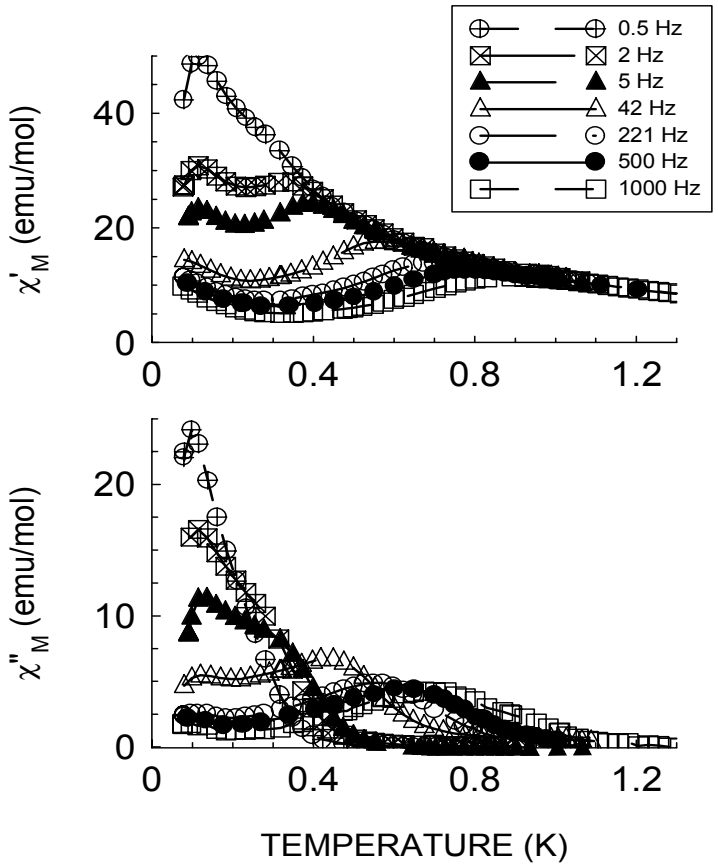

Figure 4.13 *Temperature dependence of the real (top) and imaginary (bottom) components of the Ac susceptibility of* ***Fe4*** *measured at seven frequencies. The inset shows the temperature dependence of the relaxation time evaluated from the maximum in χ''. The line corresponds to the best fit of Arrhenius behavior.*

While the anomalies observed in the 0.5-1.0 K range agree with the typical behavior of super-paramagnets and slow relaxing magnetic molecular clusters,[30-36] the very low temperature behavior might be due either to long-range ordering of the magnetic moments or to the presence of minority fast relaxing species.[37,38] This latter hypothesis seems to be quite reasonable on the basis of the results of both single crystal HF-EPR and INS which showed the axial Spin Hamiltonian parameters for the three isomers to consistently differ between them.

The maxima in the out-of-phase component of the susceptibility provide the relaxation time of the magnetization, which is given in an Arrhenius plot in the inset of Figure 4.13. The few available points agree with a thermally activated behavior, with τ_0=1.1*10^{-6} s and Δ=3.5 K. The pre-exponential factor compares well with the values observed in other slow relaxing clusters,[30,31,39] while the height of the barrier is much lower than that obtained by the above described spectroscopic techniques. The underestimation of the barrier height determined by extrapolation of AC measurements has been previously observed in other slow relaxing molecular nanomagnets [30,40] and it has been attributed to the effect of thermally activated quantum tunneling which opens a new channel of relaxation thus resulting in a faster process.

4.7.2 NMR

Spin dynamics on a polycrystalline sample of ***Fe4*** was recently studied also by mean of NMR.[17] ^{1}H NMR linewidth and ^{1}H NMR spin-lattice relaxation rate, $1/T_1$, as a function of temperature (0.5-295 K) and external magnetic field (0.3-7.2 T) were measured. $1/T_1$ was obtained as weighted average over all the protons of the system, and given the large number of inequivalent nuclei the spectrum is inhomogenously broadened by the distribution of paramagnetic shifts. The linewidth was shown to be proportional to the susceptibility down to 50 K, which is the lowest temperature at which the NMR spectra could be detected, while the width of the spectrum increased linearly with increasing magnetic field. This behavior of the NMR linewidth is typical of a paramagnetic system whereby the proton inhomogeneous broadening was ascribed to the dipolar interaction of the nuclei with the Iron(III) magnetic moments. At 0.5K, the lowest temperature investigated, the proton spectrum covered a range of about 3MHz. This is of the order of magnitude of the main splitting of the proton spectrum in ***Mn12***[41,42] and ***Fe8***[43] at low temperature, where the molecules are in their high spin ground state. It was then concluded that the width of the spectrum at 0.5K in ***Fe4*** arises from the distribution of local hyperfine fields at the proton sites due to the frozen Fe(III) spin configuration in the *S*=5 ground state. This experimental observation gave an independent confirmation of the frozen state of the magnetization in ***Fe4*** on the time-scale of the hyperfine interaction (≈10^6-10^7 Hz). This is consistent with the results of the AC susceptibility measurements shown in the previous paragraph which yielded τ^{-1}≈10^3 Hz at T=0.5 K.

4.7.3 Mössbauer

Mössbauer spectroscopy is a suitable technique for the investigation of spin dynamics of Fe-containing slow relaxing clusters. Indeed, the shape of Mössbauer spectra is determined both by the static interactions between electrons and nuclei of ^{57}Fe and by the dynamics of the spins which produces fluctuations in the hyperfine fields. These fluctuations originate both from the interactions with the vibrational coordinates of the cluster and from QTM, which produces an inversion of the hyperfine field.

The first Mössbauer study concerning ***Fe4*** - appeared in 1999[44] - showed the onset of superparamagnetic like behavior on Mössbauer time scale under 35 K. Recently a more detailed work on this cluster has been carried on,[16] whose main findings are summarized and discussed here. While in the former study only thermal motion of the spins was studied in the 10-60 K range, the new analysis took into account the effect of tunneling processes M→-M at a frequency ν_m; furthermore, spectra were collected at temperatures down to 1.38 K. At this temperature, the relaxation effects on the spectrum are supposedly small and the spectrum contains maximum information about hyperfine parameters which were then determined with quite good accuracy. The obtained values are summarized in Table 4.3. Fittings of the spectra at low temperature allowed also to extract a rough estimate of the second-order Spin hamiltonian parameters: while the obtained value of *D* was reduced of about 20/30 % with respect to INS and EPR values the *E/D* ratio was smaller by an order of magnitude. However, given the large number of parameters employed in the fitting, one should consider these latter values only as indicative of the order of magnitude of *D* and of the presence of only a small degree of transverse anisotropy.

	Fe1	***Fe2***	***Fe3/Fe3'***
Δ_Q *(mm s^{-1})*	-0.55 ± 0.3	0.11 ± 0.1	-0.32 ± 0.06
IS (mm s^{-1})	0.38± 0.05	0.37± 0.07	0.42± 0.04

Table 4.3 *Hyperfine parameters of the three Fe(III) sites in* ***Fe4*** *obtained from the fitting of lowest temperature Mössbauer spectrum for* ***Fe4****. After ref. [16]*

Interesting results were obtained by the fitting of the spectra at different temperatures, which yielded the dependence of the transition probability M → M-1 as a function of the temperature. The obtained trend has been fitted by an exponential function, *W(T)=8600exp(-160/T)*, and then attributed to an Orbach mechanism involving an excited state with energy of about 160 K.

The most interesting results of Mössbauer was probably the observation that the decay rate τ-evaluated from the magnetization correlation function $\langle I(0)I(t)\rangle \propto exp(-t/\tau)$ - as temperature increases was not reproducible on the basis of a simple Arrhenius behavior. Indeed, while for T>>Δ, τ should be equal to τ_0 and then constant, it has been clearly shown that a certain temperature dependence was maintained. This has been reproduced by incorporating a temperature dependent term in τ_0:

$$\tau^{-1} = \left[\tau_0^{-1} + a\exp\left(-\frac{b}{T}\right)\right]\exp\left(-\frac{\Delta}{T}\right) \qquad (4.7.1)$$

At low enough temperature (T<15 K) the second term in square brackets could be disregarded and the usual Arrhenius behavior, with a barrier Δ is obtained. The best fit values for parameters of Eq. (4.7.1) are summarized in Table 4.4: it is worth pointing out that the value of Δ is in quite good agreement with what obtained by HF-EPR and INS measurement.

Parameter	Best fit value
τ_0^{-1}	$(1.9 \pm 0.4) \times 10^7$ s^{-1}
A	$(1.6 \pm 0.5) \times 10^{10}$ s^{-1}
B	(138 ± 13) K
Δ	(6.4 ± 0.5) K

Table 4.4 *Best fit parameters of Mössbauer data to Equation (4.7.1). After ref. [16]*

On the other hand for T>>Δ, $\tau^{-1}=[\tau_0^{-1}+a\exp(-b/T)]$ and thus on the basis of the obtained values, the trend of τ^{-1} vs T at high temperature is very similar to that of W(T), the transition probability.

4.8 Quantum effects in molecular nanomagnets

A large number of evidences now exist for occurrence of quantum tunneling of the magnetization - both in the purely quantum regime and in the thermally activated one - in various molecular nanomagnets.[3,45-49] When Quantum Tunneling occurs in the thermally activated regime thermal processes, principally phonons, promote the molecules up to high levels of the anisotropy barrier with small M_S, not far below the top of the barrier and the molecules then tunnel to the other side. In this region, much of the relaxation is accomplished through a thermal transition and as a consequence magnetization relaxation time is strongly temperature dependent. Conversely, in the low temperature region, phonon-mediated relaxation is very long and can be neglected and thus a purely quantum regime is attained. In this limit the $M_S=\pm S$ states are coupled by a tunneling matrix element Δ_{tunnel}, which is a direct consequence of the presence of a transverse term in the spin hamiltonian. In order for the tunnel between these two states to occur, it would however be necessary for the local magnetic field to be smaller than the tunnel splitting. Considering that the tunnel splitting is usually very small, of the order of 10^{-3}, 10^{-4} G, any additional field, like the dipolar field generated by the surrounding clusters in the lattice, should bring the two levels off-resonance. Prokof'ev and Stamp[50] proposed a model which considers that rapidly changing hyperfine fields due to dynamic nuclear fluctuations can broaden the resonance and allow relaxation of the magnetization of molecules for which dipolar fields are lower than hyperfine fields. Even if the number of clusters that relaxes is small, each time the magnetization of a cluster relaxes it modifies the local dipolar fields and brings other clusters which were formerly close to the resonance condition into resonance, thus allowing a continuous relaxation.

An interesting consequence of this theory is the prediction that at a given longitudinal applied field the magnetization should relax with a square root- time dependence at short times:

$$M(H,t) = M_{in} + \left[M_{eq}(H) - M_{in}\right]\sqrt{\Gamma_{sqrt}(\xi_H)\cdot t} \qquad (4.8.1)$$

here M_{in} is the initial magnetization at time t=0 and $M_{eq}(H)$ is the equilibrium magnetization. The rate function $\Gamma_{sqrt}(\xi_H)$ is proportional to the normalized distribution of energy bias $P(\xi_H)$ in the sample:

$$\Gamma_{sqrt}(\xi_H) = c\frac{\Delta^2_{tunnel}}{\hbar} P(\xi_H) \tag{4.8.2}$$

where $\hbar$ is Planck's constant and c is a constant of the order of unity which depends on the sample shape.

Thus measurements of short time relaxation as a function of applied field H may be exploited to measure $P(\xi_H)$. Furthermore Equation (4.8.2) clearly indicates that the ratio of Γ_{sqrt} with the gaussian half-width of $P(\xi_H)$ should be a constant directly related to Δ_{tunnel}. This gives a powerful method to measure Δ_{tunnel} in a way which does not depend on the parameter obtained from spectroscopic measurements, provided that a suitable measurement technique is available. Indeed, much of the work in this field has been made possible by the developing a Micro-SQUID magnetometer [51] (see Chapter 7), whose fast response and high sensitivity allow short-time measurements down to 1 ms and measurements on tiny single crystal, respectively.

A more direct method to accurately measure Δ_{tunnel} by Micro-SQUID magnetometry has been recently developed by Wernsdorfer et al.[3] based on the Landau-Zener model of tunneling.[4,52,53] Within this picture the spin hamiltonian terms containing $\mathbf{S}_x$ or $\mathbf{S}_y$ operators cause an admixture of the levels and determine an avoided crossing. A spin S is then in resonance between the two states M_s and M_s' when the local longitudinal field is close to Δ_{tunnel}. The tunneling probability is proportional to the square of the tunnel splitting and inversely proportional to the sweeping rate of the longitudinal field. This allows to calculate the tunnel splitting according to the Landau-Zener relation which gives the tunneling probability P when sweeping the longitudinal field H_z at a constant rate over the energy level anticrossing:

$$P_{M_S,M_S'} = 1 - \exp\left[-\frac{\pi\Delta^2}{2\hbar g\mu_B \mid M_S - M_S' \mid \mu_0 dH_z / dt}\right] \tag{4.8.3}$$

here, dH/dt is the constant field sweeping rate, $g \approx 2$, and $\hbar$ is Planck's constant, while M_s and M_s' obviously refer to the quantum number of the avoided energy level crossing under investigation.

To use the Landau-Zener formula for measuring Δ_{tunnel} the sample should be first saturated along the easy axis; following this, the applied field is swept at a constant rate over one of the resonance transitions and the fraction of molecules that reversed their spin is measured. This procedure yields the tunneling rate $P_{Ms,Ms'}$ and thus directly yields a measurement of the tunnel splitting. This method is particularly well suited for molecular clusters because it works even in the presence of dipolar and hyperfine fields, which spread the resonance transition provided that the field sweeping rate is not too small and the magnetization relaxation rate is not too fast with respect to the instrumental response.

As tunnel splitting is critically affected by transverse terms of the spin hamiltonian, the application of a field along an axis different from the easy one gives rise to very interesting phenomena. Indeed periodical quenches of the tunnel splitting are expected when applying a field parallel to the hard axis, whose period of oscillation are related to the second order zero field splitting parameters by:

$$\Delta H = \frac{2k_B}{g\mu_B}\sqrt{E(E+D)} \qquad (4.8.4)$$

In a semiclassical description these oscillations are due to constructive or destructive interference of quantum spin phases of two tunnel paths. Furthermore, the opposite phase for the oscillation of quenching period for tunnel splitting of transitions between M_s=-S and M_s=(S-n) with n odd or even is expected. These behaviors have indeed been observed for the first time on ***Fe8***: periodical oscillations of the tunnel splitting on varying the applied transverse field have been measured, together with a remarkable parity effect for n= 0 to 4 which is analogous to the predicted tunnel suppression for half integer spins.[3]

Both Landau-Zener method and measurement of the square root relaxation time have been recently employed to nicely demonstrate the role of the hyperfine fields in the quantum tunneling process by comparing the results obtained on standard ***Fe8*** (***stFe8***) and on ^{2}H-enriched

(***^{D}Fe8***) and ^{57}Fe-enriched samples (***^{57}Fe8***).[18,54] Relaxation measurements in the pure quantum regime (T<0.36 K) showed a striking dependence on the isotopic substitution, with the relaxation rate varying in the order ***^{57}Fe8*** > ***stFe8*** > ***^{D}Fe8***. The same trend was shown by the hyperfine level broadening measured on the three samples, thus nicely confirming that hyperfine interactions dramatically affect the tunneling rate. It is here important to stress that as the mass is increased in both the isotopically modified sample while the effect on the dynamics is the opposite, the possibility of the observed effects being due to the mass was discarded.

4.9 Quantum effects in *Fe4*

As AC susceptibility measurements, NMR and Mössbauer evidenced on different timescales a super-paramagnetic like behavior of ***Fe4*** at low temperature, which was indeed expected on the basis of the Spin Hamiltonian parameters derived by HF-EPR and INS spectra, we decided to investigate further its low temperature dynamics. In particular, the finding that a non-negligible transverse term is present in the spin hamiltonian suggested the possibility that at low enough temperature, quantum tunneling of the magnetization could be visible.

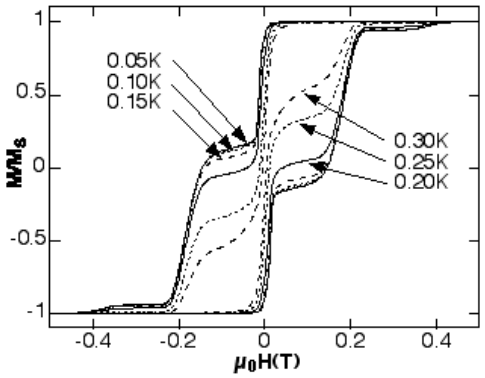

Figure 4.14 *Hysteresis loop measurements of a single crystal of Fe4 at several temperatures. The field sweeping rate was 0.014 T/s*

Magnetic measurements were performed on single crystals by using Micro-squid arrays with magnetic field applied along the easy axis direction, as derived by single crystal HF-EPR

analysis. It was readily seen that below a given temperature (ca. 0.3 K) the magnetization curve of ***Fe4*** shows hysteresis. The hysteresis loops - plotted in Figure 4.14 - show the typical stepped behavior due to resonant quantum tunneling and the position of the steps well agree with the zero-field energy pattern of the ground multiplet derived by HF-EPR and INS. Below 0.1 K the hysteresis loops become almost temperature independent, suggesting that the relaxation occurs through a direct ground state tunneling process between the M = ±5 states. This finding is confirmed by the temperature dependence of the relaxation time needed to relax 90 % of the remanent magnetization, which levels around 0.2 K. These were the first evidences of Quantum Tunneling of the Magnetization in ***Fe4***.

Following this result the measure of the tunnel splitting as a function of transverse field was attempted. As we have seen above, the tunneling probability P may be in principle measured by using a method which makes use of Landau-Zener relation (Equation (4.8.3)). Unfortunately the magnetization relaxation rate is too fast for ***Fe4*** and it proved not possible to apply directly this method. Therefore, we plotted (Figure 4.15) the reversed magnetization after one field sweep over the zero field resonance. A clear dependence on the direction of the transverse field is observed, together with a kink at about 0.15 T, which might be connected with the first quench of the tunnel splitting.

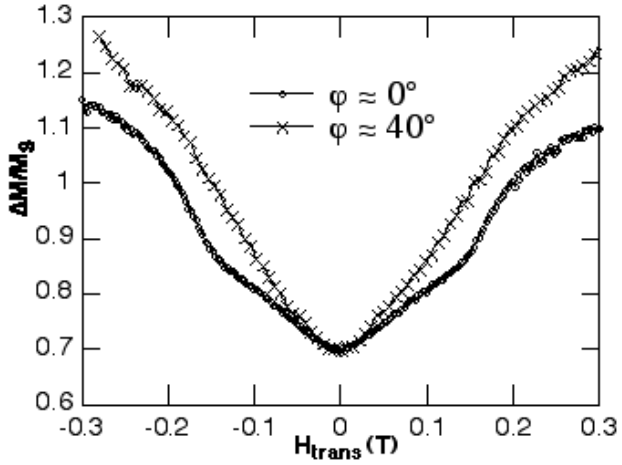

Figure 4.15 *Reversed magnetization after sweeping the field over the zero field resonance as a function of transverse field with the field applied at two azimuth angles, φ=0° and 40°. The kink around 0.2 T may be connected with the first quench of the tunnel splitting*

If one considers for the sake of simplicity only the isomer AA, the first quench of tunnel splitting calculated through Eq. (4.8.4) occurs at 700 G when using HF-EPR parameters and around 1000 G when using INS ones, in agreement with the larger value of E obtained through the latter technique. This large discrepancy with respect to the observed result is however much reduced when including the effect of B_4^4 parameters, which were demonstrated to strongly affect both the period of oscillations and the tunnel splitting. Indeed, considering for B_4^4 the value reported in Table 4.1, the first quench of tunnel splitting is obtained at a field value of H= 1250 G (Figure 4.16) and value up to H=1450 G may be explained on considering the higher limit values of D, E and B_4^4.

The partial agreement between micro-SQUID results and theoretical expectations based on spectroscopic measurements should however be considered with much caution as the determination of the field responsible for the quenching of tunnel splitting is not as direct as it was in ***Fe8***.

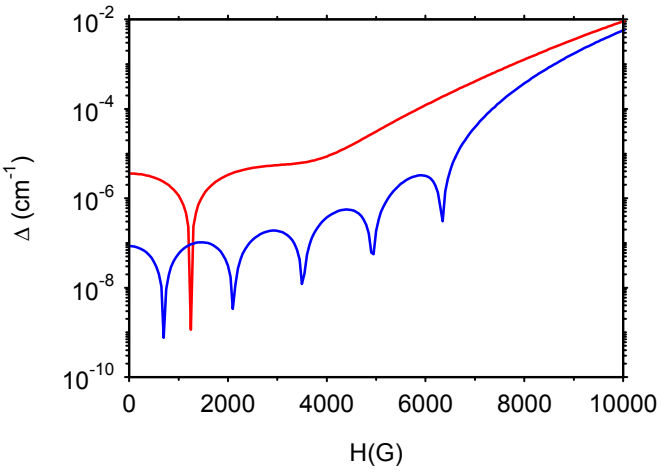

Figure 4.16 *Calculated tunnel splitting oscillations for isomer AA of* ***Fe4*** *when transverse field is applied along the hard axis. Upper and lower curve are calculated with and without inclusion of* B_4^4*, respectively.*

Despite its anisotropy barrier being significantly smaller than ***Fe8*** and ***Mn12***, the observation of quantum tunneling of the magnetization ***Fe4*** made this cluster extremely appealing for the study of isotopic substitution on the low temperature magnetization dynamics. On this respect, it presented in principle several advantages when compared to larger clusters:

its relatively simple structure allowed, as we have seen in previous paragraphs, an accurate quantitative analysis of the magnetic coupling; moreover, an almost total deuteration of the molecule is possible, while for ***Fe8*** this was not possible; finally, it does not contain nitrogen atoms, which carry a nuclear spin and cannot be replaced and thus may hide the effect of the isotopically modified nuclei.

To investigate the effect of isotope substitution on spin dynamics of ***Fe4*** at low temperature, microsquid measurements were recently performed both on completely deuterated and ^{57}Fe substituted samples of ***Fe4***. Unfortunately, a rationalization of these experimental results was not straightforward, as different samples of the same species gave different and not reproducible results, notwithstanding a careful checking of all the steps of the synthesis.[55] The problem looks likely to be due to the presence, in all of the samples, of a fast relaxing fraction of clusters in zero field. These plays the same role of hyperfine field, bringing nearby clusters in resonance and thus accelerating the relaxation process. As a consequence, a detailed analysis of the dynamic processes in function of the isotope modification is hampered. This fast relaxing fraction was tentatively identified with the isomer having the lower D value, whose anisotropy barrier is low enough to be overcome by thermal activation even at low temperature. Efforts to synthesize a ***Fe4*** derivative with ligand different from dpm are currently in progress: this would hopefully yield a molecule with the same low temperature properties of standard ***Fe4*** not showing the three-isomer disorder .

4.10 Conclusions

The careful structural and magnetic characterization of ***Fe4*** showed that this molecule behaves as a molecular nanomagnet with slow magnetic relaxation at very low temperature. Notwithstanding its apparent structural and magnetic simplicity, several problems were encountered. The presence of three isomers - which are present in the crystal as a consequence of ligand disorder for two of the peripheral iron - complicates the analysis of the spectroscopic results as a larger number of parameters has to be determined. However, the single crystal W-band EPR spectra of ***Fe4*** showed that the zfs of the ground S=5 state is quasi-axial, the unique axis being approximately perpendicular to the plane of the four Fe(III) ions. While the

qualitative analysis of the spectra have been essentially confirmed by the simulations, these showed unequivocally that the assumption of a line broadening process probably due to a D-strain is absolutely necessary to quantitatively reproduce the linewidth of the spectrum along the easy direction. This is then an additional parameter to be considered when interpreting HF-EPR spectra of SMM. Different values for the spin-Hamiltonian parameters of the three isomers could also be determined. This may explain why simple calculations performed on averaged structure allowed to reconstruct only about 30% of the experimental *D* value.[13] Presumably the differences in the ZFS parameters may give rise to different blocking temperatures, as evidenced by the presence of different maxima in the χ' vs T plots. The presence of minority species is now seen to be rather common in molecular clusters. In fact, by increasing the complexity of the molecular species it is increasingly possible to accommodate slightly different variants in the same lattice. Similar effects were previously observed by EPR in the case of isolated dimers[56] and now have been observed in the lattice of the archetypical SMM, ***Mn12:***[57] on this respect EPR, being a technique based on local probing, is extremely useful for monitoring the different structures.

Discrepancies were encountered in the value of transverse anisotropy parameters determined by INS and HF-EPR. Further study are planned in the near future, including Cantilever Torque Magnetometer which may yield an independent determination of the orientation of the anisotropy axis and of the parameters of the spin hamiltonian by use of a single crystal technique.

Results concerning dynamics of the magnetization at low temperatures were also discussed, all confirming superparamagnetic like behavior at low temperature. Moreover, the observation of a non-negligible transverse term anisotropy in the spin hamiltonian suggested us to look for resonant quantum tunneling of the magnetization at low temperature, which was indeed observed on single crystal of ***Fe4*** by means of MicroSQUID magnetometry. The observation of quantum effects in this molecule suggested this to be suitable for careful investigation of isotope effect over spin dynamics, given its simplicity: however, the presence of fast relaxing minority species have up to now hampered this analysis.

We believe that this study clearly elucidates the problems which may be encountered when investigating very subtle effects even when an apparently simple molecule like ***Fe4*** is

concerned. It also stresses the usefulness of a multitechnique approach when analyzing static and dynamic properties of molecular nanomagnet. Finally, it points out that accurate control of the synthesis is absolutely necessary to obtain a complete characterization of these systems. On this respect, synthetic efforts to obtain a molecule with the same properties of ***Fe4*** but crystallizing in only one isomeric form are currently in progress: on this respect a promising system has been recently synthesized by Saalfrank et al. [58]

References

1. A. L. Barra, D. Gatteschi, and R. Sessoli, *Phys. Rev. B* **56**, 8192 (1997).

2. A. L. Barra, D. Gatteschi, and R. Sessoli, *Chem.-Eur. J.* **6**, 1608 (2000).

3. W. Wernsdorfer and R. Sessoli, *Science* **284**, 133 (1999).

4. W. Wernsdorfer, R. Sessoli, A. Caneschi, D. Gatteschi, and A. Cornia, *Europhys. Lett.* **50**, 552 (2000).

5. W. Wernsdorfer, R. Sessoli, A. Caneschi, D. Gatteschi, A. Cornia, and D. Mailly, *J. Appl. Phys.* **87**, 5481 (2000).

6. A. Garg, *Phys. Rev. B* **64,** 094414 (2001).

7. E. Kececioglu and A. Garg, *Phys. Rev. B* **6305**, 4422 (2001).

8. L. Bokacheva, A. D. Kent, and M. A. Walters, *Phys. Rev. Lett.* **85**, 4803 (2000).

9. K. M. Mertes, Y. Zhong, M. P. Sarachik, Y. Paltiel, H. Shtrikman, E. Zeldov, E. Rumberger, D. N. Hendrickson, and G. Christou, *Europhys. Lett.* **55**, 874 (2001).

10. M. N. Leuenberger and D. Loss, *Phys. Rev. B* **63,** 054414 (2001).

11. F. Luis, F. L. Mettes, J. Tejada, D. Gatteschi, and L. J. De Jongh, *Phys. Rev. Lett.* **85**, 4377 (2000).

K. M. Mertes, Y. Suzuki, M. P. Sarachik, Y. Paltiel, H. Shtrikman, E. Zeldov, E. Rumberger, D. N. Hendrickson, and G. Christou, *Phys. Rev. Lett.* **87**, 227205 (2001).

13. A. L. Barra, A. Caneschi, A. Cornia, F. F. De Biani, D. Gatteschi, C. Sangregorio, R. Sessoli, and L. Sorace, *J. Am. Chem. Soc.* **121**, 5302 (1999).

14. A. Bouwen, A. Caneschi, D. Gatteschi, E. Goovaerts, D. Schoemaker, L. Sorace, and M. Stefan, *J. Phys. Chem. B* **105**, 2658 (2001).

15. G. Amoretti, S. Carretta, R. Caciuffo, H. Casalta, A. Cornia, M. Affronte, and D. Gatteschi, *Phys. Rev. B* **64,** 104403 (2001).

16. L. Cianchi, F. Del Giallo, G. Spina, W. Reiff, and A. Caneschi, *Phys. Rev. B* **65**, 064415 (2002).

17. D. Procissi, B. J. Suh, A. Lascialfari, F. Borsa, A. Caneschi, and A. Cornia, *46th MMM Session* (submitted).

18. R. Sessoli, A. Caneschi, L. Sorace, A. Cornia, and W. Wernsdorfer, *J. Magn. Magn. Mater.* **226-230**, 1954 (2001).

19. E. J. L. Mcinnes, C. Anson, A. K. Powell, A. J. Thomson, S. Poussereau, and R. Sessoli, *Chem. Commun.* 89 (2001).

20. K. S. Murray, *Adv. Inorg. Chem.* **43**, 261 (1995).

21. F. Le Gall, F. Fabrizi de Biani, A. Caneschi, P. Cinelli, A. Cornia, A. C. Fabretti, and D. Gatteschi, *Inorg. Chim. Acta* **262**, 123 (1997).

22. S. M. Gorun and S. J. Lippard, *Inorg. Chem.* **30**, 1625 (1991).

23. A. Bencini and D. Gatteschi, *Transition Metal Chemistry,* B.N. Figgis and G. Melson (Marcel Dekker, New York 1982) Vol. 8, p.1.

24. A. Abragam and B. Bleaney, *Electron Paramagnetic Resonance of Transition Ions* (Dover Publications, New York, 1986).

25. J. R. Pilbrow, *Transition Ion Electron Paramagnetic Resonance* (Oxford University Press, Oxford, 1990).

26. P. Fleischhauer, S. Gehring, C. Saal, W. Haase, Z. Tomkowicz, C. Zanchini, D. Gatteschi, D. Davidov, and A. L. Barra, *J. Magn. Magn. Mater.* **159**, 166 (1996).

Y. C. Zhong, M. P. Sarachik, J. R. Friedman, R. A. Robinson, T. M. Kelley, H. Nakotte, A. C. Christianson, F. Trouw, S. M. J. Aubin, and D. N. Hendrickson, *J. Appl. Phys.* **85**, 5636 (1999).

28. I. Mirebeau, M. Hennion, H. Casalta, H. Andres, H. U. Gudel, A. V. Irodova, and A. Caneschi, *Phys. Rev. Lett.* **83**, 628 (1999).

29. R. Caciuffo, G. Amoretti, A. Murani, R. Sessoli, A. Caneschi, and D. Gatteschi, *Phys. Rev. Lett.* **81**, 4744 (1998).

30. M. A. Novak and R. Sessoli, *Quantum Tunneling of Magnetization - QTM'94*, L. Gunther and B. Barbara (Kluwer Academic Publishers, 1995), p. 171.

31. A. L. Barra, P. Debrunner, D. Gatteschi, Ch. E. Schulz, and R. Sessoli, *Europhys. Lett.* **35**, 133 (1996).

32. S. M. J. Aubin, Z. M. Sun, I. A. Guzei, A. L. Rheingold, G. Christou, and D. N. Hendrickson, *Chem. Commun.* 2239 (1997).

33. S. L. Castro, Z. M. Sun, C. M. Grant, J. C. Bollinger, D. N. Hendrickson, and G. Christou, *J. Am. Chem. Soc.* **120**, 2365 (1998).

34. A. L. Barra, A. Caneschi, D. Gatteschi, D. P. Goldberg, and R. Sessoli, *J. Solid State Chem.* **145**, 484 (1999).

35. H. Oshio, N. Hoshino, and T. Ito, *J. Am. Chem. Soc.* **122**, 12602 (2000).

36. J. Yoo, A. Yamaguchi, M. Nakano, J. Krzystek, W. E. Streib, L. C. Brunel, H. Ishimoto, G. Christou, and D. N. Hendrickson, *Inorg. Chem.* **40**, 4604 (2001).

37. W. Wernsdorfer, R. Sessoli, and D. Gatteschi, *Europhys. Lett.* **47**, 254 (1999).

38. S. M. J. Aubin, Z. M. Sun, H. J. Eppley, E. M. Rumberger, I. A. Guzei, K. Folting, P. K. Gantzel, A. L. Rheingold, G. Christou, and D. N. Hendrickson, *Inorg. Chem.* **40**, 2127 (2001).

39. H. J. Eppley, H.-L. Tsai, N. de Vries, K. Folting, G. Christou, and D. N. Hendrickson, *J. Am. Chem. Soc.* **117**, 301 (1995).

40. S. M. J. Aubin, Z. M. Sun, L. Pardi, J. Krzystek, K. Folting, L.-C. Brunel, A. L. Rheingold, G. Christou, and D. N. Hendrickson, *Inorg. Chem.* **38**, 5329 (1999).

41. Y. Furukawa, K. Watanabe, K. Kumagai, F. Borsa, and D. Gatteschi, *Phys. Rev. B* **64,** 104401 (2001).

42. Y. Furukawa, K. Watanabe, K. Kumagai, Z. H. Jang, A. Lascialfari, F. Borsa, and D. Gatteschi, *Phys. Rev. B* **62**, 14246 (2000).

43. Y. Furukawa, K. Kumagai, A. Lascialfari, S. Aldrovandi, F. Borsa, R. Sessoli, and D. Gatteschi, *Phys. Rev. B* **64,** 094439 (2001).

44. A. Caneschi, L. Cianchi, F. Del Giallo, D. Gatteschi, P. Moretti, F. Pieralli, and G. Spina, *J. Phys.* **11**, 3395 (1999).

45. L. Thomas, F. Lionti, R. Ballou, D. Gatteschi, R. Sessoli, and B. Barbara, *Nature* **383**, 145 (1996).

46. J. R. Friedman, M. P. Sarachik, J. Tejada, and R. Ziolo, *Phys. Rev. Lett.* **76**, 3830 (1996).

47. J. R. Friedman, M. P. Sarachik, and R. Ziolo, *Phys. Rev. B,* **58**, R14729-R14732 (1998).

48. C. Sangregorio, T. Ohm, C. Paulsen, R. Sessoli, and D. Gatteschi, *Phys. Rev. Lett.* **78**, 4645 (1997).

49. W. Wernsdorfer, T. Ohm, C. Sangregorio, R. Sessoli, D. Mailly, and C. Paulsen, *Phys. Rev. Lett.* **82**, 3903 (1999).

50. N. V. Prokof'ev and P. C. E. Stamp, *Phys. Rev. Lett.* **80**, 5794 (1998).

51. W. Wernsdorfer, K. Hasselbach, A. Benoit, B. Barbara, D. Mailly, J. Tuaillon, J. P. Perez, V. Dupuis, J. P. Dupin, G. Giraud, and Perex A. *J. Appl. Phys.* **78**, 7192 (1995).

52. V. V. Dobrovitski and A. K. Zvezdin, *Europhys. Lett.* **38**, 377 (1997).

53. L. Gunther, *Europhys. Lett.* **39**, 1 (1997).

54. W. Wernsdorfer, A. Caneschi, R. Sessoli, D. Gatteschi, A. Cornia, V. Villar, and C. Paulsen, *Phys. Rev. Lett.* **84**, 2965 (2000).

55. A. Cornia, *private communication*.

56. A. Bencini, D. Gatteschi, C. Zanchini, O. Kahn, M. Verdaguer, and M. Julve, *Inorg. Chem.* **25**, 3181 (1986).

57. W. Wernsdorfer, R. Sessoli, and D. Gatteschi, *Europhys. Lett.* **47**, 254 (1999).

58. R. W. Saalfrank, I. Bernt, M. M. Chowdhry, F. Hampel, and G. B. M. Vaughan, *Chem.-Eur. J.* **7**, 2765 (2001).

5. The metal-radical approach to magnetic molecular materials: complexes of poly-dioxolene ligands

5.1 Introduction

One of the possible approach to prepare molecule-based magnetic materials is the so-called metal-radical approach, i.e. the design of an extended lattice containing paramagnetic metal ions whose mutual magnetic interactions are determined by appropriate bridging radical ligands. An important step for a rational design of a multidimensional collection of mutually interacting molecular systems having desirable properties is obviously the synthesis and the characterization of small molecules which may act as suitable building blocks for higher dimensional systems. Indeed, the study of discrete metal-radical complexes led to comprehension of the basic features governing of the exchange coupling between ligand and metal, thus yielding the possibility of designing systems with predictable interactions. More importantly, radicals capable of bridging two or more metal centers have led to a rich array of one-, two-, and three-dimensional coordination polymers, some of which exhibit cooperative magnetic behavior.

The families of paramagnetic ligands (see Figure 5.1) which have been studied within this approach can be divided into two broad classes: charged and neutral radicals. In particular, charged radicals include radical anions of nitrogen heterocycles,[1] semiquinones, [2-4] and cyanocarbons such as $TCNE^-$ (tetracyanoethylene anion),[5,6] TCNQ (tetracyanoquinodimethane anion),[7] and related species [8] for which applications of this strategy proved particularly successful. On the other hand, example of neutral

radicals are the most heavily studied nitronyl nitroxides,[9,10] imino nitroxides,[11,12] di- and trinitroxide ligands,[13,14] and -more recently- verdazyls radicals.[15-17]

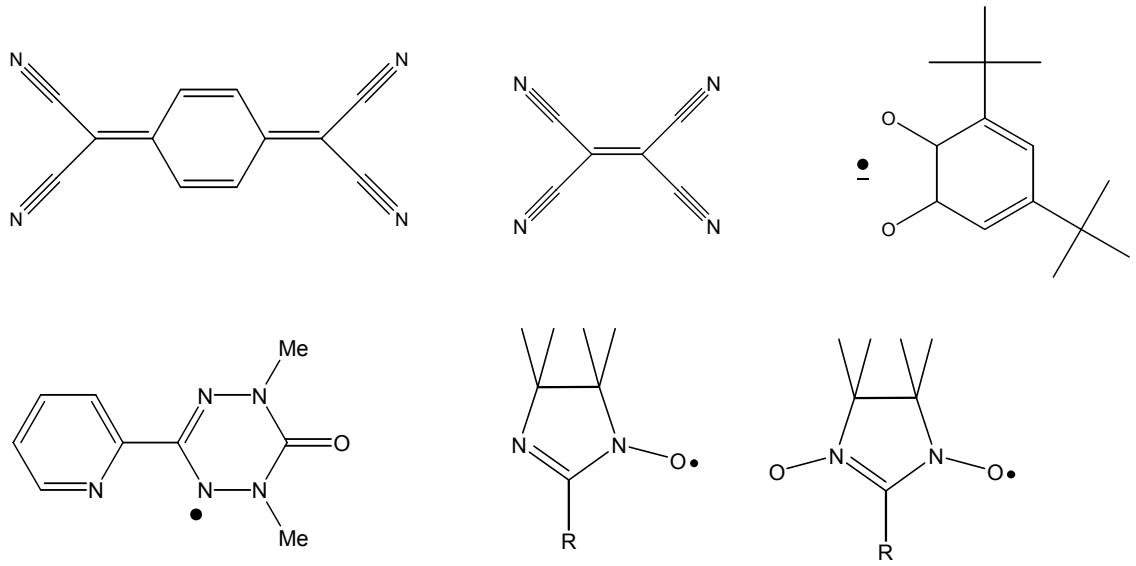

Figure 5.1 *Upper: TCNQ and TCNE in their non-radical forms and an example of semqiuinone radical. Lower: a verdazyl, an imino-nitroxide and a nitronyl-nitroxide*

In this part of thesis we will analyze the properties of a series of complexes containing poly-radical ligands coupled to paramagnetic metal ions. In particular our approach exploits the peculiar electronic and magnetic properties of metal-semiquinone complexes that will be summarized in the following paragraph. The detailed analysis of the properties of such molecules was aimed at the final goal of designing a tridimensional network of paramagnetic centers with predictable magnetic properties. This work is the result of a collaboration with the group of Prof. D. A. Shultz, North Carolina State University, where the synthesis and preliminary physical characterization of the ligands has been carried out.

5.2 Metal-Semiquinones complexes: magnetic and electronic properties

Initial interest toward the coordination chemistry of dioxolene ligands arose mainly because of their peculiar redox properties[1,3,18] these ligands may in fact coordinate to metal ions in three different electronic states, as shown in Figure 5.2. The charge localized description of dioxolene ligands which is sketched there follows from the experimental

evidences of charge delocalization within metal-quinone chelate ring not being much significant, in opposition to what has been observed for complexes of similar ligands as 1,2 dithiolene and diimine ligands.[3]

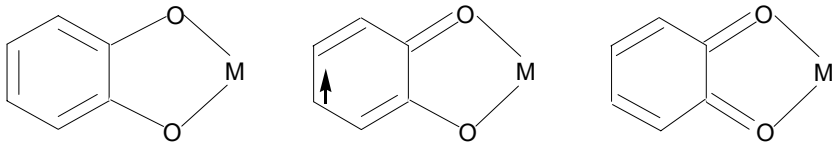

Figure 5.1 Different oxidation states of dioxolene ligands. From left to right: cathecholate, semiquinone, quinone

Interestingly, the partially reduced radical species, semiquinone, is stabilized upon coordination to metal ion: this makes these ligands potential candidates to be considered in the search for new magnetic molecular materials following the metal-radical approach.

5.2.1 Magnetic coupling in metal-semiquinone complexes

The magnetic properties of metal-semiquinonate complexes can be understood rationalizing the exchange coupling between the metal ion and the radical through a very simple model.[2] Indeed, the sign and intensity of the direct exchange coupling interaction between the two spins are governed by the overlap between the magnetic orbitals – i.e. the orbitals containing unpaired electrons - of the two centers. According to well established model[19,20] antiferromagnetic coupling is expected when the magnetic orbitals of the two centers have a non-zero overlap, S, the coupling constant J being proportional to S^2. On the other hand if no overlap occurs, i.e. the magnetic orbitals are orthogonal to each other, the expected coupling is ferromagnetic. In this latter situation global zero overlap usually results from overlapping region with different signs of overlap and the magnitude of the coupling depends on the overlap density in these regions. On this respect, the strong donor ability of semiquinone ligand was correctly expected to give rise to large magnetic coupling with metal ions.

From what we have said it follows that the magnetic properties of transition metal complexes with semiquinones can be easily analyzed on the basis of simple symmetry considerations about the magnetic orbitals. Indeed, the magnetic orbital of the radical is the

antibonding π-orbital depicted in Figure 5.3, while those of the metal ions are, to a good approximation, the *3d* orbitals.

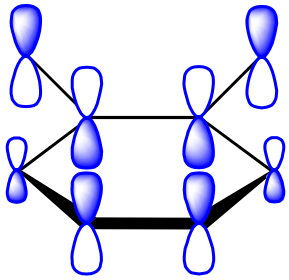

Figure 5.3 *The magnetic π*-orbital of semiquinone*

If we consider, for the sake of simplicity, octahedral coordination, then x^2-y^2 and z^2 orbitals are e_g orbitals, thus of σ- type, while *xz*, *yz*, *xy* are t_{2g} and then of π- type. Obviously, while e_g orbitals will be orthogonal to magnetic orbital of semiquinones, thus leading to ferromagnetic coupling, t_{2g} will have a large non-zero overlap leading to antiferromagnetic coupling. Thus sign and magnitude of exchange coupling may be predicted on the basis of the electronic configuration of the metal ion. In agreement with this interpretation strong antiferromagnetic coupling (J >500 cm^{-1}) has been observed in Chromium(III), Iron(III), and Manganese(III) complexes while quite strong ferromagnetic coupling has been observed for Copper(II) and Nickel(II) derivatives.[2] It is worth stressing here that while a strong antiferromagnetic coupling indicates that interaction between unpaired electrons of metal ion and ligand is very strong leading to an antiparallel alignment the spins, this does not result in a direct bond between the dioxolene ligand and the metal ion. Indeed, crystal structures of semiquinonate complexes show that bond lengths and angles of the ligand fall in an intermediate region with respect to those found for quinone and cathecholate complexes.[3,18] As a consequence of this peculiar property the charge distribution of metal-dioxolene complexes can be assigned unambiguously on the basis of X-Ray structure solution.

5.2.2 Valence tautomerism in metal-semiquinone complexes

A crucial point in the characterization of metal-dioxolene complexes lies in the determination of relative charge distribution between metal and ligand. In particular, when metal orbital energy is high with respect to HOMO π- quinonoid levels the ligand bonds as

cathecolate to an oxidized form of the metal, whereas if the reverse is true the charge resides on metal localized levels the ligand being coordinated as partially reduced semiquinones. However, the most interesting situation is encountered when the electronic levels of quinone and metal ions lie close in energy. This leads to the possibility of observing an intramolecular electron transfer process between redox isomers differing in charge distribution under equilibrium conditions, a process which has been termed valence tautomerism (see Scheme 5.1).

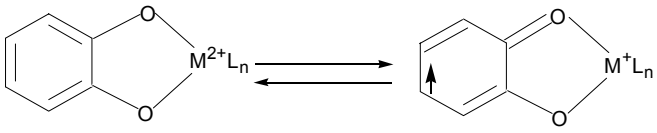

Scheme 5.1

Such an equilibrium has been reported for several transition metal ions [21-24] but among these cobalt-dioxolene complexes[21,25-34] are the most attractive from a magnetic point of view and in the following we will focus on them.

The valence tautomeric interconversion in this complexes involves an intramolecular electron transfer between a six-coordinate diamagnetic Co(III) metal ion and a coordinated catecholate ligand yielding a Co(II)-semiquinone species,[3,35] the metal ion being in the high-spin electronic configuration: *hs*Co(III)-Cat $\rightleftharpoons$ *ls*Co(II)-SQ. Thus, as a consequence of the VT process a change of spin state occurs both at the metal center and on the ligand on varying the external conditions:[21,28,29,34]

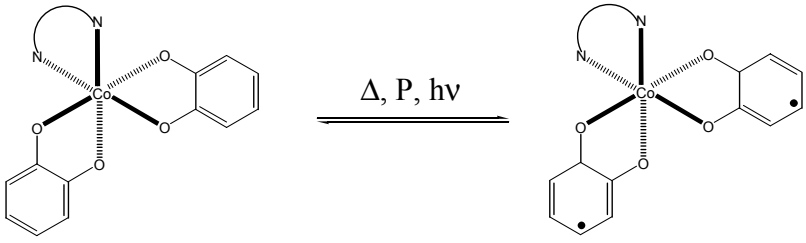

ls-$Co^{III}(SQ)(Cat)$ *hs*-$Co^{II}(SQ)_2$

Figure 5.4. *Schematized view of the Valence-tautomeric transformation which has been shown to occur in the cobalt complexes under the influence of temperature (T), pressure (P),and light(hν)*

The occurrence of this process may be explained by considering an oversimplified MO description of these complexes. In this framework the metal t_{2g} orbitals are of the correct

symmetry to interact with the dioxolene π* orbitals depicted in Figure 5.3. As dioxolene π* orbitals are slightly higher in energy than t_{2g} a MO of π symmetry with bonding character is obtained which is mainly metal based, while the antibonding one is mainly ligand based. On the other hand, the σ* orbitals of the dioxolene ligand are very low lying in energy and thus the obtained σ* MO are mainly metal based (see Figure 5.5). The relatively small interaction between metal and ligand orbitals results in a close pattern of frontier orbital energies which allows the occurrence of interelectronic energy transfer.

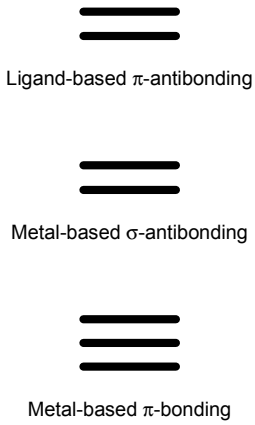

Figure 5.5 *Relative frontier orbital energies in metal-dioxolene complexes. The close spacing in energy allows the occurrence of interelectronic energy transfer.*

The main thermodynamic features of the process directly follows from this description leading to the conclusion that VT is entropy driven, while enthalpy variation is of the order of thermal energy, both tautomer being accessible on varying temperature. Indeed, while in *ls*Co(III)-Cat complexes only π-bonding metal based orbitals are occupied, in *hs*Co(II)-SQ species σ* orbitals are occupied. This results in longer Co-O distances, which are accompanied by a higher density of vibrational levels in the high spin state. Thus a large increase of vibrational entropy is expected to occur during the interconversion process. On the other hand the increase in electronic entropy, mainly due to the high-spin metal ion configuration for Co(II), may be estimated to be smaller by an order of magnitude or even more. Even if this view has been mainly confirmed by DFT-based calculations on a system exhibiting Valence Tautomerism[36] the microscopic details of changes that occur at the electronic level during the interconversion process are still debated, and are currently actively investigated both from a theoretical point of view and by means of femtosecond pulsed laser photolysis.[37-39]

From what we have said it follows that complexes undergoing Valence Tautomer equilibrium are an interesting class of electronically labile materials, inherently bistable systems whose electronic structures are a function of an external stimulus as T, P, light irradiation etc. The main parameter defining this kind of processes is $T_{1/2}$ which is the temperature for which the fraction of the two electronic states, says A and B, are the same. The possible occurrence of hysteresis with respect to the external stimulus - identified as differences in $T_{1/2}$ concerning the process occurring in the A→ B direction with respect to that concerning the B→ A one - makes these molecules appealing as basis for molecular devices. A necessary prerequisite for this to occur is the cooperativity of the process: this means that intermolecular interactions between the molecules in the two phase, A and B should be different. On this respect, the attractiveness of such a class of compounds is due to the fact that their properties, and then the relative intermolecular interactions, can be tuned by means of molecular chemistry techniques: this is a well established approach for spin-crossover complexes.[40]

Notwithstanding this, up to date the potential application of Valence Tautomer systems has been limited by the paucity of materials exhibiting thermal hysteresis. Indeed a small hysteresis width (5 K) was found to be associated to the tautomeric interconversion showed by the Co^{III}(phen)(DBSQ)(DBCat)·$C_6H_5CH_3$ complex,[21] while a rather large effect was detected for Co^{III}(3,6-DBCat)(3,6-DBSQ)(py_2O) and Co^{II}(3,6-DBSQ)$_2$(py_2O) valence tautomeric pair.[31] However in the latter system the observed behavior has been attributed to the planar/folded change in conformation due to the steric requirements of the ancillary diazine ligand. In this sense the observed magnetic behavior of this molecular system must be considered as a very interesting exception, but, because of its pure molecular origin, it cannot provide the basis for the development of a class of magnetic materials. Since the fundamental origin of valence tautomerism is molecular and the cobalt(III)-catecholate and cobalt(II)-semiquinone species involved in the interconversion are dimensionally different, a thermal hysteresis and then a memory effect must be associated with the existence of a strong cooperativity between the cobalt centers. On this respect either the use of ancillary ligands or of suitable dioxolene ligands capable to favor the formation of polymeric structure can be advised.

5.3 Design of polydioxolene ligands with predetermined magnetic properties

Design of high spin organic molecule, i.e polyradical molecules with intramolecular ferromagnetic coupling between the spins, plays a very important role in the research of new magnetic molecular materials with enhanced properties. The use of this kind of ligands may result in the assembling of extended structures, and if suitable coupling within the ligands and between ligand and metal is achieved new magnetic molecular materials may be obtained. Thus, in an effort to design multispin subunits with well defined magnetic and electronic properties, the obvious step following the characterization of simple dioxolene ligand complexes is the synthesis and characterization of linked dioxolene ligands. Indeed, as we have seen that strong magnetic-ligand coupling may be easily achieved and its nature predicted following simple criteria, metal-o-semiquinones are potential building blocks to obtain magnetic solids provided that an appropriate strategy for designing linked semiquinone ligands with suitable exchange coupling between the radical moieties is used.

On this respect the most common high-spin organic molecule design is to attach paramagnetic functional groups to a π-system acting as a coupler which is known to force ferromagnetic coupling between the attached positions. Thus high-spin dioxolene type ligands are to be expected whenever semiquinone rings will be linked through a suitable "ferromagnetic coupler".

The topology required for the π-system to favor ferromagnetic coupling may be easily understood considering biradicals systems, extension to polyradicals following on the same basis. If we consider a non-Kekule' hydrocarbons, with *n-1* bonding and antibonding orbitals and *2n* non-bonding orbitals, Hund's rule forces the electron in the non-bonding orbitals to be unpaired. Whenever the two singly occupied molecular (or atomic) orbitals are orthogonal to each other and the zero overlap between them results from the opposite contribution of two overlap regions - of in-phase and out-of-phase overlap, respectively - ferromagnetic coupling is expected. Using these simple rules trimethylenemethane and *meta*-xylylene, depicted in the Figure 5.6, have been employed as suitable ferromagnetic coupler in a multitude of diradical systems to force a triplet ground state. Following the same reasoning it is expected that a suitable precursor for any triradical may be the 1,3,5-trimethylenebenzene molecule. Indeed, trimethylenebenzene is a non-Kekulé alternant hydrocarbon in which three electrons occupy three nonbonding molecular orbitals and has been predicted to be characterized by a quartet ground-state.[41] Thus, suitable high-spin

dioxolene type ligands are to be expected whenever semiquinone linked through *m*-xylilene, trimethylenemethane and 1,3,5 trimethylenebenzene would be synthesized.

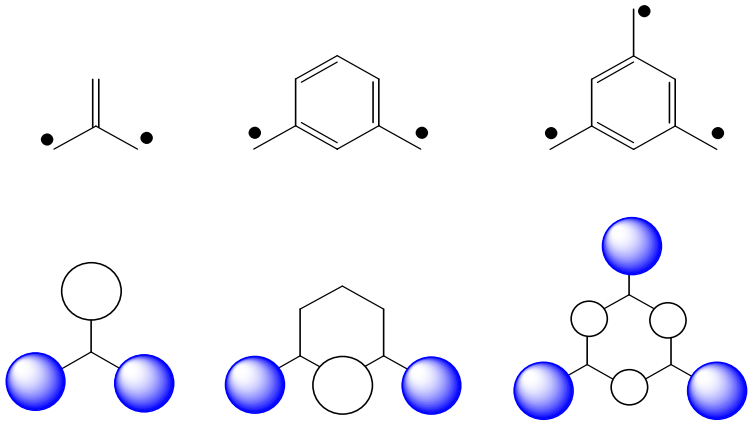

Figure 5.6 *Ferromagnetic couplers trimethylenemethane, m-xylilene and 1,3,5-trimethylenebenzene. with pictorial representations of their molecular orbitals in case of ferromagnetic coupling*

Concerning the electronic properties, redox activity characterizing linked dioxolenes makes them even more interesting than simple dioxolene ligands. Indeed, as shown in Figure 5.7 for one of the simplest of this molecule which may be thought of, namely the 4,4'-bis(1,2-benzoquinone (Q-Q), this is part of a five-membered redox chain (hereafter Q-Q, Q-SQ, SQ-SQ, SQ-Cat, Cat-Cat) in which all the members are able to act as bis-bidentate ligands.[42,43] While there is experimental evidence indicating that the SQ-SQ species is diamagnetic,[44] it is still unclear whether the electronic ground-state of this molecule is sensitive to the dihedral angle between the dioxolene planes and may therefore change from singlet to triplet. Such a change in ground state spin multiplicity might be expected for torsion angles between dioxolene planes near 90°.[45] The Q-SQ and SQ-Cat members are also paramagnetic and the Q-SQ and SQ-Cat compounds can be classified as class II or class III mixed-valence systems.[20,46] In the former case the ligands could serve as molecular switches, in accordance to the existence of two different electronic structures for the two halves of the molecule. On the other hand if the ligands are characterized by delocalized electronic structures, their application for the synthesis of extended molecule-based magnetic materials or molecular wires seems more appropriate. It should indeed be noted that as far as metal complexes are concerned, much is known about mixed-valence systems formed by metal ions in different oxidation states, but by comparison, little is

known about systems containing linked coordinated ligands in different oxidation states.[47-51]

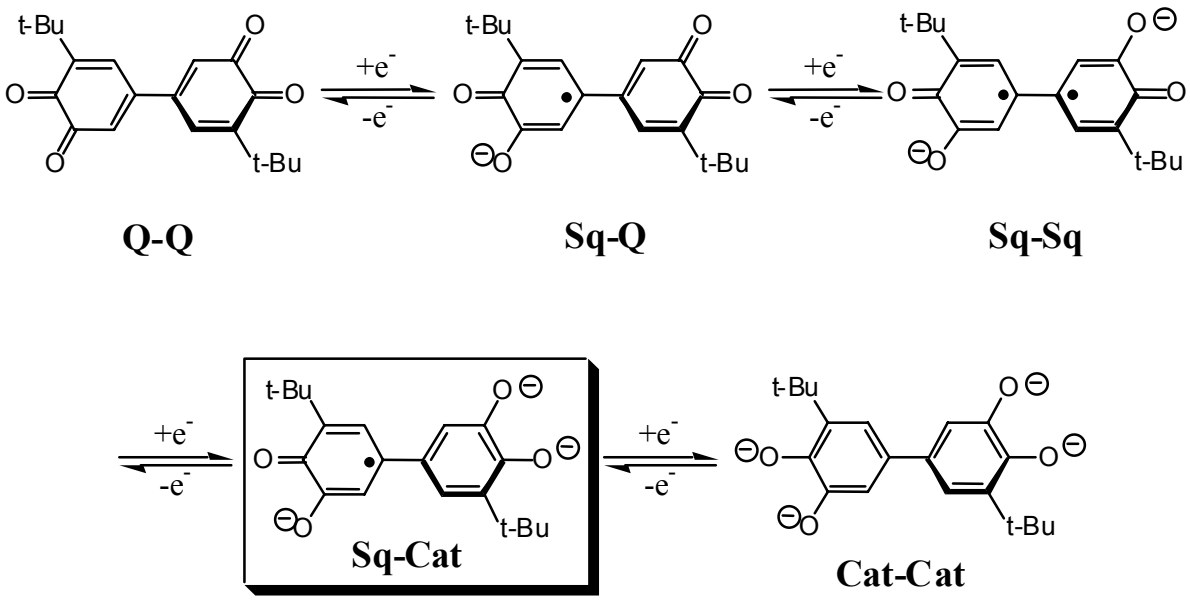

Figure 5.7 *Redox chain of bis dioxolene ligand. Species SQ-Cat, which may be considered as a mixed valent one, is evidenced.*

5.4 Dinuclear complexes of a delocalized radical bis-bidentate ligand: a combined spectroscopic and DFT study[52]

Since linked o-dioxolene ligands might behave differently according to different dihedral angles between the dioxolene planes we felt this subject worthy of an experimental and theoretical investigation. With this in mind, the ligand 5,5'-di-*tert*-butyl-3,3',4,4'-tetrahydroxy-biphenyl was synthesized, and used for preparing dinuclear cobalt(III) and chromium(III) metal complexes bridged by the paramagnetic SQ-Cat derivative, **(1)**. As the classification of mixed-valent systems is not always univocal from experimental data, it was decided to integrate the experimental characterization with quantum-chemical techniques, in the framework of the Density Functional Theory (DFT), to describe the electronic and magnetic structure of the free SQ-Cat ligand and of its complexes. Indeed, it has been recently found that quantum-chemical calculations are able to describe the ground state potential energy surfaces of a number of mixed-valent complexes and therefore they appear a valuable tool for the characterization of this class of compounds,[53-55]. Finally, since no

crystals suitable for X-ray analysis have been obtained, structure of the complexes were calculated by optimization of their geometries by using DFT calculations.

5.4.1 Experimental characterization

Complexes of formula $M_2(CTH)_2(Cat\text{-}Cat)(PF_6)_2$ (M = Co, Cr) were obtained as microcrystalline powders from the reaction between the $M(CTH)^{2+}$ cations and the Cat-Cat ligand in alkaline methanol under inert atmosphere, followed by oxidation of the metals with air and addition of an aqueous solution of KPF_6. These complexes can be formulated as Cr(III) and Co(III) derivatives on the basis of their magnetic properties and electronic spectra, which are closely related to those of the previously described mononuclear $M(CTH)(DBCat)PF_6$ metal complexes.[56,57] The chromium derivative is characterized by χT = 3.7 emu K mol^{-1} at room temperature, in agreement with the presence of two non interacting Cr(III) metal ions, whereas the cobalt complex is obviously diamagnetic. The spectrum of the chromium derivative showed a band at 15300 cm^{-1} (ε = 180) (*d-d* transition) with a shoulder at 26.000 cm^{-1}, whereas the cobalt compound shows transitions at 14500 (ε = 2100) and 23800 cm^{-1} (ε = 3150) (both LMCT in origin) with a shoulder at 19500 cm^{-1} (*d-d* transition). Therefore it was postulated that these complexes contain dinuclear cations in which the metal ions are bridged by the bis-bidentate tetranegative bis-catecholato ligand anion. The remaining coordination sites are occupied by the macrocyclic ligand that assumes a folded conformation.

Cyclic voltammetry experiments in 1,2-dichloroethane solutions of the chromium complex showed that it undergoes two sequential reversible redox processes at –0.38 and +0.12 V vs. ferricinium/ferrocene couple (Fc^+/Fc). Both of these processes involve a single electron, as supported by coulometry experiments, and are assigned to redox processes involving the tetraoxolene coordinated ligand. The more negative process is therefore assigned to SQ-Cat/Cat-Cat couple and the more positive to the SQ-SQ/SQ-Cat one. The observed values are consistent with those reported for a dinuclear Ru(II) complex formed by a similar bis(o-dioxolene) ligand.[43] The more positive values observed for the chromium derivative can be easily explained by considering the higher oxidation state of the metal ion with respect to that of the ruthenium complex.

The cyclic voltammogram of the cobalt complex is similar: two sequential one-electron, reversible waves at –0.47 and +0.02 V with respect to Fc^+/Fc, which can be assigned as in

the chromium complex. A further quasi-reversible redox process is observed at –1.25 V which, in analogy with the electrochemical behavior of mononuclear cobalt dioxolene complexes, can be attributed to the Co(III)/Co(II) couple.[57] It is worth mentioning that the difference between the two ligand-centered redox couples is the same in the two complexes (0.49 and 0.50 V, respectively) and its high value indicates a strong stabilization of the mixed-valence form of the tetroxolene ligand. From these data in fact the comproportionation constant for the equilibrium $[M_2(SQ\text{-}SQ)]^{2+} + [M_2(Cat\text{-}Cat)]^{4+} \rightleftharpoons 2\ [M_2(SQ\text{-}Cat)]^{3+}$ is ca. 10^8. It is therefore possible to isolate the mixed valence species without significant presence of the other species. Following this consideration, solid complexes of formula $M_2(CTH)_2(SQ\text{-}Cat)(PF_6)_3$ (M = Co, Cr) were prepared from the above described bis bis-catecholato complexes using ferricinium hexafluorophosphate as oxidizing reagent in dichloromethane and then precipitated as microcrystalline powders by addition of pentane.

The electronic spectrum of the cobalt derivative is rather similar to that of the chromium complex, thus indicating that the internal SQ-Cat ligand transitions involving the internal π and π^* levels strongly contribute to the spectra. However, the assignment of charge transfer transition bands is not straightforward. In terms of the usual mixed-valence approach, the pattern of bands appearing in the infrared region of the spectrum could be tentatively assigned to an intramolecular ligand-to-ligand-charge transfer in agreement with the assignment made by Lever et al. for a similar transition occurring in the spectrum of a dinuclear Ru(II) complex formed by a mixed-valence form of the bis(quinonediimine) ligand.[58] Following these authors, the existence of this transition shifting toward lower energies on increasing the donor power of the solvents (the absorption maximum shifts from 7200 cm^{-1} in dicloroethane to 6950 cm^{-1} in dimethylsulfoxide) could suggest a class II character to the present metal bridging SQ-Cat ligand. In order to understand the spectral properties a DFT investigation has been carried out, as it will be discussed below.

The electronic spectrum of the chromium derivative shows, in addition to the internal ligand transitions, a band at 20000 cm^{-1} which can be reasonably assigned to a MLCT transition, in analogy with the assignment made for mononuclear $Cr(CTH)SQ^{2+}$ chromophores.[57] The typical sharp transition around 14500 cm^{-1} characterizing all the reported mononuclear Cr(III)-semiquinonato derivatives is not observed, because of its overlapping with the internal ligand transitions.

The X-Band EPR spectra of the two $M_2(CTH)_2(SQ\text{-}Cat)(PF_6)_3$ (M = Cr, Co) complexes are shown in Figures 5.8a and 5.8b, respectively.

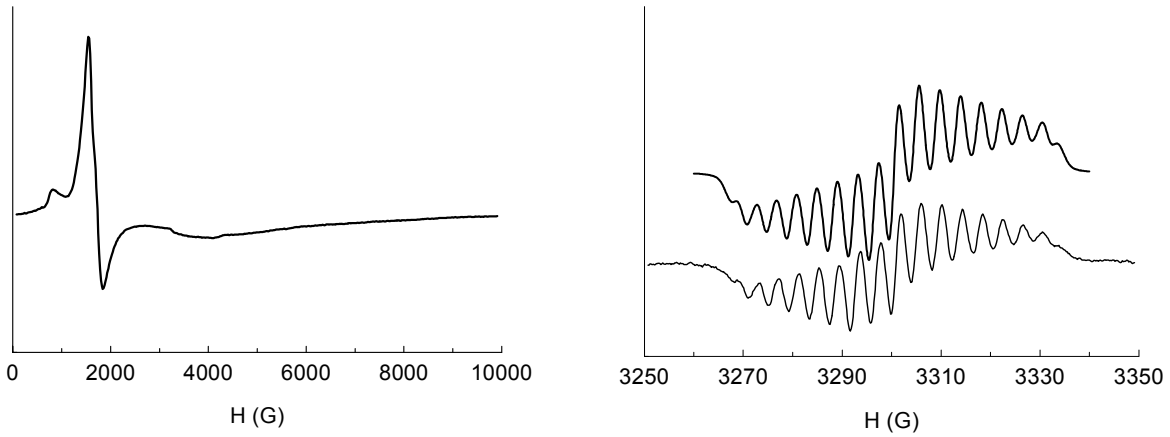

(a) (b)

Figure 5.8 *EPR spectra of $M_2(CTH)_2(Sq\text{-}Cat)(PF_6)_3$ (M=Cr, Co): a) the 4.2 polycrystalline powder spectrum of the Cr derivative; b) the fluid 1,2-dichloroethane solution spectrum of the Co(III) derivative (upper spectrum is simulated and lower is experimental).*

The 4.2 K polycrystalline powder spectrum of the chromium derivative (Figure 5.8a) shows three transitions at 850 G, 1450 G, and 1550 G, the last one being a shoulder of the second. These spectral features compare well with what reported in the literature for an S = 5/2 spin system split by a large Zero Field Splitting (D > 1 cm^{-1}) and almost complete rhombicity (E/D ~ 0.3).[59] The ESR solution spectrum of the cobalt complex (Figure 5.8b) shows 17 lines almost equivalently spaced. We attributed this spectral appearance to the hyperfine coupling of the completely delocalized unpaired electron of $SQCat^{3-}$ with two equivalent ^{59}Co (I_{Co}=7/2) nuclei and with two equivalent ^{1}H nuclei (I=1/2). The expected 45 lines, $(2n_HI_H+1)(2n_{Co}I_{Co}+1)$, collapse to 17 due to a linewidth which is comparable with the hyperfine coupling constant of the electronic spin with the two equivalent protons. The simulation of the spectrum was performed using WIN-EPR SimFonia, a program based on a second-order perturbative solution of the Spin Hamiltonian.[60] The simulated spectrum, plotted in Figure 5.8b (top), was computed with a hyperfine coupling constant for ^{59}Co, a_{Co} = 4.20 G and for ^{1}H, a_H = 2.60 G using a Gaussian line shape with linewidth of 2.70 G and g_{iso} = 2.0. These results have to be compared with what obserevd for a mononuclear Co(III)-DTBSQ adduct, for which the hyperfine coupling constant for ^{59}Co was found to be 9.50 G and that for ^{1}H, a_H = 2.00 G.[57] The value of the hyperfine coupling constant to ^{59}Co is

then in good agreement with what expected, if one considers that in this case the unpaired electron spends only half of its time on each Co(III) center, and then a value of a_{Co}=9.50 G/2=4.75 G was expected, whereas the observed coupling to the proton is much larger is in this case.

The temperature dependence of the magnetic susceptibility of the chromium complex is shown in Figure 5.9. The solid line represent the fitting of the magnetic data using the three center exchange spin Hamiltonian:

$$\mathbf{H} = J(\mathbf{S}_1 \cdot \mathbf{S}_2 + \mathbf{S}_2 \cdot \mathbf{S}_3) + J'\mathbf{S}_1 \cdot \mathbf{S}_3 \qquad (5.4.1)$$

where $\mathbf{S}_1$ and $\mathbf{S}_3$ are the spin operators of the Chromium(III) centers, S_1=S_3= 3/2, and $\mathbf{S}_2$ is the spin of the unpaired electron of the radical ligand. The data were fit by minimizing the sum of the squares of the deviation of the computed χT values from the experimental values, $\sum(\chi_o - \chi_c)^2 T$, using a Simplex minimization procedure. It is worth mentioning here that the use of a sizeable J' i.e. of an interaction between the Cr(III) centers proved to be necessary to obtain a reliable fit of the curve. The parameters used in the fit, besides J and J' of Equation (5.4.1), were the effective isotropic g value and J_{int}, i.e. the effective intermolecular exchange coupling parameter, which accounts for the observed decrease of χT at low temperature. It should be noted that in principle the decrease observed at low temperature may be due also to Zero Field Splitting of the ground state, and both the effects are considered by using the Weiss molecular field approximation using the equation:[61]

$$\chi_c = \frac{\chi}{1 - \left(J_{\text{int}} / N g^2 \mu_B^2 \right) \chi} \qquad (5.4.2)$$

here χ is the molar susceptibility computed in the absence of the interaction and $J_{int} = zj$ is the effective exchange interaction z being the number of nearest neighbors coupled by the j coupling constant. The best fit curve to the experimental data was obtained with the following parameters g = 1.97(3), J = 743(3) cm^{-1}, J'/J = 0.12(2), J_{int} = -0.14(6) cm^{-1}. It should however be stressed that given the rather large correlation between the parameters the range of values for which the fit is satisfactory is quite large. Almost equivalent fits can indeed be obtained for the following range of values: g = 1.975±0.01, J_{int} = -0.14 ± 0.01, 500 cm^{-1} < J < 800 cm^{-1}, 0.126 < J'/J < 0.096.

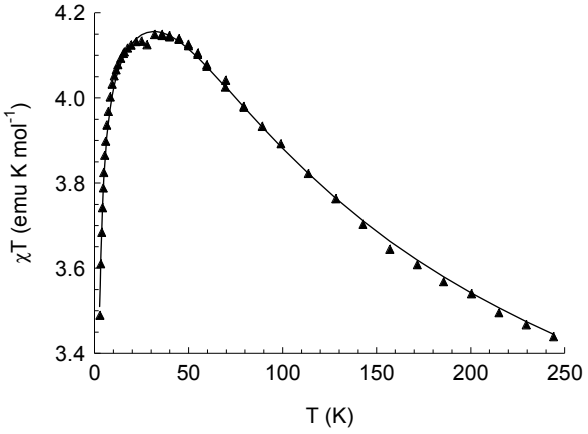

Figure 5.9 *Temperature dependence of the magnetic susceptibility of $Cr_2(CTH)_2(Sq\text{-}Cat)(PF_6)_3$. Solid line represent the best fit described in the text.*

It can be however concluded that the two equivalent Cr(III) paramagnetic centers are strongly antiferromagnetically coupled to the bridging radical ligand, in a similar way to that previously reported for the $Cr_2(CTH)_2(DHBQ)Y_3$ complexes.[62] This gives rise to a sextet ground state and - within all the range of variation – the first excited state is a quartet and the second one is a doublet, lying 100 ± 11 cm^{-1} and 275 ± 15 cm^{-1} above the ground state respectively.

5.4.2 Overview of results of DFT calculations

The calculations presented in this paragraph have been performed by Prof. A. Bencini in collaboration with the group of Prof. C. A. Daul at the University of Freibourg. For further details concerning this part of the characterization see ref. [52].

a-Electronic and Geometrical Structure of the Ligand Radical SQ-Cat^{3-}

The calculated optimized geometry of a model radical SQ-Cat^{3-} showed that the two aromatic rings are not co-planar, their optimized dihedral angle, τ, being 9° (Figure 5.10). The total energy of SQ-Cat was found to significantly depend on the τ angle, and two nearly degenerate minima in the energy profiles were computed for τ = 9° and 167° at which electronic structure and calculated properties were very close each other. The interconversion energy barrier between the two minima was calculated to be of 7.8 kcal/mol which should be high enough to prevent a fluctional behavior of the radical in solution. The calculated SOMO is a linear combination of mainly p_z orbitals of carbon and oxygen, while

the LUMO region is formed by two accidentally degenerate antibonding orbitals, one mainly localized on the methyl groups, and the other having π^* character.

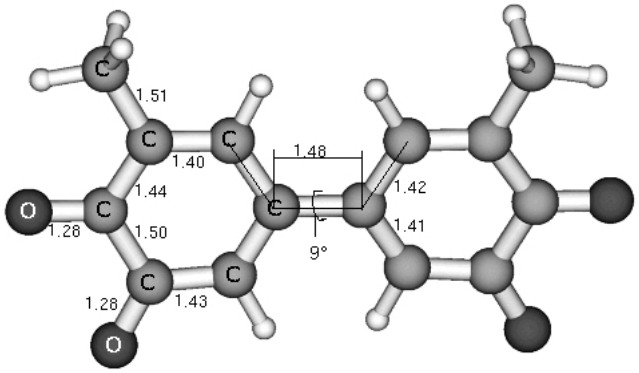

Figure 5.10 *The optimized structure of the model radical Sq-Cat^{3-} with relevant geometrical parameters*

The ^{1}H and ^{13}C-hyperfine coupling constants (Hfcc) were computed using non-relativistic unrestricted calculations and Gaussian98 for sake of comparison. As usually found in cathecholate radicals,[63,64] the largest ^{1}H-hyperfine coupling constant is computed on the proton in ortho to the methyl group. Furthermore, spin polarization effects is evident due to the negative densities computed on some carbon and hydrogen atoms, but, since these values are rather small, spin polarization should not have much relevance in the spin delocalization mechanism.

b-Electronic and Geometrical Structure of $[Co(NH_3)_4(SQ\text{-}Cat)Co(NH_3)_4]^{3+}$

The optimized geometry of the model complex $[Co(NH_3)_4(SQ\text{-}Cat)Co(NH_3)_4]^{3+}$ is shown in Figure 5.11 where relevant geometrical parameters are also indicated. The two dioxolene rings are significantly non-coplanar, their dihedral angle τ being 47°. The average value of the Co-O bond distance (1.88 Å) is intermediate between the values observed in Co(III)-semiquinonato and Co(III)-catecholato complexes,[3,18] 1.90 Å and 1.87 Å, respectively, in agreement with the delocalized nature of the unpaired electron. Also the average C-O and the C-C distances (1.34 Å and 1.42 Å) are close to the average of the values observed in semiquinonato and catecholato complexes, i.e. 1.90 Å and 1.87 Å for C-O and 1.45 Å and 1.40 Å for C-C, respectively.[18] The cobalt ion is in a cis-distorted octahedral coordination with a N_2O_2 basal plane. The unpaired electron is delocalized in the

SOMO orbital, which is close to the SOMO of the free ligand with a small anti-bonding contribution from out-of-plane π-3d orbitals of the metals. This metallic contribution to the SOMO was evidenced in the ESR spectrum of the complex in the fluid solution.

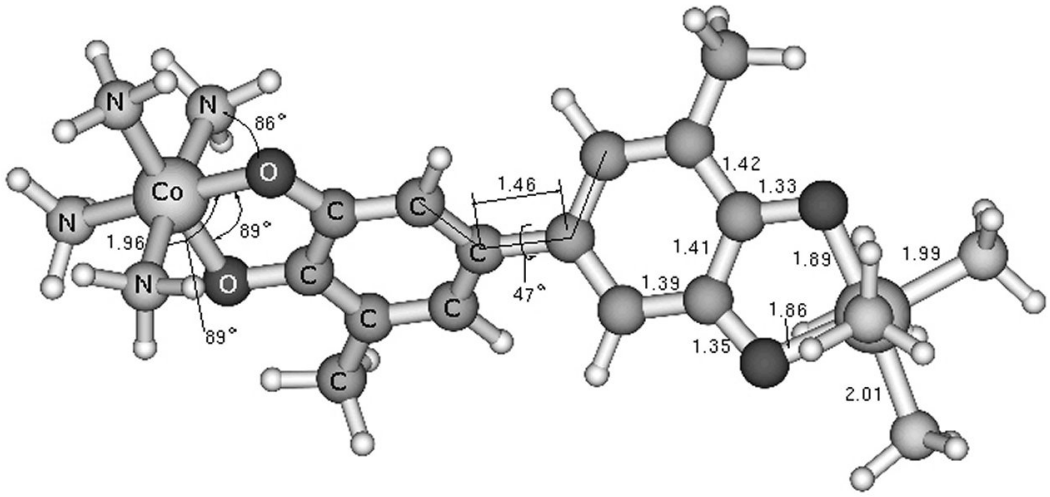

Figure 5.11 *The optimized geometrical structure of the model complex* $[Co(NH_3)_4(Sq\text{-}Cat)Co(NH_3)_4]^{3+}$ *with relevant geometrical parameters.*

It should be stressed that the ring linking C-C bond is calculated to be significantly shorter (1.46 Å) than expected for a single bond. This result is in good agreement with what has been observed by Pierpont et al. for a SQ-SQ derivative, where the corresponding bond has been found to be slightly shorter than ususally observed for biphenyl (1.49 Å) but considerably longer than the double-bond value that would be expected for strong conjugation between radical rings.[42]

Electron paramagnetic resonance parameters can be computed within the Zero Order Regular Approximation[65] (ZORA) for relativistic effects when the ground state is a Kramers doublet. Using this approach both the **g** and the **A** tensors can be computed. The principal *g* values, which have to be computed using a spin restricted calculations are: g_{xx} = 2.004, g_{yy} = 2.003 and g_{zz} = 2.01 which gives the average value g_{iso} = 2.006, in agreement with the small contribution of the metal orbitals to the SOMO. In order to include spin polarization of the inner core *s* orbitals all electron spin unrestricted calculations were performed using both scalar relativistic ZORA and non relativistic hamiltonians. The computed values were $a_{iso}(^{59}Co)$ = 2.12 and 1.89 Gauss respectively. The computed hyperfine coupling with the ^{1}H nuclei in ortho with respect to the methyl groups were,

respectively, $a_{iso}(^1H)$ = 2.12 and 2.13 Gauss. The calculations agree with the experimental observation of a sizeable proton hyperfine coupling but the hyperfine coupling with the cobalt nucleus is largely underestimated.

c- Electronic, Geometrical and Magnetic Structure of $[Cr(NH_3)_4(SQ\text{-}Cat)Cr(NH_3)_4]^{3+}$

This model complex possesses several spin states arising from the magnetic coupling between the spin of the Cr(III) ions (S_{Cr} = 3/2) with the unpaired electron of the SQ-Cat^{3-} radical ligand. The high spin state of the complex has the total spin S = 7/2 and it is representable by a single Slater determinant. On this state we have performed the geometry optimization of the model complex. The calculated molecular structure (Figure 5.12) is close to that of the Co(III) complex except for the angle τ which is now 38° and the Cr-N bond distances which are longer, as expected in Cr(III) complexes.

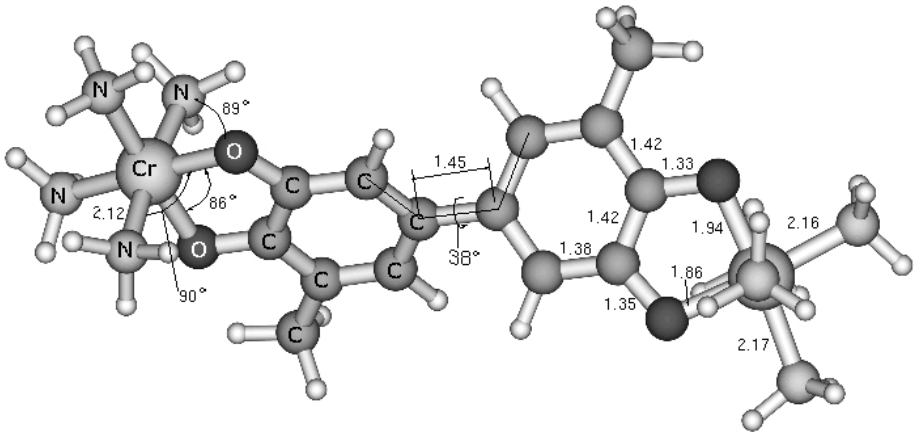

***Figure 5.12**. The geometrical structure of the model complex $[Cr(NH_3)_4(Sq\text{-}Cat)Cr(NH_3)_4]^{3+}$ optimized with relvant geometrical parameters.*

The calculation of the multiplet structure of $[Cr(NH_3)_4(SQ\text{-}Cat)Cr(NH_3)_4]^{3+}$ can be performed using the Broken Symmetry approach (BS) which has been widely applied in the last years.[55,66] This approach is based on a one-to-one correspondence between the SCF energies of appropriate single determinants representing eigenstates of S_z, and the diagonal elements of the spin Hamiltonian (5.4.1) in a basis set of products of single center spin functions. The total spin states arising from the magnetic interaction can be labeled using the eigenvalue of the intermediate spin operator $\mathbf{S}_{13}^2=(\mathbf{S}_1+\mathbf{S}_3)^2$ and of the total spin $\mathbf{S}^2=(\mathbf{S}_{13}+\mathbf{S}_2)^2$ and $\mathbf{S}_z$, i.e. with kets $|S_{13}\, S\, M_S>$. In the product basis of the three spin function

$\{|m_1 m_2> m_3>\} \equiv \{|s_1\ m_1>|s_2\ m_2>|s_3\ m_3>\}$ we can write the spin eigenfunction corresponding to the high spin state S = 7/2 and M_S = 7/2, namely |3 7/2 7/2> = |3/2 1/2 3/2> and to the antiparallel spin state, corresponding to M_s = 5/2, namely |5/2> = |3/2 -1/2 3/2>. This last wavefunction is not eigenfunction of $\mathbf{S}^2$, but only of $\mathbf{S}_z$, and it can be also called the antiferromagnetic, AF, state. These two spin arrangements can be associated to two single Slater determinants called the high spin state and the Broken Symmetry state, BS_1. Since single determinants cannot, in the general case, represent spin eigenfunction and hence their energies are not the energies of the spin multiplets, their energies were associated in a first approach to the diagonal elements of **H**, or, alternatively, spin projection techniques and decomposition of these energies in terms of pure multiplet energies are applied. A second rather widely used approach assumes that the largest part of the electron correlation, both static and dynamic, is accounted for by the functional of the electron density and associate these energies to the pure state energies obtained from the diagonalization of the spin Hamiltonian (5.4.1).[67,68] With this last approach a better agreement with the experimental data is generally achieved, although it has been recently found that the modeling of the real system can be crucial in judging the agreement between spin Hamiltonian parameters calculated on model complexes and the experimental data. Both approaches have been followed, the relevant equations for the first and second one being (5.4.3-4) and (5.4.5-6), respectively.

Using the energy of the single determinants, $E(HS)$ and $E(BS_1)$, obtained by independent SCF convergences we can calculate the J value, in the first approach, according to:

$$E(HS) - E(BS_1) = 3J \tag{5.4.3}$$

The calculation of J' requires the evaluation of the energy of another determinant which can be easily set up by the spin configuration |3/2 1/2 -3/2>. This is an eigenstate of $\mathbf{S}_z$ with eigenvalue 1/2 and will be indicated as BS_2. The relevant equation is:

$$E(HS) - E(BS_2) = \frac{3}{2}J + \frac{9}{2}J' \tag{5.4.4}$$

The equation relevant for the calculation of J assuming that the single determinant energies are close to the multiplet energies, i.e. using the second approach, are:

$$E(HS) - E(S_{13} = 3, S = \frac{5}{2}) = \frac{7}{2}J \quad (5.4.5)$$

$$E(HS) - E(S_{13} = 0, S = \frac{1}{2}) = \frac{3}{2}J + 6J' \quad (5.4.6)$$

Spin Hamiltonian parameters obtained by equation (5.4.3-4) and (5.4.5-6) represent limiting values, the exact values being in between these two extremes. The computed values of J for $[Cr(NH_3)_4(SQ\text{-}Cat)Cr(NH_3)_4]^{3+}$ are J = 590 cm^{-1}, J' = 11.4 cm^{-1} and J = 506 cm^{-1}, J' = 29.6 cm^{-1}, using equations (5.4.2-3) and (5.4.4-5) respectively. With both set of parameters the ground spin multiplet is |3 5/2> with next excited states |2 3/2> and the |1 1/2> at 261 cm^{-1} and 534 cm^{-1}, and at 164 cm^{-1} and 360 cm^{-1}, respectively. These findings are in nice qualitative agreement with the results of the fitting of the magnetic susceptibility data, which gave the |3 5/2> state as the ground state with the |2 3/2> and the |1 1/2> states at 98 cm^{-1} and 285 cm^{-1}, respectively.

5.5 Magnetic properties of complexes containing a Biradical semiquinonate ligand

Following the strategy outlined in paragraph 5.3 to synthesize high spin ligands the synthesis of *m*-xylylene-type ligand 1,3-bis(3',4'-dihydroxy-5'-*tert*-butylphenyl)-5-*tert*-butylbenzene (*m*-Ph($CatH_2$)$_2$, **(2),** see Scheme 5.2) has been reported and indeed EPR experiments suggest that the dianionic bis(semiquinone), *m*-Ph(SQ)$_2$, is a triplet ground state.[69]

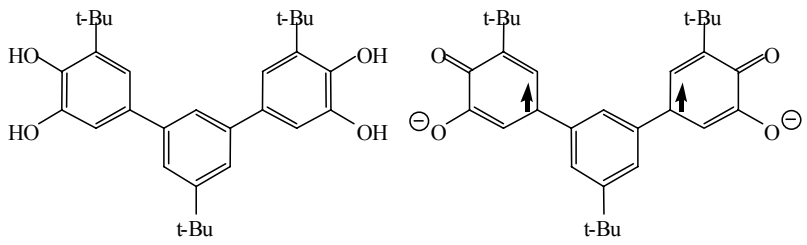

m-Ph($CatH_2$)$_2$, **(2)** *m*-Ph(SQ)$_2$

Scheme 5.2

According to the considerations about magnetic coupling in metal-semiquinone complexes outilined in paragraph 5.2, in the past it has been shown that Ni(CTH)(DBSQ)Y (CTH = dl-5,7,7,12,14,14-hexamethyl-1,4,8,11-tetraazacyclotetradecane, DBSQ = 3,5-di-*tert*-butylsemiquinone, Y = ClO_4, PF_6) and Cu(Me_3[12]N_3)(DBSQ)Y (Me_3[12]N_3 = 2,4,4-trimethyl-1,5,9-triazacyclododec-1-ene) complexes are characterized by quartet and triplet ground-states, respectively, arising from the ferromagnetic coupling of the metal ions with the radical ligand. [56,70,71] In a similar fashion, the Cr(CTH)(DBSQ)Y_2 complex was shown to be a triplet ground state, arising from the antiferromagnetic coupling of the two magnetic centers.[72]

On the basis of these results the corresponding dinuclear Ni(II), Cr (III), and Cu(II) complexes using the above bis(semiquinone) ligand were then prepared with the aim of exploring the possibility of obtaining complexes characterized by septet, quintet, and quintet electronic states, respectively.

The reactions of **(2)** with basic solutions containing the above nickel and copper macrocycle acceptors under inert atmosphere were followed by aerial oxidation. This procedure yielded solutions containing the $[Ni_2(CTH)_2(m\text{-}Ph(SQ)_2]^{2+}$ and $[Cu_2(Me_3[12]N_3)_2(m\text{-}Ph(SQ)_2]^{2+}$ complexes which in turn were precipitated as the hexafluorophosphate salts. The same procedure using Cr(II)-CTH lead to the isolation of $Cr_2(CTH)_2(m\text{-}Ph(Cat)_2(PF_6)_2$, which was converted to the bis(semiquinone) derivative $[Cr_2(CTH)_2(m\text{-}Ph(SQ)_2](PF_6)_4 \cdot 2H_2O$ by treatment with Ce(IV). All attempts at obtaining crystals suitable for structural analysis were unsuccessful. However, the bis(semiquinone) character of the ligand in the isolated complexes is clearly supported by the magnetic, electrochemical and spectral properties of the three isolated complexes, as it will be discussed below. Therefore it is postulated that these complexes contain dinuclear cations in which the metal ions are bridged by the bis-bidentate m-Ph$(SQ)_2$ ligand. The remaining coordination sites are occupied by the macrocyclic ligand that assumes a folded conformation.

5.5.1 Electronic properties

The electronic spectra of acetonitrile solutions of the three isolated bis (semiquinone) derivatives are shown in Figure 5.13. Their features are strictly similar to those observed for the mononuclear DBSQ analogues.[56,70-72] The absorptions appearing in the near-UV region and in the red region of the electronic spectra can be assigned to π-π* and *n*-π*

internal transitions of the semiquinone ligand, respectively. The other bands appearing in the spectra can be reasonably attributed to metal-to-ligand charge transfer transitions.

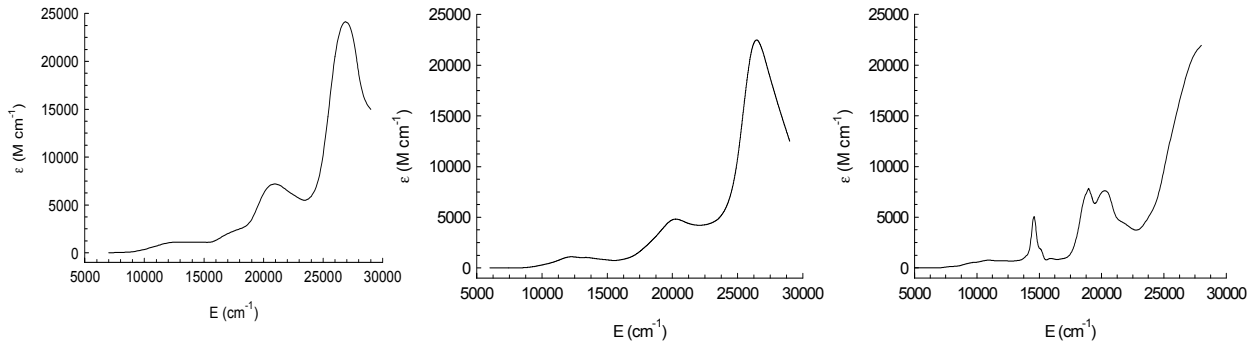

Figure 5.13 *Room temperature electronic spectra of acetonitrile solution of Cr(III) derivative (left), Ni(II) derivative (center) and Cu(II) derivative (right)*

The cyclic voltammogram of a de-aerated acetonitrile solution of the nickel complex shows that it undergoes two sequential one-electron reversible redox processes at –0.73 and –0.64 V and one irreversible couple at ca. +0.2 V vs. ferrocinium/ferrocene couple (Fc^+/Fc). The copper derivative shows similar behavior with two reversible couples at –0.44 V and –0.35 V, and one irreversible couple at ca. +0.1 V vs. Fc^+/Fc. Similar considerations hold for the chromium complex which shows two reversible redox processes at –0.17 and –0.07 V vs. Fc^+/Fc and an irreversible couple at +0.7 V. Following the observed electrochemical properties of the mononuclear DBSQ derivatives,[56,71,72] it is reasonable to attribute the reversible processes to the semiquinone-catecholate (SQ-Cat) couples and the irreversible ones to the semiquinone-quinone (SQ-Q) redox processes.

As previously suggested,[71] the irreversible character of the latter couples can be ascribed to the instability of the metal(II)-Q adducts. The more positive values observed for the chromium derivative can be easily explained by considering the higher oxidation state of the metal ion with respect to the other divalent metal complexes. Furthermore, the difference observed for the ligand centered redox processes associated with the SQ-Cat couples for the Cu(II) and Ni(II) complexes can be explained taking into account the different coordination numbers of the two metal complexes. A stronger metal-ligand interaction is expected to occur in five-coordinate complexes with respect to six-coordinate ones with stabilization of the catecholate ligand.

Finally, it should be stressed that, according to the ca. 90 mV difference observed for the SQ-Cat couples, the comproportionation constant for the equilibrium: $[M_2(m\text{-}Ph(SQ)_2]^{2+}$ + $M_2(m\text{-}Ph(Cat)_2)$ $\rightleftharpoons$ $2[M_2(m\text{-}Ph(SQ)(Cat)]^{+}$ is ca. 33. Even though there is some stabilization of the mixed-valent form, it is not possible to investigate this species without significant presence of the two reactants.

5.5.2 Magnetic properties

The temperature dependence of the magnetic susceptibilities of the three derivatives is shown in Figure 5.14. According to the postulated structure, we fit the experimental magnetic properties with the exchange hamiltonian $\mathbf{H} = J_1(\mathbf{S}_1\mathbf{S}_2 + \mathbf{S}_3\mathbf{S}_4) + J_2(\mathbf{S}_2\mathbf{S}_3)$, where J_1 and J_2 are the exchange coupling constants depicted in Scheme 5.3:

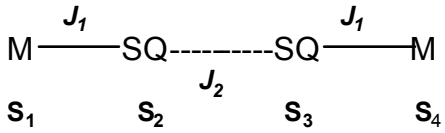

Scheme 5.3

The decreasing of χT values occurring in the low temperature region for all the complexes was simulated using a Weiss correction for the magnetic susceptibility.[61] The equation used for the correction is $\chi_{eff} = \chi/(1-\theta\chi)$, with $\theta = -2zJ_{inter}/Ng^2\beta^2$. It should be stressed here that this is a simple phenomenological approach, and that the same behavior may be caused by the different population of the M_s states due to zero-field splitting and saturation effects.

The temperature dependence of the magnetic susceptibility of $[Ni_2(CTH)_2(m\text{-}Ph(SQ)_2](PF_6)_2$ in the range 4 – 150 K is shown in Figure 5.14, top. The χT vs. T curve is essentially flat in the range 100 – 150 K, the value being 4.9 emu K mol^{-1}, and increases on decreasing temperature, reaching a value of 6.2 emu K mol^{-1} at 11 K and 1.0 Tesla. This behavior is consistent with an incompletely populated septet electronic ground state ($S = 3$) arising from the ferromagnetic coupling of the four magnetic centers characterizing the complex. We wish to point out that the mononuclear $[Ni(CTH)(DBSQ)](PF_6)$ complex shows a χT value of 2.28 emu K mol^{-1} in the temperature range 4 – 300 K, as a result of a strong ferromagnetic interaction between the paramagnetic metal ion and the semiquinone

radical ligand. Thus, a value equal to 4.5 – 4.6 emu K mol^{-1} (2 x 2.28 emu K mol^{-1}) was expected for the present dinuclear derivative if the two paramagnetic Ni(II)-SQ moieties were uncorrelated. The observed experimental behavior, therefore, suggests that a further magnetic interaction occurs leading to a ferromagnetic interaction among the four magnetic centers, and leads to a septet electronic ground state. Following the guidelines discussed above, the experimental data were fitted[73] within the assumption of isotropic coupling and including a weak intermolecular interaction, θ, yielding g = 2.22, J_1 < - 400 cm^{-1}, J_2 = -27 cm^{-1}, and θ = -0.33 K. It should be noted that with these parameters, the S=2 state is lying only 9 cm^{-1} above the ground state and one S=1 and S=0 are lying only within 18 cm^{-1}. The low experimental value of the χT product can then be attributed to the uncompleted population of the ground spin state.

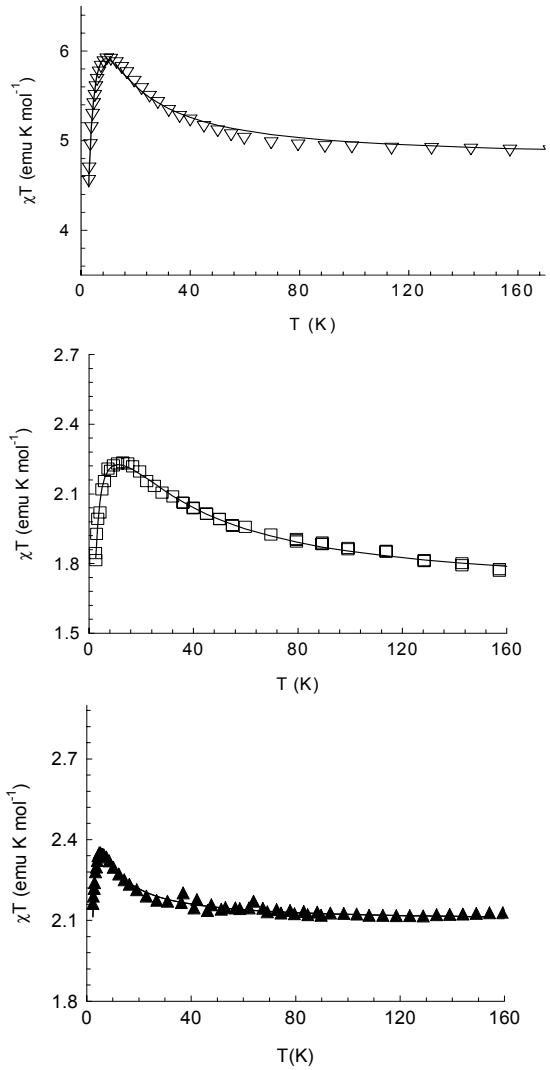

Figure 5.14 *Temperature dependence of χT for Ni(II) derivative (top), Cu(II) derivative (center), Cr(III) derivative (bottom) and best fit curves obtained with the parameters reported in the text.*

To rule out any other possibility we performed *M* vs. *H* measurement at low *T* (figure 5.15). At high field the magnetization is almost completely saturated, showing a value of 6.5 μ_B at 7 T and 2.1 K. This is in nice agreement with the expected saturation value of 6.6 μ_B for an *S*=3 with *g*=2.2. The magnetization curve was satisfactorily reproduced by considering the relative populations of the ground and first excited states and a *D* value of 0.6 cm^{-1} for the ground state.

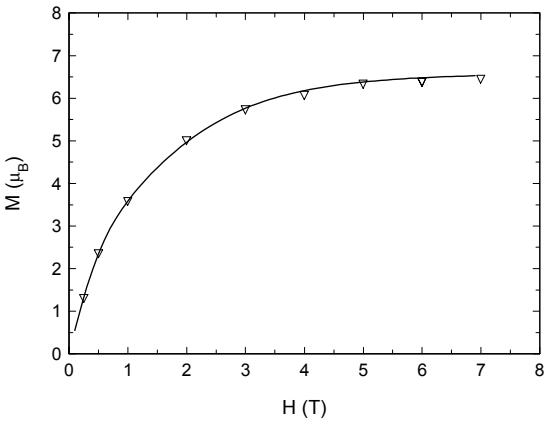

Figure 5.15 *M vs. H measurement for the Nickel derivative at 2.1 K. The line is the theoretical curve obtained with the parameters reported in the text.*

The temperature dependence of the magnetic susceptibility of copper derivative is shown in Figure 5.14, center. The χT vs. T curve increases on decreasing temperature reaching a maximum at 13 K. Fitting of the data using the above four-spin Hamiltonian yields best fit values of g = 2.106, J_1 = -34.7 cm^{-1}, J_2 = -6.3 cm^{-1}, and θ = -0.55 K, thus indicating a quintet electronic ground state with lower multiplicity levels which are still significantly populated at low T. As in the Ni(II) case this result arises from the ferromagnetic coupling of the four magnetic centers in the molecule.

Finally, the magnetic properties of the chromium derivative (Figure 5.14, bottom) can be interpreted by assuming again a quintet ground-state of the molecule. The best-fit parameters were g = 1.99, J_1 > 400 cm^{-1}, J_2 = -32 cm^{-1}, and θ = -0.25 K. As expected,[2,3,56] a strong antiferromagnetic coupling characterizes the Cr(III)-SQ interaction, whereas the two SQ halves experience a weaker ferromagnetic interaction similar to the one observed in the Ni(II) complex.

It should be pointed out that for the nickel and chromium complexes the J_1-values are the same as the corresponding values observed for mononuclear metal-semiquinone analogues. The J_1-value observed for the copper complex is rather low when compared with

the value of +104 cm^{-1} observed for the mononuclear Cu(DBSQ) analogue. This is most likely due either to poorer metal-semiquinone overlap, or to the fact that the orthogonality between the magnetic orbitals of the paramagnetic centers is less rigorously maintained in this dinuclear complex.

The intraligand exchange coupling in *m*-$Ph(SQ)_2$ is ferromagnetic, in agreement with the connectivity of the spin coupler. Considering the spin densities of the semiquinone group,[74] and the exchange parameter for *meta*-xylylene,[75] the expected $J_{SQ\text{-}SQ}$ (J_2) value should be larger than those derived from the χT plots here presented. Based on the precedent for *J*-modulation due to bond torsions in organic biradicals,[76] we propose that torsions between SQ and meta-phenylene units in *m*-$Ph(SQ)_2$ could be responsible for the small ferromagnetic *J*-values. If this hypothesis holds, this mechanism seems particularly efficient for offering an explanation of the small J_2 value observed for the copper complex.

This finding is in agreement with the recently reported investigation on dioxolene bridged dimolybdenum(V) derivatives.[77] These calculations confirm the role of the dihedral angle between the planes of the SQ rings in determining the value of the ferromagnetic coupling constant.[76] In agreement with these calculations it can be suggested that also in the present case the ferromagnetic coupling characterizing the *m*-$Ph(SQ)_2$ ligand results essentially from a spin polarization mechanism.

5.6 Induction of thermal hysteresis in valence tautomerism by using a bis-bidentate dioxolene ligand[78]

Following the simple considerations outlined in paragraph 5.2 for the design of systems showing thermal hysteresis of valence tautomeric interconversion we thought that efforts of the research must be focused towards the design of molecular assemblies with metal centers mutually interacting through a polymeric structure. Bearing this in mind, we have synthesized a 1,10-phenanthroline-cobalt adduct of the above described dioxolene ligand 3,5-bis(3',4'-dihydroxy-5'-*tert*-butyl-phenyl)-1-*tert*-butyl-benzene, **(2)**.[69]

As we have seen in paragraph 5.5 this molecule may act as bis-bidentate ligand towards two different metal ions. Moreover, once coordinated it may originate by one electron oxidation the trinegative radical anion we indicate as SQ-Cat, which, although not physically characterized, can be expected to behave as a class III mixed valence radical

ligand, according to the results discussed in paragraph 5.4 concerning the simpler ligand **(1)**. A further one electron oxidation leads to the diradical SQ-SQ species, which according to its topological properties, is characterized by a triplet electronic ground state. We have already discussed in paragraph 5.5 how the topology of this ligand may enforce the achievement of high multiplicity ground-states when the SQ-SQ is coordinated to two paramagnetic metal ions.[79]

The reaction of Cobalt(II) chloride, 1,10 phenanthroline and L in 1:1:1 ratio in ethanol-dichloromethane 1:2 mixture (v/v) in the presence of a stoichiometric amount of triethylamine (4:1) affords a black green powder (30% yield) of analytical formula $Co(phen)L\cdot 1/2CH_2Cl_2$. This compound, **(3)**, is insoluble in common organic solvents. It is reasonable to believe that this compound contains six-coordinated cobalt ions like all the $Co(N\text{-}N)(diox)_2$ (N-N = diazine ligand, diox = catecholate or semiquinone) previously described.[3,32] The main difference between this compound and previous ones is the fact that each dioxolene ligand is paramagnetic and coordinated to two different cobalt ions, thus giving rise to a polymeric structure.

The temperature dependent magnetic behavior of this compound is shown in Figure 5.16. The observed magnetic behavior is consistent with the presence of a Cobalt(III)-catecholato-semiquinonato dominant species at low temperature undergoing a thermally-induced valence tautomeric transition to a high spin cobalt(II)-bis(semiquinonato) one according to the equilibrium:

$$[(Co^{III}/2)SQ\text{-}Cat(Co^{III}/2)]_n \rightarrow [(Co^{II}/2)SQ\text{-}SQ(Co^{II}/2)]_n \qquad (5.6.1)$$

At 310 K, the highest temperature value we measured, it can be estimated from χT value that both tautomers are present in equal concentration: indeed, the expected χT value for a Co(II) center and two SQ units would be about 3.3 emu K mol^{-1}.[80] Using the nomenclature currently used for spin-crossover systems, the transition can be classified as gradual; nevertheless a thermal hysteresis width of about 12 K is observed (see Figure 5.17), though the optimum conditions for observing this phenomenon, i.e. the full conversion to *hs*Co(II), are not reached. This result was obtained in three independent measurements repeated on the same sample, using 30 minutes for each point to ensure sample thermal equilibration. These experimental data, therefore, suggest the existence of a strong cooperativity between the magnetic centers. A comprehensive analysis of magnetic data is

not straightforward due to the high complexity of the different magnetic interactions occurring in the present system and the orbital degeneracy of octahedral Co(II). Moreover the χT value characterizing the Co(II)-bis(semiquinonato) species is unknown.

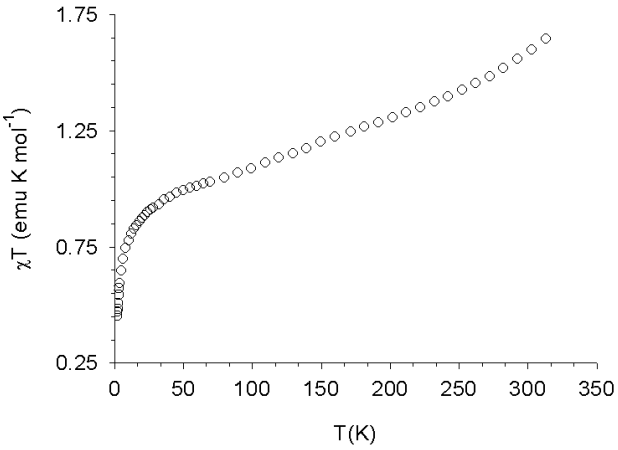

Figure 5.16 *χT values vs. T for compound* ***(3)*** *reported for a single Co center It is evident the gradual transition due to a valence tautomeric process occurring above 50 K.*

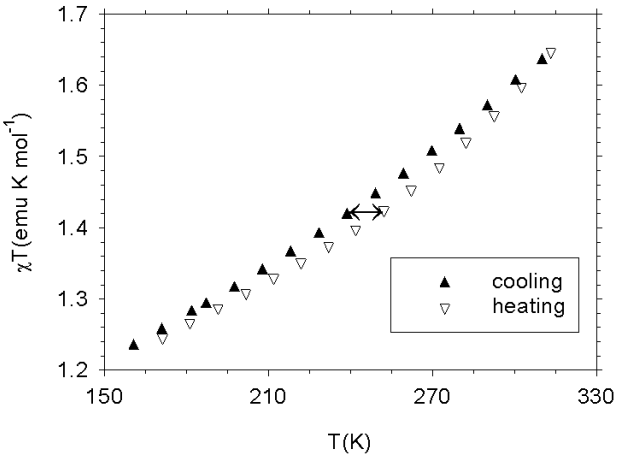

Figure 5.17 *The figure shows the difference in the measured χT when heating (empty triangles) and cooling (full triangles) sample of* ***(3)****, respectively. The arrow evidences the maximum width of thermal hysteresis, about 12 K at 250 K*

Powder ESR spectrum (see Figure 5.18) recorded at 4 K shows a broad transition at 1530 G (g=4.3) and a sharper one at 3300 G (g=2). The transition at g = 2 can be assigned to a Co(III)-SQ species and is detected also at room temperature, whereas the transition at g=4.3 seems to be due to the presence of a Co(II)-SQ or Co Co(II)-$(SQ)_2$. This assignment

is supported by the fact that these absorptions disappear as the temperature rises to 40 K (Figure 5.18 inset), which is a typical behavior for Co(II) species. Detection of the g=2 signal at room temperature deserves some reflections since under fast interconversion between the Co(III) and Co(II) centers, this transition should not be detected on the ESR time scale.

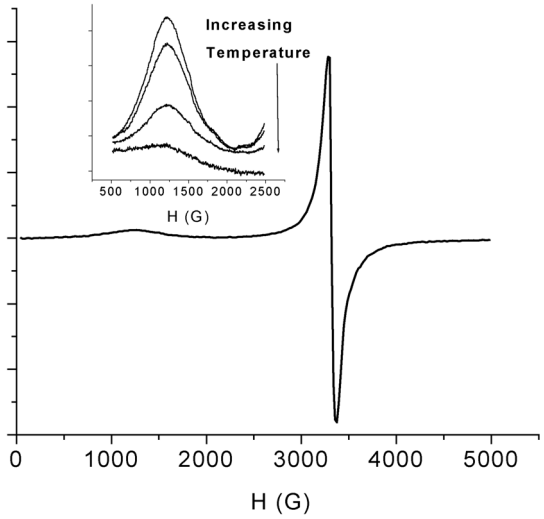

Figure 5.18 *EPR spectrum of* ***(3)*** *at 4 K. The inset shows the temperature evolution of the low-field transition at 4 K, 10 K, 20 K and 40 K, respectively.*

The most important finding of the present experimental results is the strong cooperativity shown by the compound, a property that we were looking for in designing this peculiar molecular system. We feel that the observed properties can be easily manipulated by changing the dioxolene substituents, the diazine acceptors as well the crystallization solvent, in agreement with the suggestions of the previous work concerning the more simple molecular $Co(NN)(diox)_2$ complexes.

5.7 A triradical tris-bidentate semiquinonate ligand enforcing high spin state

The obvious next step following the above reported characterization of a biradical system has been the synthesis and the characterization of a triradical system. Following the consideration outlined in paragraph 5.3 concerning the design of high-spin organic molecule the potentially tris-bidentate ligand 1,3,5-tris(3',4'-dihydroxy-5'-*tert*-butyl-phenyl)benzene $(TBCat)_3Ph$, **(4)**, see Scheme 5.4) was synthesized with the aim of isolating a tris-

semiquinone $(TBSQ)_3Ph$) derivative in which, according to its topology, directly resembling that of 1,3,5-trimethylenebenzene molecule, the three unpaired electrons are expected to couple ferromagnetically to each other. We thought that this topologically predetermined ferromagnetic coupling within the triradical might enforce a high-spin electronic ground state in certain metal complexes of paramagnetic metal ions. In order to facilitate the analysis of the magnetic data we have selected two paramagnetic metal ions characterized by non-degenerate electronic ground states. Following above cited previous studies,[71,79] we used as metal acceptors the Ni(II)-tetraazamacrocycle ($Ni(CTH)^{2+}$, CTH = dl-5,7,7,12,14,14-hexamethyl-1,4,8,11-tetraazacyclotetradecane), and the Mn(II)-hydrotris[3-(4'-cumenyl)-5-methylpyrazolyl]borate ($Mn(Tp^{Cum,Me})^{+}$) complexes, towards which the trianion $(TBSQ)_3Ph$) was found to act as tris-bidentate ligand. The corresponding complexes were isolated in the solid state and their spectroscopic and magnetic characterization will be described in the following pages.

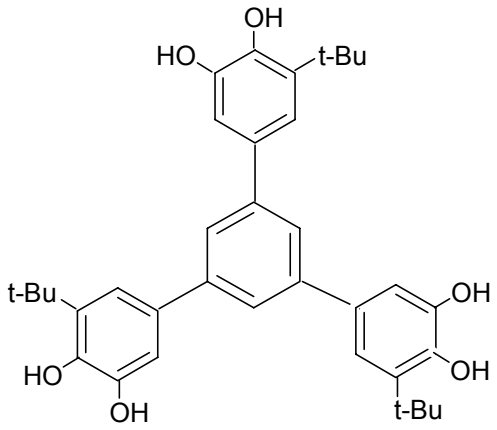

Scheme 5.4

The reaction of (**3**) with a stoichiometric amount of $Ni(CTH)(PF_6)_2$ in basic methanol under argon followed by aerial oxidation gave a brown microcrystalline powder of analytical formula $Ni_3(CTH)_3(tris(diox)Ph)(PF_6)_3 \bullet 1.5H_2O$ **(5)**. We postulate that this compound contains three six-coordinate nickel(II) cations bridged by the tris-bidentate dioxolene ligand.

In a similar fashion the $Mn(Tp^{Cum,Me})$ adduct of **(4)** was synthesized since it has been previously found that the tris(pyrazolyl)borate ligand may allow the isolation of manganese(II)-semiquinone adducts.[81,82] These complexes are expected to be five-coordinated on the basis of steric constraints of the ligand and characterized by quintet

electronic ground-state arising from a strong antiferromagnetic coupling between the S =5/2 metal ion and the radical ligand.[2,23] Based on previous results for Zn^{II}, Cu^{II}, and Co^{II},[82] we believe that the $Mn_3(Tp^{Cum,Me})_3((diox)_3)Ph)$ **(6)** contains five-coordinated manganese cations bridged by this dioxolene ligand.

All attempts at obtaining crystals suitable for structural analysis were unsuccessful. However, the formulation of the obtained compound as metal(II)-semiquinone derivative is clearly indicated from its electronic spectrum, electrochemical properties, and magnetic data discussed below.

5.7.1 Electronic spectra and electrochemistry.

The features of the electronic spectrum of the nickel complex **(5)**, which shows bands at 12,300, 20,200 and 26,300 cm^{-1}, are the same as those observed for the mononuclear Ni(CTH)(DBSQ)Y and some related complexes.[71,79] The band at 12,300 and 26,300 cm^{-1} can be assigned as internal semiquinone transitions, whereas the band at 20,200 cm^{-1} can be assigned as a metal-to-ligand charge transfer transition. The cyclic voltammogram of deaerated 1,2-dichloroethane solution of this compound shows three sequential one electron reversible redox processes at -1.08, -0.97 and -0.86 V and one irreversible at +0.1 V vs ferrocenium/ferrocene reference couple. In agreement with the electrochemical properties of the mononuclear derivatives the three reversible processes can be assigned to the semiquinone/catecholate couples whereas the irreversible one to the quinone/semiquinone couples. It is rather clear from these data that the species obtained working under aerobic conditions is the suggested tris-semiquinonato one. As a further consideration, it is also clear that it is not possible to characterize species containing mixed-valent forms of the ligand, i.e. one catecholate and two semiquinones or two semiquinones and one catecholate, without a significant presence of its reduced and oxidized species. In fact the comproportionation constant for the equilibrium:

$$Ni_3CTH_3((SQ)_2(Cat)Ph)^{2+} + Ni_3CTH_3((Cat)_3Ph) \rightarrow 2\ Ni_3CTH_3((SQ)(Cat)_2Ph)^{+} \qquad (5.7.1)$$

is about 33, according to the electrochemical data. Similar considerations hold for the comproportionation constant of the formation of the second intermediate species, namely $Ni_3CTH_3((SQ)_2(Cat)Ph)^{2+}$. These data show that the energies of the frontier orbitals of the

three dioxolene fragments of the ligand are the same, taking into account the differences in the solvation free energy changes and statistical factors.

The electronic spectrum of the manganese derivative **(6)** shows a pattern of transitions in the red region of the spectrum (11,600, 12,900 and 14,200 cm^{-1}) which are usually found to characterize the semiquinone ligands. The shoulder at 24,100 cm^{-1} could be also consistent with a semiquinone ligand-centered transition. A strong absorption is also detected at 21,300 cm^{-1} and can be probably assigned to a charge transfer transition. The feature of the spectrum therefore are consistent with the formulation of this manganese compound as tris-semiquinone $Mn_3(Tp^{Cum,Me})_3((TBSQ)_3Ph)$ derivative.

5.7.2 Magnetic properties

The χT vs T curve for the $Mn_3(Tp^{Cum,Me})_3((TBSQ)_3Ph)$ complex is shown in Figure 5.19. At room temperature (300 K) the obtained value of χT is 9.07 emu·K·mol^{-1}, and its tendency is to slowly decrease on increasing temperature. This value is much lower than that expected for three spins S=5/2 and three spins S=1/2 uncorrelated (χT_{theor}= 14.25 emu K mol^{-1}), while it is in perfect agreement with what expected for three S=2 centres with g=2.00 (3 x 3.00 emu·K·mol^{-1}). This is then a clear indication that each Mn(II) is strongly antiferromagnetic coupled to each semiquinone radical, while the interaction between the radicals is not evident at this temperature. On lowering T, χT increases and at the lowest temperature (2 K), it reaches the value of 19.7 emu K mol^{-1}. It should however be noted that the value is still growing at this temperature. This behavior suggests the existence of a ferromagnetic coupling between paramagnetic centers. The observed χT value is consistent with an S = 6 ground-state (theoretical value 21 emu K mol^{-1}) and the low observed value can be again explained by assuming an incomplete population of the ground state, even at low temperature.

This interpretation is confirmed by the M vs. H curves at low T (2.5 and 4.5 K, shown as reduced magnetization in Figure 5.20) which at 6 T are almost saturated to the expected value of 12 μ_B. The plot of M vs. H/T clearly shows that the two curves are almost perfectly superimposed and this suggests that only a very small zero-field splitting exists in this complex. This result is in agreement with the presence in the system of very isotropic species, namely Mn(II) (a ^6S ion) and semiquinone radicals. Interestingly, the X-Band EPR spectra show the presence of a fine structure due to a small Zero Field Splitting: preliminary

interpretation of HF-EPR spectra confirms the S=6 ground state and a value of D<0.1 cm^{-1} (see Figure S5.2).

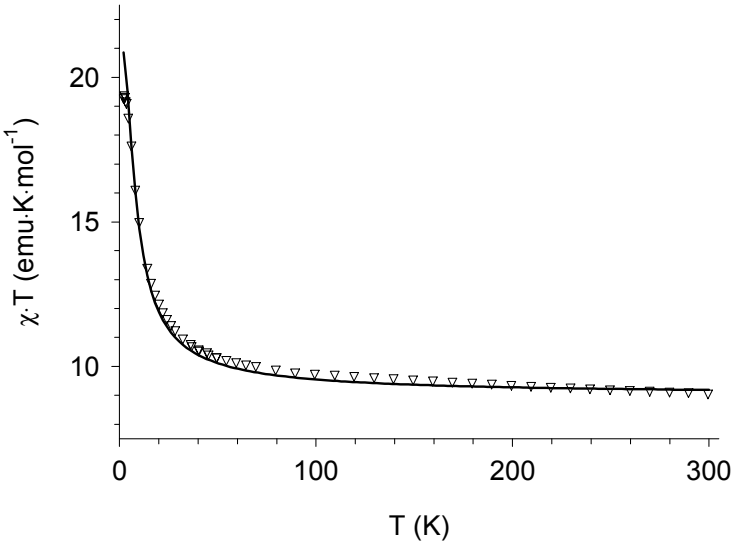

Figure 5.19 *χ·T vs T curve for complex $Mn_3(Tp^{Cum,Me})_3(TBSQ)_3$ (empty triangles). The continuous line is the result of the best fit obtained with both the models described in the text, which yielded superimposable curve. Best fit parameters for the two models are reported in the text.*

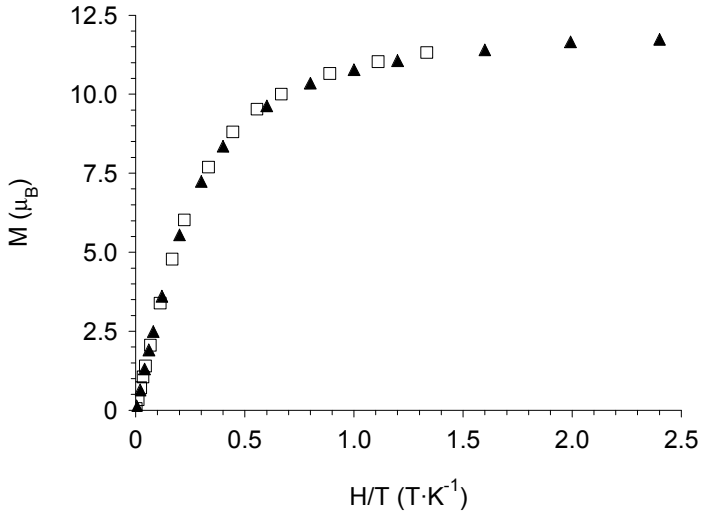

Figure 5.20 *Reduced magnetization data for $Mn_3(Tp^{Cum,Me})_3(TBSQ)_3$, measured at 2.5 K (full triangle) and 4.5 K (empty squares) respectively. The presence of only a small Zero Field Splitting is evidenced by the almost perfect coincidence of the two curves.*

Following this preliminary interpretation, two fits of the χT data were attempted. We assumed a C_3 symmetry for the exchange interactions which, given the lack of a crystal structure, cannot be experimentally confirmed. However, the following discussion will show

that even with the use of a reduced number of parameters we could get a very reasonable explanation of the observed magnetic properties of the $Mn_3(Tp^{Cum,Me})_3((TBSQ)_3Ph)$ complex.

In the first simple model we assumed the manganese(II)-semiquinone antiferromagnetic coupling to be so strong to consider the system as virtually built up by three S=2 ferromagnetically interacting spins, and we then employed only one J-value to analyze the data. The exchange Hamiltonian describing the system is then that of a regular triangular spin structure:

$$\mathbf{H} = J(\mathbf{S}_1\mathbf{S}_2+\mathbf{S}_2\mathbf{S}_3+\mathbf{S}_1\mathbf{S}_3) \qquad (5.7.2)$$

In this approach, the energy of each state is a function of total spin only:

$$E(S_T) = \frac{J}{2} S_T(S_T+1) \qquad (5.7.3)$$

The derivation of the analytic expression of the Van Vleck equation is then straightforward:[20]

$$\chi T = \frac{Ng^2\beta^2}{k_B} \cdot \frac{\left(546\cdot e^{21x} + 660\cdot e^{15x} + 540\cdot e^{10x} + 336\cdot e^{6x} + 150\cdot e^{3x} + 18\cdot e^{x}\right)}{\left(13\cdot e^{21x} + 22\cdot e^{15x} + 27\cdot e^{10x} + 28\cdot e^{6x} + 25\cdot e^{3x} + 9\cdot e^{x} + 1\right)} \qquad (5.7.4)$$

where $x = \frac{J}{k_B T}$.

The best fit (shown in Figure 5.19) was obtained by using a value J = - 1.12±0.05 cm^{-1} and gave an agreement factor, R= $\frac{1}{(N-n_P)}\sqrt{\frac{\sum(\chi_{calc}T-\chi_{obs}T)^2}{\sum(\chi_{obs}T)^2}}$ = $6.7*10^{-4}$, where N is the number of experimental points and n_P is the number of parameters. The error on the calculated coupling constant is obtained assuming a Dx=90% and an error on the experimental χT values equal to the square root of the mean quadratic error.[83]

Even if this fit was satisfactory and confirmed our qualitative analysis, it does not give us any indication about the value of the "real" coupling between the semiquinones. This can be evaluated by considering that the projection coefficient of the spin S=1/2 of each radical over the S=2 state of the Mn(II)-radical unit is equal to 1/6.[84] This leads to an estimate of J_{SQSQ} which is 36 times the value of the effective coupling between the three spin S=2, i.e J_{SQSQ} = 40 cm^{-1}. To obtain this parameter from a fit based on a more refined model we

considered as variable parameters both the coupling constant between radicals and Mn(II) and the coupling constant between each pair of semiquinones. The Hamiltonian of the system is then the one describing the pattern of Scheme 5.5:

$$H = J_1(\mathbf{S}_1\mathbf{S}_2+\mathbf{S}_3\mathbf{S}_4+\mathbf{S}_5\mathbf{S}_6)+J_2(\mathbf{S}_1\mathbf{S}_3+\mathbf{S}_3\mathbf{S}_5+\mathbf{S}_1\mathbf{S}_5) \quad (5.7.5)$$

where $\mathbf{S}_1$, $\mathbf{S}_3$ and $\mathbf{S}_5$ identify the radical spins and $\mathbf{S}_2$, $\mathbf{S}_4$ and $\mathbf{S}_6$ the metal ion ones.

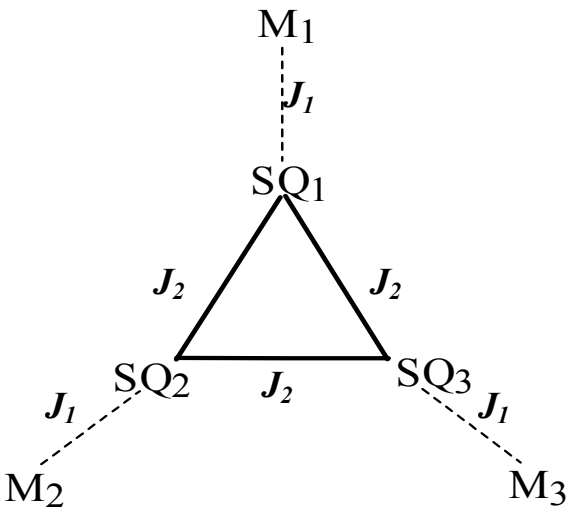

Scheme 5.5

	ΔE (cm^{-1}) **Model 1**	**ΔE (cm^{-1})** **Model 2**
S=6	Ground State	Ground State
S=5-S=6	6.72	6.5
S=4-S=5	5.6	5.7
S=3-S=4	4.48	4.6
S=2-S=3	3.36	3.5
S=1-S=2	2.24	2.3
S=0-S=1	1.12	1.15

Table 5.1 *The table shows the difference in energy between subsequent levels obtained by the best fit of χT data with Model 1 and 2, respectively*

The best fit parameters gave the following results: g=2.00 (fixed) J_1>350 cm^{-1}, in agreement with the predicted strong antiferromagnetic coupling between Mn(II) and

semiquinone, and J_2 =-40 cm^{-1}, with an agreement factor R=5.7*10^{-4}). Notwithstanding a certain systematic deviation from the experimental value the correlation between the parameters is very small and the fit is very stable. Varying J_1 from 350 cm^{-1} to 500 cm^{-1} results in a variation over J_2 of less than 0.3 cm^{-1}, without appreciable effect over the calculated curve. It is also interesting to note here that the two models yielded the same theoretical curve: indeed, a comparison of the energies of the low-lying spin levels shows a very good agreement between the two fitting models (see Table 5.1).

Finally, we introduced a lower symmetry (C_2) for the exchange pattern in both the model employed, but this did not lead to an improvement of the fit, thus confirming that the assumption of a three-fold symmetry for the exchange is completely justified.

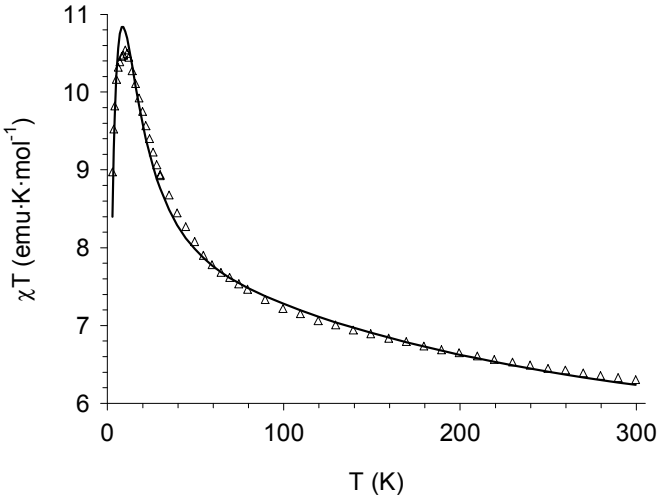

Figure 5.21 *χT vs T curve for complex $Ni_3(CTH)_3((TBSQ)_3Ph)(PF_6)_3$ (empty triangles). The continuous line is the result of the best fit obtained with the parameters reported in the text.*

Given this result, we employed the same exchange pattern of Scheme 5.5 for the interpretation of the magnetic data of the $Ni_3(CTH)_3((TBSQ)_3Ph)(PF_6)_3$ complex, whose χT vs. T curve is shown in Figure 5.21. The room temperature value (6.25 emu·K·mol^{-1}) is higher than expected for three uncoupled Ni(II) ions and three semiquinones (theoretical value = 4.7 emu·K·mol^{-1}, assuming g = 2.2 for Ni(II) ions). However, we wish to point out that the mononuclear [Ni(CTH)(DBSQ)]PF_6] complex shows a χT value of 2.28 emu·K·mol^{-1} at 300 K,[71] as a result of a strong ferromagnetic interaction between the paramagnetic metal ion and the radical ligand. Thus, a value equal to 6.7 – 6.8 emu K mol^{-1} (3 x 2.28 emu·K·mol^{-1}) was expected for the present trinuclear derivative if the coupling between metal and semiquinonato had not changed. The observed value at room

temperature is then suggesting that, while there is a ferromagnetic coupling between Ni(II) and semiquinonato which is effective even at room temperature, this is smaller than in the mononuclear parent derivative. On decreasing the temperature the value of χT increases, thus indicating that a ferromagnetic coupling is active between the three semiquinone radicals, as found in our Mn(II) derivative.

The curve passes through a maximum of 10.53 emu·K·mol^{-1} at 10 K, and then decreases. It has to be stressed that the maximum χT value is substantially lower than expected for a completely populated S = 9/2 state (13.6 emu·K·mol^{-1}) but can be explained by population of spin states with lower multiplicity. A magnetization measurement performed at low temperatures yielded a value of 8.70 μ_B at 6.5 T and 2.5 K, where the sample is still unsaturated (Figure 5.22). This is again in agreement with a ground S = 9/2 spin state and near excited state of lower spin multiplicity, whose population reduces the magnetization to a value lower than expected for an S = 9/2 (theoretical M_{sat} value around 9.6 μ_B assuming g = 2.15, see below). The picture emerging from the interpretation of the magnetic data is then consistent with our hypothesis of an S = 9/2 ground spin-state, due to the expected ferromagnetic coupling between nickel and semiquinone and the smaller ferromagnetic coupling between the three unpaired electrons of the ligand.

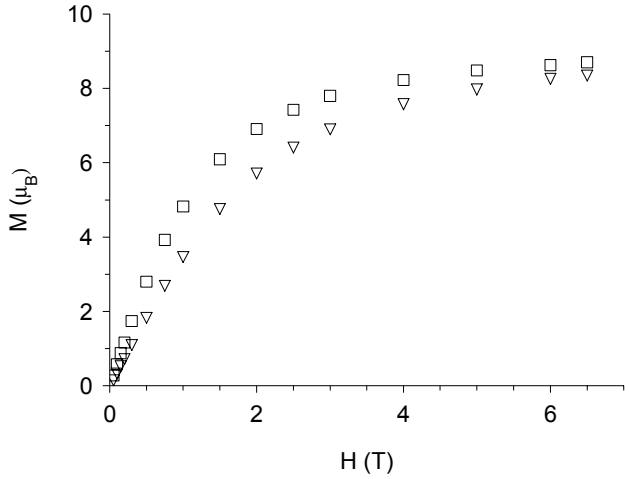

Figure 5.22 *Magnetization curves for $Ni_3(CTH)_3((TBSQ)_3Ph)(PF_6)_3$ complex, measured at 2.5 (empty squares) and 4.5 K (empty triangles) respectively.*

The fitting model in this case includes a correction to account for the decrease in χT below 10 K, assuming intermolecular antiferromagnetic interactions as described in paragraph 5.5.[61] The same caveat we raised in paragraph 5.5 concerning the use of a

phenomenological molecular field correction θ has to be considered. Indeed even if zero-field splitting terms were not included in the Hamiltonian they are likely to play a non-negligible role on the low temperature part of the χT curve, given the anisotropy of Ni(II) ions. Unfortunately, HF-EPR spectra only showed an uninformative very broad band around g=2.2 (see Figure S5.3), thus not allowing the determination of the anisotropy of the system. It should be noted that in the case of Mn(II) derivative there was no need for intermolecular interaction correction because the intermolecular interactions are supposed to be reduced to a minimum by the bulky ancillary ligand we used and the zero-field splitting is presumably very small.

In addition to the phenomenological correction we assumed the presence of a small amount of paramagnetic impurity, which is expected to play a relevant role in agreement with the trinuclear nature of the system. The best-fit curve (Figure 5.21, continuous line) obtained in such a way yielded the following parameters for the spin Hamiltonian: J_1 = -173 cm^{-1}, J_2 = -26.5 cm^{-1} g = 2.14, θ = -0.25 K with a factor $R=3.9*10^{-4}$.With these values of the coupling constants, the lowest excited-states are doubly degenerate S = 7/2, 12 cm^{-1} higher in energy with respect to the ground-state. The g-value of 2.14 is in agreement with what expected for a Ni(II) and a semiquinonato ferromagnetically coupled. Indeed, for a system with such a coupling scheme the global g-value may be related to the individual ones by the relation $g = 2/3g_{Ni}+1/3g_{SQ}$.[84] Then, if one assumes g_{SQ} = 2.00, a global g = 2.14 implies g_{Ni} = 2.21, which is a well-established value for the Ni(II) ion.[85]

It has to be noted that the Ni(II)-semiquinonato ferromagnetic coupling is strongly reduced with respect to the single center systems.[71] This phenomenon is analogous to what we have observed for the bis-semiquinonate system described in paragraph 5.5 and points out that while the qualitative behavior of this metal radical interaction can be easily predicted, its intensity can vary largely when passing from one family to another.

The semiquinonato-semiquinonato coupling within the tri-radical are, as expected, ferromagnetic and the value of the coupling between the semiquinonato units of the radical is of the same order of that obtained for the homologous biradical in paragraph 5.5.[79] A comparison of the obtained value for the coupling between radicals in the two derivatives shows that this is higher in the manganese complex than in the Ni(II) one, thus suggesting that a variation in the dihedral angle between the plane of the semiquinone is likely to occur when passing from the Ni(II) complex to the Mn(II) one.[2,52,79,86] This is probably due to the different diamagnetic ligand employed in the two cases, which imply a penta-

coordinated Mn(II) and an hexa-coordinated Ni(II) and then a different accommodation of the paramagnetic ligands as well.

5.8 Conclusions

We have shown how an appropriate strategy in designing linked o-semiquinone ligands can be used to fix the magnetic properties of a collection of paramagnetic centers. In particular, for ligand **(1)** the combined use of DFT and spectroscopic data allowed us to achieve a deep understanding of the electronic structure of the $M_2(CTH)_2(SQ\text{-}Cat)(PF_6)_3$ (n = 3; M = Cobalt(III), Chromium(III); CTH = tetraazamacrocycle) complexes. In particular, our results strongly suggest a fully delocalized electronic structure description for the trinegative radical ligand 5,5'-di-*tert*-butyl-3,3',4,4'-tetraoxo-biphenyl and their homodinuclear metal complexes. This description is independent from the value of the dihedral angle between the phenyl rings, taking into account the existence of a binary symmetry axis within the molecule. Therefore, if the current chemical terminology is used, as we have done in the text, a description of the SQ-cat ligand as a class III mixed valence species seems appropriate. This conclusion however cannot in principle hold if the symmetry of the bis-dioxolene molecule is broken by introducing different ring substituents or by coordination to different metal ions. A more complete characterization through Resonance Raman spectroscopy is currently in progress in order to test the hypothesis of a class III behavior.

On the other hand we have shown that the ligand 1,3-bis(dioxolene)-benzene, **(2)** and 1,3,5-tris(dioxolene)-benzene, **(4)** may be used to create a bis(semiquinone) and tris(semiquinone) ligand characterized by a triplet and a quartet ground-state, respectively. It should be stressed that the strategy based on the substitution of some sp^2 radical carbons of a non Kekulè hydrocarbon with other radical groups has been in general used for obtaining ferromagnetically coupled biradicals.[45] We have also shown that with both these ligands the coordination of paramagnetic metal ions enforces high-spin ground-states in the resulting metal complexes. In particular the the magnetic coupling the tris-semiquinone ligand induces an S = 9/2 electronic ground-state in the Ni(II) complex and an S = 6 electronic ground-state in the Mn(II) complex according to our expectations, thus showing how an appropriate linker between the paramagnetic centers may propagate the desired

magnetic interactions. At this step there is therefore the problem concerning the utility of these metal-polyoxolene complexes as building blocks for a network coordination polymer. It has been suggested that in order to achieve this goal the chemist should predetermine the structure of the network and in this sense simpler units to be assembled than those we propose should be required.[87]

However, a first result in the direction of obtaining a polymeric structure has been achieved by the synthesis and characterization of the polymeric system described in paragraph 5.6 which is capable of undergoing a valence tautomer process. On this respect the most important experimental result is the strong cooperativity shown by the valence tautomer interconversion process, a property that we were looking for in designing this peculiar molecular system. Indeed, this is induced by the polymeric structure of the compound, which is on its turn a consequence of the peculiar bis-bidentate radical ligand. We feel that the observed properties can be easily manipulated by changing the dioxolene substituents, the diazine acceptors as well as the crystallization solvent, in agreement with the suggestions of the previous work concerning the more simple molecular $Co(NN)(diox)_2$ complexes. The extension of this approach to the tris-bidentate radical ligand **(4)** is actually in progress, in view of obtaining a more complex structure with enhanced cooperativity.

References

1. W. Kaim, *Coord. Chem. Rev.* **76**, 187 (1987).
2. A. Dei and D. Gatteschi, *Inorg. Chim. Acta* **200**, 813 (1992).
3. C. G. Pierpont and C. W. Lange, *Prog. Inorg. Chem.* **41**, 331 (1994).
4. C. G. Pierpont, *Coord. Chem. Rev.* **216**, 99 (2001).
5. J. S. Miller , J. C. Calabrese, Rommelmann H., Chittapeddi S., J. H. Zhang, W. M. Reiff, and A. J. Epstein, *J. Am. Chem. Soc.* **109**, 769 (1987).
6. J. M. Manriquez, Yee G. T. , R. S. McLean, A. J. Epstein, and J. S. Miller, *Science* **252**, 1415 (1991).
7. H. H. Zhao, R. A. Heintz, K. R. Dunbar, and R. D. Rogers, *J. Am. Chem. Soc.* **118**, 12844 (1996).
8. E. J. Brandon, R. D. Rogers, B. M. Burkhart, and J. S. Miller, *Chem.- Eur. J.* **4**, 1938 (1998).

9. A. Caneschi, D. Gatteschi, R. Sessoli, and P. Rey, *Acc. Chem. Res.* **22**, 392 (1989).
10. D. Gatteschi, *Adv. Mater.* **6**, 635 (1994).
11. K. Inoue and H. Iwamura, *J. Am. Chem. Soc.* **116**, 3173 (1994).
12. K. Inoue and H. Iwamura, *Adv. Mater.* **8**, 73-& (1996).
13. K. Inoue, T. Hayamizu, H. Iwamura, D. Hashizume, and Y. Ohashi, *J. Am. Chem. Soc.* **118**, 1803 (1996).
14. H. Iwamura, K. Inoue, and T. Hayamizu, *Pure Appl. Chem.* **68**, 243 (1996).
15. T. M. Barclay, R. G. Hicks, M. T. Lemaire, and L. K. Thompson, *Chem. Commun.* 2141 (2000).
16. R. G. Hicks, M. T. Lemaire, L. K. Thompson, and T. M. Barclay, *J. Am. Chem. Soc.* **122**, 8077 (2000).
17. T. M. Barclay, R. G. Hicks, M. T. Lemaire, and L. K. Thompson, *Inorg. Chem.* **40**, 5581 (2001).
18. C. G. Pierpont and R. M. Buchanan, *Coord. Chem. Rev.* **38**, 87 (1981).
19. O. Kahn, *Angew. Chem. Int. Ed. Engl.* **24**, 834 (1985).
20. O. Kahn, *Molecular Magnetism* (VCH, Weinheim, 1993).
21. D. M. Adams, A. Dei, A. L. Rheingold, and D. N. Hendrickson, *J. Am. Chem. Soc.* **115**, 8221 (1993).
22. A. S. Attia and C. G. Pierpont, *Inorg. Chem.* **37**, 3051 (1998).
23. A. Dei and A. Caneschi, *Angew. Chem. Int. Ed. Engl.* **37**, 3005 (1998).
24. G. Speier, Z. Tyeklar, P. Toth, E. Speier, S. Tisza, A. Rockenbauer, A. M. Whalen, N. Alkire, and C. G. Pierpont, *Inorg. Chem.* **40**, 5653 (2001).
25. A. S. Attia, O. S. Jung, and C. G. Pierpont, *Inorg. Chim. Acta* **226**, 91 (1994).
26. O. S. Jung and C. G. Pierpont, *Inorg. Chem.* **33**, 2227 (1994).
27. O. S. Jung and C. G. Pierpont, *J. Am. Chem. Soc.* **116**, 1127 (1994).
28. D. M. Adams, B. L. Li, J. D. Simon, and D. N. Hendrickson, *Angew. Chem. Int. Ed. Engl.* **34**, 1481 (1995).
29. C. Roux, D. M. Adams, J. P. Itie, A. Polian, D. N. Hendrickson, and M. Verdaguer, *Inorg. Chem.* **35**, 2846 (1996).
30. D. M. Adams and D. N. Hendrickson, *J. Am. Chem. Soc.* **118**, 11515 (1996).
31. O. S. Jung, D. H. Jo, Y. A. Lee, B. J. Conklin, and C. G. Pierpont, *Inorg. Chem.* **36**, 19 (1997).
32. P. Gutlich and A. Dei, *Angew. Chem. Int. Ed. Engl.* **36**, 2734 (1997).

33. A. Caneschi, A. Cornia, and A. Dei, *Inorg. Chem.* **37**, 3419-+ (1998).
34. A. Caneschi, A. Dei, F. Fabrizi de Biani, P. Gütlich, V. Ksenofontov, G. Levchenko, A. Hoefer, and F. Renz, *Chem.-Eur. J.* **7**, 3926 (2001).
35. D. A. Shultz, *Magnetism: Molecules to Materials II - Molecule Based Materials* J. S. Miller and M. Drillon (Wiley-VCH, New York, 2001).
36. D. M. Adams, L. Noodleman, and D. N. Hendrickson, *Inorg. Chem.* **36**, 3966 (1997).
37. S. Klokishner, *Chem. Phys.* **269**, 411 (2001).
38. F. V. R. Neuwahl, R. Righini, and A. Dei, *Chem. Phys. Lett.* (submitted for publication).
39. A. Bencini, C. Carbonera, and A. Dei, *Proceedings of 9th International Conference on the Applications of DFT in Chemistry and Physics*, Madrid (2001).
40. O. Kahn and C. Jay-Martinez, *Science* **279**, 44 (1998).
41. C. R. Kemnitz, R. R. Squires, and W. T. Borden, *J. Am. Chem. Soc.* **119**, 6564 (1997).
42. G. A. Abakumov, V. K. Cherkasov, V. I. Nevodchikov, V. A. Kuropatov, B. C. Noll, and C. G. Pierpont, *Inorg. Chem.* **37**, 6117 (1998).
43. L. F. Joulie, E. Schatz, M. D. Ward, F. Weber, and L. J. Yellowlees, *J. Chem. Soc., Dalton Trans.* 799 (1994).
44. L. Horner and K.-H. Weber, *Chem. Ber.* **100**, 2842 (1967).
45. A. Rajca, *Chem. Rev.* **94**, 871 (1994).
46. A. B. P. Lever, *Inorganic Electronic Spectroscopy* (Elsevier, Amsterdam, 1984).
47. K. W. Penfield, J. R. Miller, M. N. Paddon-Row, E. Cotsaris, A. M. Oliver, and N. S. Hush, *J. Am. Chem. Soc.* **109**, 5061 (1987).
48. D. A. Shultz, S. H. Bodnar, R. K. Kumar, and J. W. Kampf, *J. Am. Chem. Soc.* **121**, 10664 (1999).
49. D. A. Shultz and R. K. Kumar, *J. Am. Chem. Soc.* **123**, 6431 (2001).
50. J. Sedo, D. Ruiz, J. Vidalgancedo, C. Rovira, J. Bonvoisin, J. P. Launay, and J. Veciana, *Adv. Mater.* **8**, 748 (1996).
51. T. Nakamura, T. Momose, T. Shida, T. Kinoshita, T. Takui, Y. Teki, and K. Itoh, *J. Am. Chem. Soc.* **117** , 11292 (1995).
52. A. Bencini, C. A. Daul, A. Dei, F. Mariotti, H. Lee, D. A. Shultz, and L. Sorace, *Inorg. Chem.* **40**, 1582 (2001).
53. V. Barone, A. Bencini, I. Ciofini, C. A. Daul, and F. Totti, *J. Am. Chem. Soc.* **120**, 8357 (1998).

54. A. Bencini, I. Ciofini, C. A. Daul, and A. Ferretti, *J. Am. Chem. Soc.* **121**, 11418 (1999).
55. I. Ciofini, C. A. Daul, and A. Bencini, *Recent Advances in Density Functional Methods* V. Barone, A. Bencini, and P. Fantucci (World Scientific, Singapore, Part III, 2001).
56. C. Benelli, A. Dei, D. Gatteschi, H. U. Güdel, and L. Pardi, *Inorg. Chem.* **28**, 3089 (1989).
57. C. Benelli, A. Dei, D. Gatteschi, and L. Pardi, *Inorg. Chim. Acta* **163**, 99 (1989).
58. P. R. Auburn and A. B. P. Lever, *Inorg. Chem.* **29**, 2553 (1990).
59. F. E. Mabbs and D. Collison, *Electron Paramagnetic Resonance of Transition Metal Complexes* (Elsevier, Amsterdam, 1992).
60. *Win-EPR SimFonia*, Version 1.25; Bruker Analytische Messtechnik GmbH.
61. C. J. O'Connor, *Prog. Inorg. Chem.* **29**, 203 (1982).
62. A. Dei, D. Gatteschi, L. Pardi, and V. Russo, *Inorg. Chem.* **30**, 2589 (1991).
63. C. O. Felix and R. C. Sealy, *J. Am. Chem. Soc.* **104**, 155 (1982).
64. J. Spenget-Larsen, *Int. J. Quantum Chem.* **18**, 365 (1980).
65. E. van Lenthe, A. E. Ehlers, and E. J. Baerends, *J. Chem. Phys.* **110**, 8943 (1999).
66. L. Noodleman, C. Y. Peng, D. A. Case, and J. M. Mouesca, *Coord. Chem. Rev.* **144**, 199 (1995).
67. E. Ruiz, P. Alemany, S. Alvarez, and J. Cano, *J. Am. Chem. Soc.* **119**, 1297 (1997).
68. E. Ruiz, J. Cano, S. Alvarez, and P. Alemany, *J. Am. Chem. Soc.* **120**, 11122 (1998).
69. D. A. Shultz, A. K. Boal, D. J. Driscoll, J. R. Kitchin, and G. N. Tew, *J. Org. Chem.* **60**, 3578 (1995).
70. O. Kahn, J. Reedijk, R. Prins, and J. S. Thompson, *Inorg. Chem.* **26**, 3557 (1987).
71. C. Benelli, A. Dei, D. Gatteschi, and L. Pardi, *Inorg. Chem.* **27**, 2831 (1988).
72. C. Benelli, A. Dei, D. Gatteschi, and L. Pardi, *Inorg. Chem.* **29**, 3409 (1990).
73. D. Gatteschi and L. Pardi, *Gazz. Chim. Ital.* **123**, 231 (1993).
74. D. E. Wheeler, J. H. Rodriguez, and J. K. Mccusker, *J. Phys. Chem. A* **103**, 4101 (1999).
75. P. G. Wenthold, J. B. Kim, and W. C. Lineberger, *J. Am. Chem. Soc.* **119**, 1354 (1997).
76. D. A. Shultz, *Magnetic Properties of Organic Materials* P. Lahti (Marcel Dekker, New York, 1999).

77. A. Bencini, D. Gatteschi, F. Totti, D. N. Sanz, J. A. Mc Cleverty, and M. D. Ward, *J. Phys. Chem. A* **102**, 10545 (1998).
78. S. H. Bodnar, A. Caneschi, A. Dei, D. A. Shultz, and L. Sorace, *Chem. Commun.* 2150 (2001).
79. A. Caneschi, A. Dei, H. Lee, D. A. Shultz, and L. Sorace, *Inorg. Chem.* **40**, 408 (2001).
80. A. Caneschi, A. Dei, and V. Tangoulis, *Inorg. Chem.* (accepted for publication).
81. M. Ruf, A. M. Lawrence, B. C. Noll, and C. G. Pierpont, *Inorg. Chem.* **37**, 1992 (1998).
82. M. Ruf, B. C. Noll, M. D. Groner, G. T. Yee, and C. G. Pierpont, *Inorg. Chem.* **36**, 4860 (1997).
83. *Numerical Recipes* (Cambridge University Press, Cambridge, 1986).
84. A. Bencini and D. Gatteschi, *EPR of Exchange Coupled Systems* (Springer-Verlag, Berlin, 1990).
85. J. S. Griffith, *The Theory of Transition Metal Ions* (Cambridge University Press, Cambridge, 1961).
86. A. Bencini, D. Gatteschi, F. Totti, D. Nieto, J. A. Mc Cleverty, and M. D. Ward, *J. Phys. Chem.* **102** , 10545 (1998).
87. A. W. Misiolek and J. E. Jackson, *J. Am. Chem. Soc.* **123**, 4774 (2001).

6. Crystal field and exchange coupling in rare earth-semiquinonato complexes: an experimental approach

6.1 Introduction

Suitable strategies have been developed to work out new magnetic molecular complexes containing *3d* ions with orbitally non-degenerate ground state and/or open-shell ligands with desired properties. This is due to the possibility of controlling, to some extent, the factors governing the nature, antiferro- or ferromagnetic, and the intensity of the exchange-coupling interaction [1-3]: we have shown in Chapter 5 how it is possible to predict the sign of the coupling between dioxolene radicals and *3d* metal ions by simple considerations on the symmetry of the magnetic orbitals of the two centers. We also suggested in Chapter 3 some useful strategies to control the magnetic anisotropy of polynuclear transition metal ions systems by rationalizing the magnetic anisotropy of their building blocks on the basis of Ligand Field arguments.

The control of these magnetic features is very important, as molecules which are characterized by high spin electronic ground states and large anisotropy are actively investigated as possible candidates for developing molecular based materials of technological interest.[2,4-10]. On this respect complexes of rare earth ions, which can provide both very high spin and large anisotropy are attracting increasing interest in the field of molecular magnetism.[11-24] Notwithstanding this interest, not much is known about the nature of the exchange interactions of rare earth ions between themselves and with other magnetic groups, because until recently few simple compounds containing

magnetically coupled *f* ions were available. In the last few years things have changed because complexes of lanthanide ions with different paramagnetic ligands, ranging from metal complexes to organic radicals, have been reported[11-13,25-35]. However, the interpretation of the magnetic data of complexes containing Ln(III) ions, with the exclusion of Gd(III), is still a difficult task, due to the large orbital contribution of these ions. Furthermore, the study of the magnetic coupling in the lanthanide derivatives gives rise to additional difficulties, because these ions are usually involved in weak interactions, whose strength is comparable with that of the crystal field acting on the ion. As we will see in the following, it is precisely the difficulty in having a quantitative information of these two contributions which so far reduced the analysis of the magnetic properties of the anisotropic lanthanides mainly at a qualitative level, especially in molecular complexes.

In this chapter we will first review in some details current theories about magnetic properties of rare-earth containing systems and we will then present the results obtained on a series of rare-earth semiquinonato complexes which were characterized with the aim of obtaining some further hints on the parameters governing the exchange coupling and the anisotropy of these systems.

6.2 Magnetic properties of isolated rare-earth ions

Rare earth ions present a largely unquenched orbital momentum as the inner character of *4f* orbitals with respect to *3d* ones prevents crystal field to be effective in the quenching of orbital momentum. Exceptions to this behavior are Eu(II) and Gd(III) which - as a consequence of their $4f^7$ electronic configuration - present an orbitally non-degenerate ground state.

The $4f^n$ configuration gives rise to a ^{2S+1}L ground state, which is split by strong spin orbit coupling [36] to give states which are identified by total angular momentum, *J*:

$$|L-S|<J<L+S \qquad (6.2.1)$$

The energies of each multiplet $^{2S+1}L_J$ are easily calculated as the eigenvalues of the spin-orbit coupling hamiltonian, $\mathbf{H}=\lambda\mathbf{L}\cdot\mathbf{S}$ (see Chapter 3):

$$E(^{2S+1}L_J) = \lambda\,[J(J+1)-L(L+1)-S(S+1)]/2 \qquad (6.2.2)$$

where $\lambda=\pm\zeta/2S$. ζ is the spin orbit coupling constant which ranges between 600 and 3,000 cm^{-1} throughout the series, the highest values corresponding to the heaviest ions. In analogy to what we have seen for *d* ions in Chapter 3, the + sign applies for $n<7$, the – sign for $n> 7$. The ground states for the different rare earth ions are reported in Table 6.1. Eq. (6.2.1) and the sign of the spin orbit coupling constant λ imply that in the ground state $J= L-S$ for $n< 7$, and $J= L+ S$ for $n> 7$.

The g factor of the Zeeman hamiltonian of a given *J* multiplet is given by:

$$g_J = \frac{3}{2} + \frac{S(S+1) - L(L+1)}{2J(J+1)} \qquad (6.2.3)$$

For a $4f^n$ ion the crystal field splits the *J* multiplets in a series of Stark sublevels, whose pattern depends on the site symmetry of the Ln(III) ion. For C_1 symmetry of the crystal field, which is a situation often encountered in molecular compounds, the degeneracy of each *J* multiplet is completely removed: $2J + 1$ singlets are then expected when the number *n* of *4f* electrons is even and $J + 1/2$ doublets when *n* is odd. However, as the effect of crystal field is small all the Stark sublevels of the ground *J* multiplet are populated at room temperature and the observed magnetic moment coincide with what expected for the free-ion Curie behavior, provided that the ground *J* multiplet is well isolated with respect to the excited ones. It was early noticed [37] that this is not the case both for Eu(III) - whose first excited state $^7F_1$ is lying only at ca 350 cm^{-1} above the non-magnetic $^7F_0$ ground state - and Sm(III), for which the first excited state $^6H_{7/2}$ is lying about 700 cm^{-1} above the ground $^6H_{5/2}$ state. As a consequence these two ions show a room temperature magnetic moment which differs from the value expected for the ground *J* multiplet. Further, they show a marked temperature dependence of the magnetic moment, which is increasing with temperature due to the progressive population of excited state which are more magnetic than the ground one. However inclusion of the contribution of first excited state in calculation of the magnetic moment at room

temperature leads to a perfect agreement with the experimental observations also in this case.[37]

Ion	**State**	**S**	**L**	**J**	**g**	**Average χT (emu K/mol)**	
						Exp	**Calc**
Ce^{3+}	$^2F_{5/2}$ $^2F_{7/2}$	1/2	3	5/2	6/7	6	6.43
Pr^{3+}	$^3H_4$ $^3H_5$	1	5	4	4/5	12	12.8
Nd^{3+}	$^4I_{9/2}$ $^4I_{11/2}$	3/2	6	9/2	8/11	12	13.1
Pm^{3+}	$^5I_4$ $^5I_5$	2	6	4	3/5		7.2
Sm^{3+}	$^6H_{5/2}$ $^6H_{7/2}$	5/2	5	5/2	2/7	2.4	0.71(2.5)
Eu^{3+}	$^7F_0$ $^7F_1$	3	3	0	0	12.6	0(12)
Gd^{3+}	$^8S_{7/2}$ ^6P	7/2	0	7/2	2	63	63
Tb^{3+}	$^7F_6$ $^7F_5$	3	3	6	3/2	92	94.5
Dy^{3+}	$^6H_{15/2}$ $^6H_{13/2}$	5/2	5	15/2	4/3	110	113
Ho^{3+}	$^5I_8$ $^5I_7$	2	6	8	5/4	110	112
Er^{3+}	$^4I_{15/2}$ $^4I_{13/2}$	3/2	6	15/2	6/5	90	92
Tm^{3+}	$^3H_6$ $^3H_5$	1	5	6	7/6	52	57
Yb^{3+}	$^2F_{7/2}$ $^2F_{5/2}$	1/2	3	7/2	8/7	19	20.6

Table 6.1 *Relevant magnetic information for free rare-earth ions. After ref. [38]*

The effect of the ligands surrounding lanthanides over magnetic properties becomes important on lowering temperature, as a depopulation of the sublevels occurs and consequently $\chi_{Ln}T$ (where χ_{Ln} is the magnetic susceptibility of the Ln(III) ion) decreases, thus leading to a deviation from the Curie law. This temperature dependence complicates the interpretation of magnetic properties of systems in which the Ln(III) ion interacts with another paramagnetic species. Indeed effects due to the exchange are very small - because the unpaired electrons are in the well shielded *f* orbitals - and may be hidden by crystal field effects at low temperature. This means that the temperature dependence of χT for the compound is due to both the variation of $\chi_{Ln}T$ and the coupling between the Ln(III) ion and the second spin carrier. As a consequence information about the nature of the interactions between a Ln(III) ion with a first-order orbital momentum and the second spin carrier cannot be unambiguously deduced only from the shape of the χT vs. T curve.

6.3 Analysis of the magnetic coupling in orbitally degenerate rare earths

The main problem in evaluating the exchange coupling in systems containing orbitally degenerate ions lies in the fact that the usual isotropic spin hamiltonian approaches which have been so far employed with much success to understand and parameterize the magnetic interactions in compounds containing orbitally non-degenerate centers cannot be used.[39,40] Indeed, when systems with unquenched angular orbital momentum are considered, S is no longer a good quantum number, and the energies of the levels depend also on the value of M_S value, with $-S \leq M_S \leq S$, i.e. there will be some preferential orientation of the magnetic moment even in zero field. This is the main reason of the peculiar difficulties arising in the analysis of the magnetic behavior of the lanthanides.

The first detailed and quantitative treatment of the interactions involving one orbitally non-degenerate ion, like Fe(III), and an orbitally degenerate rare earth ion was performed by Levy[41,42] in an attempt to rationalize the exchange interactions in Yb(III) containing garnets and was later employed by Yamaguchi and Kamimura to analyze the behavior of Ho(III) garnets.[43] Within this model, the global hamiltonian

acting on the system obviously takes into account both crystal field contributions and exchange effects:

$$H=H_{ex}+H_{cf} \tag{6.3.1}$$

The crystal field hamiltonian, which acts on the ground $|LSJM_J>$ multiplet and splits it in a series of Stark sublevels may be written as:[44]

$$\mathbf{H}_{\mathrm{cf}} = \sum_{k,q,t} B_k^q (C_k^q)_t \tag{6.3.2}$$

where C_k^q are irreducible tensor operators of rank k, t numbers the electron of the configuration and B_k^q are the crystal field parameters. Both Levy and Yamaguchi obtained the B_k^q parameters by combined single crystal spectroscopic and magnetic measurements on systems where the Fe(III) was substituted by diamagnetic Y(III) thus allowing to extract the crystal field parameters characterizing the uncoupled lanthanide. On the other hand, the exchange interactions are described by an anisotropic exchange hamiltonian exploiting the formalism of irreducible tensor operators $T_q^{[k]}$:

$$\mathbf{H} = \sum_{k=0}^{2l} \sum_{q=-k}^{k} \alpha_{kq} \mathbf{T}_q^{[k]}(i) \mathbf{s}(i) \cdot \mathbf{S}(TM) \tag{6.3.3}$$

where l=3 for lanthanides, i indicates the i-th electron of the rare earth ion, S(TM) is the spin operator of the transition metal ion and α_{kq} are the exchange coupling parameters, α_{00} being the isotropic one. It is evident that the number of adjustable parameters, B_k^q and α_{kq}, is huge, especially in the low site symmetry usually characteristic for molecular complexes of Ln(III), and a meaningful fit of the experimental parameters becomes extremely difficult. Furthermore it is in principle absolutely necessary to perform anisotropic measurements because the Hamiltonian (6.3.1) is the sum of the two anisotropic hamiltonians (6.3.2) and (6.3.3).

The first application of this approach to a molecular complex was described in a series of paper by Benelli et al.[11,12] who synthesized and magnetically characterized different copper-lanthanides molecular complexes. The crystal field parameters were

obtained by an independent fit of the powder magnetic susceptibility of $[Ln(hfac)_3(H_2O)_2]$ and fixed in order to reduce the parameterization of the system. It was then possible to find out that the isotropic term of the coupling hamiltonian was antiferromagnetic while the anisotropic ones were ferromagnetic: to avoid overparameterization, however, only second order anisotropic parameters were used.

A strongly related approach has been subsequently used by different groups to get qualitative information on the type of interaction (ferro- or antiferromagnetic) in lanthanides coupled to radical or Cu(II).[32,34,35,45] Within this experimental approach the exchange interaction in coupled systems is made apparent by subtracting from χT of the complex the contribution arising from the thermal depopulation of the Stark sublevels of Ln(III), $\chi_{Ln}T$. As we have seen previously, the temperature dependence of $\chi_{Ln}T$ is directly related to the local contribution of the ligand field onto the Ln(III) ion and thus can be obtained from an isostructural Ln(III) complex with a diamagnetic surrounding. Further information may be gained by the comparison of the magnetization curves for the two derivatives: an antiferromagnetic coupling will indeed result in a lower magnetization of the coupled complex with respect to the sum of the uncorrelated spins. A value of ΔM lower than the magnetization value for uncoupled S=1/2 is then expected,[35] while the reverse is true for ferromagnetic coupling.[34] This approach has been successfully applied to the investigation of the Ln(III)-Cu(II) interactions both in bimetallic and polymeric coordination compounds by replacing the paramagnetic Cu(II) by a diamagnetic ion, either square planar Ni(II) or Zn(II), and to the investigation of Ln(III)-(nitronyl-nitroxide)$_2$ complexes, for which the molecule chosen as a diamagnetic equivalent of the radical ligand was a nitrone. More recently a quantitative determination of crystal field parameters in these latter systems has been achieved[46] through the use of Simple Overlap Model[47], an extension of purely electrostatic ligand field theory taking into account some degree of covalency. This allowed to derive the eigenfunctions and eigenvalues of the ground multiplet by using only three parameters[48] and the real structure of the complex and to subsequently evaluate the exchange interaction, in the assumption of isotropic coupling, which was sufficient to yield a reasonable fit of the powder susceptibility data.

6.4 Magnetic coupling in Gadolinium(III) containing complexes

Given the inherent difficulties in developing a suitable approach for the analysis of magnetic data of systems with largely unquenched orbital momentum, with which we have dealt in the previous paragraph, much of the data reported up to now are concerned with Gd(III) derivatives, which are orbitally non-degenerate.[26-28,31,49-51] It is then possible to treat coupled systems containing this ion with the usual isotropic hamiltonian:

$$\mathbf{H}=J\mathbf{S_{Gd}}\cdot\mathbf{S_1} \qquad (6.4.1)$$

where J is the isotropic coupling constant and $\mathbf{S_1}$ is the spin of the second magnetic center.

First reports on systems containing Gd(III) coupled either to Cu(II) ions [25]or to radicals such as nitronyl-nitroxides[25,26] invariably showed a weak ferromagnetic coupling with J ranging from -0.5 to -10 cm^{-1}, and this sign of the coupling was considered at first sight quite surprising. Indeed, the coupling constant J is the resulting of a sum of the exchange interactions between different pairs of magnetic orbitals, according to:

$$J = \frac{1}{n_1 n_2}\sum_i J_{f_i-o} \qquad (6.4.2)$$

where f_i indicates an f magnetic orbital of Gd(III) and o the magnetic orbital either of Cu(II) or of the radical; n_1 is the number of unpaired electrons on gadolinium (then n_1=7) and n_2 the number of unpaired electron on the magnetic center (then n_2=1 both for copper and mono-radical systems). The actual value of each $J_{fi\text{-}o}$ is related to the overlap between the different magnetic orbitals: if the two orbitals on the two different centers have a non-zero overlap then the spins will pair antiparallel to each other yielding an antiferromagnetic pathway, while if there is no overlap the spin will pair in a parallel way. We already pointed out in Chapter 5 that a zero overlap between two magnetic orbitals may be due either to the absence of any overlap or to opposite contribution of two overlap regions of different sign. In the former case the two magnetic orbitals are not

interacting, whereas in the latter a ferromagnetic coupling results which is roughly proportional to the square of overlap density.

For Gd(III) ions coupled to systems with only one unpaired electrons, such as Cu(II) or radicals, a maximum of six orthogonal pairs of orbitals - and thus a maximum of six ferromagnetic pathways - and only one non-zero *f-o* overlap, yielding an antiferromagnetic pathway, may be present. Thus in principle the observed overall ferromagnetic coupling might originate from a larger number of ferromagnetic pathways with respect to antiferromagnetic ones. However, if the site symmetry is low - which is usually the condition for molecular complexes – the number of orbital pairs which are orthogonal by symmetry will be considerably reduced and thus a dominating antiferromagnetic coupling would be expected. A similar situation was indeed observed for copper or radical complexes coupled to Mn(II) compounds, which yields an overall antiferromagnetic coupling.[2]

The explanation for the observed behavior cannot then lie in the interactions between ground state configurations. Indeed, since the *f* orbitals are effectively shielded from the ligand orbitals the effective overlaps are very close to zero. However the overlap of the magnetic orbital of Cu(II) or radical is relatively larger with the empty *d* or *s* orbitals of Gd(III) than with the 4*f* orbitals. Following these considerations the Florence group first suggested that a fraction of unpaired electron is transferred, with the same spin it had in the original magnetic orbital, into the empty *6s*[11] or *5d*[13] orbitals, keeping the spins of the electrons in the *f* orbitals parallel according to the Hund's rule. This may be seen as a generalization of the Goodenough-Kanamori rule suggesting a ferromagnetic pathway when a magnetic orbital of one site has non zero overlap with an empty orbital of the other site. An elementary semi-quantitative treatment of this mechanism was proposed by the group of Kahn for the copper case and yielded a value of ferromagnetic coupling in fair agreement with the experimental data, confirming at least the feasibility of the suggested ferromagnetic exchange pathway.[13]

Recently some exceptions to the ferromagnetic coupling have been reported both for Cu(II) complexes and nitronyl nitroxide radicals.[22,23,33] In particular for the latter antiferromagnetic coupling of 6 cm^{-1} was observed in a chelating nitronyl nitroxide triazole derivative. This suggests that the resulting coupling is actually the sum of two contributions, one from the direct overlap of the magnetic orbitals of the ligands with the *f* orbitals, which presumably yields an antiferromagnetic pathway, and the other from the

overlap to the *s* and *d* orbitals which gives a ferromagnetic pathway. The former may become dominant when the radical ligands become stronger donors.

6.5 First attempt of rationalization of coupling in rare-earth complexes

Following the rationalization of ferromagnetic coupling in Gd(III)-Cu(II) and Gd(III)-radical systems, Kahn first proposed a very simple model for the interaction between orbitally degenerate Ln(III) ions and radicals or Cu(II).[13] According to this model, such an interaction was predicted to be antiferromagnetic for the first half of the lanthanide series and ferromagnetic for the second half. The basis of this prediction was the assumption that the above explained mechanism of spin polarization should be active and dominant even for the other Ln(III) ions. This would again favor a parallel alignment of the electronic spin momenta of the lanthanides and of the species coupled to it. Such an alignment of the spin momenta would then lead to antiparallel alignment of the *J* momenta of the lanthanide for the first half of the series - for which $J=|L-S|$ - with respect to the spin *S*, that is to an overall antiferromagnetic interaction, while a parallel alignment of *J* and *S*, and then an overall ferromagnetic coupling, would occur one in the second half, for which $J=L+S$. This mechanism is schematized in Figure 6.1.

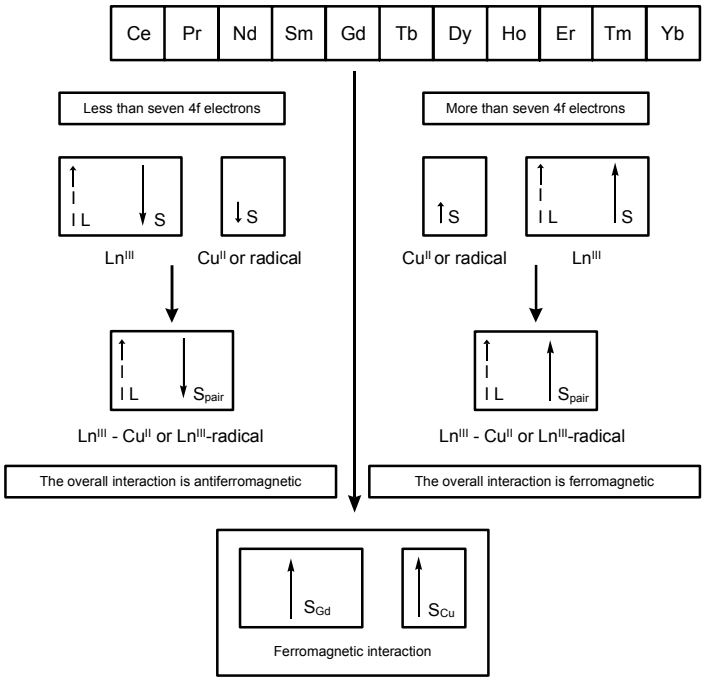

Figure 6.1 *Proposed scheme of coupling for Ln(III)-Cu(II) systems, later extended to Ln(III)-rad. After refs. [13]and[35]*

While this behavior has been recently confirmed for species containing lanthanide ions coupled to two nitronyl-nitroxides,[34,35] recently Kahn et al. showed, using the experimental approach outlined in paragraph 6.4, that for a series of chain compounds of general formula Ln_2Cu_3 such a prediction holds [45] for the whole series up to Dy but breaks down for Ho and the following lanthanides. A similar violation of that prediction was demonstrated by the group of Costes in a series of dinuclear complexes containing Cu(II) coupled to lanthanides for Tm(III) and Yb(III).[32]

6.6 Antiferromagnetic coupling in a Gadolinium(III)-Semiquinonato complex.

Following the considerations developed in paragraph 6.3 according to which stronger donors radical ligands may give rise to some overlap with *4f* orbitals, thus leading to enhanced contribution of the antiferromagnetic pathway to the resulting coupling, we decided to investigate the coupling of Gd(III) with the semiquinonato radical, which are well known to be stronger ligands than nitronyl-nitroxide.

The $Gd(HBPz_3)_2(DTBSQ)\cdot 2CHCl_3$ complex, (1), ($HBPz_3$= hydrotris pyrazolyl borate; DTBSQ= 3,5-di-*tert*-butyl-semiquinonate) was obtained by metathetical reaction between the parent metal-benzoato derivative[52] and 3,5-di-*tert*-butylcatechol in alkaline methanol. Recrystallization from chloroform-hexane mixtures yielded blue crystals of the above compound.

Cyclic voltammetry experiments in acetonitrile show that the complex undergoes a reversible one electron transfer redox process at -0.65 V and a not reversible one at +0.02 V vs Fc^+/Fc respectively. Both processes involve the coordinated dioxolene ligand, the reversible one being assigned to the semiquinonato-catecholato couple and the not reversible to the quinone-semiquinonato one. Once compared with the electrochemical properties of other metal-*o*-dioxolene complexes,[53,54] the observed behavior is that expected taking into account the different charge density of the metal acceptor. As a further support the electronic spectrum shows a band at 12,600 cm^{-1} and a pattern of bands in the region 26,400 - 28,400 cm^{-1}, which were suggested[54] to be internal transitions of the semiquinonato ligand.

6.6.1 X-Ray structure

Figure 6.2 shows an ORTEP view of the crystal structure of **(1)**, determined by X-ray crystallography. The asymmetric unit is the whole molecule, and each molecule crystallizes with two molecule of solvent in the orthorhombic space group $Pca2_1$. The coordination sphere around gadolinium comprises six nitrogen atoms from trispyrazolylborate ligands and two oxygen atoms from semiquinone. Gadolinium is eight coordinate, in a distorted square antiprism environment, O(2)N(5)N(2)N(7) lying approximately on one face and N(9)N(4)N(11)O(3) on the other one. The C-O bond distances are slightly shorter and the C19-C20 distances slightly longer than usually observed in semiquinonato metal complexes.[55,56].

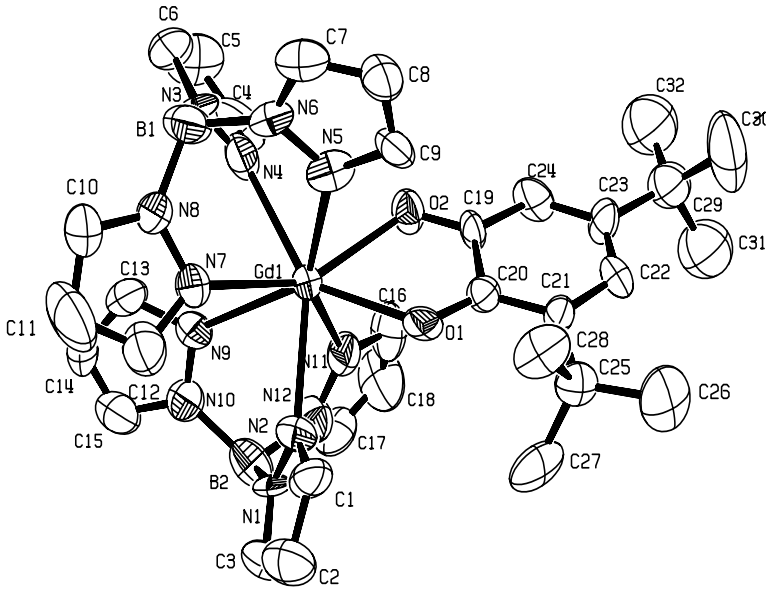

Figure 6.2 *ORTEP view of complex* ***(1)*** *(thermal ellipsoids at 50% probability); hydrogen atoms and solvent molecules are omitted for clarity*

Gd1-O1	*2.343*	*O1-Gd1-O2*	*67.7*
Gd1-O2	*2.354*	*O2-Gd1-N4*	*81.5*
Gd1-N4	*2.48*	*O1-Gd1-N2*	*73.1*
Gd1-N2	*2.503*	*O1-Gd1-N11*	*88.8*
Gd1-N11	*2.53*	*O2-Gd1-N11*	*73.8*
Gd1-N7	*2.53*	*N2-Gd1-N11*	*72.9*
Gd1-N5	*2.571*	*N4-Gd1-N7*	*79.5*
Gd1-N9	*2.585*	*N2-Gd1-N7*	*78.5*
C19-C20	*1.49*	*O1-Gd1-N5*	*75.6*
O1-C20	*1.27*	*O2-Gd1-N5*	*78.7*
O2-C19	*1.25*	*N4-Gd1-N5*	*72.3*
		N7-Gd1-N5	*71.3*
		N4-Gd1-N9	*75.4*
		N2-Gd1-N9	*74.4*
		N11-Gd1-N9	*69.3*
		N7-Gd1-N9	*72.1*

Table 6.2 *Selected bond lengths [Å] and angles [°] for complex* ***(1)***

6.6.2 Determination of exchange coupling in $Gd(HBPz_3)_2(DTBSQ)\cdot 2CHCl_3$

Magnetic susceptibility of (**1**) was measured in the temperature range 3-260 K and the corresponding plot of χT vs T is reported in Figure 6.3. The χT value at high temperature (about 7.9 emu K mol^{-1} at 260 K) is a bit lower than expected for a Curie behavior for two uncorrelated spins 7/2 and 1/2 with g=2.00 (8.25 emu K mol^{-1}), indicating that the two centers are still weakly interacting at this temperature. On lowering the temperature χT decreases, thus suggesting the presence of antiferromagnetic interactions between the two spin carriers, giving rise to an S=3 ground state and an S=4 excited state. It is also apparent that at T<10 K the value of χT is lower than expected for an S=3 state (5.98 emu K mol^{-1}): this can be attributed either to Zero Field Splitting of the ground state or to some weak antiferromagnetic interaction between the neighboring molecules. Both these effects were accounted for by using a phenomenological Weiss

correction.[57] The analytic expression with which we have fitted the experimental curve was then:

$$\chi_c = \frac{\chi}{1-\theta\chi} \tag{6.6.1}$$

where χ_c was calculated according to Van Vleck equation using the isotropic hamiltonian:

$$\mathbf{H} = J\mathbf{S_{Gd}}\cdot\mathbf{S_{SQ}} \tag{6.6.2}$$

With this formalism the two possible states, S=3 and S=4, are separated in energy by *4J*: a positive *J* value is obtained for an antiferromagnetic coupling and a negative one for a ferromagnetic coupling. The resulting expression for χ_c is then:

$$\chi_c = \frac{Ng^2\beta^2}{kT}\cdot\frac{84+180\exp\left(-\frac{4J}{kT}\right)}{7+9\exp\left(-\frac{4J}{kT}\right)} \tag{6.6.3}$$

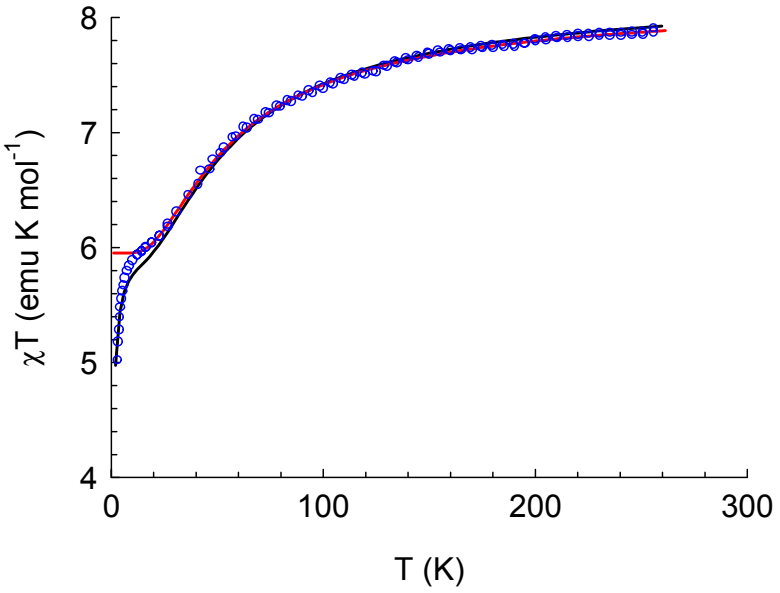

Figure 6.3 *Temperature dependence of χT for complex (**1**). The red line represents the best curve fit for data down to 10 K without assuming any correction for the low temperature decrease. The black line is the best fit curve taking into account a phenomenological correction for the decrease of χT observed at low temperature. Best fit parameters are reported in the text.*

The best fit to the experimental χT curve was obtained by using J= 13.3±0.5 cm^{-1}, θ=-0.05 ± 0.01 cm^{-1} with a global g value of 1.995 ± 0.005. Neglecting the low temperature portion of the curve and not considering the Weiss correction the best fit curve is actually the same down to 10 K, with J= 13.8±0.5 cm^{-1}.

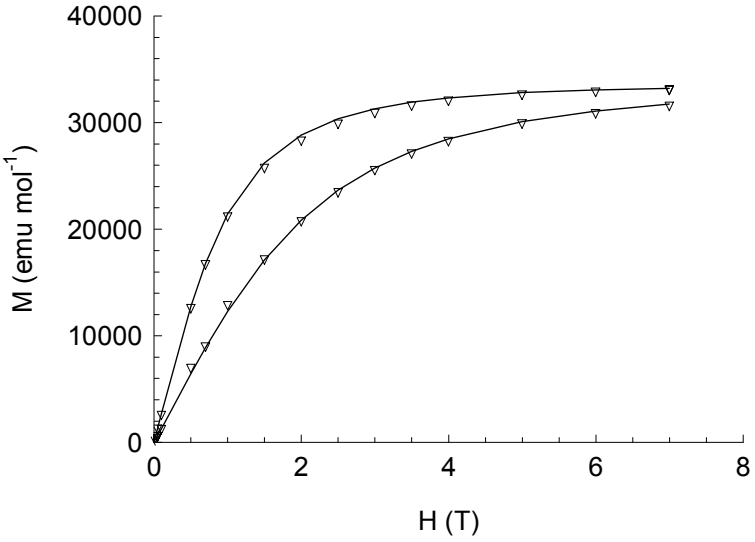

Figure 6.4 *Field dependent magnetization for complex (**1**) at 2.15 K and 4.5 K (upper and lower curve, respectively). The lines represent the Brillouin function for an S=3 state at the two temperatures. Inclusion of Zero Field Splitting values up to D=0.2 cm-1 does not change appreciably the simulated curve.*

These parameters indicate that the ground S=3 state is separated in energy from the excited one by about 80 K, thus being fully populated at low temperature, a picture which is confirmed by field dependent magnetization curves up to 7 T, measured at 2.15 K and 4.5 K (see Figure 6.4). These are indeed in good agreement with calculated Brillouin curves for a fully populated S=3 states, thus suggesting that Zero Field Splitting effects, if present, should be small (D<0.2 cm^{-1}).

The observed coupling confirms the prediction that stronger ligands may give rise to effective antiferromagnetic couplings with Gd(III). This behavior can be qualitatively justified assuming that the observed coupling is the sum of two contributions, one from the direct overlap of the magnetic orbitals of the ligands with the *f* orbitals of the lanthanide, which presumably yields an antiferromagnetic pathway, and the other from the overlap to the 6*s* and 5*d* orbitals which gives a ferromagnetic pathway by a spin-

polarization mechanism. The former may become dominant when the radical ligands become strong donors (as semiquinones).

6.7 Magnetic properties of $Ln(HBPz_3)_2$(3,5-DTBSQ) and $Ln(HBPz_3)_2$(tropolonato)

Following the results described in the previous paragraph for complex (**1**) we decided to synthesize the corresponding complexes of the remaining rare-earth ions, with the aim of investigating the different effects of exchange coupling and crystal field on their magnetic properties. We felt that this series might have some advantages with respect to similar compounds which have been studied up to now. Indeed, we have seen in previous paragraph that semiquinone ligands give rise to better overlap with *4f* orbitals and this results in larger antiferromagnetic contribution. This may be very useful to enhance the effects of the exchange with respect to those due to crystal field. Furthermore, while previously reported radical-rare earth complexes always involved more than one radical ligand (see e.g. [26,50]), these are the first isolated 1:1 rare-earth radical systems. For former systems the effects of the direct exchange between radical and rare earth is then masked not only by crystal field effects but also by the radical-radical exchange, whereas in the latter only the exchange interaction between rare earth ion and radical pathway is present. Finally, the observation of antiferromagnetic coupling in (**1**) prompted us to check if the Kahn model could successfully apply also to these systems: in this case a reverse pattern with respect to that described in Figure 6.1 should be observed.

As we have seen in paragraph 6.3 a quite diffuse experimental approach to separate the different contribution of crystal field and exchange coupling to the magnetic properties in rare earth-radical complexes involves the determination of magnetic properties of a corresponding complex in which the radical ligand is substituted by a diamagnetic analogue giving rise to comparable ligand field effects. For our complexes the diamagnetic analogue of semiquinones was found in tropolonato ligands, which presents comparable O-Ln-O bite angle and Ln-O distances with respect to semiquinonato ones.[52] The work presented in the following pages is then based on the comparison of magnetic properties and EPR spectra of complexes belonging to the homologous families $Ln(HBPz_3)_2$(3,5-DTBSQ) and $Ln(HBPz_3)_2$(Trp), where $HBPz_3$=

hydrotrispyrazolylborate, 3,5-DTBSQ = 3,5-di-*tert*-butylsemiquinone, Trp=tropolonate and Ln = Sm, Eu, Gd, Tb, Dy, Ho, Er and Yb. Both the derivatives of the rare earth series were structurally characterized by X-Ray diffractometry.

6.7.1 X-Ray structures of $Ln(HBPz_3)_2$(3,5-DTBSQ) and $Ln(HBPz_3)_2$(Trp)

The synthesis of tropolonate derivative was obtained following the synthetic procedure described in ref. [52]. Even if the series was reported to be isostructural on the basis of cell isomorphism[52] X-Ray analysis pointed out that Er(III), Ho(III), Eu(III) and Gd(III) crystallize in the tetragonal space group $P4_12_12$, whereas Sm(III), Tb(III), Dy(III) and Yb(III) crystallize in the expected space group $P2_12_12_1$ with the same cell parameters reported in ref. [52]. We then decided to solve the structure for one of the systems crystallizing in tetragonal group to check for possible structural differences. As the Holmium derivative yielded a very good set of data (see Experimental section) we solved the structure for this complex, Gd(III), Eu(III), Er(III) being assumed isostructural on the basis of cell parameters.

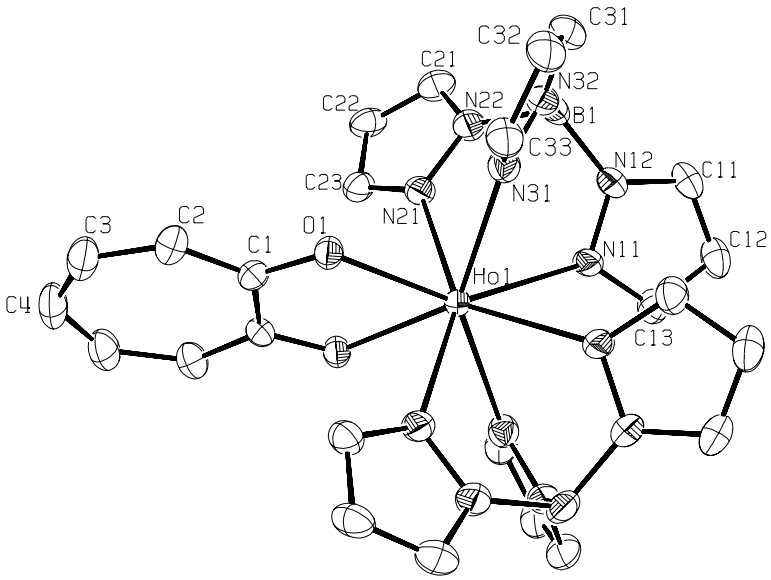

Figure 6.5 *Ortep view of $Ho(HBPz_3)_2$(3,5-tropolonate) Thermal ellipsoids shown at 30% probability. Only the atoms belonging to the asymmetric units have been labeled. Hydrogen atoms are omitted for the sake of clarity.*

The systems crystallize with 4 molecules per unit cell. A C_2 symmetry axis passes through the lanthanide ion and one of the carbon atom of the ligand (C4 in Figure 6.5):

the asymmetric unit is then half of the molecule, comprising one tris-pyrazolylborato group and half tropolonato ligand. The coordination sphere around the lanthanide ion comprises six nitrogen atoms from trispyrazolylborate ligands and two oxygen atoms from tropolonate: the lanthanide ion is as expected eight coordinated, in a slightly distorted square antiprism environment, O(1)N(11)$^{\#1}$N(21)$^{\#1}$N(31) (where the symmetry operation corresponding to #1 is -y+1,-x+1,-z+3/2) lying approximately on one face and the corresponding symmetric atoms on the other one. Bond distances and angles (Table 6.3) compare well with data reported in literature for systems crystallizing in orthorhombic space group $P2_12_12_1$.[52]

Ho1-O1	*2.292*	O1- Ho1 O1$^{\#1}$	*68.02*
Ho1-N31	*2.451*	O1- Ho1- N31	*136.40*
Ho1-N21	*2.500*	O1- Ho1- N31$^{\#1}$	*75.67*
Ho1-N11	*2.527*	O1- Ho1- N21	*76.75*
		O1- Ho1- N21$^{\#1}$	*80.73*
		O1- Ho1- N11	*145.40*
		O1- Ho1- N11$^{\#1}$	*122.18*
		N31- Ho1- N31$^{\#1}$	*146.58*
		N31- Ho1- N21	*74.31*
		N31- Ho1- N21$^{\#1}$	*113.93*
		N31- Ho1- N11	*75.31*
		N31- Ho1- N11$^{\#1}$	*77.50*
		N21- Ho1- N21	*152.77*
		N21- Ho1- N11	*134.95*
		N21- Ho1- N11$^{\#1}$	*71.24*
		N11- Ho1- N11$^{\#1}$	*70.27*

Table 6.3 *Selected bond lengths [Å] and angles [°] for Ho(HBPz$_3$)$_2$(Trp)* (#1 -y+1,-x+1,-z+3/2)

By slightly changing the recrystallization conditions with respect to that described in previous paragraph for the synthesis of (**1**), the unsolvated form of the complex Ln(HBPz$_3$)$_2$(3,5-DTBSQ) is obtained for Y(III) and all the Ln (III) ions from Sm(III) to

Yb(III).[§] Also in this case X-Ray structure solution was then necessary to check for possible structural differences with respect to solvated form (**1**) and to compare the structure with those of tropolonato derivative. The structure was solved and refined for Y(III) derivative, but the same unit cell was obtained for all the other derivatives, which will be then considered as isostructural with the former in the following.[58]

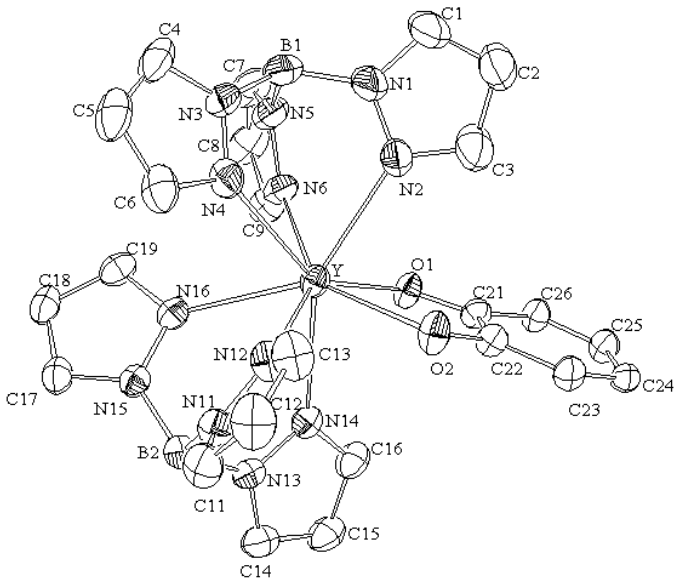

Figure 6.6 *Ortep view of Y(HBPz$_3$)$_2$(3,5-DTBSQ). Hydrogen atoms are omitted for the sake of clarity. Thermal ellipsoids are shown at 50% probability.*

Figure 6.6 shows an ORTEP view of the crystal structure of Y(HBPz$_3$)$_2$(3,5-DTBSQ) which crystallizes in the monoclinic system (P2$_1$/c), with four molecules per unit cell. The asymmetric unit is the whole molecule. In analogy to what observed for **(1)** and the tropolonato derivative the coordination sphere around Y(III) (or lanthanides) comprises six nitrogen atoms from trispyrazolylborate ligands and two oxygen atoms from semiquinone. The central ion is eight coordinated, in a slightly distorted square antiprism environment, O(2)N(4)N(2)N(12) lying approximately on one face and N(6)N(14)N(16)O(1) on the other one (see Figure 6.7).

The C-O bond distances are slightly shorter and the C19-C20 distances slightly longer than usually observed in semiquinonato-metal complexes (see Table 6.4), but this was found to be common in lanthanide-semiquinonate complexes.[59,60] Concerning the intermolecular contacts it should be noted that the four molecules of the unit cell present

[§] Tm(III) derivative was not synthesized but it is expected to be easily obtained

parallel pairs of semiquinone planes: these are quite far (12.2 Å) from each other. Finally, the smallest intermolecular distances between the magnetic centers (we actually suppose the spin density of the semiquinones being localized on the oxygens) are quite large: Ln-Ln 9.836 Å, Ln-O 8.310 Å, O-O 7.061 Å.

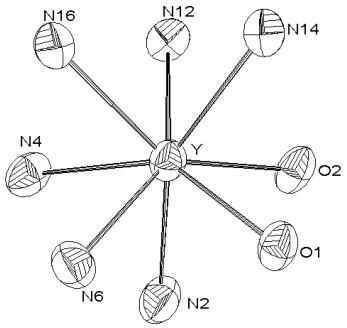

Figure 6.7 *Detail of the coordination environment of Y(HBPz$_3$)$_2$(3,5-DTBSQ), clearly showing the square-antiprismatic coordination sphere The same coordination is observed for Ho(HBPz$_3$)$_2$(Trp)*

Y-O1	2.296	O1-Y-O2	69.56	O2-Y-N2	75.79
Y-O2	2.317	O1-Y-N12	137.52	O2-Y-N16	143.64
Y-N12	2.456	O1-Y-N6	73.74	O2-Y-N14	79.25
Y-N6	2.457	O1-Y-N4	142.33	N12-Y-N6	147.01
Y-N4	2.510	O1-Y-N2	80.54	N12-Y-N4	77.50
Y-N2	2.512	O1-Y-N16	121.19	N4-Y-N16	72.65
Y-N16	2.528	O1-Y-N14	76.08	N4-Y-N14	138.39
Y-N14	2.533	O2-Y-N12	75.42	N6-Y-N2	76.06
C21-O1	1.282	O2-Y-N6	136.58	N6-Y-N16	76.42
C21-C22	1.463	O2-Y-N4	122.13	N6-Y-N14	113.57
C22-O2	1.282	N4-Y-N2	69.91	N2-Y-N14	150.45
		N2-Y-N16	137.47	N16-Y-N14	71.34

Table 6.4 *Selected bond lengths [Å] and angles [°] for Y(HBPz$_3$)$_2$(3,5-DTBSQ)*

It should be noted that bond distances and angles of the coordination sphere (Table 6.4) of this derivative - which are presumably the relevant one in determining ligand field effects - compare quite well with the homologous distances found in the tropolonate derivative, even if the Y-O distances for $Y(HBPz_3)_2$(3,5-DTBSQ) are somewhat longer than observed in the corresponding Ho-O ones in $Ho(HBPz_3)_2$(Trp) (average distances of 2.31 Å vs 2.24 Å). This small difference may however be due to the different ionic radius of the two ions which we have employed for the structure solution. Interestingly, the O-Ln-O angle turned out to be almost the same for the two families.[52] The strong similarity between the two structures is made evident in Figure 6.8. On the basis of crystal structure analysis we may then conclude that, for our purpose, the assumption of similar ligand field effects in the two families is completely justified.

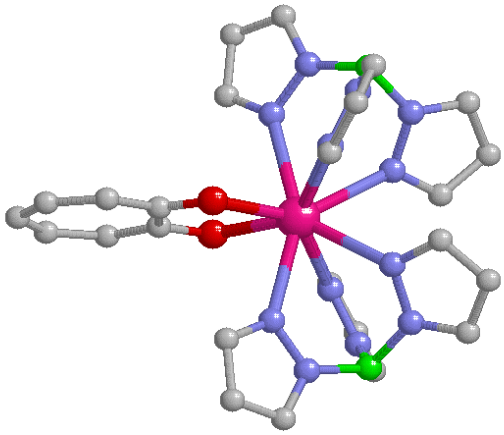

Figure 6.8 *A comparison of molecular structure of $Ln(HBPz_3)_2$(3,5-DTBSQ) and $Ln(HBPz_3)_2$(Trp) evidencing the similar coordination spheres.*

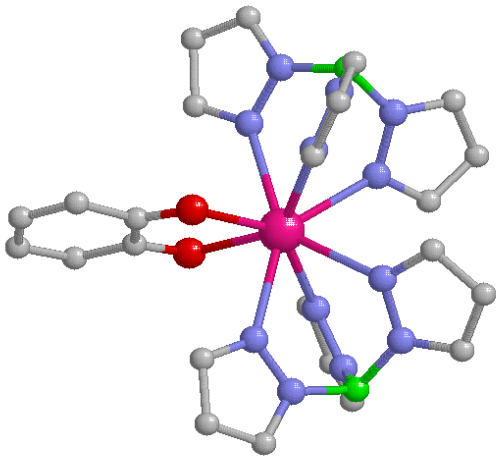

6.7.2 Origin of the anisotropy in Gd(III) derivative

We begin the analysis of ligand field effect in rare-earth semiquinonato complexes by the simplest case, i.e. Gd(III), comparing the results obtained by EPR, both X-Band and HF-EPR, for tropolonate and semiquinonate derivative. It should be stressed here that we employed the unsolvated form of the semiquinonato adduct described in the last paragraph, but a check of its magnetic properties did not show any appreciable difference with respect to those observed for the solvated form **(1)** described in paragraph 6.5.

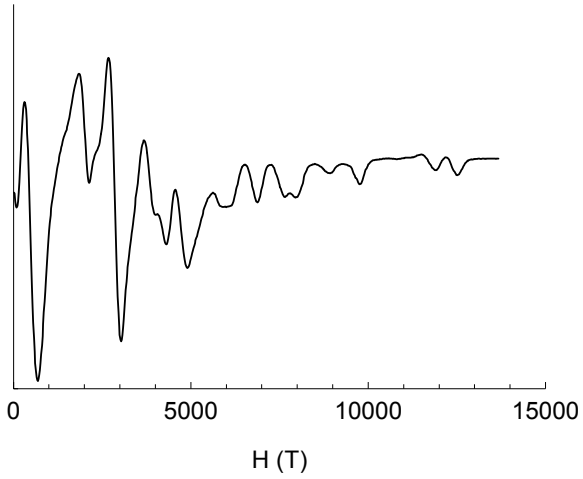

Figure 6.9 *Experimental X-Band EPR spectra of GdSQ at 4K.*

The first step was aimed at the determination of the magnetic anisotropy of $Gd(HBPz_3)_2$(3,5-DTBSQ), hereafter ***GdSQ***. Preliminary X-band powder investigation (see Figure 6.9) showed a quite complex spectrum extended up to 13000 G. Notwithstanding the complexity of the obtained pattern, some conclusion could be drawn by considering the extension of the spectrum and the two fingerprinting high-field transition, separated by about 900 G. Attempts of simulation (not shown) yielded the correct extension of the spectrum for a value of $D \approx 0.16$ cm^{-1} while a largely rhombic contribution proved necessary to get the correct splitting for the two high-field transitions ($E/D \approx 0.25$).

The obtained simulation was however not very satisfactory and we then turned to HF-EPR to get more information. Spectra recorded by HF-EPR at different frequencies (95, 190 and 285 GHz) showed the typical features of a rhombic spectrum (see Chapter 2) even if at higher frequency a large quench of the intensity of the feature around g=2.00 is observed (see Figure 6.10). This phenomenon has been tentatively attributed to

propagation effects of the incident microwaves through the sample pellet: these effects may become important when the dimension of the sample is close to the wavelength of the exciting radiation and this may explain why it is observed with major importance at higher frequency. Several authors have evidenced these effects to be active in a number of solid state systems investigated through HF-EPR.[61]

The line-line separation between neighboring lines is consistent with a *D* value around 0.122 cm^{-1} and we then started our analysis by using this parameter and a ratio E/D=0.3. The best simulation of the whole dataset was obtained by using *D*= 0.122 cm^{-1}, E/D= 0.287.

As we have seen in Chapter 3 the anisotropy of exchange coupled systems originates from three different contributions, namely single-ion anisotropy, through-bond and through-space (i.e. dipolar) interaction between the two magnetic centers. In our case the single ion contribution, which is due to ligand field effects, can only arise from Gd(III) ions, as the radical is a S=1/2 spin. Thus the global single ion contribution is $\mathbf{D_{SI}} = d_{Gd}\mathbf{D_{Gd}}$, where d_{Gd} may be calculated by projection techniques[62] to be d=1.125.

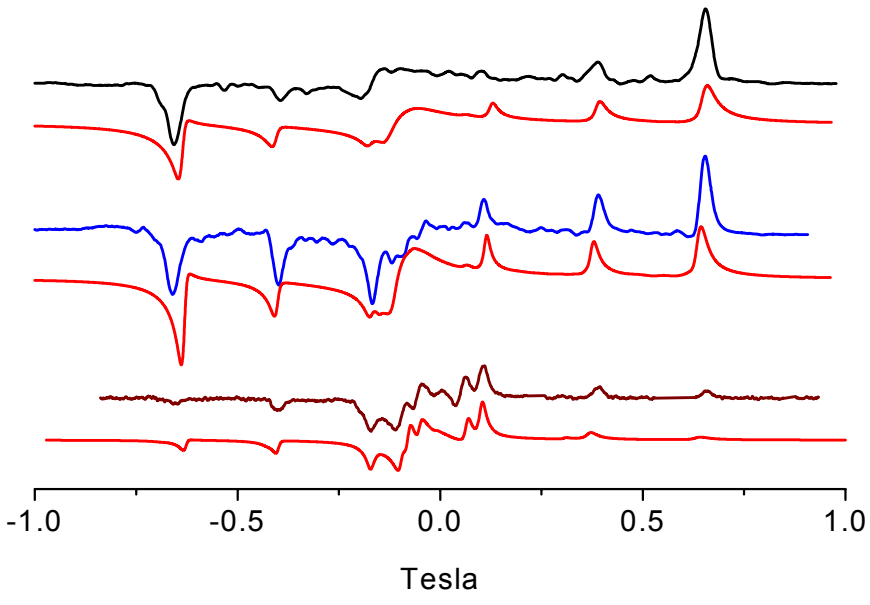

Figure 6.10 *HF-EPR spectra of* ***GdSQ*** *recorded at 95 (lower) 190 (middle) and 295 GHz (upper) and 10 K, normalized on a 2 Tesla scale (g=2.00 at H=0 T). For each frequency, lower spectrum is the simulated and the upper is the experimental one.*

An estimation of $\mathbf{D}_{Gd}$, and then of the contribution of ligand field in determining the anisotropy of ***GdSQ***, may be obtained in this case by measuring the anisotropy of the corresponding tropolonato complex, hereafter ***GdTrp***. Preliminary characterization of this system through magnetic measurements suggested that only a small ZFS should be present. Indeed, magnetization curves (Figure S6.1) are in good agreement with what expected for an S=7/2 system with small Zero Field Splitting, which may account also for the small decrease of the χT value at T< 10 K (Figure S6.2). The low temperature X-Band EPR spectrum, shown in Figure 6.11, was a bit more clear than the corresponding one of ***GdSQ*** and quite good simulations were obtained by assuming $|D|$= 0.122 cm^{-1} and E= 0.028 cm^{-1}.

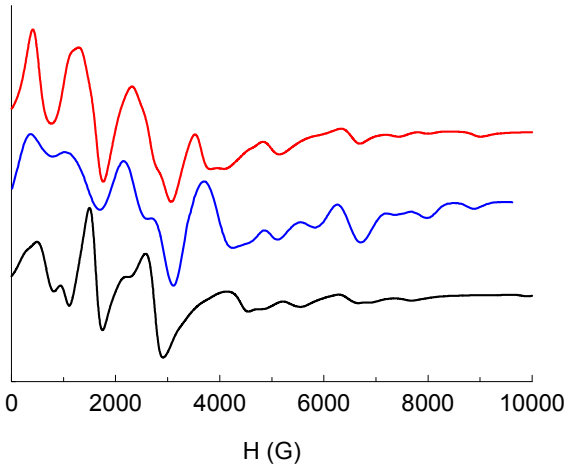

Figure 6.11 *Central line is the experimental X-Band EPR spectrum of GdTrp at 4K. Lower curve is the best simulation of X-band spectra, upper is the simulated spectrum obtained by using parameters derived by simulations of 95 GHz spectrum (corresponding parameters are reported in the text)*

Also in this case, however, HF-EPR spectroscopy provided a strong simplification of the spectra and more reliable information on the anisotropy of the complex, including the sign of *D* value. The spectrum recorded at 95 GHz and 10 K is showed in Figure 6.12 and clearly displays the features of a considerably rhombic system with negative ZFS. Indeed, it is slightly more extended at low field with respect to high field and large intensity of the g= 2.00 line is clearly observed. The spectrum could be simulated in a quite satisfactory way by imposing g=1.99 - which is common for Gd(III) ions [63]- D=-0.128 cm^{-1} and E =0.021 cm^{-1}, thus in quite good agreement with parameters obtained by

simulation of low temperature X-band EPR spectrum. A comparison of the simulation of the latter with the two sets of parameters is shown in Figure 6.11.

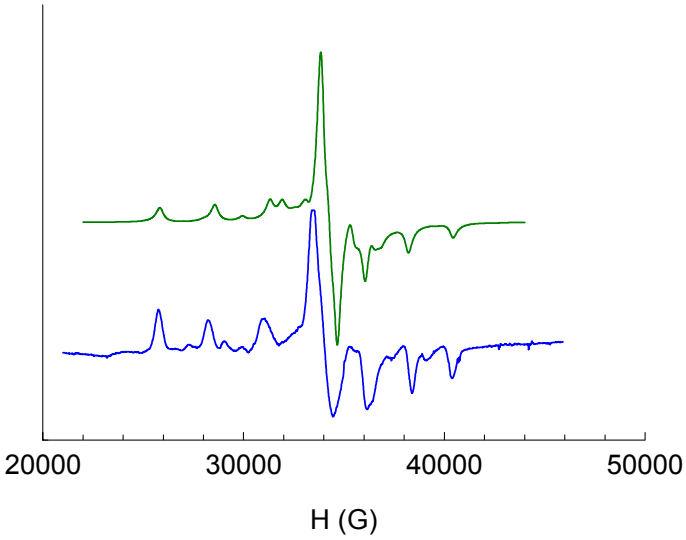

Figure 6.12 *HF-EPR spectra of GdTrp recorded at 95 GHz and 10 K.. Lower spectrum is the experimental one and the upper is simulated (parameters reported in the text).*

By projecting the obtained value of zero field splitting parameters for ***GdTrp*** on the S=3 ground state of ***GdSQ*** complex the contribution of single ion anisotropy to the global anisotropy of the complex is calculated as $\mathbf{D}_{SI}$=0.144 cm^{-1}, which is larger than the anisotropy measured through HF-EPR for ***GdSQ***. This may be due to the fact that anisotropic exchange contribution, which was found to play a major role in the determination of the anisotropy of Cu(II)-semiquinonato adducts[64], sums up to single ion contribution in a way which reduces the global anisotropy.

6.7.3 Magnetic properties of orbitally degenerate Ln(III) derivatives

Among all the systems we have synthesized we will briefly summarize in the following the preliminary interpretation of the results obtained by magnetic measurements and EPR spectroscopy for Ln(III)= Sm, Eu, Ho, Er, Yb. Experimental magnetic characterization has been performed also for Dy and Tb but no analysis of the data concerning these two systems has been yet attempted.

a-Samarium

The χT vs T curves of the Sm(III) derivatives are shown in Figure 6.13. As expected, the curve for the tropolonate derivative is markedly temperature dependent, due to the progressive population on increasing temperature, of the excited multiplet $^6H_{7/2}$. The room temperature value for the tropolonate complex (full circles) is 0.28 emu K mol^{-1}, a bit lower than the values reported in literature (0.3 emu K mol^{-1}) and the theoretical value of 0.32 emu K mol^{-1} expected for this ion.[38]

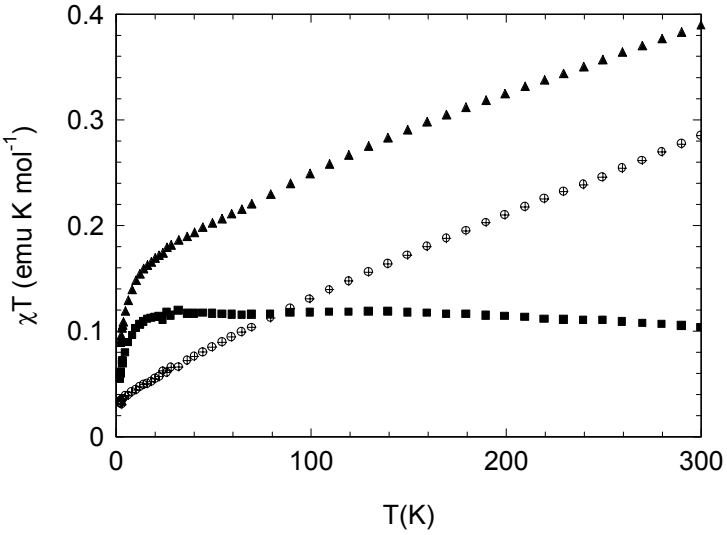

Figure 6.13 *χT vs. T curve for Sm(HBPz$_3$)$_2$(3,5-DTBSQ) (full triangles) and Sm(HBPz$_3$)$_2$(Trp) (crossed circles) and corresponding $\Delta\chi T$ values (full squares).*

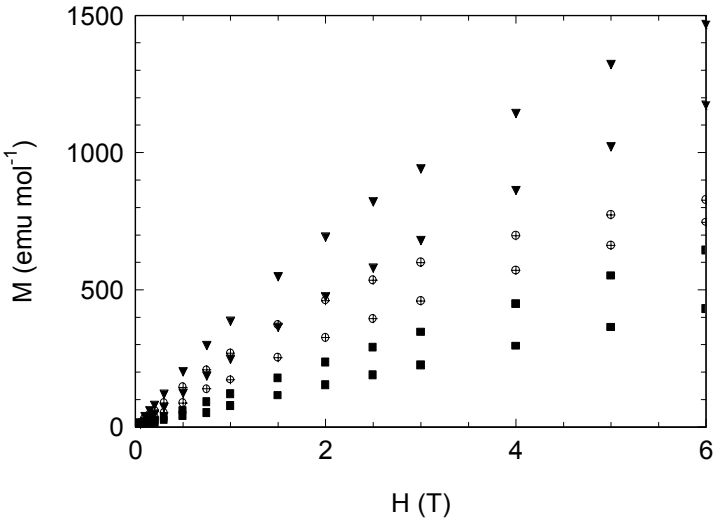

Figure 6.14 *M vs. H curves at 2.5 K and 4.5 K for Sm(HBPz$_3$)$_2$(3,5-DTBSQ) (full triangles) and Sm(HBPz$_3$)$_2$(Trp) (crossed circles) and corresponding ΔM values (full squares)*

The corresponding curve for the semiquinonato complex parallels that of tropolonato derivative for almost the whole range of temperature, indicating that, if present, exchange effects should be quite small, while crystal field effects are much probably the same in the two complexes. At low temperature a small decrease of $\Delta\chi T$ is observed, which may suggest an antiferromagnetic coupling. This behavior seems to be confirmed by the very small value of ΔM obtained by comparison of the two magnetization curves at low temperature. It is worth pointing out at this point that the difference between the two experimental χT curves is however much lower than expected for an unpaired radical and the results we suggest should be considered with much caution.

b- Europium

A similar situation is encountered in the case of the two Eu(III) complexes. Indeed, the χT of tropolonato derivative shows a large decrease on decreasing temperature due to the progressive depopulation of the excited multiplet $^7F_1$. This curve may be calculated according to the free ion approximation:[36]

$$\chi_{Eu} = \frac{\sum_{J=0}^{6}(2J+1)\chi(J)\exp[-\lambda J(J+1)/2kT]}{\sum_{J=0}^{6}(2J+1)\exp[-\lambda J(J+1)/2kT]} \qquad (6.7.1)$$

Where λ is the spin orbit-coupling coefficient and $\chi(J)$ is given by:

$$\chi(J) = \frac{Ng^2\beta^2 J(J+1)}{3kT} + \frac{2N\beta^2(g_J-1)(g_J-2)}{3\lambda} \qquad (6.7.2)$$

and g_J was defined in (6.2.3). The best simulation of the experimental χT curve was obtained by using $\lambda = 290 \pm 2$ cm^{-1}, which is in agreement with value obtained for other radical adducts.[27]

Also in this case the χT curves of the two derivatives are parallel in a wide range of temperature, thus indicating a strict similarity of crystal field effects. However, the

behavior of $\Delta\chi T$ suggest at first sight a weak ferromagnetic interaction. the same caveat we put forward for Sm(III) complexes remains valid here, as the value of $\Delta\chi T$ at room temperature is much smaller than expected for an uncoupled radical spin (0.375 emu K mol^{-1}). Furthermore, at temperature below 10 K a decrease of $\Delta\chi T$ is observed and, what seems more important, the *M* vs *H* curve of ***EuSQ*** (Figure S6.3) yields magnetization value lower than expected for a simple S=1/2 spin and does not saturate, indicating that – at least at low temperature – an antiferromagnetic process is likely to be active. Finally, the EPR spectrum of the semiquinonato derivative just show the expected radical signal at low temperature, broadened by the interaction with Eu(III) (Figure S6.4).

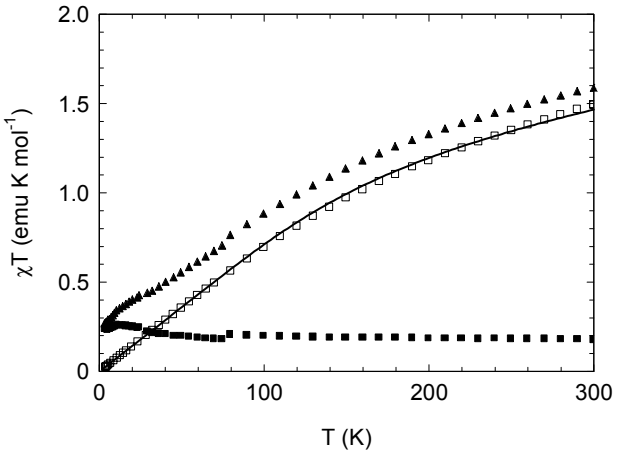

Figure 6.15 *χT vs. T curve for Eu(HBPz$_3$)$_2$(3,5-DTBSQ) (full triangles) and Eu(HBPz$_3$)$_2$(Trp) (empty squares) and corresponding $\Delta\chi T$ (full squares). The continuous line is the best simulation curve obtained for Eu(HBPz$_3$)$_2$(Trp) in the free-ion approximation by considering the depopulation of excited level $^7F_1$ (parameters reported in the text) on decreasing temperature*

c-Holmium

The χT vs. T curves of the Ho(III) derivatives are shown in Figure 6.16. The room temperature value for the tropolonate complex (full circles) is 13.44 emu K mol^{-1}, lower than the values reported in literature (13.75 emu K mol^{-1}) and the theoretical value of 14.00 emu K mol^{-1} expected for this ion (see Table 6.1). Due to depopulation of the higher states, split by the crystal field, the χT value slowly decreases on lowering temperature until 90 K and then begins to drop, reaching a value of 2.40 emu K mol^{-1} at 3.1 K. The room temperature χT value of the semiquinonate derivative differs from the tropolonato one for a value of 0.372 emu K mol^{-1} for Ho(III). This is in very good agreement with the expected 0.375 emu K mol^{-1} for an unpaired radical. It is also clear that the curves of the tropolonate derivative and of the radical derivative are almost

parallel in a large range of temperature, thus indicating that the crystal field effects are, in first approximation, the same. The deviations of the $\Delta\chi T$ curve from the value of 0.375 emu K mol^{-1}, which are becoming important at temperature lower than 100 K should then be attributed to exchange coupling between the rare earth ion and the radical. In detail, the difference curve shows that two different processes are active: at higher temperature (120-22 K), an antiferromagnetic coupling is dominant, reducing the χT of the ***HoSQ*** complex to a value lower than that of ***HoTrp***. At temperatures lower than 22 K the reverse situation occurs and $\Delta\chi T$ increases to reach a positive value. The non-monotonic behavior of the $\Delta\chi T$ curve, which is quite surprising at a first glance, may be attributed in principle to two different phenomena. The first is the existence of different processes contributing to the coupling, i.e. the effects of higher order anisotropic terms in the exchange hamiltonian which are becoming more important on lowering temperature. The second is the possibility, which cannot be completely ruled out, of having some significant difference between the crystal field effects affecting the rare earth ion in the coupled and in the uncoupled species. These differences may become more important at lower temperatures, thus leading to this somewhat unexpected behavior of the $\Delta\chi T$ curves. The dominating ferromagnetic interaction is also evident in the comparison of the low temperature magnetization curves, which results in positive value of ΔM vs H, which passes through a maximum at 1 T (Figure S6.5).

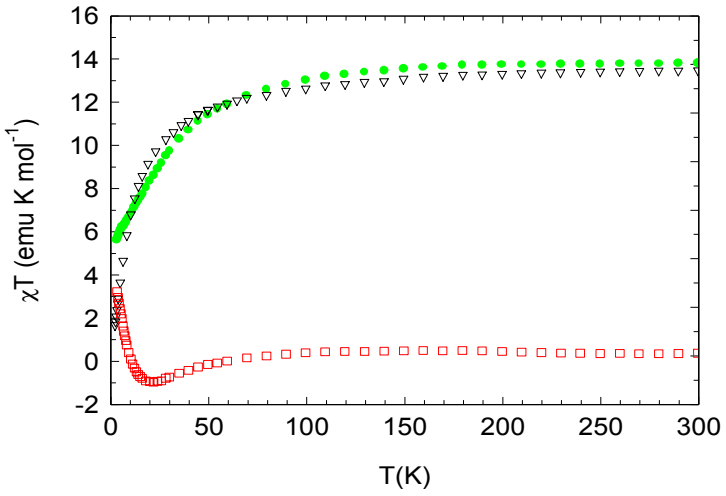

Figure 6.16 *χT vs. T curve for Ho(HBPz$_3$)$_2$(3,5-DTBSQ) (empty triangles) and Ho(HBPz$_3$)$_2$(Trp) (full circles), with corresponding $\Delta\chi T$ (empty squares) curve.*

The tropolonate derivative, ***HoTrp*** was found to be EPR-silent in X-Band at 4.2 K. This is not completely surprising, as Ho(III) (L=6, S=2, J=8) spectra have been often interpreted in terms of a pseudo S=1 spin, with very anisotropic *g*-value and a sizeable Zero Field Splitting term of the spin hamiltonian.[65] Actually one may then assume that this ZFS is too strong for a signal to be observed in X-Band EPR. The semiquinonate derivative (Figure 6.17) shows an interesting spectrum, with well defined features at low field, thus indicating that some coupling is active in modifying the magnetic characteristic of the system.

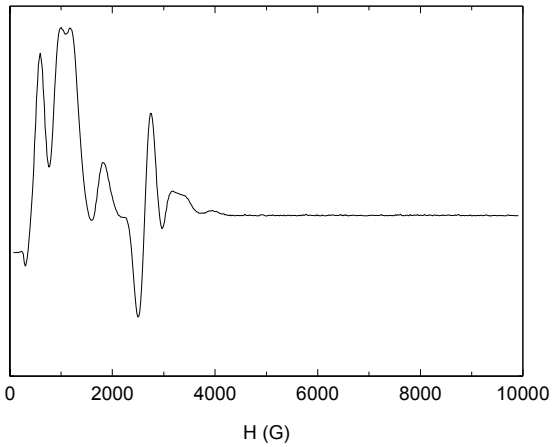

Figure 6.17 *X-Band EPR spectrum of Ho(HBPz$_3$)$_2$(3,5-DTBSQ) complex, recorded at 9.23 GHz and 4.2 K*

Also HF-EPR were recorded for this complex, showing differnt features split by large hyperfine coupling with the I=7/2 nuclear spin of ^{165}Ho [65], but their interpretation has not yet been accomplished.(Figure S6.6)

d-Erbium

Er(III) is a $^4I_{15/2}$ ion and the expected χT value at room temperature is around 11.1 emu K mol^{-1} (see Table 6.1). The measured value (Figure 6.17) is then in good agreement with this prediction and at room temperature the difference between the experimental chit curves of the two derivatives ($\Delta\chi T$=0.39 emu K mol^{-1}) well agrees with the expected value for an unpaired radical. Being well established on the basis of the previous analysis that the crystal field effects in the two derivative should be similar the observed behavior of $\Delta\chi T$ curve as a function of temperature, which monotonically

decrease on lowering temperature below 100 K, reaching a value as low as -3.5 emu K mol^{-1} at 3 K should be considered a clear signature of antiferromagnetic coupling.

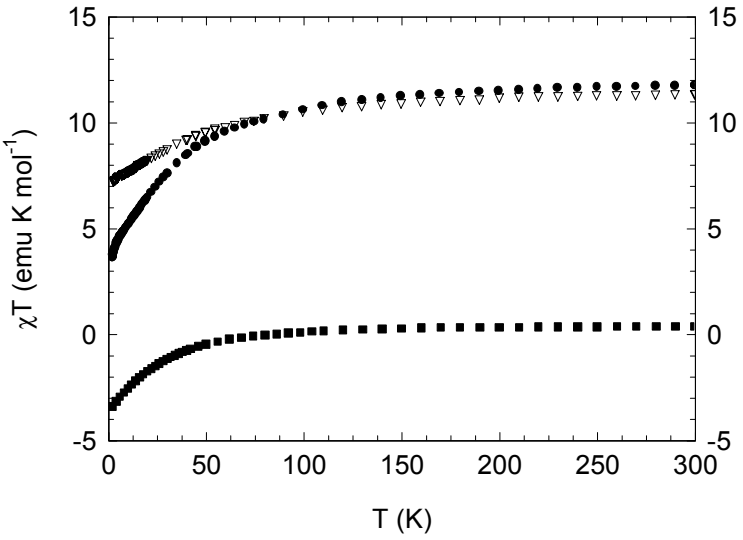

Figure 6.18 *χT vs. T curve for Er(HBPz$_3$)$_2$(3,5-DTBSQ) (empty triangles) and Er(HBPz$_3$)$_2$(Trp) (full circles) and corresponding $\Delta\chi T$ curve (full squares).*

e-Ytterbium

The χT curve for the tropolonato derivative, ***YbTrp*** (Figure 6.19) is only starting to level at the value of 2.54 emu K mol^{-1} at 300 K; the obtained value is in good agreement with the theoretical one of 2.57 emu K mol^{-1} (see Table 6.1). Due to depopulation of the higher states, split by the crystal field, the χT value of ***YbTrp*** derivative slowly decreases on lowering temperature until 90 K and then begins to drop, reaching a value of 2.40 emu K mol^{-1} at 3.1 K. The measured value of χT for semquinone derivative, ***YbSQ***, differs from that of ***YbTrp*** for a value of 0.377 emu K mol^{-1}, fully consistent with the difference being due to an unpaired radical. The value of χT for ***YbSQ*** is decreasing without abrupt change on lowering temperature down to 6 K and then falls down reaching a value of 1.55 emu K mol^{-1} at 2.45 K. As a consequence, $\Delta\chi T$ value is increasing on lowering temperature from 100 K to 16 K, thus indicating that ferromagnetic coupling between radical and rare earth ion is dominant in that range of temperature. The $\Delta(\chi T)$ value is then decreasing below 16 K, reaching the quite large negative value of –0.67 emu K mol^{-1} at 2.45 K. The negative value indicates that some kind of antiferromagnetic coupling is active in this temperature range, yielding a value for the χT of the ***YbSQ*** lower than the one observed for the ***YbTrp*** complex. It is not only the $\Delta\chi T$ which shows a completely reversed behavior with respect to Ho(III); indeed, the comparison of the magnetization

curves for ***YbTrp*** and ***YbSQ*** of *M* vs *H* curve evidences a larger magnetization for ***YbSQ*** than for ***YbTrp***, the difference being maximum around 1 T (Figure S6.7).

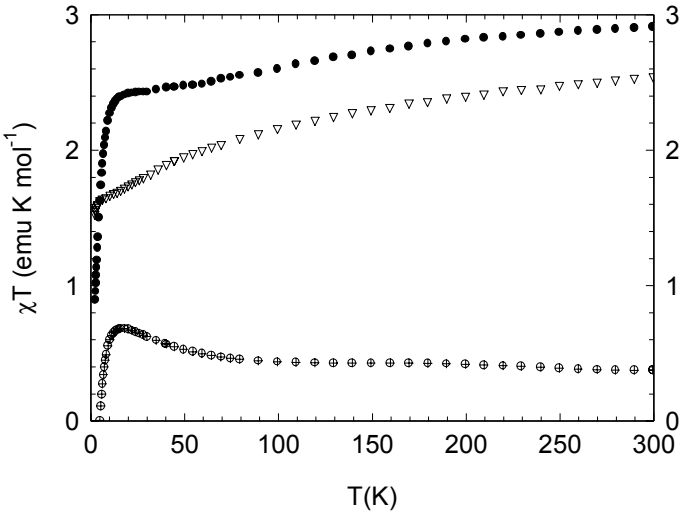

Figure 6.19 *χT vs. T curve for Yb(HBPz$_3$)$_2$(3,5-DTBSQ) (empty triangles) and Yb(HBPz$_3$)$_2$(Trp) (full circles) and corresponding ΔχT curve.*

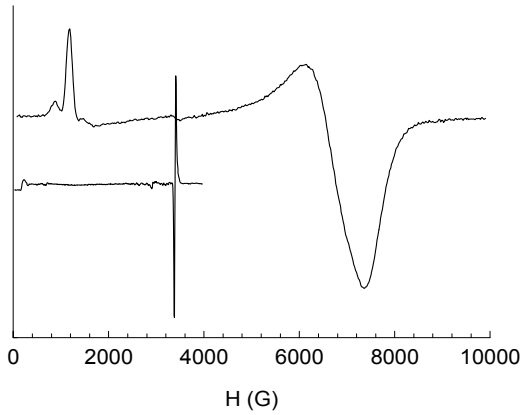

Figure 6.20 *X-Band EPR spectrum of Yb(HBPz$_3$)$_2$(3,5-DTBSQ) upper and complex, recorded at 9.23 GHz and 4.2 K*

The X-Band EPR spectrum of the tropolonate derivative of Yb(III) is shown in Figure 6.20. A very intense, perpendicular type transition is observed at high field (g=1.01), while three parallel features are well resolved at low field (g=7.54, 5.51, 4.52, respectively). As Yb(III) is a system with even multiplicity in principle only one Kramers doublet should be populated at low temperature, but this will be a complex mixture of various $|7/2,\pm M>$ states (neglecting in first approximation the contribution of the higher energy $^2F_{5/2}$ state). The degree of mixing is determined by the point-group symmetry at the rare-earth ion. This quite complex spectrum may then be explained considering the

low crystal field symmetry and the admixing of some low-lying excited doublets.[65] The spectrum of the ***YbSQ***, shown also in figure 6.20, is completely different, showing a weak transition at very low field (H = 185 G) and a narrow, intense feature centered at g=2.00 (H=3300 G).

We pointed out in the first paragraphs of this chapter that up to now the only qualitative model to explain the coupling between lanthanide ions and radicals was the extension to these systems of the model that Kahn put forward for Cu(II)-Ln(III) complexes. However, in our case the situation was completely different with respect to the preliminary assumption of Kahn model, as an antiferromagnetic coupling was observed for Gd(III) derivative with semiquinone. In agreement with these premises the purely qualitative analysis of the 5 different rare earth ions shows that the sign of the coupling seems not to follow any trend. In particular it has not been possible to find out any relation between the number of unpaired electrons and the position in the periodical table, i.e. whether the rare earth ion belongs to the first half or the second half of the lanthanide series. Indeed, both Eu(III) and Ho(III) were found to behave in a completely opposite way with respect to Sm(III) and Yb(III) respectively, while antiferromagnetic coupling is observed for Er(III).

6.8 An asymmetric spin cluster containing two Gd(III) ions and four radical centers

In order to extend our investigation to the design and synthesis of gadolinium semiquinonato systems containing more than two interacting magnetic centers, we have attempted to obtain a mononuclear bis(semiquinonato)-gadolinium complex.

Following this approach, solid compounds of formula $Gd(HBPz_3)(DTBSQ)_2$ were obtained as different solvates. Blue microcrystalline powders of $Gd(HBPz_3)(DTBSQ)_2$ stoichiometry precipitate when mixtures of a Gd(III) salt, potassium hydrotrispyrazolylborate and 3,5-di-*tert*-butyl-*o*-catechol are allowed to react in 1:1:2 ratios in basic methanol. Charge balance considerations suggest the presence of two semiquinone ligands. This was confirmed by the electronic spectrum in dichloromethane which shows a large band at 13,000 cm^{-1} (ε = 1,045 $M^{-1}\cdot cm^{-1}$), and a pattern of bands at higher energy, the most intense centered at 26,700 cm^{-1} (ε = 6,965 $M^{-1}\cdot cm^{-1}$), another one at 27,900 cm^{-1} (ε = 6,340 $M^{-1}\cdot cm^{-1}$) and a shoulder at 29,000 cm^{-1}. All these bands have

been assigned as internal transitions in the semiquinonato ligand, as it has already been reported before.[54,60]

Recrystallization at low temperature in a hexane/chloroform mixture allows the formation of blue crystals of formula $Gd_2(HBPz_3)_2(DTBSQ)_4 \cdot CHCl_3$ (**2**). The formula was determined by X-Ray crystal structure described below. Similar solvates were obtained from dichloromethane and 1,2-dichloroethane. In all the solvents investigated we have always observed the formation of the dinuclear complex, thus suggesting that **(2)** is thermodynamically favored with respect to the mononuclear complex with the same Gadolinium : semiquinone ratio. Unfortunately the reactivity of this complex as well as its solubility properties are strongly limiting our investigation in other solvents.

6.8.1 X-Ray structure

Notwithstanding numerous attempts no really good crystals could be isolated from the solutions, and therefore the X-ray crystal structure determination is of low quality. It cannot be used to describe fine details, but certainly it provides a sufficient frame for the description of the magnetic properties. Indeed X-Ray diffraction structure determination showed that the correct formulation of the complex is $Gd_2(HBPz_3)_2(DTBSQ)_4$, (**2**).

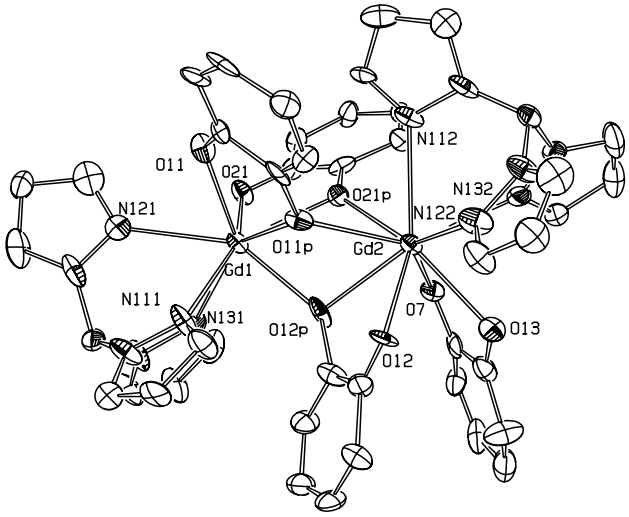

Figure 6.21 *Ortep View of (2). Thermal ellipsoids are shown at 25% of probability for clarity. For the same reason, hydrogen atoms and tert-butyl group were omitted.*

The ORTEP view of the crystal structure of (**2**) is shown in Figure 6.21. As mentioned above, the molecular unit is dinuclear. The complex is asymmetric and the

two metal ions exhibit two different coordination numbers. The coordination number of Gd(1) is eight, with a geometry which can be described as a distorted square antiprism, while Gd(2) is surrounded by nine donor atoms which define a distorted tricapped trigonal prism. The asymmetry is associated also with the semiquinone ligands: three of them are bridging, with one of their oxygen atoms, the two Gd(III) ions, while the fourth is bound, as shown in Figure 6.22, to one metal ion.

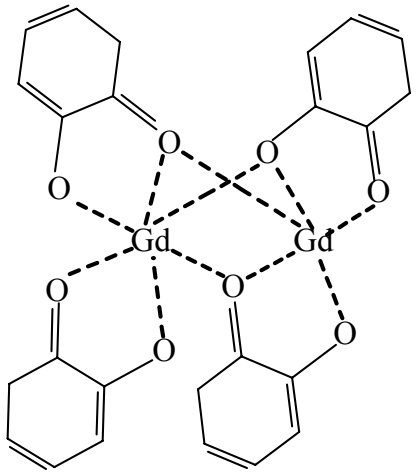

Figure 6.22 *Bond scheme of semiquinones and Gadolinium ions in (**2**).*

One of the oxygen atoms of the bridging semiquinones connects in a *μ-1,2* fashion the two gadolinium ions, while the other oxygen is bound to only one metal ion. The bridging semiquinones bind with both oxygen atoms to one gadolinium, and one of them is bound also to the other gadolinium ion. This asymmetric way of ligating has already been reported for both catecholate and semiquinone complexes formed by these ligands with transition metal ions.[55,56] The coordination polyhedron around Gd(1) is defined by three nitrogen atoms and four oxygen atoms of two chelating semiquinones, and one oxygen atom of the third semiquinone. The coordination polyhedron of Gd(2) is defined by three nitrogens of hydrotrispyrazolylborate, two oxygens of the non-bridged semiquinone, two *μ-1,2* bridging oxygens of two different semiquinones and other two oxygens of the third bridging semiquinone.

The Gd(1)-Gd(2) distance (3.755 Å) is shorter than usually observed in Gadolinium dimers reported in the literature,[66,67] but somewhat longer than the Gd-Gd distance recently reported in a dinuclear complex synthesized with phenolate ligands.[68]

It is an usual procedure to derive the oxidation state of dioxolene units bound to metal ions from the values of the distances between the two oxygen-bound carbons and from C-O links. [55,56] Interestingly, the distances found here for the chelating non-bridging semiquinonate are in agreement with the ones reported for the analogue 1:1 Gd : semiquinonate mononuclear complex.[60] The C-C distances in that complex are slightly larger and the C-O ones slightly shorter than usually observed in transition metal ions semiquinonate complexes. [55,56] For the bridging semiquinones the C-O distances involving the *μ-1,2* bridging oxygens are long (1.30(3), 1.30 (2), 1.39 (3) Å), while the distances involving the non-bridging oxygens are shorter (1.24(3), 1.29(2), 1.25(3) Å). The corresponding C-C bonds vary from 1.40(3) to 1.54(3) Å. It is apparent that, given the poor quality of the structure determination and the complex nature of the molecule, the bond distances alone cannot provide unambiguous evidence of the nature of the dioxolene ligands. Additional evidence will be obtained from the analysis of the HF-EPR and magnetic data to be described below. Considering this, and the complexity of the structure of **(2)**, with dioxolene units bridging between Gadolinium ions, attention must be paid in deriving the oxidation state of the bridging ligands from the values of these distances. However, the investigations carried on in solid state on complex **(2)** to be discussed below remove any ambiguity about the presence of only radical ligands.

As far as we know, this is the first structure of a dinuclear unit involving both a rare earth ion and a paramagnetic ligand which is reported. A similar asymmetric structure has been recently described with Gd(III) ions, but this involved a diamagnetic hexadentate ligand.[68] According to the classical chemical view, this complex can be seen as a donor-acceptor self adduct of an amphiphilic molecule. It should be stressed however that in general these interactions lead to a symmetric di- or poly-nuclear adduct and not to an asymmetric one as it is observed in this case.[4] We believe that the asymmetric nature of this complex may therefore allow the synthesis of heterodinuclear derivatives as a result of a simple acid base reaction. The structure of the resulting products should be dictated by the different acidity properties of the two different metal acceptors.

6.8.2 HF-EPR

Due to the complexity of the X-Band EPR spectrum recorded at 4.2 K, which turned out to be impossible to interpret, we chose HF-EPR to get information about anisotropy

and ground spin state of **(2)**. As we mentioned in Chapter 2 HF-EPR spectroscopy was effectively proved to be one of the most powerful techniques to gain this kind of information.[69-71]

Figure 6.23 shows the HF-EPR spectra of **(2)** recorded at 240 GHz and different temperatures ranging from 200 K to 4.2 K. At 200 K, there is essentially one broad band centered at g=2 as expected for a system containing Gd(III) and semiquinones. Two satellites are located symmetrically around the central one. On decreasing temperature the spectrum shows increasing features. At 10 K a fine structure progression is clearly resolved at low field. The spectrum at 4.2 K shows the typical simplification expected for a HF-EPR experiment[69] and may be interpreted in a qualitative way following the guidelines exposed in Chapter 2. In fact, since the Zeeman energy is larger than kT at low temperature only the lowest Ms states will be populated and one transition, - S → - S+1, is observed. The spectrum at 4.2 K shows a feature at ca. 7.87 T and two additional features, at ca. 8.8 and 9.0 T, which can be attributed to the - S → - S+1 transitions with the external field parallel to z, x and y respectively. The additional features around 7.95 T and 8.03 T correspond to the z component of the - S+1→ - S+2 and – S+2 → - S+3 transitions respectively.

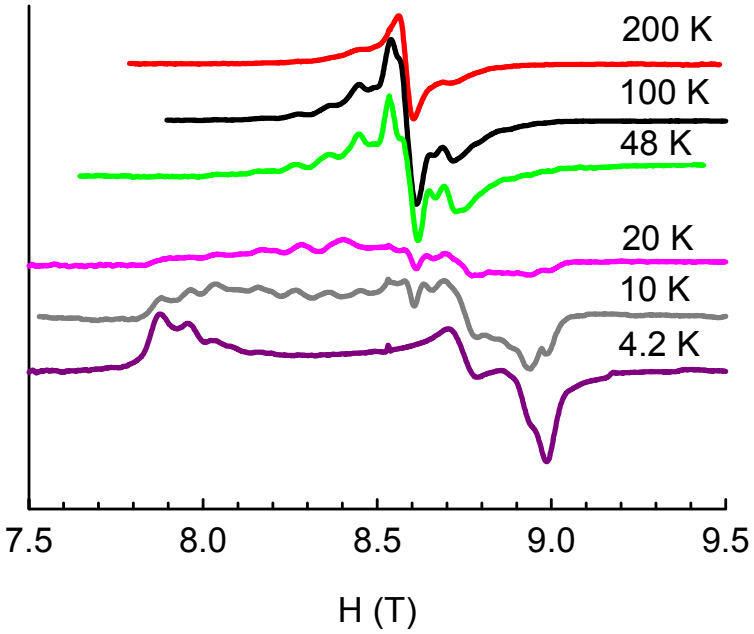

Figure 6.23 *Temperature evolution of HF-EPR spectra of* ***(2)*** *recorded at 240 GHz between 200 K and 4 K.*

The fact that the z transitions are observed at low field indicates that this is the easy axis, thus suggesting a negative axial anisotropy zero field splitting parameter D.[69] A

regular fine structure is clearly observed in the parallel region of the spectrum recorded at 10 K, with a 0.088 T separation between two successive peaks. This behavior is in favor of a high spin state, with the higher energy M_S states which are depopulated on decreasing temperature. Indeed, we showed in Chapter 2 that in the strong field limit, a spectrum of an S ground state should show 2S transitions separated in the parallel region by 2D, of which S above the center of the spectrum, and S below. If we consider that the low field parallel region is extended for 0.66 T, and that the separation between neighbouring lines is about 0.088 T, a ground spin state S = 7, and a D value of -0.044 T (-0.047 cm^{-1}) are clearly indicated. We then tried to simulate the spectra at 4.2 K and 10 K starting from these parameters. The simulations were performed using the program written by Weihe, described in some details in Chapter 2.[72]

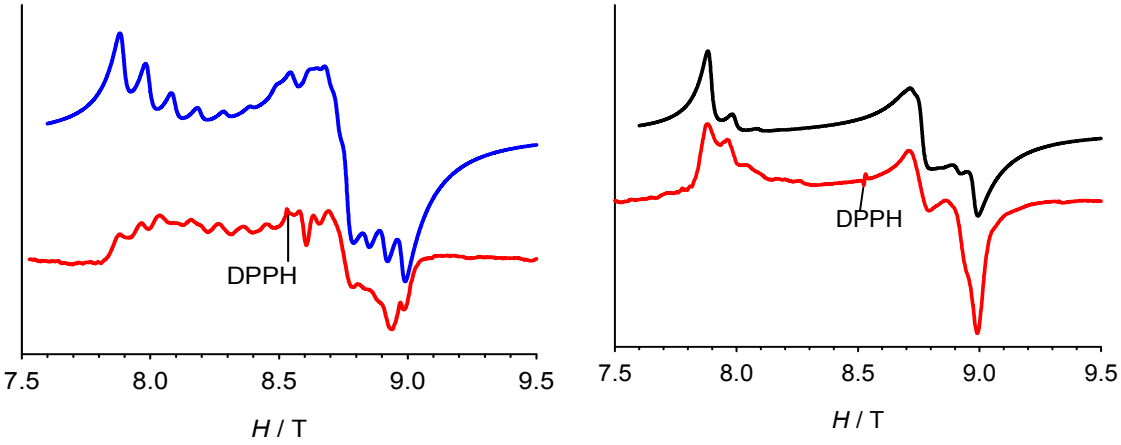

Figure 6.24 *Comparison of simulated (upper) and experimental (lower) HF-EPR spectra of* ***(2)*** *at 10 K (left) and 10 K (right). The corresponding Spin Hamiltonian parameters are given in the text.*

The best simulations (Figures 6.24) were obtained using S = 7, g_{iso} = 2.00, D = -0.0465 cm^{-1}, E = 0.0052 cm^{-1}, in good agreement with the parameter values which were estimated in the preliminary analysis of the spectra. However, the introduction of a small transverse anisotropy term ($E/D \cong 0.11$), which affects mainly the perpendicular region of the spectra, is proved to be necessary to obtain correct simulations. The temperature evolution of the spectra, as well as the position of the lines, is well reproduced even if the appearing at 10 K of excited states transitions makes the simulation process incomplete. The presence of transitions from excited states at this rather low temperature causes the impossibility of reproducing the spectra at higher temperatures. The conclusion that the

HF-EPR allows to reach is that there is an S=7 state which is either the ground state or is very close to it.

6.8.3 Magnetic Measurements

The plot of χT vs T between 2.5 K and 300 K is shown in Figure 6.25. The high temperature value of 17.24 emu K mol^{-1} is in agreement with two S = 7/2 and four S = 1/2 independent spin carriers with g = 2.00 (theoretical value 17.25 emu K mol^{-1}), as expected from the crystal structure. This is a confirmation of the assignment of the dioxolene molecules as semiquinones. Other assignments, like two semiquinones, one cathecholate and one quinone would require χT=16.5 emu K mol^{-1}. Since the overall coupling is antiferromagnetic as evidenced by the temperature dependence of χT to be described below, a high temperature limit higher than the limit for non-interacting spins would be impossible to justify. The decreasing of χT product on decreasing temperature indicates the existence of antiferromagnetic interactions between the different paramagnetic centres. However the quite high value at low temperature (10.97 emu K mol^{-1} at 2.5 K) as well as the slow decreasing of χT, seems to indicate an incomplete spin compensation.

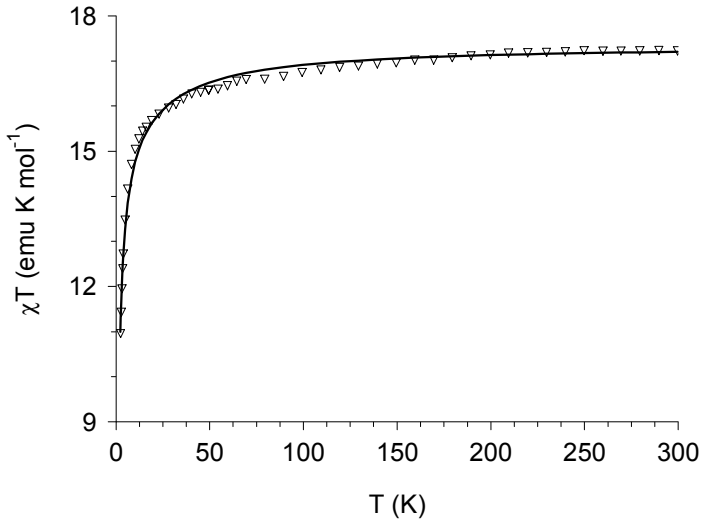

Figure 6.25 *χT vs T curve measured between 2.5 K and 300 K for (**2**) and best fit curve. Best fit parameters for the two models are reported in the text.*

The *M* vs *H* curves measured for (**2**) at two temperatures are shown in figure 6.26. The high field value of 13.7 μ_B observed at 2.4 K is slightly lower than expected for an S = 7 ground state (14 μ_B). This seems to indicate that S = 7 is the ground state in a field of 6 T. However the initial magnetization at low field is much smaller than expected for S=7, suggesting that other spin states of lower S values are populated at low field. The combined picture emerging from the analysis of the HF-EPR spectra, of the magnetic susceptibility and of magnetization is that in zero field there is an S=7 multiplet which is either the ground state or is close to the ground state. At any rate there must be several multiplets with S < 7 which are thermally populated at 4 K.

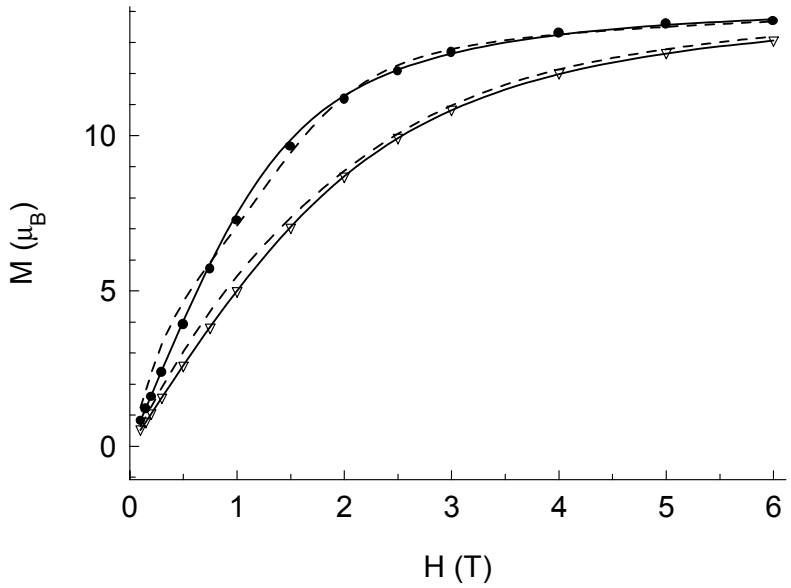

Figure 6.26 *Magnetization curves for (**2**), measured at 2.6 K and 4.7 K. The dashed lines are the best simulations obtained assuming an S=7 ground state, while the continuous line were obtained assuming an S=0 ground state.see text for further details.*

In order to try to fit the temperature dependence of χT simplifying assumptions are needed. We reduced to two possible coupling scheme, shown in Figure 6.27. To reduce the number of parameters employed in the simulation, the three bridging semiquinonate ligands were taken as magnetically equivalent in the interaction with gadolinium ions and with the same scope, all the semiquinonate-semiquinonate interactions were taken as equivalent to each other. Besides this in the first scheme, we neglected the Gd-Gd interaction; this was justified on the basis of literature data, which show only a very small

value for this coupling.[66,67] The following isotropic exchange hamiltonian was then used to simulate the χT vs T curve:

$$\mathbf{H} = J_1 (\mathbf{S}_{Gd2}\cdot\mathbf{S}_{SQ4}) + J_2 (\mathbf{S}_{Gd2}\cdot\mathbf{S}_{SQ1} + \mathbf{S}_{Gd2}\cdot\mathbf{S}_{SQ2} + \mathbf{S}_{Gd2}\cdot\mathbf{S}_{SQ3} + \mathbf{S}_{Gd1}\cdot\mathbf{S}_{SQ1} + \mathbf{S}_{Gd1}\cdot\mathbf{S}_{SQ2} + \mathbf{S}_{Gd1}\cdot\mathbf{S}_{SQ3}) +$$
$$+ J_3 (\mathbf{S}_{SQ1}\cdot\mathbf{S}_{SQ2} + \mathbf{S}_{SQ1}\cdot\mathbf{S}_{SQ3} + \mathbf{S}_{SQ1}\cdot\mathbf{S}_{SQ4} + \mathbf{S}_{SQ2}\cdot\mathbf{S}_{SQ4} + \mathbf{S}_{SQ3}\cdot\mathbf{S}_{SQ4} + \mathbf{S}_{SQ2}\cdot\mathbf{S}_{SQ3})$$

(6.8.1)

A Weiss correction[57] was introduced to better reproduce the low temperature values; the same behaviour may be explained with the introduction of a small ZFS term, as found from the HF-EPR spectra. As we have seen in Chapter 5 the introduction of a θ value is purely phenomenological and does not necessarily imply interactions between neighbouring dinuclear units (the shortest intermolecular Gd-Gd and Gd-O distances are in fact 12.6 Å).

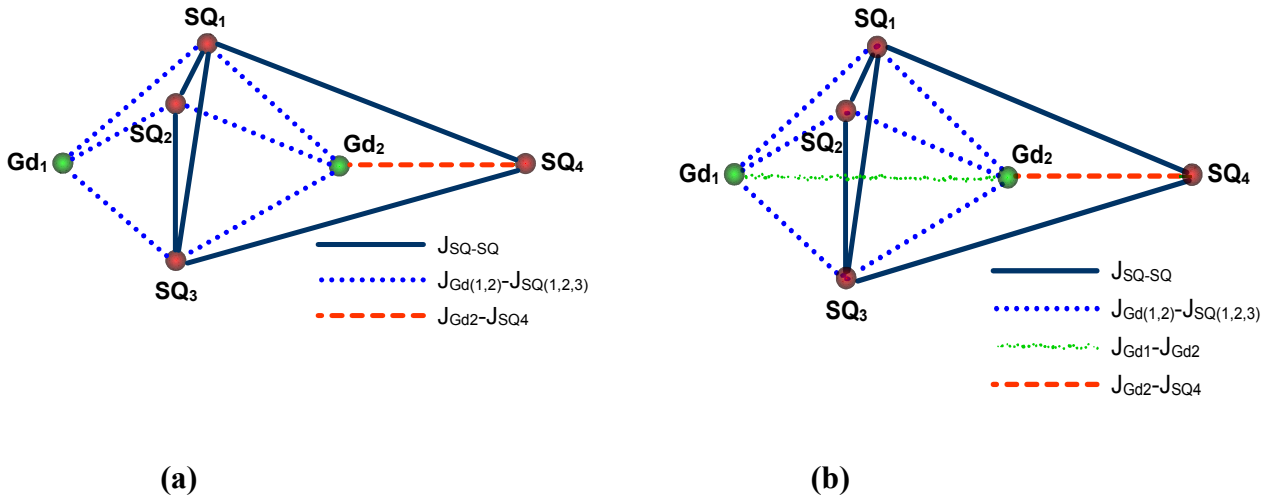

Figure 6.27 *Coupling schemes for (**2**). In **(a)** no Gd-Gd interactions was taken into account and a phenomenological Weiss correction was applied.[57] In **(b)** the Gd-Gd interactions was considered, but no Weiss correction was applied*

The best fit curve (continuous line, figure 6.25) within this model was obtained using the following parameters: J_1 = 2.51 cm^{-1}, J_2 = -0.6 cm^{-1}, J_3 = 18.15 cm^{-1}, and a θ = - 0.12 K. A second fit was attempted introducing the Gd-Gd interaction, as shown in Figure 6.25 adding a $J_{Gd1Gd2}\mathbf{S}_{Gd1}\cdot\mathbf{S}_{Gd2}$ term to the hamiltonian (6.8.1) and neglecting θ. In fact a non-zero Gd-Gd interaction was needed in order to justify the highly frustrated nature of

the ground state in Gd-NitR radical one dimensional compound.[12,16] The best fit curve obtained is perfectly superimposed over the first one, and the value for the coupling constant are in qualitative agreement with the first fit: J_1= 1.75 cm^{-1}, J_2 = 0.35 cm^{-1}, J_3 = 12.85 cm^{-1}, J_{Gd1Gd2} = 0.08 cm^{-1}.

With the values of the coupling constants derived from the first fit, the ground state is a doubly degenerated S = 7 with excited states ranging from S = 6 to S = 0 (all of them doubly degenerated) which are within 1.3 cm^{-1}. Higher in energy are the S = 8 state (12.2 cm^{-1} above the ground state) and the S = 9 (55 cm^{-1} above the ground state). On the other hand, the values of the coupling constants of the second fit require an S=0 ground state (due to the antiferromagnetic coupling between the two Gadolinium ions) and the excited states ranging from S=1 to S=7 are within 2.7 cm^{-1} in energy. Also in this case higher in energy are the S=8 (17.4 cm^{-1}) and the S=9 (48.5 cm^{-1}) states. Both of these results are in qualitative agreement with the interpretations of the HF-EPR spectra and of the magnetization data.

We tried to discriminate between these two results attempting a simulation of the magnetization curves, taking into account the population of the seven lower energy states - as derived from the two different fits of the susceptibility data - and Zero Field Splitting effects for ground and excited states. The first simulation was performed considering the relative energies of the spin states as derived from the first fit. Applying to the S=7 ground state the Zero Field Splitting parameters derived from HF-EPR we were forced to use quite large Zero Field Splitting (D = -0.3 cm^{-1}) for lower S spin states in order to obtain some agreement with the experimental curves. However, even using these values the quality of the simulation was not very good (Figure 6.26, dashed lines).

If one considers the energy levels derived from the second fit of the susceptibility data, a value of Zero Field Splitting for lower S spin states which is comparable (0.04 cm^{-1}) with the one derived from HF-EPR for S=7 is obtained for the best fit curve. It should be noted that in this case the quality of the simulation is good (fig.5, continuous line). This is then a very strong indication in favor of a spin ground state S=0, with S=7 very near in energy. In principle it would be possible to include a higher number of J parameters allowing for the low-symmetry of the compound. However we do not feel that a reliable determination of their values can be achieved.

The values of the coupling constants obtained from the susceptibility fit deserve here some comments. The coupling constant between Gd(2) and the chelating semiquinonate

is smaller than the one recently reported for a similar mononuclear complex (J = 11.15 cm^{-1})[60] with 1:1 gadolinium-semiquinonate stoichiometry. The difference in the coupling may be attributed to different factors: (i) the difference in coordination sphere around gadolinum, which is eight-coordinated in the mononuclear complex (ii) the existence of interactions involving both Gd(2) and chelating semiquinonate, with the other paramagnetic centers of the complex. This may reduce the strength of the J_1 interaction.

The very low value of J_2 may be explained considering that (i) each of the three semiquinonates are bound to the two Gd(III) ions (ii) the average bridged semiquinonate - gadolinium distances are larger than for the chelating radical. This strongly reduces the overlap between the *f* orbitals of the rare earth ions with the magnetic orbital of the radicals, which is known to be a key factor in determining the nature and the magnitude of magnetic interaction.[12,60,68] Finally, the quite high value of the semiquinonate-semiquinonate coupling constant indicates that Gd(III) ions are effective in transmitting the antiferromagnetic interaction as it has already been noted with nitronyl-nitroxide radicals.[12,16,33].

6.9 Conclusions

The antiferromagnetic coupling we observed in a simple gadolinum-semiquinonato complex is the strongest so far reported for a gadolinium-radical complex, in agreement with the fact that semiquinonate is the strongest paramagnetic ligand so far investigated for magnetic interactions with Gd (III). Notwithstanding this, when it is compared with the couplings observed for semiquinonato with other S ions, like Fe(III), the weak nature of the metal to radical interaction in the rare earth is dramatically evidenced. In fact the reported values[73,74] of J for iron(III)-semiquinonato complexes are at least ca. 600 cm^{-1}, more than one order of magnitude larger and comparison with results obtained in Chapter 5 for poly-semquinonato ligands show the same trend. However the present results show that moderate couplings can be obtained between rare earth and semiquinonato ligands. Further study is currently in progress, ranging from DFT-based calculations to Polarised Neutron Diffraction (see Figure S6.8) analysis, to get further insight into this mechanism, but to our knowledge no definitive report is available

concerning systems with *f* orbitals. Preliminary DFT results on Gd(III)-radical derivatives invariably give an antiferromagnetic coupling, much larger than the experimental ones. In no case the calculations provided ferromagnetic coupling, even with the NITR radicals.[75]

The qualitative interpretation of some of the simple 1:1 adducts between orbitally degenerate rare earth ions and semiquinonato complexes has demonstrated that no simple general model is currently available to predict the exchange coupling in systems involving lanthanides, even if Kahn model may work correctly in some cases.[35] We feel that more experimental and theoretical work is needed in order to understand the mechanism of magnetic coupling involving rare-earth ions and simple S=1/2 spins. In particular to achieve a reliable quantitative determination of both Crystal Field and anisotropic exchange parameters it is absolutely necessary to perform single crystal analysis both for magnetic measurements and EPR spectra. For this latter technique the possibility of using the experimental setup working at 95 GHz, described in Chapter 2 might prove very interesting in enhancing the resolution of the anisotropy of these systems.

Finally, we have obtained the first dinuclear complex involving Gd(III) ions and paramagnetic ligands. Its structure has been resolved by X-ray diffraction studies and shows an asymmetric unit: Gd(1) is eight-coordinated whereas Gd(2) is nine-coordinated. Moreover, the coordination mode between dioxolene ligands and gadolinum ions is double -three radicals are bridging via a single oxygen atom the rare earth ions, the last one is chelating the Gd(2) ion. These two ways of linking seem to be intimately correlated to the magnitude of the magnetic interaction between gadolinium ions and the radicals: the coupling is weaker for bridging semiquinonate ligands interacting with gadolinum ions than between the chelating radical and Gd(2) ion. The magnetic anisotropy of an excited state of **(2)** was determined through HF-EPR spectroscopy, while magnetization measurements were crucial to assign the ground spin state as S=0. It may be concluded that such a geometrical arrangement of Gadolinium and paramagnetic ligands is not favorable to obtain an antiferromagnetic coupling larger than the ones so far reported. To get better insight into this investigation, efforts to isolate the mononuclear analogue of **(2)** are currently in progress.

References

1. O. Kahn, *Angew Chem Int Ed Engl* **24**, 834 (1985).
2. O. Kahn, *Molecular Magnetism* (VCH, Weinheim, 1993).
3. *Magnetostructural Correlation in Exchange Coupled Systems* R. D. Willett, D. Gatteschi, and O. Kahn (Reidel, Dordrecht, 1985).
4. *Magnetic Molecular Materials* D. Gatteschi, O. Kahn, J. S. Miller, and F. Palacio (Kluwer Academic, Dordrecht, 1991).
5. D. P. Goldberg, A. Caneschi, and S. J. Lippard, *J. Am. Chem. Soc.* **115**, 9299 (1993).
6. J. S. Miller and A. J. Epstein, *Angew. Chem., Int. Ed. Engl.* **33**, 385 (1994).
7. R. Sessoli, H. L. Tsai, A. R. Schake, S. Wang, J. B. Vincent, K. Folting, D. Gatteschi, G. Christou, and D. N. Hendrickson, *J. Am. Chem. Soc.* **115**, 1804 (1993).
8. H. O. Stumpf, L. Ouahab, Y. Pei, P. Bergerat, and O. Kahn, *J. Am. Chem. Soc.* **116**, 3866 (1994).
9. J. K. McCusker, C. A. Christmas, P. M. Hagen, R. K. Chadha, D. F. Harvey, and D. N. Hendrickson, *J. Am. Chem. Soc.* **113**, 6114 (1991).
10. C. A. Christmas, H. L. Tsai, L. Pardi, J. M. Kesselman, P. K. Gantzel, R. K. Chadha, D. Gatteschi, D. F. Harvey, and D. N. Hendrickson, *J. Am. Chem. Soc.* **115**, 12483 (1993).
11. C. Benelli, A. Caneschi, D. Gatteschi, O. Guillou, and L. Pardi, *J. Magn. Magn. Mater.* **83**, 522 (1990).
12. C. Benelli, A. Caneschi, D. Gatteschi, O. Guillou, and L. Pardi, *Inorg. Chem.* **29**, 1750 (1990).
13. M. Andruh, I. Ramade, E. Codjovi, O. Guillou, O. Kahn, and J. C. Trombe, *J. Am. Chem. Soc.* **115**, 1822 (1993).
14. C. Benelli, A. Caneschi, D. Gatteschi, and R. Sessoli, *Inorg. Chem.* **32**, 4797 (1993).
15. C. Benelli, A. Caneschi, D. Gatteschi, and R. Sessoli, *J. Appl. Phys.* **73**, 5333 (1993).
16. C. Benelli, D. Gatteschi, R. Sessoli, A. Rettori, M. G. Pini, F. Bartolome, and J. Bartolome, *J. Magn. Magn. Mater.* **140-144**, 1649 (1995).
17. J. L. Sanz, R. Ruiz, A. Gleizes, F. Lloret, J. Faus, M. Julve, J. J. Borrasalmenar, and Y. Journaux, *Inorg. Chem.* **35**, 7384 (1996).
18. F. Bartolome, J. Bartolome, C. Benelli, A. Caneschi, D. Gatteschi, C. Paulsen, M. G. Pini, A. Rettori, R. Sessoli, and et al., *Phys. Rev. Lett.* **77**, 382 (1996).

19. T. Sanada, T. Suzuki, T. Yoshida, and S. Kaizaki, *Inorg. Chem.* **37**, 4712 (1998).
20. R. E. P. Winpenny, *Chem. Soc. Rev.* **27**, 447 (1998).
21. M. Evangelisti, F. Bartolome, J. Bartolome, M. L. Kahn, and O. Kahn, *J. Magn. Magn. Mater.* **197**, 584 (1999).
22. J. P. Costes, F. Dahan, and A. Dupuis, *Inorg. Chem.* **39**, 5994 (2000).
23. J. P. Costes, F. Dahan, A. Dupuis, and J. P. Laurent, *Inorg. Chem.* **39**, 169 (2000).
24. J. P. Costes, F. Dahan, and F. Nicodeme, *Inorg. Chem.* **40**, 5285-+ (2001).
25. A. Bencini, A. Benelli, A. Caneschi, R. L. Carlin, and A. Dei, *J. Am. Chem. Soc.* **107**, 8128 (1985).
26. C. Benelli, A. Caneschi, D. Gatteschi, J. Laugier, and P. Rey, *Angew. Chem. Int. Ed. Engl.* **26**, 913 (1987).
27. C. Benelli, A. Caneschi, D. Gatteschi, L. Pardi, P. Rey, D. P. Shum, and R. L. Carlin, *Inorg. Chem.* **28**, 272 (1989).
28. M. Sakamoto, M. Hashimura, K. Matsuki, N. Matsumoto, K. Inoue, and H. Okawa, *Bull. Chem. Soc. Jpn.* **64** , 3639 (1991).
29. O. Guillou, R. L. Oushoorn, O. Kahn, K. Boubekeur, and P. Batail, *Angew. Chem. Int. Ed. Engl.* **31**, 626 (1992).
30. I. Ramade, O. Kahn, Y. Jeannin, and F. Robert, *Inorg. Chem.* **36**, 930 (1997).
31. J. P. Costes, A. Dupuis, and J. P. Laurent, *J. Chem. Soc., Dalton Trans.* 735 (1998).
32. J. P. Costes, F. Dahan, A. Dupuis, and J. P. Laurent, *Chem.-- Eur. J.* **4**, 1616 (1998).
33. C. Lescop, D. Luneau, E. Belorizky, P. Fries, M. Guillot, and P. Rey, *Inorg. Chem.* **38**, 5472-+ (1999).
34. J. P. Sutter, M. L. Kahn, and O. Kahn, *Adv. Mater.* **11**, 863-+ (1999).
35. M. L. Kahn, J. P. Sutter, S. Golhen, P. Guionneau, L. Ouahab, O. Kahn, and D. Chasseau, *J. Am. Chem. Soc.* **122**, 3413 (2000).
36. J. S. Griffith, *The Theory of Transition Metal Ions* (Cambridge University Press, Cambridge, 1961).
37. R. L. Carlin and van Duyneveldt A. J., *Magnetic Properties of Transition Metal Compounds* (Springer-Verlag, New York, 1977).
38. J. H. Van Vleck, *The Theory of Electric and Magnetic Susceptibility* (Oxford University Press, Oxford, 1932).
39. J. J. Borras-Almenar, J. M. Clemente-Juan, E. Coronado, A. V. Palii, and B. S. Tsukerblat, *Phys. Lett. A* **238**, 164 (1998).

40. J. J. Borras-Almenar, J. M. Clemente-Juan, E. Coronado, A. V. Palii, and B. S. Tsukerblat, *J. Phys. Chem. A* **102**, 200 (1998).
41. P. M. Levy, *Phys. Rev.* **135**, 155 (1964).
42. P. M. Levy, *Phys. Rev.* **147**, 311 (1966).
43. H. Kamimura and T. Yamaguchi, *Phys. Rev. B* **1**, 2902 (1970).
44. B. G. Wybourne, *Spectroscopic Properties of Rare Earths* (John Wiley and Sons, New York, 1965).
45. M. L. Kahn, C. Mathoniere, and O. Kahn, *Inorg. Chem.* **38**, 3692 (1999).
46. J. P. Sutter, M. L. Kahn, K. P. Mortl, R. Ballou, and P. Porcher, *Polyhedron* **20**, 1593 (2001).
47. P. Porcher, M. C. Dos Santos, and O. Malta, *Phys. Chem. Chem. Phys.* **1**, 397 (1999).
48. M. L. Kahn, *Ph. D. thesis*, University of Bourdeaux I, France, 1999.
49. J. P. Costes, F. Dahan, and A. Dupuis, *Inorg. Chem.* **39**, 165 (2000).
50. J.-P. Sutter, M. L. Kahn, S. Golhen, L. Ouahab, and O. Kahn, *Chem.-Eur. J.* **4**, 571 (1998).
51. C. Benelli, A. Caneschi, D. Gatteschi, and L. Pardi, *Inorg. Chem.* **31**, 741 (1992).
52. M. A. J. Moss and C. J. Jones, *J. Chem. Soc., Dalton Trans.* (1990).
53. C. Benelli, A. Dei, D. Gatteschi, H. U. Güdel, and L. Pardi, *Inorg. Chem.* **28**, 3089 (1989).
54. C. Benelli, A. Dei, D. Gatteschi, and L. Pardi, *Inorg. Chem.* **28**, 1476 (1989).
55. C. G. Pierpont and R. M. Buchanan, *Coord. Chem. Rev.* **38**, 87 (1981).
56. C. G. Pierpont and C. W. Lange, *Prog. Inorg. Chem.* **41**, 331 (1994).
57. C. J. O'Connor, *Prog. Inorg. Chem.* **29**, 203 (1982).
58. A. Dei, D. Gatteschi, J. Pecaut, S. Poussereau, L. Sorace, and K. Vostrikova, *C. R. Acad. Sci. Ser. II-C* **4**, 135 (2001).
59. A. Dei, D. Gatteschi, C. A. Massa, S. Poussereau, L. A. Pardi, and L. Sorace, *Chem. -- Eur. J.* **6**, 4580 (2000).
60. A. Caneschi, A. Dei, D. Gatteschi, L. Sorace, and K. Vostrikova, *Angew. Chem. Int. Ed. Engl.* **39**, 246 (2000).
61. L. C. Brunel, A. Caneschi, A. Dei, D. Friselli, D. Gatteschi, A. K. Hassan, L. Lenci, M. Martinelli, C. A. Massa, L. A. Pardi, F. Popescu, I. Ricci, and L. Sorace, *Res. Chem. Interm.* (in press).

62. A. Bencini and D. Gatteschi, *EPR of Exchange Coupled Systems* (Springer-Verlag, Berlin, 1990).
63. R. D. L. Carlin, *Magnetochemistry* (Springer-Verlag, Berlin, 1986).
64. A. Dei, D. Gatteschi, L. Pardi, A. L. Barra, and L. C. Brunel, *Chem. Phys. Lett.* **175**, 589 (1990).
65. A. Abragam and B. Bleaney, *Electron Paramagnetic Resonance of Transition Ions* (Dover Publications, New York, 1986).
66. S. Liu, L. Gelmini, S. J. Rettig, R. C. Thompson, and C. Orvig, *J. Am. Chem. Soc.* **114**, 6081 (1992).
67. A. Panagiotopoulos, T. F. Zafiropoulos, S. P. Perlepes, E. Bakalbassis, I. Masson Ramade, O. Kahn, A. Terzis, and C. P. Raptopoulou, *Inorg. Chem.* **34**, 4918 (1995).
68. I. A. Setyawati, S. Liu, S. J. Rettig, and C. Orvig, *Inorg. Chem.* **39**, 496 (2000).
69. A. L. Barra, L. C. Brunel, D. Gatteschi, L. Pardi, and R. Sessoli, *Acc. Chem. Res.* **31**, 460 (1998).
70. A. L. Barra, D. Gatteschi, and R. Sessoli, *Chem.-Eur. J.* **6**, 1608 (2000).
71. A. L. Barra, A. Caneschi, D. Gatteschi, and R. Sessoli, *J. Am. Chem. Soc.* **117**, 8855 (1995).
72. C. J. H. Jacobsen, E. Pedersen, J. Villadsen, and H. Weihe, *Inorg. Chem.* **32**, 1216 (1993).
73. A. Dei and D. Gatteschi, *Inorg. Chim. Acta* **200**, 813 (1992).
74. L. S. Kessel, R. M. Emberson, P. G. Debrunner, and D. N. Hendrickson, *Inorg. Chem.* **19**, 1170 (1980).
75. A. Bencini and C. Carbonera, *private communication* .

7. Experimental section

Chapter 3

HF-EPR spectra of a polycrystalline powder of $Mn(dbm)_2(CH_3OH)_2Br$ were recorded on a laboratory-made spectrometer [1] at the Grenoble High Magnetic Field Laboratory (France). The radiation source used was a solid state Gunn diode generator operating at 95 GHz and equipped with a second and third-harmonic generator. The powder was pressed in pellet to avoid preferential orientation in the strong magnetic field.

Chapter 4

Prismatic single crystals of $Fe_4(OCH_3)_6(dpm)_6$ were prepared as described in ref. [2] and any possible twinning was excluded after collection of low-θ frames with a Siemens-CCD diffractometer. The relative orientation of the crystallite facets was carefully determined after the collection of 25 reflections on a CAD4 Enraf Nonius four circle diffractometer, equipped with graphite monochromated Mo K_α radiation.

The measurements were performed with a continuous wave W-band EPR spectrometer (Bruker E600) with cylindrical cavity operating at 94 GHz, equipped with a split-coil superconducting magnet (Oxford) mounted on a rotating base. Both the sample holder and the magnet could be rotated around a vertical axis. The temperature variation was achieved with a continuous flow cryostat (Oxford CF935 dynamic), operating from room temperature (RT) down to 4.2 K.

For W-band experiments, the oriented single crystals were mounted on silica grade tubes with 0.9 mm outer diameter, embedded either in silicon grease or in glue, in order to have them well fixed and to protect them from the surrounding atmosphere. The crystals

were either stuck onto the flat polished bottom of the tubes or on a flat polished side, along the vertical axis of the tube, in order to obtain the desired orientations (see Figure 4.4). Orientational errors of up to 5^0 can occur due to the visual procedure of alignment.

Single crystal EPR studies were performed also at X-band (9.4 GHz), in a Bruker ESP 300E spectrometer equipped with a continuous flow cryostat (Oxford ESR910) for temperature variations from RT down to 2.4K. Eventually, several oriented crystals were mounted together on the sample holder in order to increase the signals. Correspondence of the resulting spectra with real single crystal measurements was checked. The same precautions of protecting the crystals from deterioration by covering them with silicon grease were taken.

HF-EPR spectra of polycrystalline sample of ***Fe4*** were recorded at the Grenoble High Magnetic Field Laboratory (France).

Polycrystalline powder EPR spectra were measured at X-band (9.23 GHz) with a Varian ESR9 spectrometer, equipped with a ^{4}He continuous flow cryostat. To avoid preferential orientation, ground crystallites of ***Fe4*** were embedded in wax.

The magnetic measurements were made on single-crystal samples by using an array of micro-SQUIDs which measures the magnetic field induced by the magnetization of the crystal. Each micro-SQUID has a very high sensitivity that can reach 10^{-16} electromagnetic units, depending on the coupling factor.[3] The time resolution of the micro-SQUIDs is about 1 ms, allowing short-term measurements. The magnetometer works in the temperature range between 35 mK and 6 K and in fields up to 1.4 T with a field stability better than 10^{-6} T. The field can be applied in any direction of the micro-SQUID plane with a precision much better than 0.1 micron by separately driving three orthogonal coils. The array of micro-SQUID was fabricated by electron beam lithography in L2M, Bagneux, France.

Chapter 5

The temperature dependence of the magnetic susceptibilities of samples $Cr_2(CTH)_2(Sq\text{-}Cat)(PF_6)_3$, $Ni_2(CTH)_2(m\text{-}Ph(SQ)_2(PF_6)_2$, $Cu_2(Me_3[12]N_3(m\text{-}Ph(SQ)_2\ (PF_6)_2$, $Cr_2(CTH)_2(m\text{-}Ph(SQ)_2\ (PF_6)_4{\cdot}H_2O$,between 2.5 K and 250 K was measured using a Metronique MS02 SQUID Magnetometer with an applied field of 1.0 T. Magnetization measurements of $Ni_2(CTH)_2(m\text{-}Ph(SQ)_2(PF_6)_2$ were performed at 2.3 K with field up to 7 T using the same

instrument. Magnetic susceptibilities of polycrystalline powder samples of complexes **(3),** $Mn_3(Tp^{Cum,Me})_3((TBSQ)_3Ph)$ and $Ni_3(CTH)_3((TBSQ)_3Ph)(PF_6)_3$ were measured between 2 and 300 K at an applied magnetic field of 0.1 and 1 T using a Cryogenic S600 SQUID magnetometer. Magnetization measurements were performed on the same samples with the same instrument at 2.5 K and 4.5 K with field up to 6.5 T.

Data were corrected for sample holder contribution that was determined separately in the same temperature range and field. The underlying diamagnetism of the samples was estimated from Pascal's constants. Finally, the susceptibilities data were fit by minimizing the sum of the squares of the deviation of the computed χT values from the experimental values, using a Simplex minimization procedure. The theoretical susceptibilities were calculated employing CLUMAG,[4]except when stated otherwise.

EPR spectra were recorded both for compounds $Cr_2(CTH)_2(Sq\text{-}Cat)(PF_6)_3$ and $Co_2(CTH)_2(Sq\text{-}Cat)(PF_6)_3$ at X-band frequency (9.23 GHz) on a Varian ESR9 spectrometer. EPR spectrum on the Co compound was recorded at room temperature on a 0.5 mM acetone solution. Polycrystalline powder EPR spectra on the Cr compound were recorded at 4.2 K equipping the spectrometer with a continuous flow ^{4}He cryostat.

Chapter 6

Crystal data and structure refinement for [Gd(Hbpz$_3$)$_2$(dtbsq)] ·2CHCl$_3$. Data collection was made on a four circle CAD 4 ENRAF NONIUS diffractometer,with graphite monochromated MoKα radiation (λ= 0.71069 Å), ω-2θ scan, 293 K. Intensities were corrected for absorption (ψ-scan). The symmetry and systematic absences of the reciprocal lattice were found to be consistent with the orthorombic space groups $Pca2_1$ (29) and Pbcm (57). Structure could be successfully solved by direct methods (SIR97) [5] only for $Pca2_1$; remaining atoms were identified by successive Fourier difference syntheses using SHELXL97.[6] The structure was refined against F^2 with full matrix least squares refinement using 4074 independent reflections (of which 2804 observed, $I>4\sigma(I)$)), 12 restraints and 500 parameters. Anisotropic thermal factors were used for 53 on 57 non-hydrogen atoms. 38 Hydrogen atoms were placed in calculated positions.

Details: Crystal dimensions: 0.15x0.35x0.30 mm. Empirical Formula: $C_{34}H_{42}B_2Cl_6GdN_{12}O_2$; M_r=1042.37; orthorombic, space group $Pca2_1$ (29), a= 19.776(5) Å,

b= 12.069(5) Å, c= 18.975(5) α= 90.050(5)° β= 89.990(5)° γ= 90.000(5)° V= 4529(3) $Å^3$, Z=4, ρ_{calcd}= 1.529 g/cm^3, μ= 1.863 mm^{-1} 2.66° <θ< 24.97°. F(000) 2088 GOF on F^2 1.016. Final R index [I>4σ(I)] R1 = 0.0635, R index (all data) R1 = 0.1215. Absolute structure parameter .02(3). Largest diff. peak and hole 2.145 and -1.365 e. $Å^{-3}$, located near gadolinium ion.

*Crystal data and structure refinement for [Y(Hbpz$_3$)$_2$(dtbsq)]***.** Data collection was made on a Bruker Smart diffractometer equipped with a CCD area detector, Mo K_α radiation (λ= .71069 Å) graphite monochromator, φ-ω scans, 298 K. The system was found to crystallize in a monoclinic lattice. Structure was successfully solved by direct methods using SHELXS-97. The structure was refined against F^2 with full matrix least squares refinement using 9151 independent reflections (of which 3949 observed, I>2σ(I))), no restraints and 450 parameters using SHELXL-97. Anisotropic thermal factors were used for all the non-hydrogen atoms. All hydrogen atoms were placed in calculated positions.

Details: Crystal size: 0.05x0.2x0.2 mm. Empirical formula: $C_{32}H_{38}B_2YN_{12}O_2$; M_r=733.27; monoclinic, space group $P2_1/c$ (14), a= 12.814(1) Å, b= 15.115(1) Å, c= 19.663(1) β= 98.440(1)° V= 3767.2(5) $Å^3$, Z=4, ρ_{calcd}= 1.293 g/cm^3, μ= 1.593 mm^{-1} 1.71° <θ< 28.96°. F(000) 1516 GOF on F^2 0.845. Final R index [I>2σ(I)] R1 = 0.0445, R index (all data) R1 = 0.1510. Largest diff. peak and hole 0.246 and -0.262 e$Å^{-3}$.

*Crystal data and structure refinement for [Gd(Hbpz$_3$)$_2$(dtbsq)]$_2$·CHCl$_3$***.** A small crystal was sealed in a glass capillary containing a small amount of solvent. Data collection was made on a 4 circle CAD 4 ENRAF NONIUS diffractometer, Mo K_α radiation (λ= .71069 Å) graphite monochromator, ω-2θ scan, 293 K. Intensities were corrected for absorption (ψ-scan). The system was found to crystallize in a triclinic lattice. Structure was successfully solved by direct methods using SIR92 both for P1 and P-1. Due to the large number of parameters involved, refinement was performed only in P-1 space group. Remaining atoms were identified by successive Fourier difference syntheses using SHELXL93. The structure was refined against F^2 with full matrix least squares refinement using 12179 independent reflections (of which 6222 observed, I>2σ(I))), no restraints and 863 parameters. Anisotropic thermal factors were used for 86 on 102 non-hydrogen atoms. 98 Hydrogen atoms were placed in calculated positions. The quite high value of the residual electronic density, located near gadolinium ions, may be attributed to satellite peaks.

As the final R value turned out to be quite high, we tried to refine the structure performing the absorption correction through DIFABS, after location of all non-hydrogen isotropic atoms. The structure refined in such a way showed only minor improvement (R ($I>2\sigma$) = 9.58%, maximum density peak=2.46 $eÅ^{-3}$) with respect to the one obtained through ψ-scan correction and no significant differences in angles and distances.

Details: Crystal size: 0.15x0.15x0.3 mm. Empirical formula: $C_{75}H_{104}B_2Cl_3Gd_2N_{12}O_8$; M_r=1740.55; triclinic, space group P-1, a= 16.735(5) Å, b= 17.705(5) Å, c= 19.553(5) α= 99.680(5)° β= 109.960(5)° γ= 107.350(5)° V= 4956.8 (24) $Å^3$, Z=2, ρ_{calcd}= 1.165 g/cm^3, μ= 1.455 mm^{-1} 2.50° <θ< 22.04°. GOF on F^2 1.012. Final R index [$I>2\sigma(I)$] R1 = 0.0997, R index (all data) R1 = 0.2193.

*Crystal data and structure refinement for [Ho(Hbpz$_3$)$_2$(tropolone)]***.** Data collection was made on a CAD 4 four-circle ENRAF NONIUS diffractometer, with graphite monochromator MoKα radiation (λ= 0.71069 Å), ω-2θ scan, 293 K. Intensities were corrected for absorption (ψ-scan). The symmetry and systematic absences of the reciprocal lattice were found to be consistent with the tetragonal space groups $P4_12_12_1$. Structure was solved by direct methods which gave the positions of all non-hydrogen atoms, using SIR97. The structure was refined against F^2 with full matrix least squares refinement using SHELX97 and 3099 independent reflections (R(int)=0.0451) of which 2630 observed, $I>2\sigma(I)$, and 192 parameters.

Details: Empirical formula: $C_{12.50}H_{12.50}BHo_{0.50}N_6O$; M_r=356.06; tetragonal, space group $P4_12_12_1$, a= 9.417(5) Å, b= 9.414(5) Å, c= 32.226(5) V= 2857 (2) $Å^3$, Z=8, ρ_{calcd}= 1.656 g/cm^3, μ= 2.817 mm^{-1} 2.25° <θ< 26.98°. GOF on F^2 1.319. Final R index [$I>2\sigma(I)$] R1 = 0.0295, R index (all data) R1 = 0.0505.

Crystallographic data (excluding structure factors) for three over four of the structures reported in this thesis have been deposited with the Cambridge Crystallographic Data Centre as supplementary pubblication no. CCDC-129619 ([Gd(Hbpz$_3$)$_2$(dtbsq)]·2$CHCl_3$), CCDC-146291 (Y(Hbpz$_3$)$_2$(dtbsq)) CCDC-144025 ([Gd_2(Hbpz$_3$)$_2$(dtbsq)$_4$]·$CHCl_3$). Copies of the data can be obtained free of charge on application to CCDC, 12 Union Road, Cambridge CB21EZ, UK (fax: int.code + 44 1223 336033; e-mail: deposit@ccdc.cam.ac.uk)

Magnetic susceptibilities were measured on polycrystalline powders between 2 and 300 K and with an applied magnetic field of 0.1 and 1 T using a Cryogenic S600 SQUID magnetometer. Powders were pressed in pellets to prevent preferential orientation of the crystallites. Data were corrected for the magnetism of the sample holder which was determined separately in the same temperature range and field. The diamagnetism correction was estimated from Pascal's constants. Magnetization measurements were performed on the same samples at 2.5 and 4.5 K with field up to 6 T.

Polycrystalline powder EPR spectra were recorded for all the compounds at X-band frequency (9.23 GHz) on a Varian ESR9 spectrometer equipped with a continuous flow ^{4}He cryostat to work at 4.2 K. All the spectra were recorded both blocking the powder in wax and leaving them free. However, no difference between the spectra has been detected, thus excluding the possibility of orientation.

HF-EPR spectra were recorded at the High Field High Frequency Electromagnetic Resonance Laboratory hosted by IFAM-CNR in Pisa whose spectrometer was described in paragraph 2.3. The measurements were performed with a field sweep rate of 0.2 T/min. at 239.1 GHz (using CH_3I as laser gas) on a ground microcrystalline powder pressed in pellet together with n-eicosane to avoid orientation of the sample. Field calibration was obtained using DPPH as reference.

References

1. F. Muller, M. A. Hopkins, N. Coron, M. Greenberg. L.-C. Brunel, G. Martinez *Rev. Sci. Instrum.* **60,** 3681 (1989)

2. A. L. Barra, A. Caneschi, A. Cornia, F. Fabrizi de Biani, D. Gatteschi, C. Sangregorio, R. Sessoli and L. Sorace *J. Am. Chem. Soc.* **121**, 5302 (1999)

3. W. Wernsdorfer, Ph. D thesis, Joseph Fourier University, Grenoble, France, (1997)

4. D. Gatteschi and L. Pardi, *Gazz. Chim. Ital.* **123** 231 (1993)

5. Altomare, M. C. Burla, M. Camalli, G. L. Cascarano, C. Giacovazzo, A. Guagliardi, A. G. G. Moliterni, G. Polidori and R. Spagna, *J. Appl. Cryst.* **32,** 115-119 (1999).

6. G. M. Sheldrick, *SHELX97 - Programs for Crystal Structure Analysis (Release 97-2)* ; Institüt für Anorganische Chemie der Universität, Institüt für Anorganische Chemie der Universität, Göttingen (Germany), (1998).

8. Supplementary Material

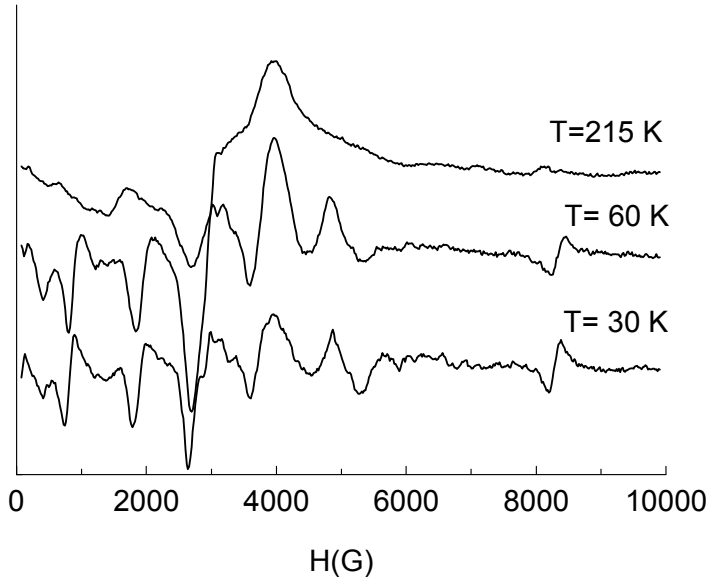

Figure S4.1 *Earlier X-Band EPR Spectra of* ***Fe4****, formerly attributed to an excited state S=4. See Chapter 4 for further details*

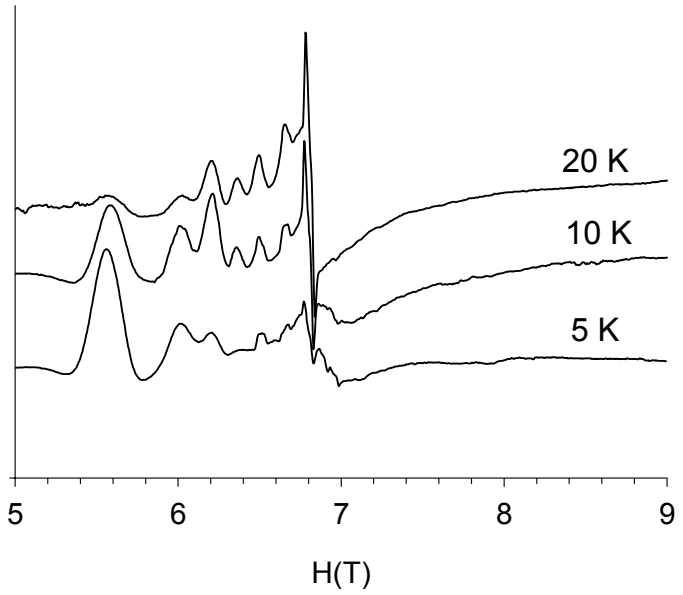

Figure S5.1 *Evolution of HF-EPR spectra (190 GHz) of* $Mn_3(Tp^{Cum,Me})_3((TBSQ)_3Ph)$ *with temperature. Spectra recorded on loose powder The six transition at low field identifying an S=6 state are clearly visible*

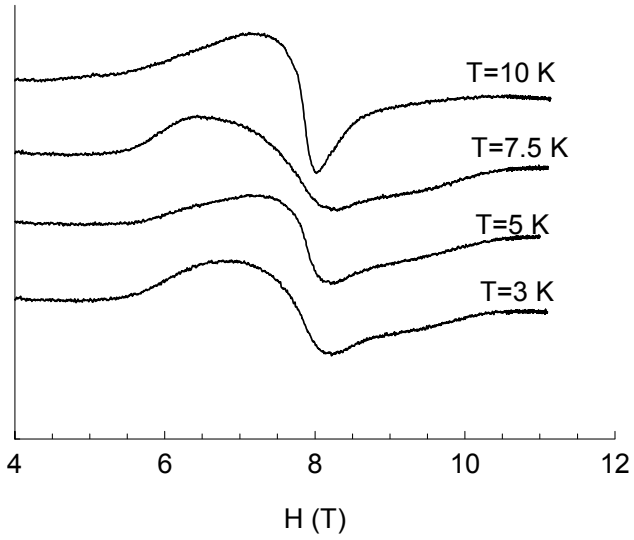

Figure S5.2 *Evolution of HF-EPR spectra (190 GHz) of $Ni_3(CTH)_3((TBSQ)_3Ph)(PF_6)_3$ with temperature. Spectra recorded on pressed pellet to avoid orientation of the crsytallites.*

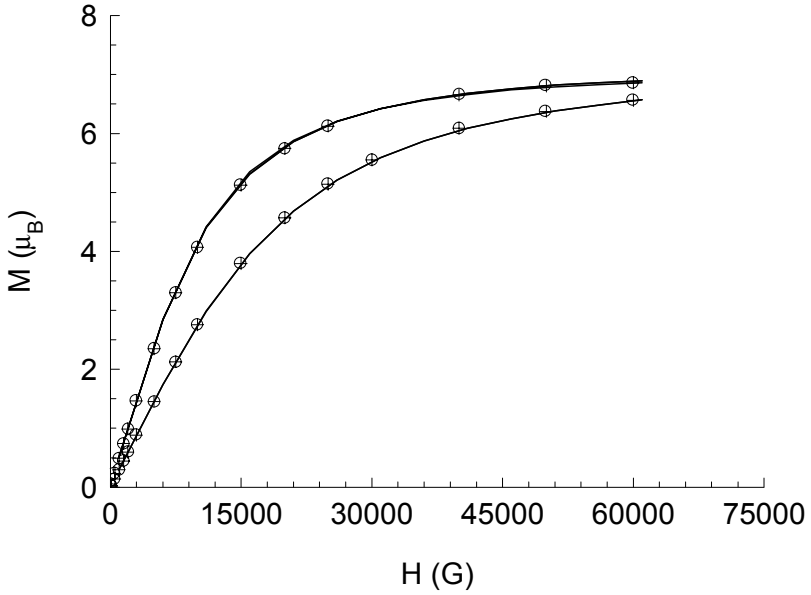

Figure S6.1 *Magnetization curves for $Gd(HBPz_3)_2(Trp)$ measured at 2.5 K (upper) and 4.5 K (lower) respectively. The continuous line is the curve calculated by using the parameters of HF-EPR*

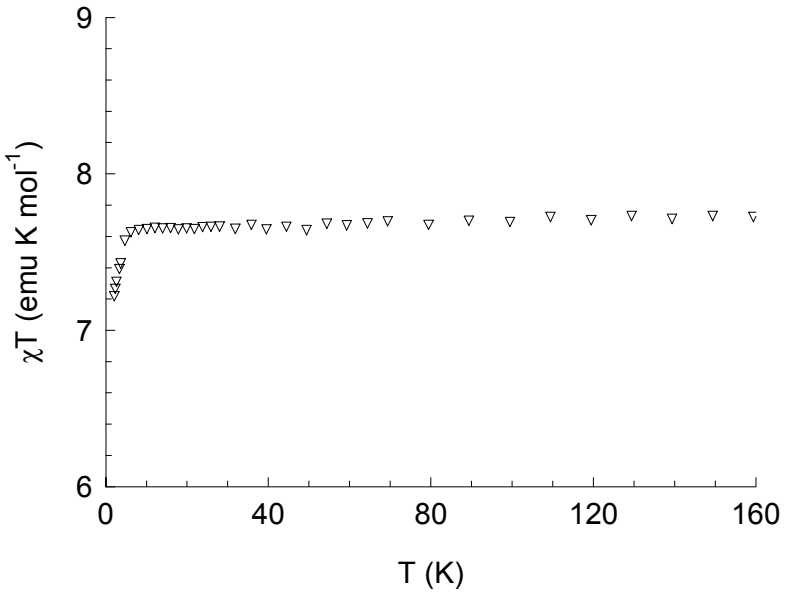

Figure S6.2 *χT vs T curve for Gd(HBPz$_3$)$_2$(Trp)*

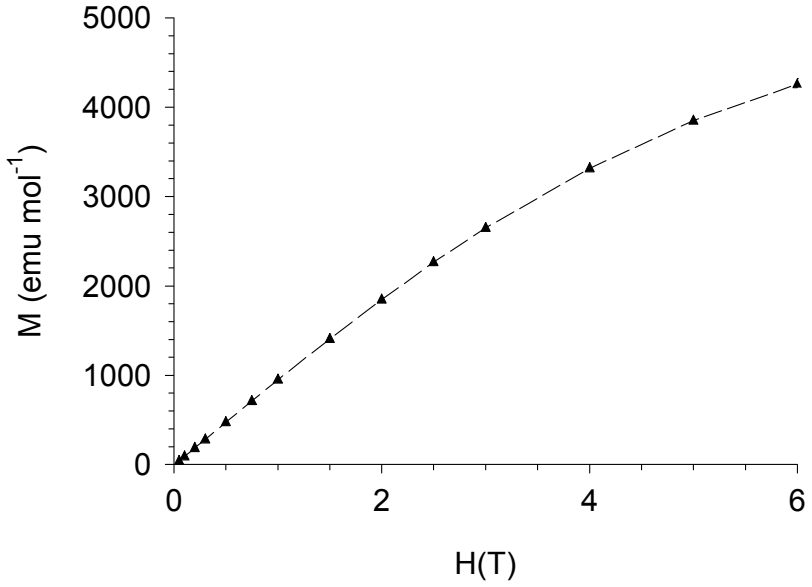

Figure S6.3 *Magnetization curve at 3K for Eu(HBPz$_3$)$_2$(3,5-DTBSQ). The dashed line is a guide to the eye*

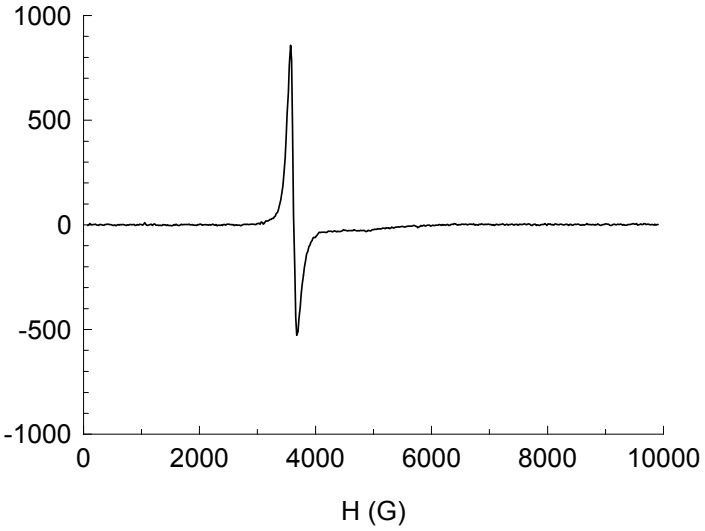

Figure S6.4 *X-Band EPR spectrum at low temperature of Eu(HBPz$_3$)$_2$(3,5-DTBSQ)*

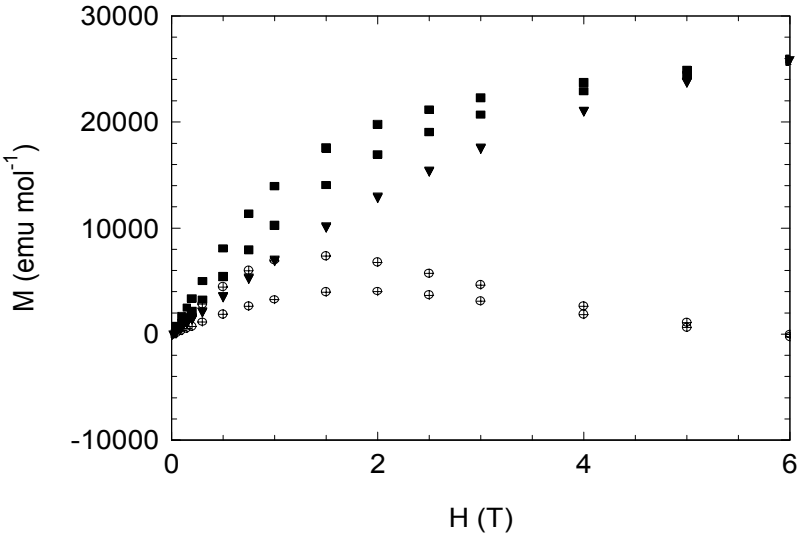

Figure S6.5 *M vs. H curves at 2.5 K and 4.5 K for Ho(HBPz$_3$)$_2$(3,5-DTBSQ) (full squares) and Ho(HBPz$_3$)$_2$(Trp) (full triangles) and corresponding ΔM values (crossed circles)*

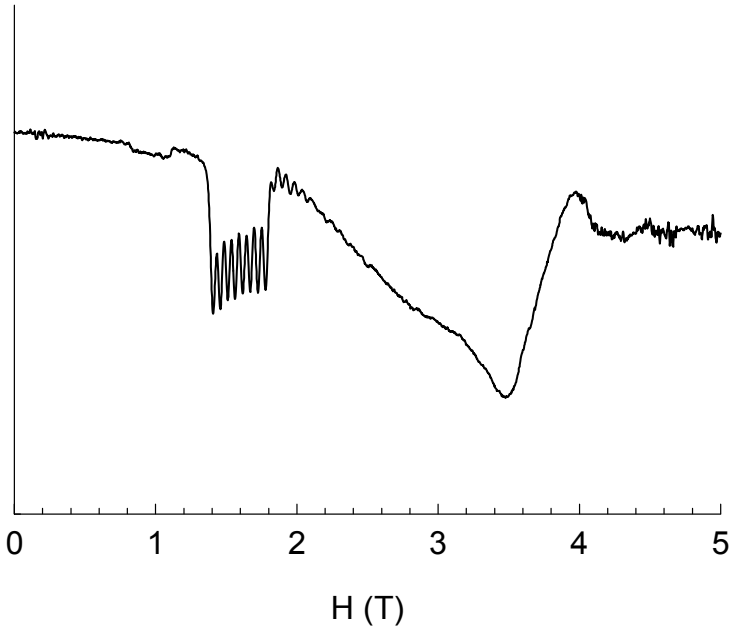

Figure S6.6 *HF-EPR spectrum recorded at 245 GHz and 10 K for* ***HoSQ****. The strong hyperfine coupling to the I=7/2 nuclear spin of* ^{165}*Ho is evident*

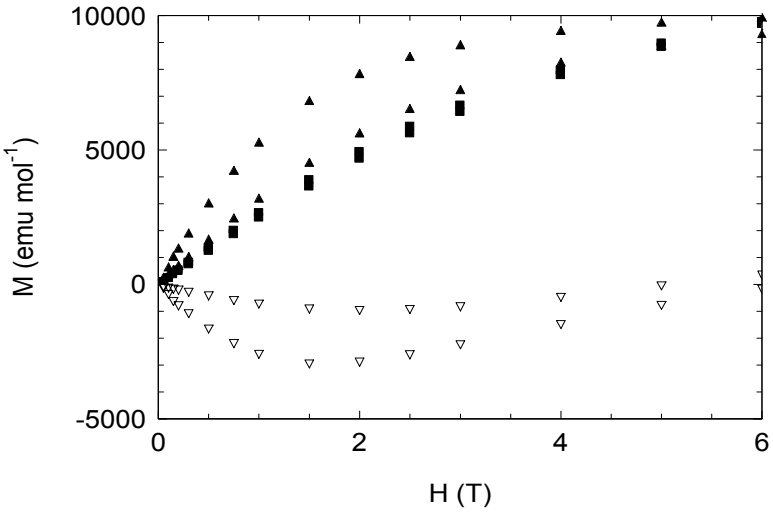

Figure S6.7 *M vs. H curves at 2.5 K and 4.5 K for Yb(HBPz$_3$)$_2$(3,5-DTBSQ) (full squares) and Yb(HBPz$_3$)$_2$(Trp) (full triangles) and corresponding ΔM values (empty triangles)*

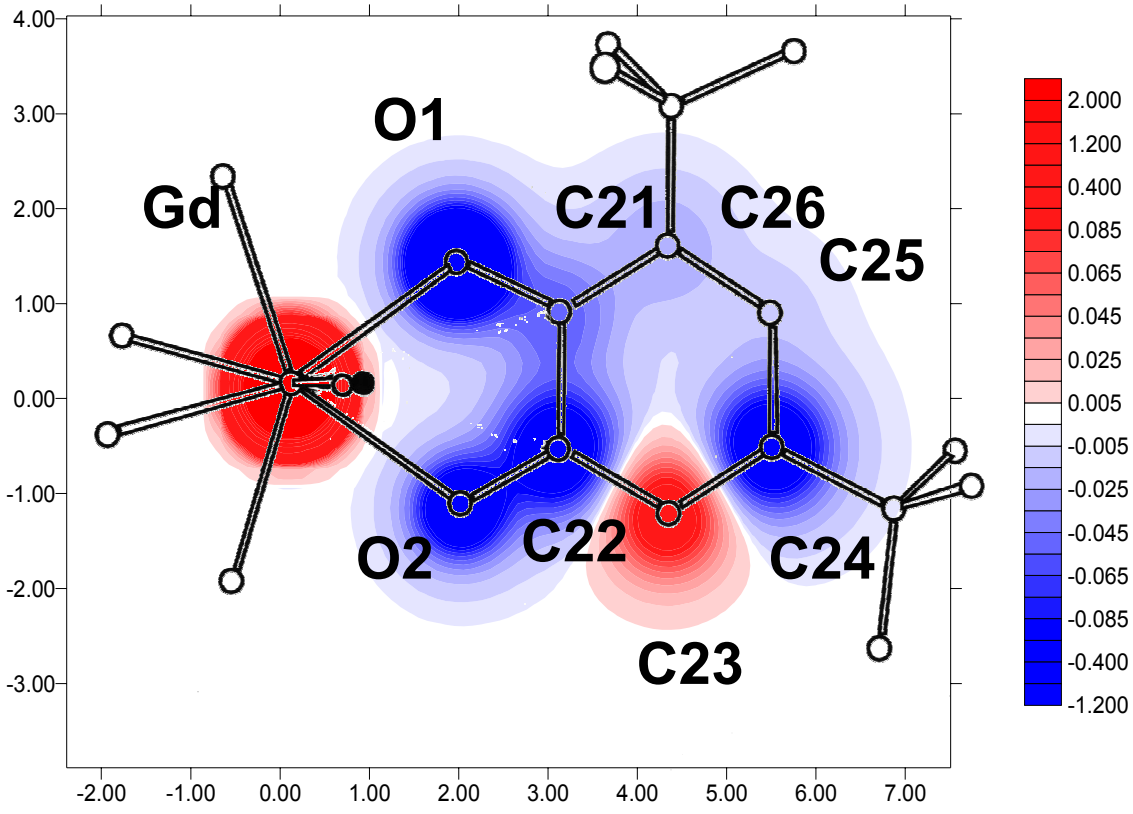

Figure S6.8 *Projection of the induced spin density in the direction perpendicular to the C22C21C25 plane in Gd(HBPz$_3$)$_2$(3,5-DTBSQ) at 1.5K under 7 Tesla*